Rigorous characterisation of photonic devices incorporating novel phase change materials

By

Junchao Song

Thesis Submitted for the Degree of

Doctor of Philosophy

School of Mathematics, Computer Science and Engineering

City, University of London

Feb 2020

Table of contents

page

List of tables

Table **Page**

List of Figures

Fig. **Page**

Acknowledgements

First and foremost, I would like to express my sincere gratitude to my supervisor, Prof. B. M. Azizur Rahman, for his abundant assistance, guidance, suggestions, and encouragement during the preparation and completion of this dissertation. His keen and vigorous academic observation enlightens me not only in this dissertation but also in my future study.

I would like to thank my colleague, Dr. Souvik Ghosh, for his impressive kindness and patience, valuable advice, and technical support throughout my research project. I would also like to sincerely thank all other colleagues in the Photonics Modelling Research group for maintaining a friendly and joyful work atmosphere.

Most importantly, I do appreciate the love, understanding and unremittingly supporting from my dearest wife Mrs. Ruby Song, my father Mr. Jinhua Song and my mother Mrs. Xiaolan Min. Without them, this thesis would never have been possible.

Declaration

I do sincerely declare that I am the only author of this dissertation and the work in this dissertation was carried out in accordance with the requirements of the regulations by City, University of London, UK. Any use of books, journal papers, dissertations and other academic resources in which copyright exists are cited carefully with the title and its authors. The contents of the dissertation are original and have not been submitted for any academic or professional degree.

I grant the power of discretion to the Librarian at City, University of London to allow the thesis to be copied in whole or in part without further reference to the author. This permission covers only single copies made for study purposes, subject to normal conditions of acknowledgement.

Junchao Song

Feb 2020

Abstract

The primary aim of this research work is to develop compact Si Photonic devices incorporating with novel phase change material at the operating wavelength of 1.55 μm. Miniaturisation of active photonic devices, such as optical modulators and switches is crucial to improve the integration density of photonic integrated circuits (PICs). The photonic device based on COMS compatible Si-on-insulator platform have shown great promising due to the footprint reduction and lower power consumption. However, Si modulation is not only limited in the electro-optic but also the thermo-optic effect, and the plasma dispersion effect is also not efficient. The phase change material (PCM) exhibiting a larger refractive index change during its phase transition can be integrated with Si waveguide to mitigate the present Si modulation limitations. The reversible phase transition can be triggered thermally, electrically, and optically in nanosecond. PCM such like GST also possess the self-holding features, so no sustaining power is required to maintain a given state.

Design, optimisations, and performance evolution of those Si-PCM composite waveguides are carried out by a full-vectorial **H**-field finite element method. Initially, modal solutions of a GST-clad Si waveguide and a GST-clad Si nanowire are investigated for comparison for a variety of waveguide parameters. The electro-absorption design is preferred due to a very high loss incurred in electro-refraction design. The coupling loss at input/output junctions for the composite waveguides are also analysed by the least squares boundary residual method. A compact 2-5 μm long electro-absorption modulator incurs only 0.36 dB insertion loss and more than 20 dB extinction ratio is shown to be possible. The new low-loss material GSST is also considered and shown that a 4.75 μm long modulator have a 0.135 dB insertion loss, only 38% of the GST based design and more than 20 dB extinction ratio. The proposed device design is also verified by a finite difference time domain method (FDTD). Additionally, an electrically driven optical switch based co-directional coupling between Si nanowire and ITO-GST-ITO waveguide is also investigated. The modal evolution of the complex supermodes is studied and employed to optimize the coupling length and ITO spacing. The phase-matching condition of the GST thickness is also achieved for efficient power transfer between the waveguides. A 1.7 μm long ON-OFF switch can be obtained with 0.56 dB insertion loss and 22 dB extinction ratio. Finally, a 1 x 2 optical switch based on a directional coupler comprises of a Si nanowire and GSST-loaded Si waveguide is reported. Seven combination parameter sets are reported for the desire coupling length ratio R = 2. The FDTD is used to verify the proposed design and study the power transmission characteristics. A compact and fabrication tolerant 12-16 μm long switch can be achieved based on an optimised directional coupler design with 15-20 nm GSST layer on the Si nanowires shows 0.33-0.35 dB insertion loss.

List of Symbols and Acronyms

Symbols

λ	Wavelength
n	Real part of the refractive index
k	Imaginary part of the refractive index (extinction coefficient)
n_e	Real part of effective index
k_e	Imaginary part of effective index
L_c	Coupling length
k_0	Wavenumber
α	Attenuation constant
β	Propagation constant
ϵ_r	Relative permittivity
μ_r	Relative permeability
ω	Angular frequency
E	Electric field vector
H	Magnetic field vector
D	Electric flux density
B	Magnetic flux density
Si	Silicon
SiO_2	Silica
VO_2	Vanadium dioxide
GST	Germanium-antimony-tellurium
GSST	Germanium-antimony-selenium-tellurium
ITO	Indium tin oxide

Acronyms

PIC	Photonic integrated circuit
SOI	Silicon-on-insulator
CMOS	Complementary metal-oxide-semiconductor
EO	Electro-optical
TO	Thermo-optical
PCM	Phase change material
TE	Transverse electric
TM	Transverse magnetic
MZI	Mach-Zehnder interferometer
FV-FEM	Full-vectorial finite element method
FDM	Finite difference method
FDTD	Finite difference time domain method
LSBR	Least squares boundary residual
ER	Extinction ratio
EA	Electro-absorption
IL	Insertion loss
CT	Cross talk
WG	Waveguide
NW	Nanowire
DC	Directional coupler
R	Coupling length ratio
AM	Amorphous
CR	Crystalline

List of Publications

Published Journal Articles

- **J. Song**, S. Ghosh, N. Dhingra, H. Zhang, L. Zhou, and B. M. A. Rahman, "Feasibility study of a $Ge_2Sb_2Te_5$-clad silicon waveguide as a non-volatile optical on-off switch", *OSA Continuum*, **2**(1), pp. 49-63 (2019).

- **J. Song**, S. Ghosh, H. Zhang, L. Zhou, and B. M. A. Rahman, "Design, optimization, and performance evaluation of GSST clad low-loss non-volatile switches", *Applied Optics*, **58**(31), pp. 8687-8694 (2019).

- H. Zhang, L. Zhou, B. M. A. Rahman, X, Wu, L. Lu, Y. Xu, **J. Song** and J. Chen, "Ultra-Compact Si-GST Hybrid Waveguides for Nonvolatile Light Wave Manipulation", *IEEE Photonics Journal*, **10**(1), pp. 2200110 (2018).

- N. Dhingra, **J. Song**, G. J. Saxena, E. K. Sharma, B. M. A. Rahman, "Design of a Compact Low-Loss Phase Shifter Based on Optical Phase Change Material", *IEEE Photonics Technology Letters*, **31**(21), pp. 1757-1760 (2019).

Conference Papers

- N. Dhingra, **J. Song**, S. Ghosh, L. Zhou, and B. M. A. Rahman, "Design of phase change $Ge_2Sb_2Te_5$ based on-off electro-optic switch", *Silicon Photonics XIII, SPIE. Photonics West, San Francisco, California, United States*, **10537**, pp. 105370Z (2018).

Chapter 1

Introduction

1.1 Aims and objectives

As the Moore's law predicted as early in 1965, that the number of integrated electronic components in a chip would double every two years, the integrated electronic circuit have a frenetic and unparalleled development in past few decades. However, entering 21st century, as the continuous scaling down in electronic chips, the Moore's law has shown its throughput limiting factor not only the processing power but also the electrical interconnect bottleneck problem. One solution is to replace the conventional integrated circuits with photonic integrated circuits (PICs), which use light (photons) instead of electrons can provide numerous advantages including higher speed, greater bandwidth also lower energy loss [1].

Miniaturisation of photonic devices can have significant contributions towards achieving the large-scale PICs. Over the past decade, Si-on-insulator (SOI) platform based photonic devices have emerged and shown a considerable promise not only owing to PIC's footprint and power consumption reduction but also their compatibility with the well-developed complementary metal-oxide-semiconductor (CMOS) manufacturing process.

An optical modulator or optical switch is an essential component for on-chip PICs and today, electro-optical (EO) effect and thermo-optical (TO) effect are the primary design mechanism for optical modulation/switching. Several Si-waveguide based modulator/switch designs have already been investigated and

shown fast modulation frequency (>1 GHz) and larger modulation depth (>15 dB) than the conventional $LiNbO_3$-based modulators to date [2-3]. However, due to Si's weak electro-optic coefficient, it requires a 10 μm long interaction length for Mach–Zehnder interferometer (MZI) based modulators, hence a large device footprint [2]. High-quality micro-ring resonator devices require a smaller device length but still limited to a very narrow spectral bandwidth and strong wavelength dependence [3]. The inefficient TO and EO effects in Si provide a very poor refractive index tuning, and these effects based photonic device are all volatile, which means need a huge power consumption for turning and continuous power to maintain during the modulating/switching.

The phase change material (PCM), exhibits a drastic change in its optical property (refractive index and extinction coefficient) during a solid-state phase transition, and can be integrated with the SOI platform as active material to design a compact and efficient Si optical modulator/switch. The most common PCMs used in photonic applications are transition metal oxides (VO_2, V_4O_7, $NdNiO_3$) and chalcogen-based alloys (GeTe, $GeSb_2Te_4$, $Ge_2Sb_2Te_5$). The phase transition of PCMs is very fast in nanosecond and can be triggered by thermally, optically or electrically. The state change of the PCMs is reversible and can be switched more than 10^4 cycles with stable composition [4]. Some chalcogen PCMs also possess the "self-holding" feature, which means it only requires energy to switch from one state to another, but no continuous energy is needed to maintain a given state [5]. Both real and imaginary parts of refractive index of PCMs have significantly increases in the crystalline phase, mainly due to the chemical bonding. The high refractive index difference in the phase transition is an outstanding feature can be implemented to reduce Si device's footprint. Moreover, as the phase transition can be controlled, the switchable reconfigurable photonic devices can be achieved [6]. By carefully controlling the heating or stimulating pulses, intermediate phases of PCMs can be achieved, which allowing for multi-level photonic applications.

The main aim of this thesis is the design, optimisation and performance evolution of a compact, low loss and self-sustained optical switch based on the novel Si-PCM hybrid waveguide at the telecommunication wavelength of 1.55 μm.

Design, fabrication, characterisation, error analysis, and possible redesign are the fundamental needs of the photonic devices' development. Here, the numerical simulations play an important role to analyse the devices before costly fabrication and experimental validation. A compact optical modulator or switch may comprise many of isolated or composite optical waveguides with multi layers. Investigation and enhancement of fundamental light guiding phenomenon and wave propagation characteristics through the numerical simulations are necessary for their effective designs. The rigorous full-vectorial finite element method (FV-FEM) have shown its high efficiency for design, optimisation, and performance analysis of complex structured waveguides compare to other modelling methods [7], which will be used in this thesis as a powerful numerical tool.

The primary objectives of this research work can be summarized as follows:

- To implement the rigorous, accurate, and efficient **H**-field based full-vectorial finite-element method (FV-FEM) in conjunction with the perturbation technique to analysis the variety of PCM-loaded Si waveguides.
- To implement the FV-FEM to achieve the modal solutions with the variations of the hybrid waveguide width and height of different layers to determine the suitable device modulating/switching mechanism, compact device length and the lower modal insertion loss.
- To implement the least squares boundary residual (LSBR) method combined with the modal solutions obtained from the FV-FEM to calculate the coupling loss at the butt-coupled junctions to determine the optimal waveguide parameters in order to achieve a lower insertion loss and a higher extinction ratio of the device.
- To implement the finite difference time domain (FDTD) simulations to verify the validity and device performance of the proposed PCM clad low-loss non-volatile switches which have been designed by the FV-FEM and the LSBR.

- To implement the FDTD simulations to investigate the propagation and power transfer characteristics of the PCM-loaded Si waveguide and Si nanowire composed directional coupler based 1 x 2 optical switch.

1.2 Thesis outline

This thesis comprises eight chapters, including the current introduction chapter and Appendices. The chapter contents are briefly described as follows:

Chapter 2 represents a brief historical review starting from the electronic integrated circuit throughput limitations, the PIC's development and advantages, the working function of the waveguide to the advantages and disadvantages of the Si photonics. Several basic effects for electro-refraction (ER) and electro-absorption design (EA) are introduced, Si modulation is not only limited in the electro-optic effect but also the thermo-optic effect. Plasma dispersion effect also discussed which is still not efficient for Si modulator/switch. Followed, the phase change material and its outstanding features are reviewed, the most common PCMs (VO_2, GST, GSST) are introduced in detail including its refractive index, phase transition stimulation methods, limitations, and state-of-the-art photonic applications. Key publications reporting on the PCM-Si hybrid photonic devices are reviewed and presented in a tabular form.

Chapter 3 consists of discussion on the numerical modelling methods used for the design, optimisation, and performance evolution of the Si-PCM hybrid waveguides and devices in this research work. The full-vectorial **H**-field finite element method (FV-FEM) is redeveloped especially for an accurate modal analysis of Si-PCM hybrid waveguides. In order to study the waveguide junctions and modal losses, the least squares boundary residual (LSBR) method and perturbation formulation are used in simulation combined with the FV-FEM. The three-dimensional finite difference time domain method (3D-FDTD) is also reviewed and will be used for studying light propagation, power transfer and mode conversion problems in this thesis. The advantages, disadvantages and modelling procedures of the 3D-FDTD are also discussed in detail.

Chapter 4 presents the design optimisation of a thermo-driven 1x1 EA modulator based on a GST-clad Si rib waveguide and a GST-clad Si nanowire for comparison at the wavelength 1.55 μm. Initially, the FV-FEM is used to simulate the Si-GST waveguide in order to study the modal field profiles of the input and active sections. The complex modal solutions with effect of Si slab thickness, waveguide width, and GST layer thickness for both waveguides are investigated by using FV-FEM. The ER or EA type device design is determined by the insertion loss and device length obtained from the modal solutions, and the 20 dB EA design is preferred due to a very high loss incurred in the ER design. The coupling loss at input/output junctions for two hybrid waveguides with effect of slab thickness and GST thickness are calculated by using LSBR. The device length and the total insertion loss comprises of both modal loss and junction loss of the modulator is optimised by a combination of the waveguide width, Slab thickness, GST thickness. In the next section, the device fabrication and measurement process, experimental and simulation results comparison are also described.

Chapter 5 describe a novel co-directional coupling design between Si nanowire and ITO-GST-ITO waveguide and is incorporated in the design of a "ON-OFF" electro-optic switch. The phase matching condition at GST crystalline state is determined by the modal effective index of the even and odd supermodes of the composited waveguide, which are investigated by using FV-FEM for the optimisation of ITO and GST thicknesses. The variations of fundamental mode profiles, mode loss and coupling length of the hybrid waveguide are presented in order to determine the optimal ITO spacing and the phase-matching GST thickness. The power coupling efficient at the input junction, device length and power evolution of the phase-matched composited waveguide with optimal parameters are validated by using 3D-FDTD. The total insertion loss and extinction ratio of the device is also calculated and presented as the Figure-of-Merit of this switch.

Chapter 6 presents a new low-loss phase change material GSST incorporated with Si rib waveguide design and its application of a 1x1 electro-absorption modulator at the 1.55 μm wavelength. The GSST layer is loaded on a standard single-mode Si rib waveguide to form the active section of the device. The

fundamental mode field profile, modal solutions are calculated by FV-FEM to determine the ER or EA type design. The effect of GSST layer thickness and Si slab thickness on device length and modal insertion loss are also investigated and optimised. The LSBR is used to calculate the both input/output coupling loss to identify the optimal waveguide parameter combination to achieve a lower IL and higher ER. The device performance is comprised with the GST results in Chapter 4 and presented in a table. Moreover, the proposed device performance (device length, ER) validation by using the 3D-FDTD simulations is are carried out and analysed in detail.

Chapter 7 describes the design of a GSST-loaded Si waveguide composited with a Si nanowire to form a two-waveguide asymmetrical directional coupler (DC) and its application in 1x2 optical switching. The phase matching condition at GSST amorphous state is determined by the modal effective index of isolated waveguide, which calculated from the FV-FEM with waveguide width and GSST layer thickness variations. A variety 2D and 3D contour modal field profiles of the composite waveguide are presented. The effect of Si nanowire width, waveguide height and GSST layer on device coupling length at GSST amorphous and crystalline states and its ratio (R) are investigated. The GSST layer thickness and waveguide gap are optimised for the desire target R = 2 is presented in a table. The propagation and power transfer characteristics for the proposed design DC is studied by the 3D-FDTD, the power evolution at different launching ports, power transfer between two waveguides at both states, maximum output power, IL and ER are calculated and analysed. At last, the fabrication process and the fabrication tolerance with the effect of waveguide width and gap variations are presented.

Finally, in **Chapter 8**, general conclusions achieved from this thesis are summarised. Possible future research work is also suggested.

Chapter 2

Overview of Si photonics and Phase Change Material

2.1 Photonics Integrated circuit (PIC)

2.1.1 Photonics

Photonics, a well-known physical science, can be described as a research field whose goal is to perform generation, detection and manipulation of light or other energy carried by photons. Photonics is a developed as an emerging field, began with the invention of the laser in 1960^{s}, however, nowadays the photonics covers a large range of science and technology applications, including laser manufacturing, biological and chemical sensing, medical diagnostics and therapy, display technology, and optical computing. It is worth noting that most photonics applications are in the narrow range of visible and near-infrared wavelengths [8].

2.1.2 Photonics integrated circuit

Over 60 years since Jack Kilby's initial demonstration of a working integrated circuit in Texas Instruments, the development progress in electronic integrated circuits has been astounding. Gordon Moore have already foreseen the exponential growth of integrated circuits and introduce the Moore's Law in 1965, it was predicted that the number of integrated electronic components in a chip would roughly double every 18 months [9]. It can be described as transistors in integrated circuits become more efficient, computers become smaller and faster. However,

experts agree that computers should reach the physical limits of Moore's Law at some point in the 2020s. The high temperatures of transistors eventually would make it impossible to create smaller circuits due to the energy consumption for cooling down the transistors could be much more than the energy that already passes through the transistors [10].

The main function of the photonics integrated circuit (PIC) is used to integrate individual optical components such as laser, modulator, detectors, optical amplifiers and waveguides in one optical circuit. The PICs can transmit and process light in an analogue way similar as how electronic integrated circuits work with an electronic signal. The first PIC was introduced by S.E. Miller in 1969 [11], when he proposed to fabricate an integrated optical circuit comprise all the optical components onto a single substrate.

The main reason for using photons instead of electrons because of the higher frequency of light, which translates into a very large bandwidth. The larger the bandwidth, the greater the amount of information that can be transferred. Electronic system is limited by physical problems, an electrical signal with higher frequency will not only reduce the propagation capacities also need in short distance. However, the optical signals can travel through dielectric media at much higher frequencies than the electrical signal in transmission, where materials can be treated as transparent to light. As the higher frequencies, the range of wavelengths are relatively short (0.5-2 μm), which enables fabricate the compact optical circuit and devices [1].

It can be noted that through combining various optical functions onto a single photonic device, the costs of advanced optical devices fabrication will be lower, so that will have a significantly reduction of the advanced optical systems' total cost. It can be concluded that the main objective by photonics integration is to develop miniaturised optical circuits with high functionality on a common substrate.

2.1.3 Waveguide

The optical waveguide is the most essential building block of a PIC. The waveguides are used to connect or interconnect all the optical components such as laser, modulator and photodetector which already integrated on a single chip to

form a workable photonic device. The main function of waveguide is to confine the light locally and then guide it in a specific direction. Waveguide usually can be made of Si, SiO_2, polymer, semiconductors or the other different optical materials depending on the applications.

The first optical channel waveguide was demonstrated in the mid of 1970s using a diversity of materials [1]. Lithium Niobate ($LiNbO_3$) was the material widely used, which can allow for low-loss channel waveguides with high efficiency electro-optic effect. While dielectric materials such as silica glass, polymers, and semiconductors like indium phosphide (InP) and gallium arsenide (GaAs) were also being investigated and employed as suitable material for photonic circuits. Nowadays, the preferences of the optical materials depend on the specific application, owing to the dissimilar optical properties of the material, it has shown that $LiNbO_3$ is mainly used for modulators, InP and GaAs for lasers and photodetectors and SiO_2 for passive devices [12]. Nonetheless, these materials are very difficult to integrate with each other and uneconomic for high-volume production. In order to evolve the photonic integrated circuit technology to the same level as electronic integrated circuit, it will be of great significance to find a material have the high integration density and low cost for large-scale PICs.

6.2 Si photonics platform

Silicon (Si) photonics is one of the most promising platforms having multiple advantages over the other conventional substrate materials.

The concept of Si photonics was introduced by R. Soref in the mid of 1980^s [13]. One of the advantages to use Si for photonics integration is because Si is transparent at the infrared wavelength at which optical communication systems operate (around 1.3 - 1.6 µm). It also has been known that Si is an inexpensive material, because Si is the second most abundant element on earth, next to oxygen which great for cost reduction and mass production. Another advantage of Si photonics is the strong optical confinement offered by the high index contrast, such as between Si and SiO_2. This strong refractive index contrast as Si ($n = 3.45$) and SiO_2 ($n = 1.45$) makes it possible to reduce the size of the photonics circuits [14].

Moreover, a unique advantage of Si photonics derives is the possibility of integration of electronics and photonics on the same chip, leading to submicron device footprints.

Over the past decade, silicon-on-insulator (SOI) platform based photonic devices have shown considerable promise due to significant reduction in PICs size and power consumption along with their compatibility with the microelectronic circuits based on CMOS technology. The SOI wafer consists of a thin Si waveguide layer as the waveguide core on top of a buried oxide (SiO_2) as the cladding layer on a Si substrate with no optical functionality [15]. In Si photonics, normally the strip-type Si waveguide with a rectangular core and a rib-type waveguide are used. The first Si waveguide was a rib waveguide with a large cross-section and developed by Bookham Technology. This rib waveguide has less loss and it can be coupled with fibre easily as the larger spot-size, however, this rib waveguide needed a large bending radius [16]. On the other hand, the Si strip waveguide consisting of a rectangular Si core and SiO_2 cladding has very high index core with a low index cladding, it leads to extremely strong light confinement. The core size of this waveguide can be designed less than 1 μm at 1.55 μm wavelength with a few micrometres bending radius [17].

However, besides the multiple advantages discussed before, there are still limitation of Si as the material in photonics integration. One major limitation is that, Si is an indirect band gap semiconductor so that it will leads to inefficient band to band light emission so that Si cannot amplify the light [18]. Moreover, due to the inversion symmetry of the crystal structure of Si, the linear electro-optic effect will be absence in the Si based PIC. Additionally, the packaging and coupling of fiber optics is a challenge in Si photonics, the coupling losses are critical and must be minimised [14].

However, these limitations did not stop the researchers enter the Si photonics, but rather more researches have been participating in this field. It caused the emergence of Si photonic integration applications such as, modulator, laser, optical filter, coupler and detector in the recent years.

2.3 Limitations in Si modulating and switching

An optical modulator is a device, which is used to modulate a beam of light (characteristic change) which is propagating either in free space or through an optical waveguide. Depending on the characteristics of a light beam which is controlled, modulators may be classified as amplitude modulators, phase modulators or polarization modulators, etc [19].

According to the optical properties of the materials that are used to modulate the light beam, modulators also can be divided into two groups: electro-absorption modulators and electro-refraction modulators. In electro-absorption modulators the imaginary part of the refractive index (extinction coefficient) of the material is changed, whereas in electro-refraction modulators the real part of the refractive index of the material is changed. In order to change the imaginary part of the material refractive index in the electro-absorption modulator, there are several effects such as Franz-Keldysh effect, the Quantum-confined Stark effect, excitonic absorption, changes of Fermi level, or changes of free carrier concentration can be used [20]. On the other hand, the electro-optic effect often used to change the real part of the material refractive index to perform an electro-refraction modulator.

Inducing an electric field on the material is the primary and useful approach to achieve the Pockels effect and the Kerr effect for the conventional electro-optic modulator design. Pockels effect, also known as the linear electro-optic effect, the refractive index change is proportional to the electric field. The Pockels effect occurs only in crystals that lack inversion symmetry, such as $LiNbO_3$. The Kerr effect, also called the quadratic electro-optic effect, is a change in the refractive index of a material is directly proportional to the square of the applied electric field. All materials show some Kerr effect, but certain liquids have more strongly affect than others. However, it has been shown that due to the centro symmetric lattice structure of the Si, the Pockels effect is absence in the pure Si [21]. However, Kerr effect is also very weak in Si, it only can be achieved a reactive index change of 10^{-4} in Si under a such high electric field $E = 10^6$ V/cm at the telecommunications wavelengths of 1.3 μm and 1.55 μm, therefore modulation of light is not possible

[20]. The thermal modulation can be used due to the large thermo-optic coefficient of Si, but this modulation approach is too slow for the high frequency applications because it only offers 0.01 refractive index change of Si with every 100 °C temperature variation [22].

At present, one of the most common method of achieving modulation in Si devices has been to unitize the plasma dispersion effect. The plasma dispersion effect contributes in changing the both real and imaginary parts of refractive index by electrical manipulating the free-carrier concentration in Si waveguide and can be performed by carrier injection and carrier depletion [21]. For carrier injection modulation, carriers are injected by forward biasing the PN junction. This type of the modulation has the advantage that it can allow large changes in the carrier density and therefore can achieve a higher modulation efficiency. But it is limited in speed by the recombination rate of the carriers and consume relatively high power [23]. On the other hand, carrier depletion, which modulates carrier density by reverse biasing the junction, which is relatively fast and consumes less power as little current flows through the junction. However, it requires a higher overlap between the PN junction and the optical field, which leads to a larger insertion loss due to the initial doping of PN junction and lower modulation efficiency due to the small change in depletion width [24].

2.4 Phase change material (PCM)

The optical phase change material (PCM) comprising at least two reversible phase states have been considered as one of the most promising approaches to overcome the fundamental limitations in today's Si based photonic devices [25]. Owing to the large difference exhibit in both real and imaginary parts of PCM's refractive index when undergoing a solid-state transition, PCM can be used as an active component to modulate the transmitted light when integrated with Si photonic waveguides. The integration of PCM with Si photonics platform have already been investigated extensively and variations of ultrafast and ultra-compact optical devices have been reported [26].

The research on PCM for optical applications started as early as 1968, when first time it was discovered by S. R. Ovshinsky [27]. The phase change was usually realized by laser irradiation. The first commercially application of PCMs was in rewritable optical data storage. In the meantime, several physical features of the PCM haven been researched as it used in data memory [28]. It was found that the size effect of PCM is not only dominating in its crystallization speed and temperature but also the work function contrast [29]. The PCM distinct features are not only the transformation time between two phase states can be as fast as in sub-nanosecond but also the ability to remain stable at the room temperature for a long time [30]. Consequently, a wide tunability of the PCM's optical and electrical properties can be exploited for nonvolatile optical applications such as display, optical signal processing [31], and optical switching [32].

The most common PCMs used in photonic applications are transition metal oxides (VO_2, V_4O_7, $NdNiO_3$, $PrNiO_3$) and chalcogen-based alloys (GeTe, $GeSb_2Te_4$, $Ge_2Sb_2Te_5$). Several common phase change materials will be studied in this section and its integration with the Si platform will also be reviewed.

2.4.1 Vanadium dioxide (VO_2)

In recent years, the scope for PCM has been extended to include oxides, such as vanadium dioxide (VO_2). VO_2 is a correlated electron material that has an insulator-metal phase transition (IMT) at 68 °C [33]. The phase transition of VO_2 between insulator and metal states can be triggered by using thermal heating (beyond $T_c \approx 340$ K at standard pressure) [34], electric fields applying ($E = 10^5$ V/cm^{-1}) [35], carrier density injections ($n_e \approx 10^{18} cm^{-3}$) [36], terahertz pulses [37], and surface charge accumulations [38]. The phase transition is reversible, and the insulating phase can be restored by removing the stimuli. However, the threshold for the metal-insulator (MIT) transition is lower compared to the threshold in the IMT due to the inherent hysteresis [39].

Unlike other competitive optical materials, such like SiGe, where the applied electric field slightly changes the bandgap energy, the bandgap energy of VO_2 at the near-infrared wavelength range completely disappears, which leads to a large

change in its refractive index. The complex refractive index of the insulating phase is changing from 2.9 + *j**0.4 to 2.0+ *j**3.0 in the metallic phase. As a result, the absorption modal loss of the waveguide between two states changes from 0.4 dB/μm to 3.1 dB/μm, which can enable devices with Extinction Ratio (ER) exceeding > 15 dB and device length less than 7 μm [40]. The large change in the refractive index of VO_2 and its hysteresis make it an attractive material for optical applications. The real part of VO_2 refractive index change is suitable for spectral tuning and phase control, while the imaginary part changes are widely used for amplitude switching and mode suppression, also the hysteresis is useful for optical memory applications [41].

VO_2 can be employed in designing the active photonic devices due to its large refractive index contrast which can make the devices more compact and reduce the overall size of the system on the chip. However, apart from the large refractive index changes of VO_2 across IMT, the excessive optical loss in both the insulating and metal phases is an inevitable issue for optical applications [42]. The VO_2 should be hybridized with low loss guide platform like Si waveguide or surface Plasmon metal hybrid waveguide for VO_2 based photonic device design.

The first Si optical modulator incorporating VO_2 was described by Briggs, it comprises of patterned VO_2 thin films deposited on top of a single mode SOI waveguide [43]. The optical modulation was achieved by heating the entire sample above 68 °C and therefore triggering the phase transition in VO_2. It was shown that when the single-mode waveguides are used at λ = 1550 nm, the optical modulation of the guided transverse-electric (TE) mode of is more than 6.5 dB with 2 dB insertion loss over a 2 μm active device length. However, the modulator switching time was very slow due to the thermal actuation.

2.4.2 $Ge_2Sb_2Te_5$ (GST)

In recent years, the chalcogenide phase change materials have shown considerable promising in rewritable optical recording [44] and optical memory [4] due to their significant electrical and optical properties contrast between the amorphous and crystalline state.

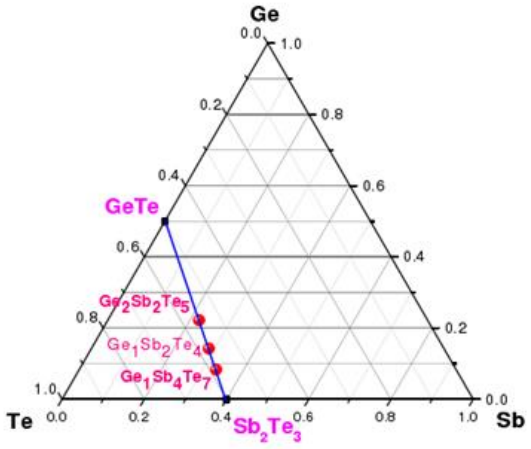

Fig. 2.1. Phase diagram of the GeSbTe ternary alloy system. [46]

In the Ge-Sb-Te (Germanium-antimony-tellurium) alloy system, the GeTe-Sb_2Te_3 pseudo-binary compound are widely used for PCM and it can be considered as a mixture of the two binary compounds GeTe and Sb_2Te_3. The phase diagram of the Ge-Sb-Te ternary alloy system shown in Fig. 2.1 helps classify different PCMs based on Ge-Sb-Te alloys. GeTe was the first chalcogenide-based PCM material to show a relatively fast crystallization speed with a large optical constant due to excess vacancies move the Fermi energy to the extended states area [45]. Subsequently, several Ge-Sb-Te alloys such as $Ge_1Sb_4Te_7$, $Ge_2Sb_2Te_5$, and $Ge_1Sb_2Te_4$ were identified all along a pseudo-line that connects the GeTe and Sb_2Te_3 compounds. Moving from GeTe towards Sb_2Te_3 on the pseudo-line, crystallization speed increase, melting and glass transition temperature decrease and the data retention (retention of the amorphous state) decrease [46]. In the other words, Sb_2Te_3 offers the fastest crystallization speed, but its amorphous state is unstable. In contrast, GeTe offers a very stable amorphous state but a long crystallization time. Therefore, a compromise between the crystallization speed and the amorphous state stability can be considered by selecting the Ge-Sb-Te alloys at the centre of the pseudo-line. For instance, $Ge_2Sb_2Te_5$ offers a fast crystallization speed (< 20 ns) [47] with a moderate glass transition temperature (100-150 ℃) that ensures the long-term data retention (~10 years) [48].

$Ge_2Sb_2Te_5$, common known as GST, is a typical phase change material of the chalcogenide glasses group which will be discussed in detail in this section also integrated with Si waveguide for photonic devices design in the **Chapter** 4 and 5.

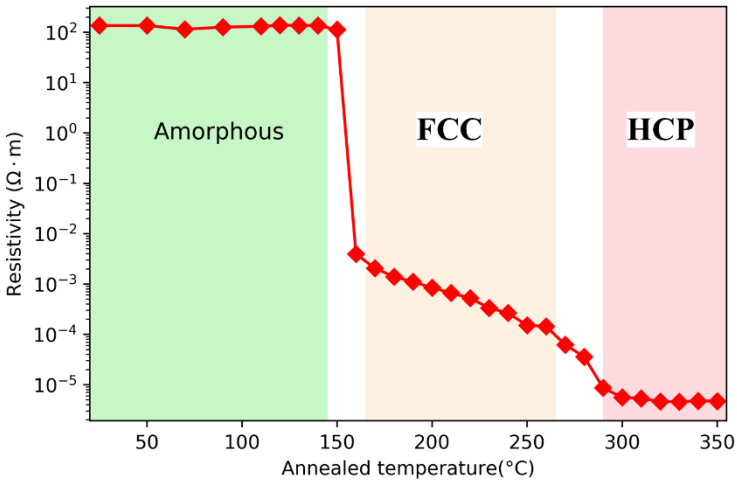

Fig. 2.2. Resistivity of $Ge_2Sb_2Te_5$ as a function of annealed temperature [49].

The large electric resistivity contrast between amorphous (high) and crystalline (low) phases is a significant electric property of $Ge_2Sb_2Te_5$ (GST). P. Guo have reported a GST resistivity measurement to characterize the phase transition during the annealing process in [49]. The As-deposited GST thin film in amorphous state was created by using magnetron sputtering, then the samples are placed on a hot plate and heated from 25 ℃ to 350 ℃ for 2 min, then the sample is cooled down to room temperature. The resistivity of GST as a function of annealing temperature is shown in Fig. 2.2 and it can be observed that there are two distinct phase transitions in this figure. The first transition occurs near 150 ℃, the amorphous state GST is crystallized to a face-centred-cubic (FCC) phase with a huge decrease in resistivity. Then with the annealed temperature increase to 300 ℃, the FCC phase GST will transform to a hexagonal close-packed (HCP) phase GST [50]. The intermediate states comprise of the mixture of amorphous state and crystalline state also appeared in the amorphous to FCC phase transition and FCC to HCP phase transition during the annealing.

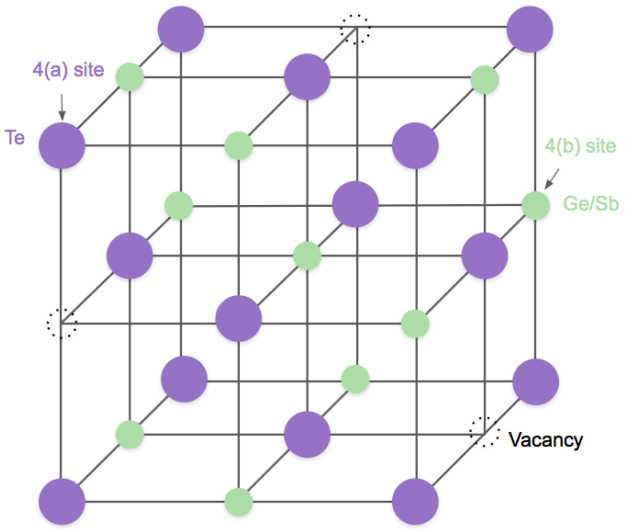

Fig. 2.3. Atomic structure of the FCC crystalline GST [51].

It is important to study the atomic structure property of the GST after crystallization. As discussed before, by heating the amorphous state GST to 150 ℃, GST alloys will form an FCC (rock-salt) lattice structure. If continuing heat the GST to 300 ℃, it will form a stable hexagonal structure. A. Pirovano have reported that since the GST amorphous state can be crystallized to FCC phase faster, the crystalline GST is always at the FCC phase in fast phase-change operation, and its lattice structure is shown in Fig 2.3 [51]. It can be noted the 4(a) type sites is only occupied by Te atoms, however, the 4(b) type sites are occupied by Ge, Sb atoms and intrinsic vacancies randomly. On the other hand, for the crystalline GST with HCP structure have space groups *P*3*m* or *R*3*m*, which the Ge, Sb, and Te atoms are stacked along of the *c* axis [52].

Unlike the crystalline state, the arrangement of atoms in the amorphous state is a subject of debate. Some studies have assumed that the atoms in amorphous state locally similar as the crystalline state, but it lacks the long-range atomic order observed in the crystalline state. On the other hand, several experimental X-ray spectroscopies have introduced a difference in the local arrangement of atoms in amorphous and crystalline states. The Ge atoms that occupy octahedral positions in the crystalline state phase are switched to tetrahedral coordination in the amorphous phase [53].

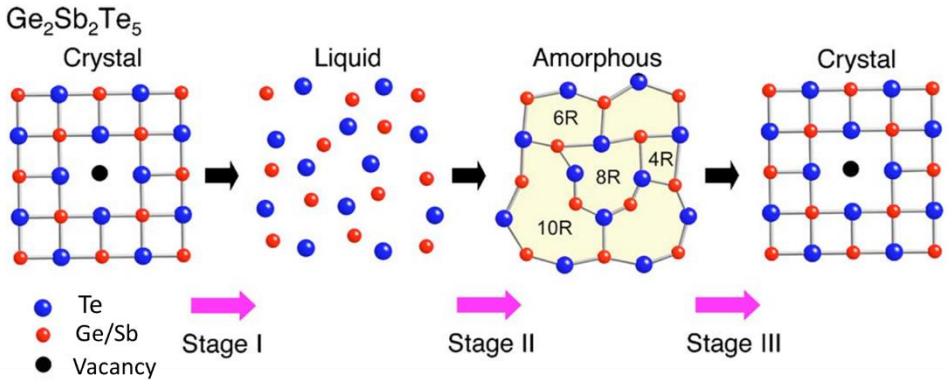

Fig. 2.4. Schematic presentation for the possible ring size transformation in Re-amorphization and crystallization process in $Ge_2Sb_2Te_5$. [54]

S. Kohara also have carried out an x-ray diffraction study to investigate the reason of the GST fast crystallization speed [54]. The mechanisms of crystal-liquid-amorphous process and amorphous-crystal (crystallization) transition in GST are represented by ring statistics and shown in Fig. 2.4. It can be noted that, in the stage I of the crystal-liquid process, atomic configuration of the GST is disarranged and melted in liquid. Then at stage II, in the liquid-amorphous process, only even-numbered rings are created in GST amorphous state. In the stage III, amorphous-crystal phase-change process, the GST amorphous phase only transforms the large-size even-numbered (8-, 10- and 12-fold) rings to GST crystalline phase FCC structure (4- and 6-fold) rings. In this process, Ge (Sb)–Te bonds are formed and no bond is broken. It can be concluded that the only even-folded ring structure of the GST amorphous state is the key for the fast crystallization speed.

This significant change in bonds also results in a great difference in optical property such like refractive index during the GST phase transition. The optical constants of GST are important for investigating how the light interacts with the GST-based optical devices. Since the amorphous state of GST is constructed from predominantly covalent bonds, it tends to have a lower refractive index as: $n_{(AM)} = 4.6 + j*0.12$ [55]. On the other hand, the large refractive index of GST in crystalline state due to the highly polarizable delocalized p-orbital resonant bonding, it will lead to a larger real and imaginary parts of refractive index as:

$n_{(CR)}$ = 7.45 + *j**1.49 [56]. This high index contrast is a significant property in integrated photonics as it allows for the implementation of smaller footprints. As the state change can be triggered reversible and repeatable, the GST have great potential for switchable reconfigurable photonic devices.

Despite the large optical property contrast, unlike other phase change materials, GST possesses the self-holding feature, which means it requires energy only to support the phase changed from one state to another state, but continuous power supply is not needed to maintain a given state.

Hence, these outstanding electric and optical properties of phase change material GST can be utilized in development of on-chip non-volatile photonic applications such as Nano pixel display, photonic synapse, optical memories, optical modulation, and reconfigurable optical switching.

2.4.3 $Ge_2Sb_2Se_4Te_1$ (GSST)

The optical PCM, exemplified by metal oxide such as VO_2 and chalcogenide alloys such as GST have been investigated extensively and exploited in a wide range of photonic applications including photonic memory, optical switches and electro-absorption modulator due to the large extinction coefficient contrast. However, both of these PCM based devices are generally suffer from large optical losses even in the dielectric state and amorphous state. GST in amorphous state is optically absorbing at the telecommunication 1550 nm due to its small bandgap which will lead to an inter-band absorption. On the other hand, the crystalline GST is plagued by high free carrier absorption in the mid-wave and long-wave infrared wavelength. This large optical loss can limit many conventional PCM based photonic device performance.

Y. Zhang and her group have reported a new class of optical PCM, Ge-Sb-Se-Te (GSST) alloys in 2017 [57]. A group of GSST thin films with compositions of $Ge_2Sb_2Se_xTe_{5-x}$ (x = 1, 2, 3, 4, 5) have been tested by using thermal evaporation. The Se experiments have confirmed that the Se element substitution of Te element will increase the optical bandgap of the material, which enable low loss can be achieved in the 1310 nm and 1550 nm telecommunication wavelengths. On the

other hand, the Hall measurements also have shown that the GSST have reduced free carrier concentration and mobility compared to the GST, which will suppress the free carrier absorption in the infrared wavelength. Moreover, unlike GST exhibits an intermedia FCC phase during phase transition, the GSST will be crystallized directly into a stable hexagonal structure.

Y. Zhang also have reported the enhanced optical performance of GSST compared to GST on a single mode SiN waveguide-based resonator device [57]. They have shown that the device integrated with GSST material have a large ON/OFF extinction ratio of 41 dB and an insertion loss of 0.2 dB, which show great improvement than present GST-based device.

The complex refractive index of $Ge_2Sb_2Se_4Te_1$ (GSST) at operating wavelength 1550 nm are reported as: n (AM) = 3.4 + j*0.00018 and n (CR) = 5.1 + j*0.5, respectively. The low optical extinction coefficient of GSST amorphous state, which is only 0.00018, over 600 times smaller than that of the GST [58]. The large optical property contrast between the two states in GSST can permit different modal confinement factors in the two states. The GSST based photonic device can be designed to have large modal confinement within the GSST layer when it is in the low loss amorphous state, and minimal optical field overlap with GSST when it is switched to the lossy crystalline phase. Such enhanced optical performance of the GSST will open up numerous emerging applications based on non-volatile photonic reconfiguration compared to conventional PCM.

Several researches work on photonic modulators and switches incorporating phase change material hybrid with the Si waveguide based on SOI platform have been reported and an overview of those published results are listed in the Table 2.1. In this thesis, our work is mainly focused on the design and optimisation of Si-PCM hybrid waveguide based photonic switches and modulators for low insertion loss (IL), high extinction ratio (ER), and compact device length with better fabrication tolerances.

Table 2.1 Published works on phase change material and Si hybrid waveguide based photonic device

Photonic device	Device length	Phase change material	Operating wavelength	Device performance (IL/ER/CT)	Evaluation method and reference
VO_2 clad Si rib WG on SOI based modulator (TE)	2 μm	65 nm VO_2, thermally $n_i = 3.21 + j*0.17$ $n_m = 2.15 + j*2.79$	1550 nm	IL = 2 dB, ER > 6.5 dB	Experimental and simulation [43]
Cu-SiO_2-VO_2-SiO_2-Cu plasmonic WG modulator	200nm	50 nm VO_2, electrically $n_i = 3.243 + j*0.3466$ $n_m = 1.977 + j*2.53$	1550 nm	IL = 1 dB, ER = 10 dB	Simulation [59]
VO_2 clad Si rib WG on SOI based switch (TE)	1 μm	150 nm VO_2, electrically $n_i = 2.9 + j*0.4$ $n_m = 2.0 + j*3.0$	1550 nm	IL = 5 dB, ER = 12 dB	Experimental [42]
SPP-VO_2 WG on SOI based switch	7 μm	280 nm VO_2, thermally Same as above	1550 nm	IL = 6 dB, ER = 16.4 dB	Experimental and simulation [40]
Si-SiO_2-VO_2-Cu plasmonic WG 1x1 loss modulator	500nm	120 nm VO_2, electrically $n_i = 3.243 + j*0.346$ $n_m = 1.977 + j*2.53$	1550 nm	TE: IL = 2.73 dB, ER = 3.87 dB TM: IL = 1.79 dB, ER = 8.7 dB	Simulation [60]
Si-SiO_2-VO_2-SiO_2-Si and NW based DC modulator	9.47μm	10 nm VO_2, electrically (Same as above)	1550 nm	IL_{off} = 0.77 dB, ER = 3.4 dB	Simulation [61]
TE/TM polarizer based on SOI	1 μm	120 nm VO_2 $n_i = 3.21 + j*0.17$ $n_m = 2.15 + j*2.79$	1550 nm	TE: IL = 0.7 dB, ER = 2.1 dB TM: IL = 0.8 dB, ER = 14.2 dB	Simulation [62]

Table 2.1 Published works on phase change material and Si hybrid waveguide based photonic device (continued)

Photonic device	Device length	Phase change material	Operating wavelength	Device performance (IL/ER/CT)	Evaluation method and reference
(N-Si/GST/N-Si) MZI based 2x2 switch (TM)	38 μm	10 nm GST, electrically $n_{AM} = 4.05 + j*0.006$ $n_{CR} = 6.8 + j*0.4$	2100 nm	Cross state (AM): IL = 0.5 dB, CT = - 15 dB	Simulation [63]
2WG DC 2x2 switch (TM)	67 μm	(Same as above)	2100 nm	Cross state (AM): IL = 0.8 dB, CT = - 15 dB	Simulation
1x1 loss modulator	2 μm	(Same as above)	2100 nm	AM: IL (TE) = 0.075 dB IL(TM) = 0.12 dB	Simulation
GST/Si DC on SOI based 1x2 switch (TE)	80 μm	40 nm GST, thermally $n_{AM} = 3.844 + j*0.002$ $n_{CR} = 6.063 + j*0.841$	1578 nm	Cross state (AM) IL = 7 dB, ER = 25 dB	Experimental [64]
Si-GST hybrid WG on unbalanced MZI	1 μm	20 nm GST, thermally $n_{AM} = 3.9027+j*0.0055$ $n_{CR} = 6.0769 + j*0.904$	1550 nm	IL = 0.05 dB, ER = 3.67 dB	Simulation and Experimental [65]
GST-gated Si MMI based Memristive switch	12 μm	30 nm GST, electrically Diameter = 1.2 μm (unknown)	1500-1600 nm	IL = 4.03 dB, ER = 18.59 dB	Experimental [66]
Cu-GST-Si on SOI WG based 1x1 modulator (TE)	0.5 μm	30 nm GST, electrically $n_{AM} = 4.6 + j*0.12$ $n_{CR} = 7.45 + j*1.49$	1550 nm	IL = 0.5 dB, ER = 5.5 dB	Simulation [67]

Table 2.1 Published works on phase change material and Si hybrid waveguide based photonic device (continued)

Photonic device	Device length	Phase change material	Operating wavelength	Device performance (IL/ER/CT)	Evaluation method and reference
AMZI-coupled ring resonator integrated with GST	2μm	15 nm GST, optically $n_{AM} = 3.9027+j*0.0055$ $n_{CR} = 6.0769 + j*0.904$	1520-1580 nm	Maximum ring resonator transmission contrast > 20 dB between AM and CR state.	Simulation and experimental [89]
Si-GST-ITO Strip waveguide	1 μm	30 nm GST, $n_{AM} = 3.94 + j*0.045$ $n_{CR} = 6.11 + j*0.83$	1550 nm	Optical excitation: IL = 0.21 dB, ER = 11.58 dB, Operation speed = 8 ns. Electrical excitation: IL = 2.34 dB, ER = 7.91 dB, Operation speed = 70 ns	Experimental and Experimental [94]
GST disk loaded Multimode interferometer (MMI)	12.4 μm	Same as above	1550 nm	Optical excitation: IL = 0.59 dB, ER = 12.85 dB, Operation speed = 6 ns. Electrical excitation: IL = 0.56 dB, ER = 12.66 dB, Operation speed = 46 ns.	Simulation and Experimental [94]

Table 2.1 Published works on phase change material and Si hybrid waveguide based photonic device (continued)

Photonic device	Device length	Phase change material	Operating wavelength	Device performance (IL/ER/CT)	Evaluation method and reference
GSST clad SiN strip WG 1X2 switch	40 μm	60 nm GSST, electrically $n_{AM} = 3.4 + j*1.8x10^{-4}$ $n_{CR} = 5.1 + j*0.42$	1550 nm	AM: IL = 0.06 dB, CT = -27 dB CR: IL = 0.4 dB, CT = -50 dB	Simulation [58]
2WG DC on SOI based 1x2 switch (TE)	16.7 μm	80nm GSST, electrically $n_{AM} = 3.3258 + j*1.8x10^{-4}$ $n_{CR} = 5.083 + j*0.35$	1550 nm	Cross state (AM): IL = 0.0.083 dB, CT < 12.8 dB	Simulation [68]
3WG DC on SOI based 2x2 switch (TE)	15.4 μm/ 17.4 μm	(Same as above)	1550 nm (BW = 58 and 70 nm)	Cross state (AM): IL = -0.018 dB, CT < 31.3 dB IL = 0.046 dB, CT < 38.1 dB	Simulation [68]
3WG DC based 3D-mode DeMUX (TE)	17.65 μm	220 nm GSST, thermally $n_{AM} = 3.39 + j*1.8x10^{-4}$ $n_{CR} = 5.14 + j*0.42$	1550 nm	ON state (AM) IL = 0.16 dB, ER = 15.76 dB CT = -15.91 dB	Simulation [69]
2 WG DC based 3D-Mode Multiplexer (TE)	12 μm	100 nm GSST, thermally (Same as above)	1550 nm	OFF state (AM) IL = -0.38 dB, ER = 18.25 dB CT = -18.63 dB	Simulation [70]
GSST-SiO_2-SiN phase shifter (TE)	21.88 μm	58 nm GSST, thermally $n_{AM} = 3.413 + j*1.8x10^{-4}$ $n_{CR} = 5.074 + j*0.425$	1550 nm	IL = -0.5 dB, CT = -24.5 dB	Simulation [71]

2.5 Summary

This chapter provide a detailed overview of the Si photonics integrated circuit technology and the novel optical phase change material. The photonic integrated circuit have witnessed a rapid development in recent years can be considered to overcome the electronic integrated circuit throughput problem owing to the higher frequency of light. Compare to other conventional substrate materials, Si platform have shown its promise due to low cost, high refractive index contrast allows smaller footprint, low power consumption and compatibility with CMOS for large-scale PICs. However, the Si modulation is not only limited in the electro-optic effect but also the thermo-optic effect. Plasma dispersion effect also not efficient for Si modulator. The phase change material which provides a large refractive index difference can be integrated with Si platform to achieve both strong electro-refraction and electro-absorption effect for Si modulating and switching. The electronic and optical property, phase transition process and stimulation approach, limitations and stat-of-the-art photonic applications of the typical phase change material VO_2, GST and GSST are discussed in detail. All the important Si-PCM hybrid photonic device and their PCM optical property, device performance, operation wavelength, relevant to this work are tabulated in a simplified form.

Chapter 3

Numerical Methods

Nanoscale photonic device require design, characterisation, error analysis, possible redesign and performance optimisation before its expensive high-volume manufacturing. The computerised numerical modelling is an efficient tool to investigate the proposed photonic device at a low cost and also timesaving before the final production. Simulation also can help to study the novel phenomenon that may be hindered with experimental. The analytical, semi-analytical, and closed-form solutions were the major methods for simple device modelling but become limited in nowadays complex devices. In recent years, with the development of computer technology, it become possible to modelling those complex photonic waveguides and devices using computerised codes based on various numerical methods.

3.1 Frequency Domain Methods

The initial step of a waveguide design is to study its fundamental modal properties such as propagation constant, effective index, modal loss, effective area, dispersion, confinement factor and the modal field profiles. Various numerical methods such as the transfer matrix method, finite difference method (FDM) [72], method of lines (MoL) [73], and finite element method (FEM) [74] are already available for modelling photonic devices suitable for user's requirement. Not a single method can be considered as superior than others in all the points. Among them, the finite element-based frequency domain approach is the most powerful

method due to its versatility, high accuracy, less computation resources and manipulation of multiple layers hybrid waveguide with composite materials.

3.1.1 Finite-Element Method (FEM)

The fundamental concept of a FEM is that, a numerical technique to provide an approximate solution at a set of governing equations can be in the form of algebraic, differential, or integral equations with a discretisation process of a problem domain.

The fundamental process of a FEM simulation can be explained as: discretise a complex problem domain into an equivalent set of many smaller simpler sub-domains (elements), rather than solving the original problem as a whole domain in one step, the solutions are formulated by each element in a simplified manner expressed in terms of the values at several points of an element (nodes), and then combine them to obtain the solutions of the original whole domain.

There are two well-known features in FEM that make it superior over other methods such as the finite difference method (FDM). Firstly, a geometrically complex domain of the problem is characterised as a collection of finite number of geometrically simple sub-domains, called "element", which could be different shapes, such as, triangular or rectangular. Secondly, over each element, the approximation functions are derived using the fundamental idea that any continuous function can be connected to by a linear combination of algebraic polynomials.

3.1.2 Variational method and Galerkin method

In general, the FEM can be built up by two approaches: the variational method (Rayleigh-Ritz) and Galerkin method (weighted residual method). Both approaches can generate expression which could be discretised with the FEM and obtain the eigenvalue matrix equations [75].

Galerkin method, is also a form of weighted residual method, directly solves the governing differential equation and discretise it in smaller domains, the contributions from which are summed up, and uses the basis and weight functions to yield the eigenvalue matrix equations. Although, the Galerkin method is straight forward to apply with the FEM, however, for problems with arbitrary domains and

irregular shaped boundaries, the Galerkin method is insufficient to satisfy the natural boundary conditions which may need a tedious computational effort.

For variational method, the differential equation is minimised in terms of variables such as fields, also with respect to a small variation in these variables. The minimisation is conducted by expressing the field as an expansion of trial/basic functions with unknown coefficients to yield the eigenvalue matrix equation. The variational approach is more superior than the Galerkin method, because only one single parameter such as the mode effective index, or resonant frequency is evaluated as the final solution [75]. It is easy to set up numerical methods by using variational approach and couple with perturbation analysis. The matrices in variational approach are always symmetric which provide a great simplification in the computation. Moreover, for majority of electromagnetic problem, the natural boundary condition can be left free.

Therefore, the variational approach is more suitable to solve a range of electromagnetic problems. In this thesis, the FEM used has been derived and implemented by using the variational formulations.

3.1.3 Variational formulation

In general, the scalar formulation and the vector formulations are the two typical formulations used by the variational method with the FEM.

The scalar formulation was first used with the finite element method (FEM) in the 1960^{s} to investigate the electromagnetic waveguide problems [74]. Although, the scalar formulation-based FEM can solve solutions on quasi-TE, quasi-TM or any one-dimensional optical waveguide problem accurately. However, the scalar formulation has significantly difficult for solving hybrid modes of anisotropic or inhomogeneous two-dimensional optical waveguides.

On the other hand, a vectorial wave analysis with at least two field components, can be used to solve these hybrid modes two-dimensional waveguide problems more rigorously. There are several kinds of the vector formulations FEM based on different electromagnetic field components or a combination can be considered, which are shown as followed [76]:

- using the longitudinal (axial) components of E_z and H_z of the electromagnetic fields of **E** and **H**.
- using the both the full vector **E** and **H** fields (all six electromagnetic field components).
- using the full vector electric field components, **E**.
- using the full vector magnetic field components, **H**.

For the FEM based vectorial formulation using the using the longitudinal components of E_z and H_z, it was primary developed for microwave waveguides but later extend to optical waveguide problem. Both the E_z and H_z fields are continuous at the material interfaces. However, the E_z and H_z formulation ends with a non-standard eigenvalue problem, extra computational work needs to convert it into conventional standard form. It is also found that it is significantly difficult for this method to enforce the boundary conditions on a waveguide with arbitrary dielectric distribution.

The full vector **E** and **H** formulations FEM results in all six components of the electric and magnetic fields, will create complicated problems when solving the matrix equations and no extra benefit compare to full vector **E** or **H** formulations [77].

A FEM based on vector **E** field formulation was used to analyse cylindrical, anisotropy and loss-less waveguides. It is found that **E** field does not follow the continuity at the boundaries, the boundary conditions need to implement externally in the **E** field formulation [78].

The first vectorial formulations based on FEM in terms of the **H** field, the **E** field or both was suggested by A. Berk in 1956 for loss-less anisotropic waveguides and resonators [76].

This vector **H**-field formulation is further developed by Rahman and Davies for general anisotropic problems with a non-diagonal permittivity tensor [79] [80]. For optical waveguide analysis, the magnetic field for this formulation is continuous everywhere and that for the natural boundary condition it corresponds to electric wall, in which it is relatively simple to enforce and that it can be left free for arbitrary shaped structures.

The full **H**-field vector-formulation can then be written as [81]:

$$\omega^2 = \frac{\int[(\nabla \times \boldsymbol{H})^* \cdot \varepsilon^{-1} \cdot (\nabla \times \boldsymbol{H}) dxdy]}{\int \boldsymbol{H}^* \cdot \mu \cdot \boldsymbol{H} dxdy} \quad (3.1)$$

Where, * denotes a complex conjugate, ε and μ are the general anisotropic permittivity and permeability of the medium, respectively. While, ω is the angular frequency and $dxdy$ is the integration carried over the waveguide cross-section.

3.1.4 Spurious solutions

The appearance of non-physical or spurious solutions is a major disadvantage of the vector FEM. However, the scalar formulation has no problem with spurious solutions due to the operator is positive definite. It has been found that spurious solution will not appear if the zero-divergence trial field satisfies the condition (div **B** = 0) precisely. However, in the **H**-field finite element formulation, the $(\nabla \cdot \boldsymbol{H})$ is not satisfied and caused the spurious solutions [82].

Rahman and Davies proposed a successful approach to eliminate the spurious solutions by a penalty function approach [80]. A global weighting factor close to the value of $\left(\frac{1}{n_{eff}^2}\right)$ was considered to satisfy the divergence condition (div **B** = 0). In the penalty approach, the value of $(\nabla \cdot \boldsymbol{H})$ is calculated over the complete cross section of the waveguide for each solution. The calculated solution with a lower value of $(\nabla \cdot \boldsymbol{H})$ is considered as real physical mode, while those higher values are the spurious modes.

Therefore, the functional of the vectorial **H**-field finite element formulation with the penalty term can be expressed as [80]:

$$\omega^2 = \frac{\int[(\nabla \times \boldsymbol{H})^* \cdot \varepsilon^{-1} \cdot (\nabla \times \boldsymbol{H}) \; + \; \rho(\nabla \times \boldsymbol{H})^* \cdot (\nabla \times \boldsymbol{H})] \, dxdy}{\int \boldsymbol{H}^* \cdot \mu \cdot \boldsymbol{H} dxdy} \quad (3.2)$$

Where, **H** is the full-vectorial magnetic field, * denotes a complex conjugate and transpose, ω^2 is the eigenvalue, ε and μ are the permittivity and permeability, respectively, and ρ is a weighting factor for penalty term.

The solutions of the equation (3.2) provide the eigenvalues and corresponding eigenvectors. Implementing this equation with FV-FEM, the Si-PCM hybrid waveguides can be analysed and optimised accurately.

3.1.5 Discretisation of the computational domain

The first step of the FV-FEM implementation is to discretise the defined domain into many smaller sub-domains called "element". Such element can be chosen in different shapes and sizes which match with the geometry and the boundary of the computational domain. These small elements altogether can form a mesh which could be either regular or irregular. The irregular meshing is superior than the regular mesh, for instance, finer elements can be used in the particular interest regions and coarse elements can be formed elsewhere could provide great accuracy of simulation. It is also important to select the shape and size of the boundary elements so that the elements can match the complete boundary shape well. Various element geometries can be used such as straight edge elements, iso-parametric elements, infinite elements, and edge elements. The straight edge elements which include triangles, rectangular, and quadrilaterals are the mostly useful for the 2D domains with less curved boundary which will be used in FV-FEM for this research work.

3.1.6 Interpolation or Shape function

Once the domain is discretised with suitable number of elements, it is essential to describe the element shape function in terms of the unknown field distribution. Polynomials are the most popular shape function type, as it is easier to be performed in operation both algebraically and computationally. The chosen shape functions are required have the same type of continuous function within the element and across the boundaries. Otherwise, it would be impossible to add the individual element contribution to achieve the final solution of the variation formulation. The number of terms in the shape function (polynomial) should have the same number of the nodes associated with the element. For example, a triangular element needs a shape function with three terms. Figure 3.1 shows the Pascal triangular structure

which exhibits the relation between the number of nodes and number of terms in the polynomials for a 2D domain discretisation [75].

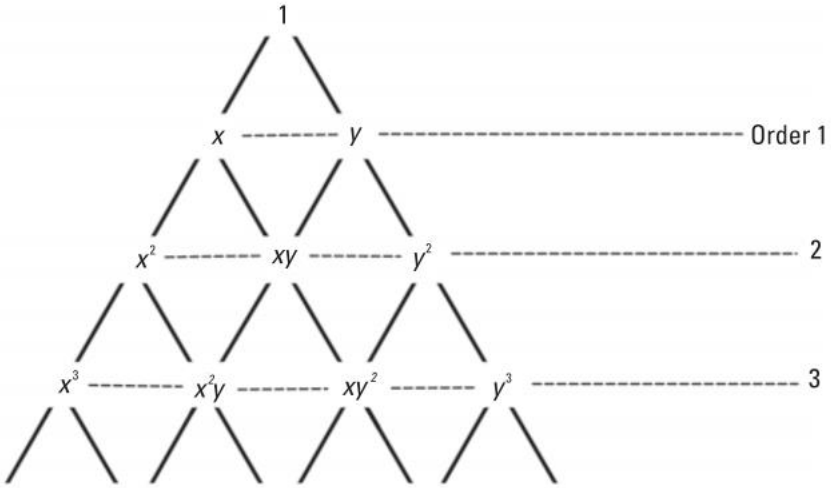

Fig. 3.1. The pascal triangle function and number of terms are needed to perform a complete polynomial up to order 3. [75]

Lagrange interpolation polynomials are used to create the shape functions for the elements of different shape or size. For a 2D liner triangular element, the Lagrange polynomials can be described as:

$$L_i^e = \frac{1}{2A^e}[a_i^e + b_i^e + c_i^e] \tag{3.3}$$

Here, the A^e is the area of a 2D triangular element, the subscript i represents the element number, and the a_i^e, b_i^e, c_i^e are the constant coefficients.

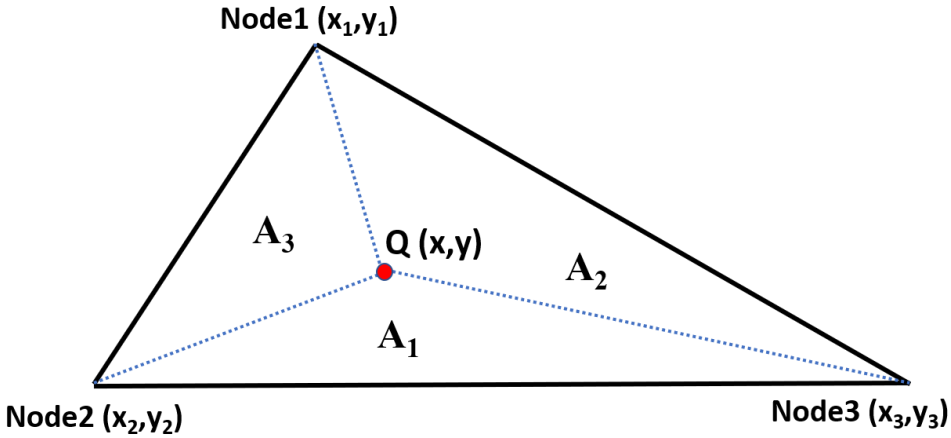

Fig. 3.2. Linear triangular element for 2D domain discretisation.

If an arbitrary point Q have (x,y) coordinate is considered inside a 2D triangular element as shown in Fig. 3.2, the sub-elements from the each element can be achieved. Now, the Q point divides the triangular element into three sub-elements (nodes) and each have the area of A_1, A_2 and A_3.

The area A1 defined by the point Q (x,y) and nodes 2 and 3 :

$$A_1 = \frac{1}{2}\begin{vmatrix} 1 & x & y \\ 1 & x_2 & y_2 \\ 1 & x_3 & y_3 \end{vmatrix}$$

$$= \tfrac{1}{2}\left[(x_2y_3 - x_3y_2) + x(y_2 - y_3) + y(x_3 - x_2)\right] \qquad (3.4)$$

Using these constant coefficients (a_i^e, b_i^e, c_i^e), the L_i^e function of all the three nodes of a triangular element can be defined as:

$$\begin{bmatrix} L_1^e \\ L_2^e \\ L_3^e \end{bmatrix} = \frac{1}{A^e}\begin{bmatrix} A1 \\ A2 \\ A3 \end{bmatrix} = \frac{1}{2A^e}\begin{bmatrix} a_1^e & b_1^e & c_1^e \\ a_2^e & b_2^e & c_2^e \\ a_3^e & b_3^e & c_3^e \end{bmatrix}\begin{bmatrix} 1 \\ x \\ y \end{bmatrix} \qquad (3.5)$$

Here, A_1, A_2 and A_3 represents the area formed by the point Q and two opposite nodes.

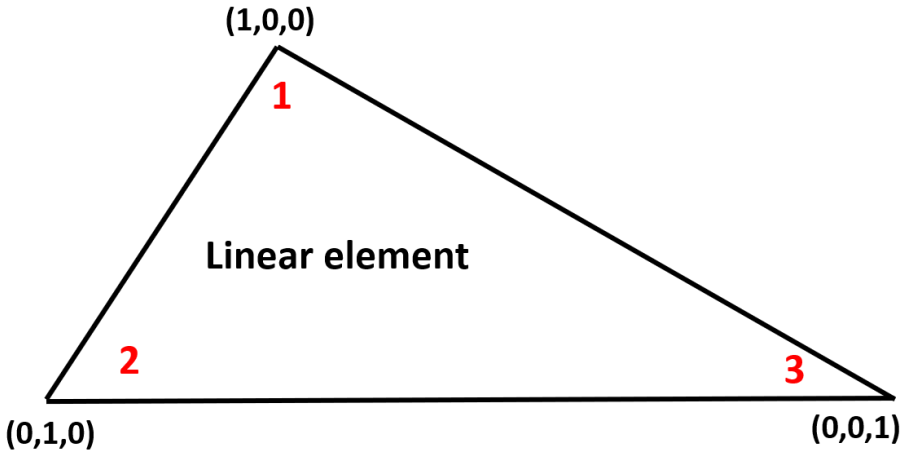

Fig. 3.3. Linear 2D elements with the mode numbering scheme.

In order to formulate the shape function, each node of the triangular element should be numbered, shown in Fig. 3.3. The nodes 1, 2, and 3 of the linear triangular elements are numbered as (100), (010) and (001), respectively.

Thus, the shape function (N_i^e) correlated with a node (i), can be expressed as:

$$N_i^e = Q_p^{(1)} L_1^e \cdot Q_q^{(1)} L_2^e \cdot Q_r^{(1)} L_3^e \tag{3.6}$$

here $(p + q + r) = n$

The p, q and r are the individual digits of a node number and n denote corresponding element order. For instance, in the Fig. 3.3, the nodes 1, 2 and 3 of a linear triangular element can be numbered as (100), (010) and (001), respectively.

The generalised form of equation (3.6) can be written as:

$$Q_{x=p,q,r}^{(1)} L_1^e = \frac{1}{x!} \prod_{m=1}^{x-1} (L_1^e - m) \tag{3.7}$$

when $p > 0$

Here, the $Q_0^{(1)}$ is considered as 1 and the relations between the shape functions and Lagrange polynomials for a liner triangular element shown in Fig. 3.3, can be formed by equations (3.6) and (3.7) as:

$$\begin{cases} N_i^e = Q_{p=1}^{(1)} L_1^e \cdot Q_{q=0}^{(1)} L_2^e \cdot Q_{r=0}^{(1)} L_3^e = L_1^e \\ N_2^e = Q_{p=0}^{(1)} L_1^e \cdot Q_{q=1}^{(1)} L_2^e \cdot Q_{r=0}^{(1)} L_3^e = L_2^e \\ N_3^e = Q_{p=0}^{(1)} L_1^e \cdot Q_{q=0}^{(1)} L_2^e \cdot Q_{r=1}^{(1)} L_3^e = L_3^e \end{cases} \tag{3.8}$$

Once the domain is discretised with enough number of elements, any unknown ζ function can be approximated at individual nodes in terms of the constant coefficients and node coordinates:

$$\zeta_i^e(x, y) = a_i^e + b_i^e x_i + c_i^e y_i \tag{3.9}$$

where i= 1, 2, and 3.

Next, by solving the constant coefficients (a_i^e, b_i^e, c_i^e) for a specific element, the unknown function (ζ^e) can be interpolated for an element as:

$$\zeta^e = \sum_i^n N_i^e \zeta_i^e \tag{3.10}$$

3.1.7 FV-FEM for modal analysis

As the element matrices derived in this section are based on the full **H**-field variational expression of Equation (3.2). For the **H**-field, the three field components H_x, H_y and H_z have been considered. For 2D formulations, the **H**-field is considered to be a continuous function of x and y [75].

$$\boldsymbol{H}(x, y) = \begin{bmatrix} H_x(x, y) \\ H_y(x, y) \\ H_z(x, y) \end{bmatrix} \tag{3.11}$$

It is found that within each triangular element, the three unknown magnetic field components of H_x, H_y and H_z associated with triangular shape functions (N_1, N_2, and N_3) can be written as:

$$H_x(x,y) = [N_1 \quad N_2 \quad N_3]\begin{Bmatrix} H_{x1} \\ H_{x2} \\ H_{x3} \end{Bmatrix} \tag{3.12}$$

$$H_y(x,y) = [N_1 \quad N_2 \quad N_3]\begin{Bmatrix} H_{y1} \\ H_{y2} \\ H_{y3} \end{Bmatrix} \tag{3.13}$$

$$H_z(x,y) = [N_1 \quad N_2 \quad N_3]\begin{Bmatrix} H_{z1} \\ H_{z2} \\ H_{z3} \end{Bmatrix} \tag{3.14}$$

Here, H_{xi}, H_{yi} and H_{zi} (for i = 1,2,3) represents the x, y and z components of the nodal magnetic fields.

Therefore, the nodal magnetic field vector $[H]_e$ can be defined as:

$$[H]_e = \begin{bmatrix} N_1 & N_2 & N_3 & 0 & 0 & 0 & 0 & 0 & 0 \\ 0 & 0 & 0 & N_1 & N_2 & N_3 & 0 & 0 & 0 \\ 0 & 0 & 0 & 0 & 0 & 0 & N_1 & N_2 & N_3 \end{bmatrix} \begin{Bmatrix} H_{x1} \\ H_{x2} \\ H_{x3} \\ H_{y1} \\ H_{y2} \\ H_{y3} \\ H_{z1} \\ H_{z2} \\ H_{z3} \end{Bmatrix} \tag{3.15}$$

In a simplified manner, Equation (3.15) could be written as:

$$[H]_e = [N]\{H\}_e \tag{3.16}$$

Where $\{H\}_e$ is the column vector which consists the nodal field values of the three components in the element and [N] is the matrix of the shape function.

Substituting equation (3.16) into the vector variational formulation in equation (3.2), the integrated formulation can be expressed as:

$$\omega^2 = \frac{\int[(\nabla \times [N]\{\boldsymbol{H}\}_e)^* \cdot \varepsilon^{-1} \cdot (\nabla \times [N]\{\boldsymbol{H}\}_e)dxdy]}{\int([N]\{\boldsymbol{H}\}_e)^* \cdot \mu \cdot [N]\{\boldsymbol{H}\}_e dxdy} \tag{3.17}$$

The cross product $(\nabla \times H)_e$ in Equation (3.17) can be written in matrix form as:

$$(\nabla \times H)_e = [\nabla \times][N]\{H\}_e = \begin{bmatrix} 0 & -\frac{\partial}{\partial z} & \frac{\partial}{\partial y} \\ \frac{\partial}{\partial z} & 0 & -\frac{\partial}{\partial x} \\ -\frac{\partial}{\partial y} & \frac{\partial}{\partial x} & 0 \end{bmatrix} [N]\{H\}_e = [Q]\{H\}_e \tag{3.18}$$

Where the matrix [Q] can be defined as:

$$[Q] = \begin{bmatrix} [0] & -\frac{\partial[N]}{\partial z} & \frac{\partial[N]}{\partial y} \\ \frac{\partial[N]}{\partial z} & [0] & -\frac{\partial[N]}{\partial x} \\ -\frac{\partial[N]}{\partial y} & \frac{\partial[N]}{\partial x} & [0] \end{bmatrix} = \begin{bmatrix} [0] & -j\beta[N] & \frac{\partial[N]}{\partial y} \\ -j\beta[N] & [0] & -\frac{\partial[N]}{\partial x} \\ -\frac{\partial[N]}{\partial y} & \frac{\partial[N]}{\partial x} & [0] \end{bmatrix} \tag{3.19}$$

Where,

$$[0] = [0 \quad 0 \quad 0]$$

$$[N] = [N_1 \quad N_2 \quad N_3]$$

$$\frac{\partial[N]}{\partial x} = [b_1 \quad b_2 \quad b_3]$$

$$\frac{\partial[N]}{\partial y} = [c_1 \quad c_2 \quad c_3] \tag{3.20}$$

The coefficients of the shape functions b_1, b_2, b_3, c_1, c_2 and c_3 have been defined in Equations (3.20).

Considering [Q], the simplified form of equation (3.17) can be written as:

$$\omega^2 = \frac{\int[([Q]\{\boldsymbol{H}\}_{\boldsymbol{e}})^* \cdot \varepsilon^{-1} \cdot ([[Q]\{\boldsymbol{H}\}_{\boldsymbol{e}})dxdy]}{\int([N]\{\boldsymbol{H}\}_{\boldsymbol{e}})^* \cdot \mu \cdot [N]\{H\}_e dxdy} \tag{3.21}$$

Considering the conjugate and transpose, the simplification can be made as:

$$([Q]\{\boldsymbol{H}\}_{\boldsymbol{e}})^* = \{\boldsymbol{H}\}_e^*[Q]^* \tag{3.22}$$

$$([N]\{\boldsymbol{H}\}_{\boldsymbol{e}})^* = \{\boldsymbol{H}\}_e^*[N]^* \tag{3.23}$$

Substituting equations (3.22) and (3.23) into variational form:

$$\omega^2 = \frac{\int[\{\boldsymbol{H}\}_e^*[Q]^* \cdot \varepsilon^{-1} \cdot \{\boldsymbol{H}\}_e^*[Q]dxdy]}{\int\{\boldsymbol{H}\}_e^*[N]^* \cdot \mu \cdot \{\boldsymbol{H}\}_e^*[N]dxdy} \tag{3.24}$$

Assuming that $\{\boldsymbol{H}\}_{\boldsymbol{e}}$ and the shape function $[N]$ is a real matrix, and the material is isotropic then the vector H-field formulation for an element could be written in the form of a functional as:

$$F_e = \int_{xy} \{\boldsymbol{H}\}_e^T[Q]^* \cdot \varepsilon^{-1} \cdot \{\boldsymbol{H}\}_e^*[Q]dxdy - \omega^2 \int_{xy} \{\boldsymbol{H}\}_e^T[N]^T \cdot \mu \cdot \{\boldsymbol{H}\}_e^*[N]dxdy \tag{3.25}$$

Here the functional F_e describes the numerical errors that occurs due to domain discretisation. T and * denote the transpose and complex conjugate. By minimizing the variational functional by $\frac{\partial}{\partial\{\boldsymbol{H}\}_{\boldsymbol{e}}} F_e = 0$, a stationary solution can be obtained.

$$\frac{\partial}{\partial\{\boldsymbol{H}\}_{\boldsymbol{e}}}\left[\{\boldsymbol{H}\}_e^T \int_{xy} [Q]^* \cdot \varepsilon^{-1} \cdot [Q]dxdy\,\{\boldsymbol{H}\}_e - \omega^2\{\boldsymbol{H}\}_e^T \int_{xy} [N]^T \cdot \mu \cdot [N]dxdy\{\boldsymbol{H}\}_e\right] = 0 \tag{3.26}$$

Here, the two integral parts of the equations can be represented by two matrices, $[A]_e$ and $[B]_e$. Both of them are real symmetric and can be defined as:

$$[A]_e = \varepsilon^{-1} \int_{xy} [Q]^* \cdot [Q] dxdy \tag{3.27}$$

$$[B]_e = \mu \int_{xy} [N]^T \cdot [N] dxdy \tag{3.28}$$

Thus, the equation can be simplified as:

$$\frac{\partial}{\partial \{\boldsymbol{H}\}_e} [\{\boldsymbol{H}\}_e^T [A]_e \{\boldsymbol{H}\}_e - \omega^2 \{\boldsymbol{H}\}_e^T [B]_e \{\boldsymbol{H}\}_e] = 0 \tag{3.29}$$

As 2D computational domain is divided into many smaller triangular elements, thus, solving the vectorial variational formulation for a single element and then summing up contributions of all elements, the equation (3.29) can be expressed as a compact global eigenvalue equation as [75]:

$$\left[[A][\boldsymbol{H}] - \omega^2 [B][\boldsymbol{H}]\right] = 0 \tag{3.30}$$

Where

$$[A] = \sum_e [A]_e = \sum_e \varepsilon^{-1} \int_{xy} [Q]^* \cdot [Q] dxdy \tag{3.31}$$

$$[B] = \sum_e [B]_e = \sum_e \mu \int_{xy} [N]^T \cdot [N] dxdy \tag{3.32}$$

Here, ω^2 define the eigenvalue, $[\boldsymbol{H}]$ a column matrix and contains all the **H**-field nodal values at the full cross section of the waveguide. [A] and [B] are the global matrices can be derived by summing up all the $[A]_e$ and $[B]_e$ element matrices, the detailed derivation of $[A]_e$ and $[B]_e$ will be shown in **Appendix A**.

3.1.8 Boundary conditions

In the absence of the surface charge and surface current, the electromagnetic boundary conditions can be obtained as:

- The tangential components of the electric field must be continuous across the boundary. Here, the $\mathbf{E}_1$ and $\mathbf{E}_2$ represent the electric field vectors at the region 1 and the other region, then:

$$\hat{n} \times (\boldsymbol{E}_1 - \boldsymbol{E}_2) = 0 \tag{3.33}$$
$$\therefore \boldsymbol{E}_{t1} = \boldsymbol{E}_{t2}$$

- The tangential of the magnetic field must be continuous:

$$\hat{n} \times (\boldsymbol{H}_1 - \boldsymbol{H}_2) = 0 \tag{3.34}$$
$$\therefore \boldsymbol{H}_{t1} = \boldsymbol{H}_{t2}$$

- The normal components of the electric flux density must be continuous at the interface:

$$\hat{n} \times (\boldsymbol{D}_1 - \boldsymbol{D}_2) = 0 \tag{3.35}$$

Therefore, $\epsilon_1 \boldsymbol{E}_{n1} = \epsilon_2 \boldsymbol{E}_{n2}$

$$\boldsymbol{E}_{n1} \neq \boldsymbol{E}_{n2}$$

Here, the ϵ_1 and ϵ_2 are the optical permittivity in medium 1 and 2, and at the interface, $\epsilon_1 \neq \epsilon_2$.

- The normal components of the magnetic flux density must be continuous at the interface:

$$\hat{n} \times (\boldsymbol{B}_1 - \boldsymbol{B}_2) = 0 \tag{3.36}$$

Therefore, $\mu_1 \boldsymbol{H}_{n1} = \mu_2 \boldsymbol{H}_{n2}$

As most of the optical medium are non-magnetic, the relative permeabilities in region 1 and region 2 is equal ($\mu_1 = \mu_2 = 1$), thus $\boldsymbol{H}_{n1} = \boldsymbol{H}_{n2}$. Which implies equality of the normal component of the magnetic field vectors at the boundary.

Moreover, two more boundary conditions are encountered in practical waveguide problems.

- For a perfectly electric conductor (PEC) or electric wall (EW)-the electric field is continuous the boundary:

$$\hat{n} \times \boldsymbol{E} = 0 \quad \text{or} \quad \hat{n} \cdot \boldsymbol{H} = 0 \tag{3.37}$$

In the absence of surface currents, this boundary condition requires that certain magnetic field vector components must vanish. That is $\boldsymbol{H}_n = 0$, in the absence of surface of surface currents $\boldsymbol{J} = 0$ and $\boldsymbol{H}_t = 0$.

- For a perfectly magnetic conductor (PMC) or magnetic wall (MW)-when one of the two media become a perfect magnetic conductor:

$$\hat{n} \times \boldsymbol{H} = 0 \text{ , or } \hat{n} \cdot \boldsymbol{E} = 0 \tag{3.38}$$

This "perfect magnetic wall" boundary condition illustrates magnetic field vector, **H** remains continuous at the boundary, while the electric field vector, **E**, vanishes. The solutions of Maxwell's equations satisfy the boundary conditions and can be used to describe the whole electromagnetic fields inside any photonic device.

3.1.9 Least squares boundary residual method (LSBR)

In some cases, a complete photonic device designs may have discontinuity between two waveguide sections where the tangential component of the electric and magnetic field must be continuous at this interface. This disruption will cause reflection, scattering, and limit transmission of the propagating light when through at this interface. The simple overlap integral approach can be used to investigate this discontinuity interface. In this thesis, a least squares boundary residual (LSBR) method in conjugation with FV-FEM developed by Rahman and Davies will be

employed as an efficient tool to determine the reflection, transmission and scattering coefficients at the interface [83].

To carry out LSBR analyses, a full-vectorial FEM is used to find the modal field profiles of the cross-section at both sides of a discontinuity interface. Then, the LSBR method is used to calculate the power transfer efficiency by enforcing the required continuity of the tangential **E** and **H** fields at the junction interface to obtain the transmission and reflection coefficients of the fully hybrid modes at the discontinuity interfaces. The LSBR method looks for a stationary solution by minimizing the error energy functional J, to satisfy the continuity conditions of the tangential **E** and **H** fields in a least squares sense over the interface, as given by [83]:

$$J = \int |E_t^1 - E_t^2|^2 + \sigma \cdot z_0^2 \, |H_t^1 - H_t^2|^2 d\Omega \tag{3.39}$$

Where Z_0 is the free-space wave impedance and σ is the dimensionless weighting factor to balance the electric and magnetic components of the error functional. Here, 1 and 2 superscripts are used to identify fields in sides 1 and 2, respectively, and the integration is carried out over the two junction interfaces, Ω.

3.1.10 Perturbation analysis

Waveguide modal loss is an important property that must be considered for photonic waveguide and device design. As PCM have a complex refractive index n, the eigenvalue equation needs to be complex also need a complex solver. Complex solver not only suffer from the double the memory space, but also slow the simulation time. Perturbation analysis is a powerful method for modal loss calculation that can be coupled with the FV-FEM code for 2D structures with multiple material layers.

For a lossy waveguide structure, the perturbation technique can be applied directly once the unperturbed modal field and phase constant values are achieved. The perturbation formula can be derived by approximating the solution with a series expansion or directly from the variation expression. Perturbation method can be implemented for the loss analysis of the optical waveguide by approximating the

perturbated phase constant, β and field profile **H** and **E** due to modal loss from the corresponding unperturbed phase constant and field profile values. This approximation is valid with small amounts of loss, so that the attenuation constant, α, of a waveguide due to material loss can be obtained as:

$$\alpha = \frac{P_d}{2P_0} \tag{3.40}$$

Where P_D, is the dissipated power in the material and P_0, defines the time-averaged power flow.

By considering a cross section, *dxdy*, of an optical waveguide, with any number of sub-domains, k which have the material loss can be expressed as a complex dielectric constant, ε_k for each sub-domain. the attenuation constant α of the whole waveguide can be expressed in terms of electromagnetic fields as [84]:

$$\alpha = \frac{\omega \sum_k \varepsilon_{rk} \tan\delta_k \int |\boldsymbol{E_0}|^2 dxdy}{2Re \int (E_0 \times \boldsymbol{H_0^*}) \cdot \hat{z} dxdy} \tag{3.41}$$

Where the ω is the angular frequency, $\hat{z}$ is the unit vector along z-axis. $\mathbf{E}_0$ and $\mathbf{H}_0$ are the unperturbed electric and magnetic field vectors for the lossless state. The $\tan\delta_k$ is the loss tangent of each subdomain defined by k:

$$\tan\delta_k = \frac{\varepsilon_{ik}}{\varepsilon_{rk}} \tag{3.42}$$

Where the ε_{rk} and ε_{ik} are the real and imaginary parts of the dielectric constant of each subregion, respectively, and the summation is carried over all sub-domains. This perturbation condition assumes that the unperturbed electric and magnetic field $\mathbf{E}_0$ and $\mathbf{H}_0$ remain unchanged in the presence of loss and loss tangent has very small value, that is, $\varepsilon_{rk} \cong \varepsilon_{ik}$.

3.2 Time Domain Methods

3.2.1 Introduction

The photonics switch or modulator design usually needs a full realization of how the light will propagates through the waveguides before the device is fabricated. However, most of the photonics devices comprise variations of the waveguide structures, when the light propagates, it will lead to several reflections, interference, scattering and radiation, interaction between multi modes, also the mode profile changes.

3.2.2 finite difference time domain method (FDTD)

Several time-domain approaches such as finite difference time domain (FDTD) and finite element time domain (FETD) can be used to solve those wave propagation problems. The most general and rigorous time-domain approach is the finite difference time domain method (FDTD), as it is a numerical technique for solving the three-dimensional Maxwell equations [85]. The FDTD operates in the time domain and simulates the propagation of a pulse of light which comprise a spectrum of wavelengths variations. The related total system's response of this short pulse is obtained through the transmission spectrum via the Fourier transform. Therefore, an individual FDTD simulation provides the response of the optical system for a wide variation of wavelengths at once time. The physical significance of the FDTD solution is to rotate the **H**(**E**) field with the time change in **E**(**H**) field. Thus, the FDTD cannot solve the **E** and **H** field components at the same location at the same instant of time, and a small time-step need to use as an accurate solution [86].

The 3D FDTD technique can construct the waveguide which have the materials are dispersive and nonlinear. The FDTD is good at analysing the interaction of light with multi waveguides as FDTD is an exact numerical calculation of Maxwell's equation, because the accuracy converges to the approximately solution as the spatial discretisation is reduced. The Limitation of the 3D FDTD simulation is that as the simulation time step is sub-femtosecond, which requires high computational

resources and time for the accurate solution, however it can be solved by additional computing resources. It is also noted in the FDTD simulation, only the rectangular grids are used for the domain discretisation [87]. So that, it is very difficult to solve some arbitrarily and circularly shaped waveguides with curved boundary.

Several commercial FDTD programs are available, including Synopsys RSoft, Photon Design, Acceleware FDTD. In this thesis, the Lumerical FDTD solutions will be used as the FDTD modelling tool, it is efficiently and accurately modelling the light propagation through the different waveguides, and provide the optical transmission of the system which can be verify the validity of the proposed device design based on the FV-FEM with the LSBR.

3.2.3 FDTD modelling procedure

The general simulation process of the Lumerical FDTD solutions can be illustrated as follows:

- Define all the optical material included of the designed device, ensuring they are appropriate for the simulation, accurate and consistent material complex refractive index are important for the design validity.

- Draw the device structure, it includes defining the geometries for the substrate, cladding, Si waveguide core, and other materials.

- Define the simulation region, normally it is effectively set the simulation region smaller than the total waveguide structure. Several simulation parameters need to be set:
  Mesh: the mesh needs to be defined by the number of mesh points per wavelength in the material.
  Boundary conditions: Perfect Matching layers (PML) are the general option which are used to absorb all the light in the simulation.
- Add the optical source. The general source used in Si photonics device is a mode source, as the light is injected into a specific waveguide mode. It can be completed by calculating the modes of the source waveguide,

then choose the fundamental TE/TM mode, and launching field into the access waveguide. The operating centre wavelength or the time-domain parameter need to be specified at 1550 nm with or without any optical bandwidth. The sources need to be placed within the simulation region, away from the boundary.

- Add the monitors to measure the optical field profiles, both **E** and **H** field, at the chosen locations. The frequency domain field profile monitor is most common used as it can plot the field profile and generate the optical transmission of the devices. The geometry of the monitors can be set as a single point, a 2D line, or the entire 3D region to measure the optical power transmission of the device at specific position accurately.

- Add mode expansion monitor. It is useful to study the excitation of high-order modes at the output field, as the field can be decomposed into eigenmode. Once the mode expansion monitor added at the position along the progradation direction, the power transmission of the selected modal field (fundamental or high order) can be calculated. Moreover, these monitors also calculate the forward/backward transmission which means it can be determine how much power is transmitted or reflected of the fundamental or higher-order modes at specific position of the proposed device. The relevant examples and simulations will be shown in the following chapters.

3.3 Summary

The frequency and time domain numerical methods which will be used for rigorous design, characterisation and optimisation of the Si-PCM hybrid waveguide based photonic devices have been briefly discussed and presented in this chapter.

A full vectorial **H**-field FEM has been discussed in first section as a mode solver for analysing the fundamental modal properties of waveguides. In particular, the principle, advantages and variational method approach of the FEM are introduced as the fundamental. Then, several vector formulations and full **H**-field vector formulation of FEM with spurious solutions are also described in detail. Moreover, the implementation process of the FEM including the domain discretisation, shape functions, natural boundary conditions and the formation of the element and global matrices are also evaluated. At last, the LSBR and perturbation technique also discussed and will be along with the FV-FEM for modelling the Si-PCM hybrid waveguides.

On the other hand, the 3D FDTD technique is also introduced for solving the wave propagation problems. In particular, the principle characteristic of the FDTD and its advantages and disadvantages are studied, and the Lumerical FDTD solutions modelling procedures are also investigated in detail for simulating the complete photonic device. The application of these methods to characterise and optimise the performance of various Si-PCM waveguides and photonic devices will be presented in the subsequent chapters.

Chapter 4

Feasibility study of a Si-$Ge_2Sb_2Te_5$ hybrid waveguide as a non-volatile loss modulator

4.1 Introduction

Although VO_2 undergoes a large refractive index change during its phase transition, but the excessive loss in both phases are rather high which makes the device volatile and need sustaining power to maintain each state. For instance, A. Joushaghani have fabricated an electrically-driven VO_2 cladded Si rib waveguide based optical switch, and this compact 1 μm long device also has a higher 12 dB extinction ratio. However, this switch has an unacceptable 5 dB insertion loss at VO_2 dielectric phase which will critically limit the device performance [42].

Several photonic devices based on the phase change material $Ge_2Sb_2Te_5$ (GST), have been reported to have optical performance superior to that of the phase change material VO_2 [64] [65] [66]. In a recent work, N. Ali reported photonic switch design as GST is embedded in partially etched and fully etched Si nanowire. He demonstrated that for GST integrated with partially etched Si nanowire, a 920 nm compact device with 34 dB extinction ratio and 0.49 dB insertion loss can be achieved. Similarly, for GST integrated with full etched Si nanowire, a 1.02 μm long device with 14 dB extinction ratio and 1.36 dB insertion loss also can be obtained. Both of these designs have significant lower insertion loss and higher extinction ratio compare to VO_2 based device [88].

The GST phase transition can be triggered thermally. Crystallization is achieved by heating the amorphous GST above the transition temperature (140 ºC) and then slowly cooling down. Re-amorphization is achieved by heating the crystalline GST above the melting point (~600 ºC) followed by fast quenching [67].

The GST phase transition also can be triggered electrically, the Si can be lightly doped to be used as a resistive heater. The doping concentration can be in the order of 10^{16} to 10^{17} cm^{-3} and the doping induced optical absorption is negligible. The Si slab beside the waveguide can be highly doped to make an ohmic contact with aluminium wires. The doping region is separated by at least 0.5 μm from the Si waveguide to reduce the free-carrier absorption. In this approach, an electrical pulse applied to the Si resistor will raise the temperature and subsequently stimulate the phase change of GST deposited on top of the lightly doped Si waveguide [66].

The phase change of GST also can be triggered all optically by using an optical pulse at 1550 nm wavelength. Because both the amorphous and crystalline states have non-zero extinction coefficient, the light power can be absorbed to stimulate the phase change. The optical pulse can be pumped from the waveguide, making full use of the planar integration. In particular, the crystallization of GST can be induced by a sequence of identical optical pulses with a width 50 ns and peak power 21 mW. On the other hand, the re-amorphization can be induced by a single pulse with a width 20 ns and peak power 53 mW [89].

In this Chapter, the design optimisation of a thermally driven 1 x 1 loss modulator based on a GST-clad Si rib waveguide and a GST-clad Si nanowire waveguide at the telecommunication wavelength 1.55 μm is presented. Here, a rigorous full-vectorial **H**-field finite-element method (FV-FEM) in conjunction with the perturbation technique is used to find the complex modal effective indices with the variations of the waveguide width and height of different layers. Following that, the least squares boundary residual (LSBR) method, a rigorous junction analysis approach, is used to calculate the coupling loss at the butt-coupled junctions to determine the optimal waveguide parameters in order to achieve a lower insertion loss and a higher extinction ratio of a compact self-sustained modulator.

4.2 Schematic and principle

4.2.1 schematic and cross-section view

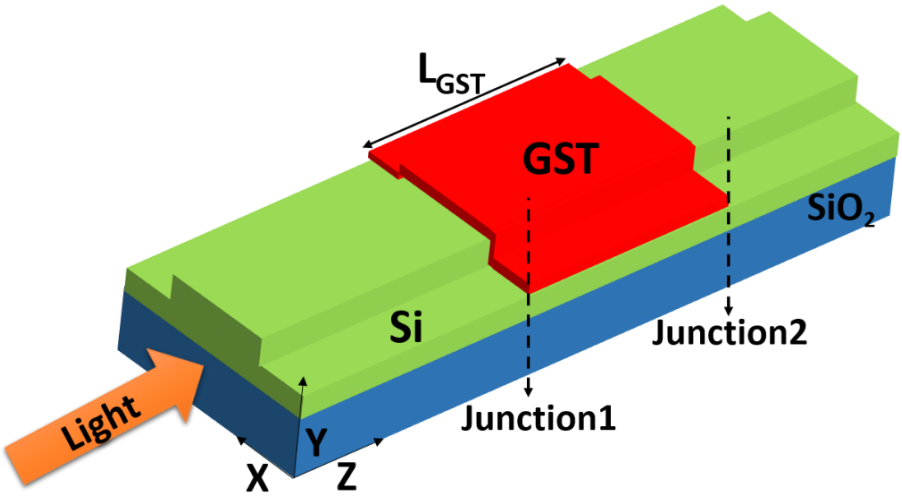

Fig. 4.1. Schematic of the optical modulator (WG1 based)

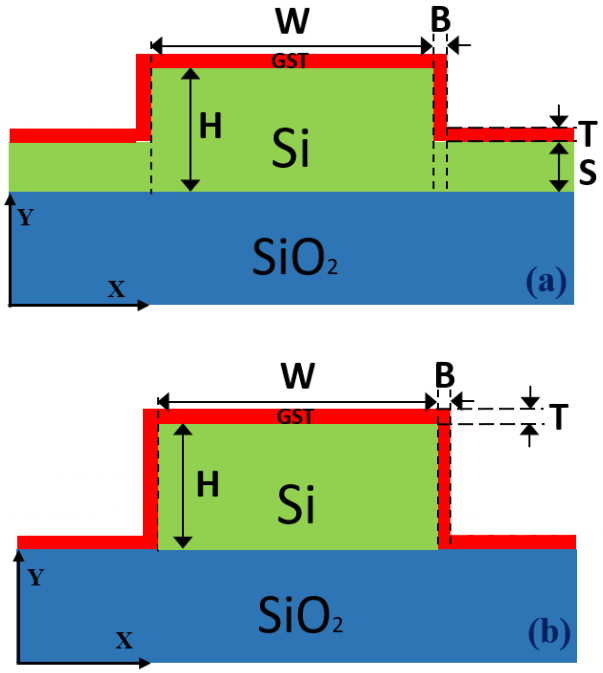

Fig 4.2. (a) Cross-sectional view of the active section Si-GST rib waveguide WG1. (b) Cross-sectional view of the active section Si-GST nanowire WG2.

Figure 4.1 shows the 3D schematic of an optical modulator based on a Si-GST rib waveguide, identified here as WG1. Here, outer two waveguide sections are passive single-mode Si rib waveguide, while the central section is active. The active

section consists of a standard single-mode Si rib waveguide with a GST top-clad layer.

The cross-sectional view of the WG1 is shown in Fig. 4.2 (a). Here, the thickness of the Si core is identified as H and fixed at 220 nm, its width is taken as W, and the slab layer thickness is taken as S. The GST patch thickness is taken as T on the top and B at the sides, as it has been observed that thickness at the sides are often only 40% of that in the top. The length of GST section, deposited on top of the Si rib waveguide to form the hybrid waveguide for optical modulating, is taken at L_{GST}.

Alternatively, if the waveguide is etched fully (S = 0 nm), then this represents a standard Si nanowire waveguide (NW) shown in Fig. 4.2 (b), identified here as WG2. The WG2 with its width W and height H can also be wrapped with a GST clad layer with thickness T. Both these Si waveguide structures will be evaluated through numerical simulations and comparison will be made for better design optimisation of the photonic modulator.

4.3 Numerically simulated results

4.3.1 Optical properties of the material for simulation

Exact evaluation of the optical constants is critical for simulating practical applications in integrated optical devices, such as modulators, filters and optical switches. In order to improve simulation accuracy, the traditional theoretical refractive index from literature resource were not used in this simulation. In this case, the refractive index of GST is measured by using VASE ellipsometer from our collaborator H. Zhang at Shanghai Jiaotong University (SJTU) will be used for FV-FEM simulation. The real (n) and imaginary (k) part of the GST refractive index as a function of wavelength is shown in Fig. 4.3 is adapted from H. Zhang's measurement [65].

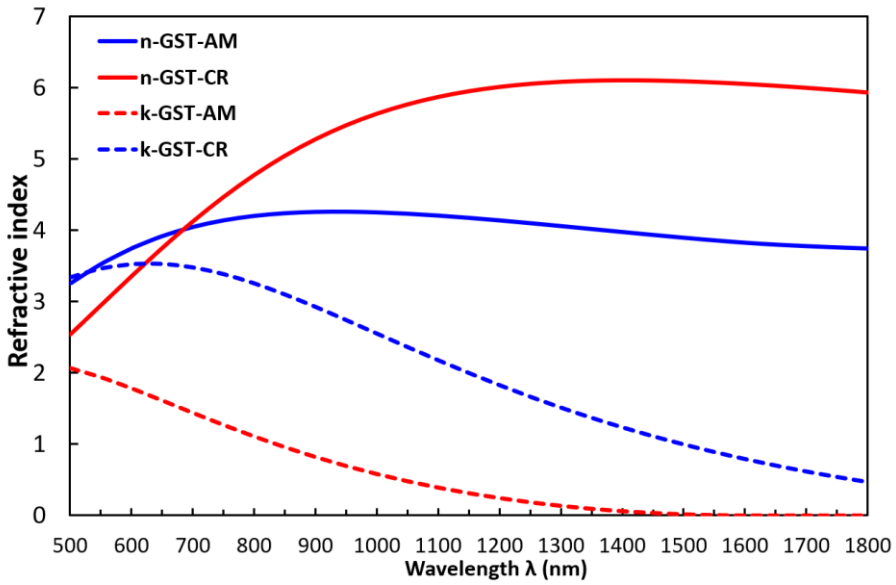

Fig. 4.3. Real (n) and imaginary (k) part of GST refractive index as a function of wavelength λ (nm) [65].

In Fig. 4.3, it can be noted that for the crystalline state, the real part n increases smoothly from 2.5 to a higher value around 6.2 with the wavelength increase from 500 to 1300 nm then it remains stable around 6. While the imaginary part k decreases monotonically from 3.5 to 0.5 with the wavelength increase to 1800 nm. On the other hand, for the amorphous state, the real part n increases from 3.5 to its maximum 4.2 with the wavelength increase from 500 to 900 nm, the it decreases slightly to around 4. The imaginary part k decreases steadily from 2 to the bottom close to 0 with the wavelength increase from 500 to 1800 nm.

It also can be noted that, for the telecommunication wavelength 1.55 μm, the complex refractive indices of GST, are taken as: n (AM) = 3.861 + j*0.03746, n (CR) = 6.0735+ j*0.8916, for amorphous and crystalline states, respectively and these will be used in the FV-FEM simulation for better accuracy so that can be compared with experimental results. In this case, the refractive indices of air cladding, Si and SiO_2 at operating wavelength at 1.55 μm are taken as n (air) = 1.0, n (Si) = 3.481, n (SiO_2) = 1.44468.

4.3.2 Fundamental mode field profiles

In this section, both for the FV-FEM and LSBR approaches, in-house codes, are used for numerical simulations. For the quasi-TE mode, H_y is the dominant and H_x and H_z are the non-dominant components of the magnetic field, **H**.

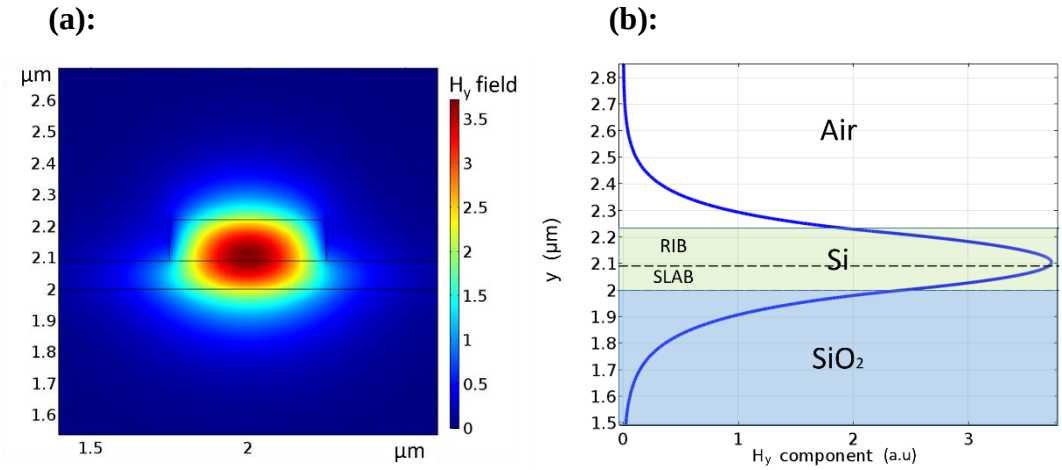

Fig. 4.4 (a) H_y field profile, (b) H_y variation along the vertical direction, for input Si rib waveguide with W = 500 nm, H = 220 nm, and S = 90 nm.

At first, a representative case, the input Si rib waveguide with W = 500 nm, H = 220 nm, S = 90 nm is simulated, and the H_y field profile of the quasi-TE H_y^{11} modes of this waveguide is shown in Fig. 4.4 (a). It can be observed that its field is confined in the Si rib core and extends slightly to the upper air and lower SiO_2 buffer regions. It also extends a bit laterally into the lower slab region.

The mode effective index ($n_e = \beta/k_0$) is calculated as 2.5319 for the passive input waveguide. Here, β is the propagation constant and k_0 is the free-space wavenumber. Additionally, variation of the H_y component of the H_y^{11} mode along the vertical directions is shown in Fig. 4.4 (b). The SiO_2 buffer region is shown by a blue shade and Si region with a light green shade and a dashed line inside shows the interface between the rib and slab region. Here, it can be noted that, the maximum H_y component value is inside the rib and near to the interface between the Si rib and slab. The H_y field decays exponentially both in upper clad air region and lower SiO_2 substrate region. As the decay in the lower substrate is slower so H_y value at this interface is slightly higher than that at the Si/air interface.

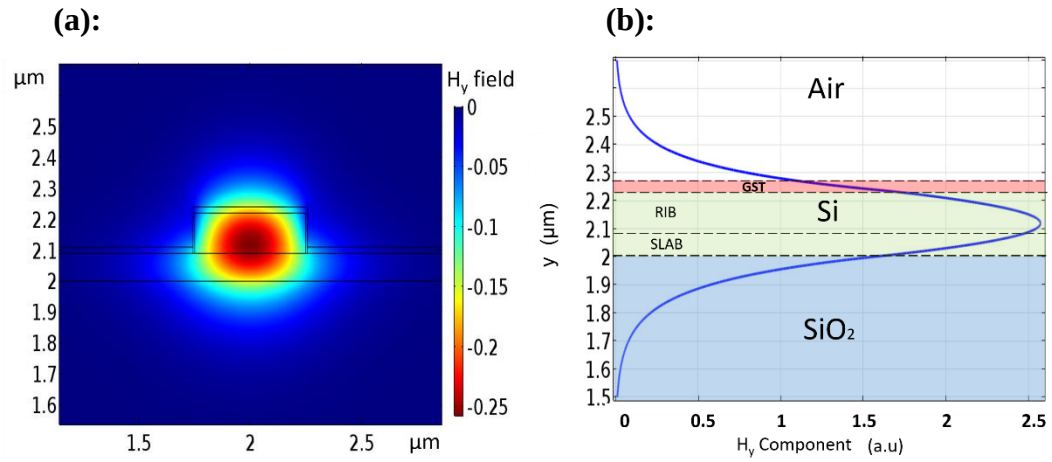

Fig. 4.5 (a) H_y field profiles, (b) H_y variation along the vertical direction, for WG1 in amorphous state with W = 500 nm, H = 220 nm, S = 90 nm, T = 20 nm.

Subsequently, an ultra-thin GST layer can be deposited on top of the Si rib waveguide to form a hybrid waveguide (WG1) for optical modulating and switching. Although GST states can be changed by optical, electrical and thermal approaches, however, in this design, we have assumed that the state of the GST is changed from its initial amorphous to the crystalline state by thermal annealing.

The H_y field of the H_y^{11} mode of WG1 in the amorphous state is shown in the Fig. 4.5 (a). It shows that when the GST is in the amorphous state, the guided mode is more confined in the middle of Si rib region and slightly extends to the top GST layer and air which is similar like Fig. 4.4 (a). Variation of H_y along the y-axis at the centre of the waveguide is shown in Fig. 4.5 (b). The GST layer is shown by a pink shade and Si region with a light green shade and a dashed line inside shows the separation between the rib and the upper Si slab. It can be observed that the maximum H_y value is inside the Si rib but shifts a little upward than that in Fig. 4.4-(b) due to the presence of extra GST layer on top.

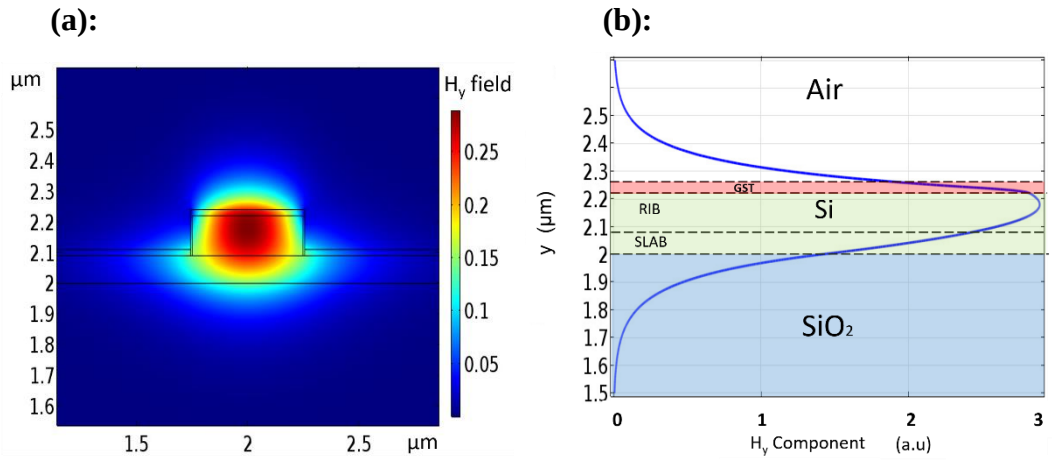

Fig. 4.6.(a) H_y field profiles, (b) H_y variation along the vertical direction, for WG1 in crystalline state with W = 500 nm, H = 220 nm, S = 90 nm, T = 20 nm.

However, when the GST is switched to a crystalline state, its refractive index is increased considerably, and the H_y field profile of the H_y^{11} mode of WG1 in crystalline state is shown in Fig. 4.6 (a). It can be observed that although the field is confined well in the Si rib layer, but a small amount of modal field is also extended to the top GST layer. It suggests that when the GST turns to crystalline state, more power is confined into the GST layer.

The H_y field profile along the vertical direction is shown in Fig. 4.6 (b). It can be noted that in the crystalline state, the maximum H_y value is still inside the Si rib layer but moved closer to the interface between the Si rib and the top GST layer. Compared to the GST in amorphous state shown in Fig. 4.5 (b), a larger modal field is presented in the top Si rib region and less into the Si slab region when the GST is in the crystalline state.

4.3.3 Modal solution characteristics

Following the modal analysis, when the GST in amorphous state, the mode effective index of WG1 can be written as ($n_{e1} + j*k_{e1}$), and while in crystalline state this is written as ($n_{e2} + j*k_{e2}$). The mode absorption loss α of the waveguide in dB per micrometer for each state, can be calculated from the imaginary part of their effective indices k_e, as:

$$\alpha = 4.343 \times \left(\frac{4\pi k_e}{\lambda}\right) \tag{4.1}$$

	n_e	k_e	Mode loss α (dB/μm)
Amorphous	2.6768	0.0029	0.1036
Crystalline	2.9382	0.1841	6.4811
Difference	0.2614	0.1811	6.3775

Table 4.1. Modal solution characteristics

The calculated modal solution parameters for the H_y^{11} mode of WG1 (W = 500 nm, S = 90 nm, T = 20 nm and B = 8 nm) are given in Table 4.1. It can be noted that when GST is in crystalline state, the waveguide has a larger effective index, both in real and imaginary parts, which also suggests a larger mode loss. The WG1 here has a strong electro-refraction (ER) = (n_{e2}-n_{e1}) = 0.2614 and also a strong electro-absorption (EA) = (k_{e2}-k_{e1}) = 0.1811, because there are significant changes in both real and imaginary parts of GST refractive indices induced by the phase change. Electro-refraction, which considers the differential real part of the effective index, is widely used to design optical modulators and switches. The optical devices can be comprised of either a Mach-Zehnder interferometer (MZI) with two branches or a directional coupler incorporating two adjacent waveguides. However, sometimes ER-based devices need additional requirements like ER>>EA. For a MZ-based device, we would prefer a higher ER values for a compact device but also prefer lower loss values for both the states. On the other hand, the Electro-absorption effect also can be utilized for modulation, where the differential mode loss between the two states is exploited to achieve the optical modulating.

In the following sections, variations of both ER and EA characteristics of the WG1 with waveguide width and height of different layers are thoroughly investigated. Similar results for the WG2, a standard Si nanowire waveguide, are also shown for comparison.

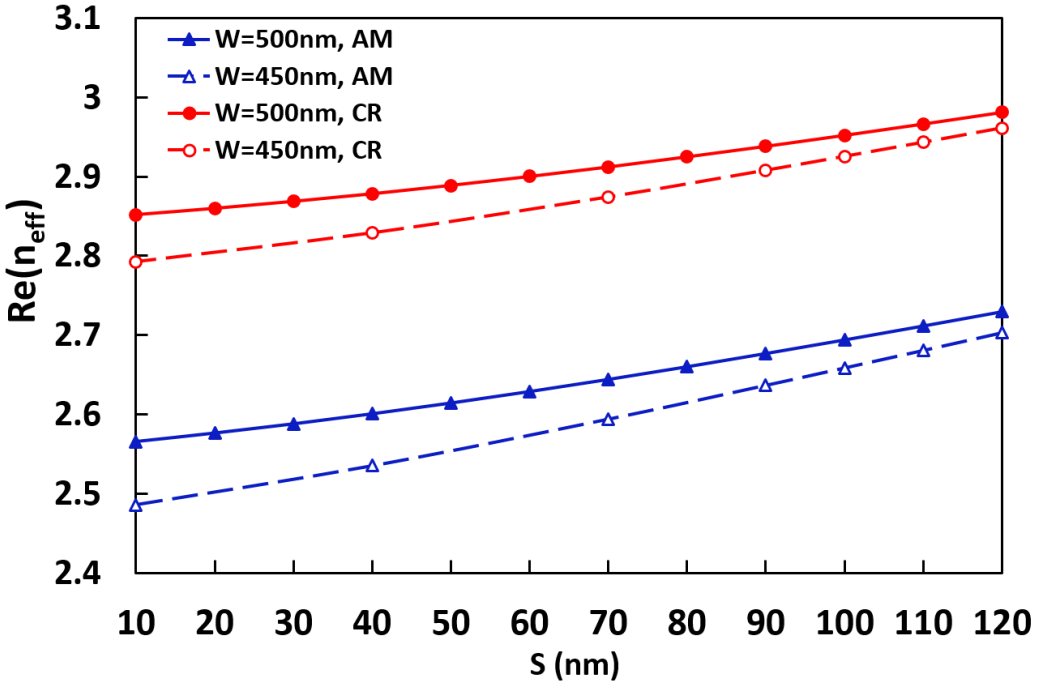

Fig. 4.7. Variations of the real part of effective indices of WG1 in amorphous and crystalline states with the slab height, S, for two different widths.

Variations of the real part of the effective index with the slab height, S, are shown in Fig. 4.7. Results for amorphous state (AM) are shown by blue lines and similarly those for the crystalline state (CR) are shown by red lines. The results for W = 500 nm are shown by solid lines with solid symbols and those for a narrower W = 450 nm are shown by dashed lines with hollow symbols. When GST is in amorphous state, it can be observed that for W = 500 nm and T = 20 nm, shown by a solid blue line, the n_{e1} increases with slab thickness S as the waveguide core area increases. However, it should be noted that the modal confinement in the rib core will be reduced as more field will extend to the slab region.

On the other hand, the real part of the effective index for the crystalline state shown by a solid red line, also increases with S, but with higher values than the amorphous state's values. This is because, when the GST is in crystalline state, its

refractive index is 1.5 times larger than that of the amorphous state so that the WG1 will have higher effective index values for the crystalline state. When the W reduces to 450 nm, the real effective index of WG1 for both the states, shown by the dashed red and blue lines are lower than that for W = 500 nm. It can be concluded that the wider Si waveguide will have higher n_e values for both the states when the slab height S increases from 10 to 120 nm.

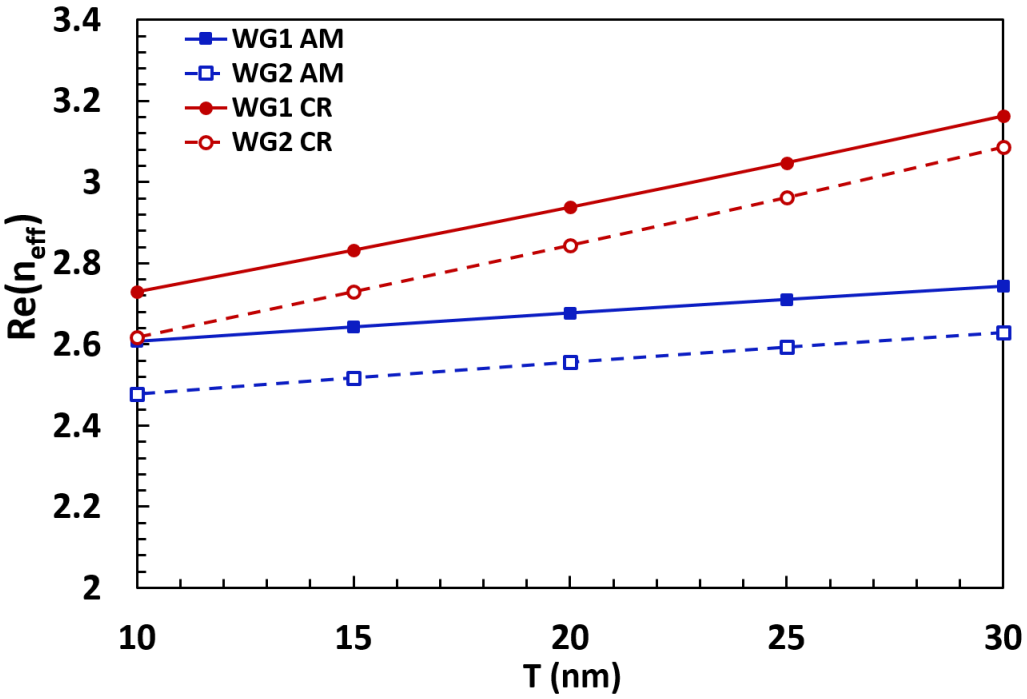

Fig. 4.8. Variations of the real part of effective indices for amorphous and crystalline states with the GST thickness, T, for WG1 and WG2.

Next, effect of GST thickness T on the modal solutions is studied. Here, we have considered a fixed width, W = 500 nm and for WG1, the slab thickness is kept fixed at S = 90 nm. In Fig. 4.8, the real effective index of WG1 for amorphous state n_{e1} is shown by a solid blue line. When the GST thickness T increases from 10 to 30 nm, the n_{e1} also increases slowly from 2.607 to 2.743.

On the other hand, the real effective index for the crystalline state n_{e2}, shown by a solid red line, increases more rapidly from 2.73 to 3.16, compared to its amorphous state. When the waveguide is changed to a Si nanowire waveguide (i.e. S = 0), the real effective index of WG2 for both the states are shown by the dashed

red and blue lines for comparison. It can be concluded that the Si rib waveguide, WG1 have higher n_e values for both the states when the GST thickness T increases from 10 to 30 nm.

In modulating or switching, the phase change Δφ is the product of the differential propagation constant Δβ and the device length L, which affects the transfer of light to the output port. Here, Δφ is given as:

$$\Delta\varphi = \Delta\beta L = \left(\frac{2\pi}{\lambda}\right) \cdot \Delta n_e \cdot L = \left(\frac{2\pi}{\lambda}\right) \cdot (n_{e2} - n_{e1}) \cdot L = \left(\frac{2\pi}{\lambda}\right) \cdot ER \cdot L \qquad (4.2)$$

If the Mach-Zehnder interferometer (MZI) is used for switch geometry, the value of "Δφ" needs to be π radians, and the length of such devices can be calculated as:

$$L_\pi = \frac{\pi}{\Delta\beta} = \frac{\lambda}{2 \cdot \Delta n_e} = \frac{\lambda}{2 \cdot (n_{e2} - n_{e1})} = \frac{\lambda}{2 \cdot ER} \qquad (4.3)$$

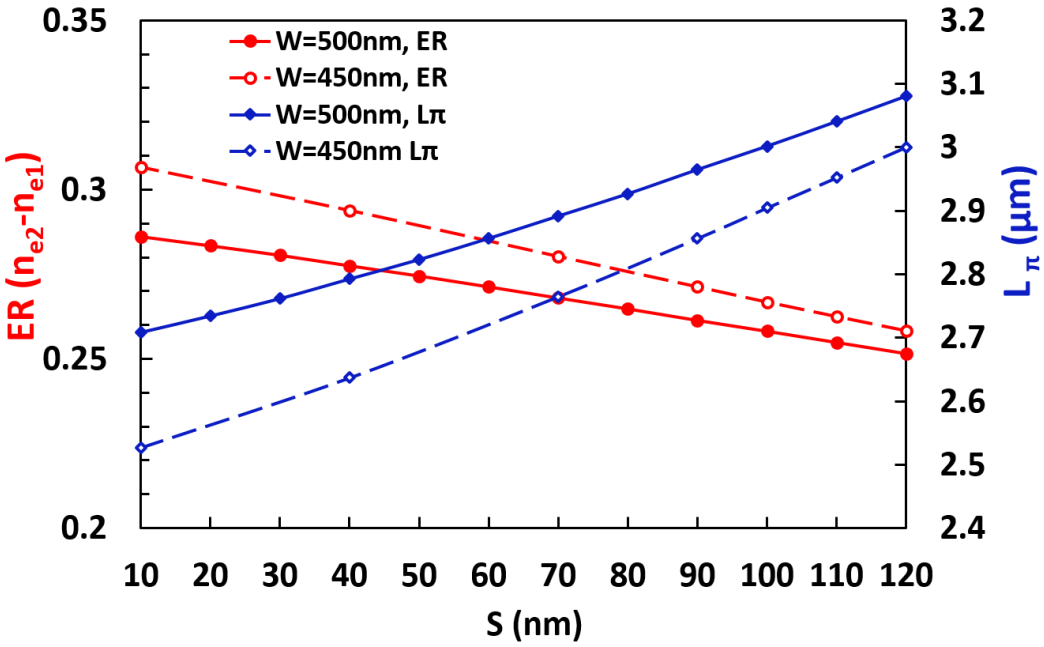

Fig. 4.9. Variations of the ER and L_π of WG1 between the amorphous and crystalline states with Si slab height, S.

Next, effects of the waveguide parameters, on the ER and MZI active waveguide length, L_π are studied. In Fig. 4.9, when W is set at 500 nm and GST height T at 20 nm, the ER (n_{e2}-n_{e1}) of WG1 between amorphous and crystalline states is shown by

a solid red line using the left-hand side scale. With the steady increase of slab height S from 10 to 120 nm, the ER shows an opposite trend, which is reducing from 0.286 to 0.252. The L_π of the WG1 is shown by a solid blue line using the right-hand side scale. The L_π of the WG1 increases gradually from 2.71 to 3.08 μm, as slab thickness S is increased. When the W reduces to 450 nm, the ER shown by a dashed red line (left scale) also reduces, but these values are always higher than the solid line, which was for width W = 500 nm and their differences become smaller with the increasing S. On the other hand, the L_π of the 450 nm wide waveguide, shown by a dashed blue line using the right-hand side scale, also increases, but this is always lower than the solid line shown for W = 500 nm and their differences become smaller with the higher S.

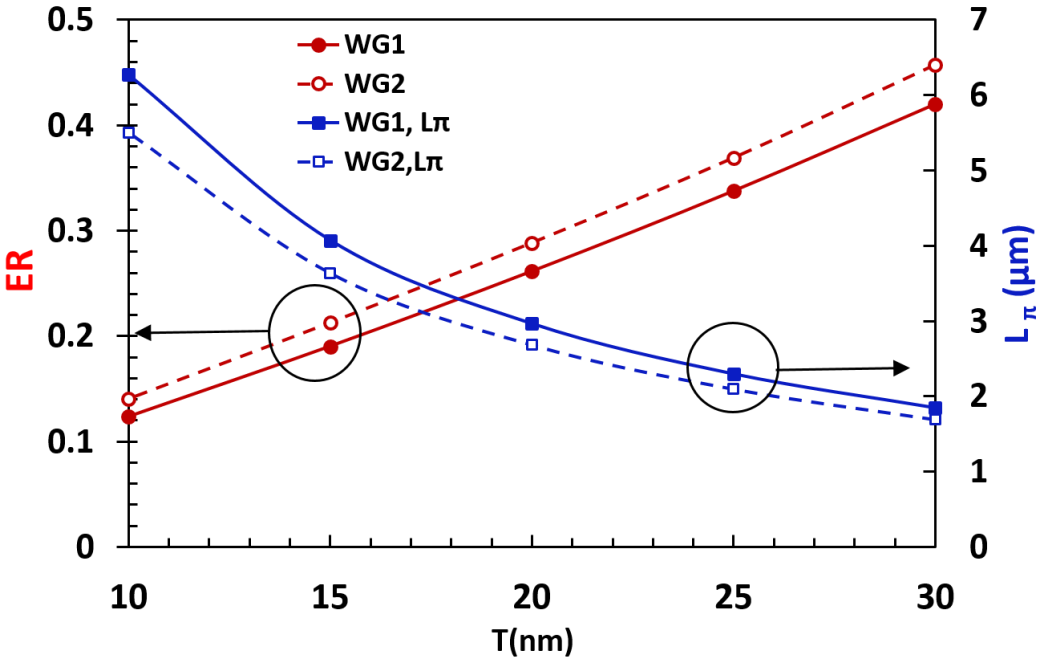

Fig. 4.10. Variations of the ER and L_π between amorphous and crystalline states with GST thickness T for WG1 and WG2.

In Fig. 4.10, we have considered a fixed width of W = 500 nm, and for WG1 the slab height S is also kept fixed at 90 nm. Variations of ER (Δn_e) are shown by red lines, using the left-hand side scale, while the L_π variations are shown by blue lines using the right-hand side scale. It can be observed, the variation of ER for the WG1 shown by a solid red line increases with the GST thickness T. When the waveguide

core is changed to Si nanowire waveguide (NW), the ER of WG2 is shown by a dashed red line, where it can be observed that NW WG2 can achieve a slightly higher ER and their differences also increase when the T increases steadily from 10 to 30 nm.

On the other hand, variation of L_π for the WG1 shown by a solid blue line decreases with the GST thickness T. The L_π of the WG1 rapidly decreases from a higher value of 6.27 μm to a lower value of 1.85 μm when T is increased from 10 nm to 30 nm. Variation of the L_π of the WG2 is shown by a dashed blue line, which also decreases with T but with lower values compared to that of the WG1. It can be concluded that the Si rib waveguide WG1 will have longer L_π and their difference between two waveguides becomes smaller when T increases steady from 10 to 30 nm. It is clearly shown here, GST thickness is the most critical parameter in the design of optical devices. A very compact device of 2-6 μm long is feasible by using either a Si rib or a Si nanowire waveguide.

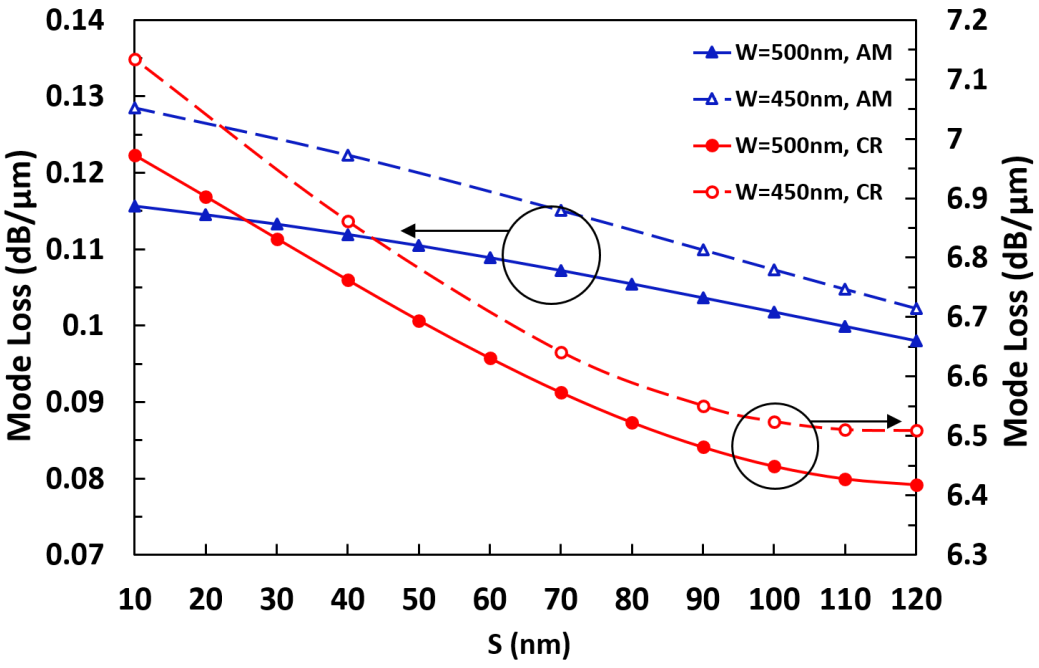

Fig. 4.11. Variations of mode loss of WG1 in amorphous and crystalline states with S of two different values of W.

As GST introduces material loss, so next the variations of modal loss for these two states with the Si slab thickness S are shown in Fig. 4.11. Results for the

amorphous state (AM) are shown by blue lines, using the left-hand side scale, while those for the crystalline state (CR) are shown by red lines using the right-hand side scale. The results for W = 500 nm are shown by solid lines with solid symbols and those for W = 450 nm are shown by dashed lines with hollow symbols. When GST is in amorphous state, it can be observed that for W = 500 nm and T = 20 nm, shown by a solid blue line, the mode loss decreases with the slab thickness S, as the waveguide core area increases.

On the other hand, the mode loss for the crystalline state, shown by a solid red line, also decreases with S, but these values are nearly two orders of magnitude larger than those in the amorphous state. This is because, for the GST in the crystalline state, imaginary part of its refractive index is much larger than that in the amorphous state. When the W reduces to 450 nm, the mode loss of WG1 for both the states, shown by the dashed red and blue lines, increases. It can be concluded that a wider Si waveguide can yield smaller mode loss values for both the states when the slab thickness S increases steadily from 10 to 120 nm.

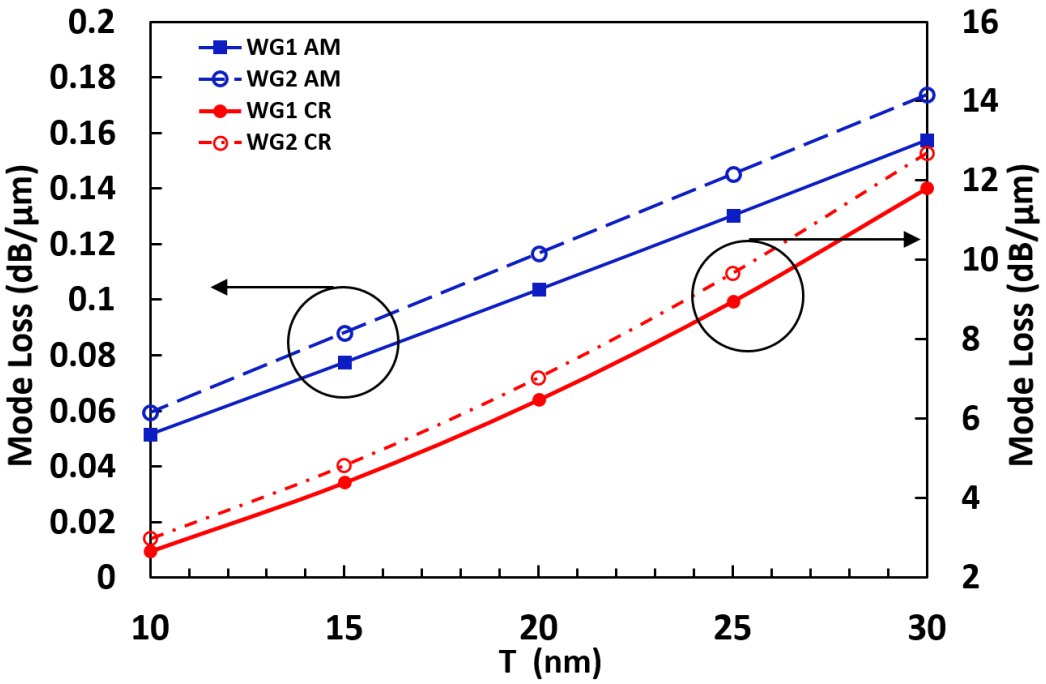

Fig. 4.12. Variations of the mode loss between amorphous and crystalline states with GST thickness T for WG1 and WG2.

The variations of modal loss for WG1 and WG2 with the GSST thickness T are shown in Fig. 4.12. Results for the amorphous state (AM) are shown by blue lines, using the left-hand side scale, while those for the crystalline state (CR) are shown by red lines using the right-hand side. When W is kept fixed at 500 nm and S at 90 nm, a steady increase of GST thickness T from 10 to 30 nm leads to large increase in the mode loss values of WG1 in both amorphous and crystalline states. However, when the WG1 is changed to a Si nanowire core WG2, it will have a larger mode loss in both amorphous and crystalline states compare to WG1.

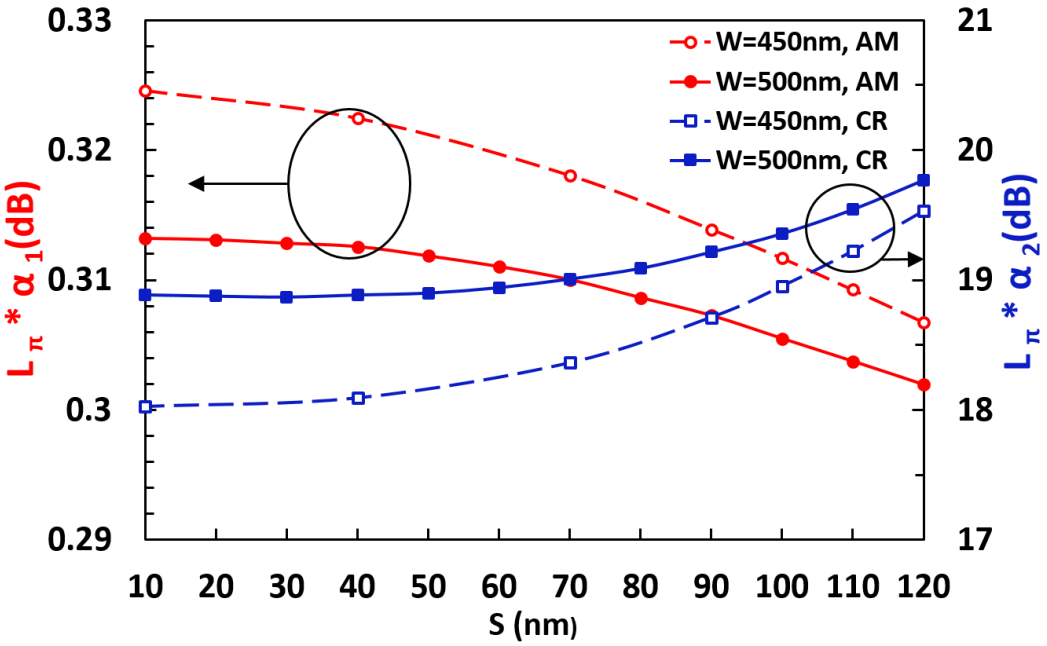

Fig. 4.13. Total modal loss of WG1 in amorphous and crystalline states with varying S for two different widths.

Variations of the total modal loss ($L_\pi*\alpha_1$) of WG1 with the slab thickness, S, for device length = L_π, W = 500 nm and T = 20 nm for the amorphous state is shown by a solid red line in Fig. 4.13. With the steady increase of Si slab height S from 10 to 120 nm, the total loss value reduces slightly from 0.313 to 0.302 dB.

On the other hand, the total modal loss for the crystalline state ($L_\pi*\alpha_2$) shown by a blue solid line increases slightly from 18.89 to 19.77 dB with the slab height. These values are much higher than those in the amorphous state. When the width W reduces to 450 nm, the total modal loss of WG1 for both the states are shown by the two dashed lines. It can be concluded that the wider Si waveguide core can

achieve a smaller total modal loss for amorphous state and larger loss values in crystalline state while the slab height S increases from 10 to 120 nm. Although the smaller L_π may yield a possible compact MZI design with a lower total modal loss in the amorphous state for both the WG1 and WG2 designs, but 18-20 dB modal loss for the crystalline states will cause incomplete power cancellation and thus a poor switching extinction ratio.

As it is clear from the above discussion that the ER based approach is not suitable for a possible GST based photonic device, next the EA (k_{e2}-k_{e1}) effect will be considered for the possible device design. Here, we assume that the device has a total extinction ratio of 20 dB between amorphous and crystalline states, which means only 1% power at the "OFF" state compared to the "ON" state. However, any other preferred extinction ratio can also be considered. In this particular case, the corresponding device length L_b can be calculated as:

$$L_b(\mu\text{m}) = \frac{20}{(\Delta\alpha)} = \frac{20}{(\alpha_2 - \alpha_1)} \tag{4.4}$$

If we consider a GST-clad section of length L_b, then the modal loss for the crystalline state would be 20 dB higher than that of the amorphous state.

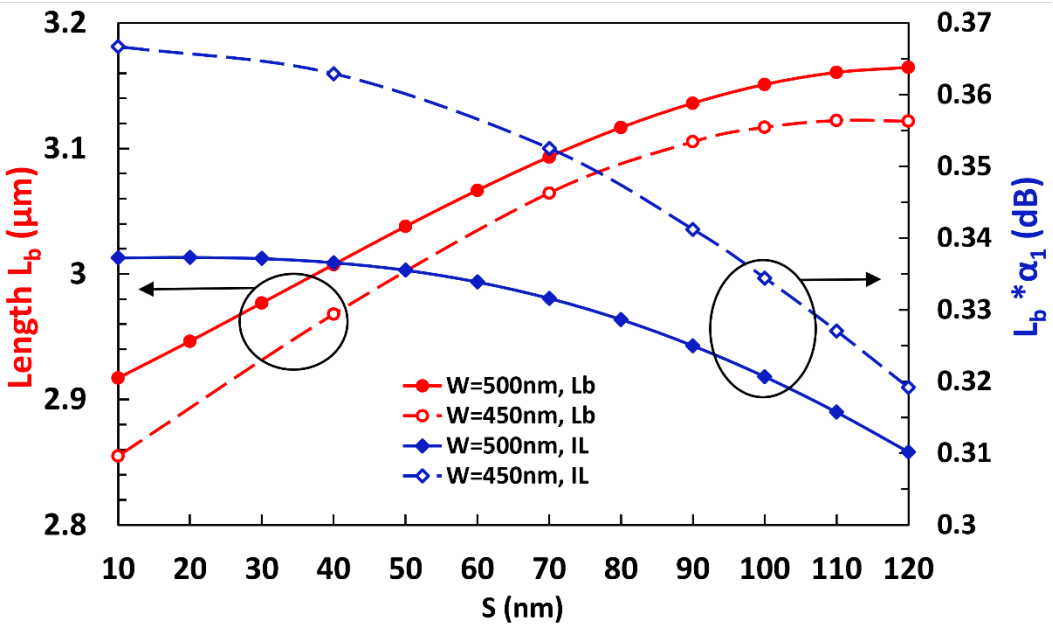

Fig. 4.14. L_b and total modal loss in amorphous state with varying S for two different widths.

Variations of device length L_b and modal loss of amorphous state ($L_b*\alpha_1$) with the slab height S are shown in Fig. 4.14. When W is fixed at 500 nm and T = 20 nm, the device length L_b is shown by a solid red line. With the steady increase of S from 10 to 120 nm, the device length L_b increases monotonically from 2.92 to 3.16 µm, which also shows that a novel compact device is possible. For W = 450 nm shown by a dashed red line, it can be noticed that the L_b also increases but these values are always smaller than that of a wider waveguide.

On the other hand, total modal loss of the device for the low loss amorphous state is shown by blue lines on the right scale. For the W = 500 nm, the total modal loss of the amorphous state shown by a solid blue line reduces from 0.34 to 0.31 dB when S increases to 120 nm. Similarly, for W = 450 nm shown as a dashed blue line, the total loss also reduces but always has larger loss values than those of the 500 nm wide waveguide. It can be concluded here, a lower slab thickness S can yield a shorter device, but the total modal loss for amorphous state would be higher. However, a Figure-of-Merit, which could be taken as their product, remains almost constant. Similarly, a narrower Si width W not only requires a longer device length but also suffers from a larger modal loss, which is thus may not be a preferred design.

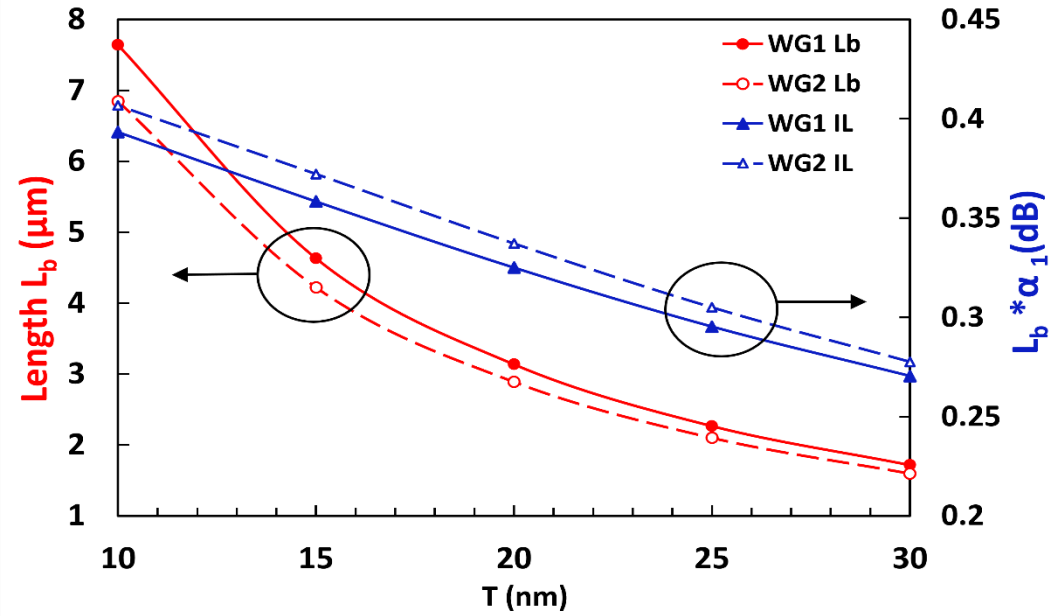

Fig. 4.15. L_b and total modal loss in amorphous state with varying T for WG1 and WG2.

Variations of the device length and total modal loss in amorphous state with the GST thickness, T are shown in the Fig. 4.15. In this case, when W is fixed at 500 nm and S = 90 nm, the device length L_b's of WG1 and WG2 are shown by a solid red line and a dashed red line, respectively, using the left-hand side scale. It can be noted that when the GST thickness, T increases from 10 to 30 nm, modal loss for crystalline state reduces rapidly, but not shown here. But as a result, the device length L_b for both WG1 and WG2 decrease from 7 μm to a lower 2 μm value to achieve 20 dB extinction ratio, as shown here by red lines. However, L_b of WG1 with a rib structure always needs to be slightly longer, but their difference will become smaller as the T increases to 30 nm.

On the other hand, the total modal loss for amorphous state of WG1 and WG2 is shown by blue solid and dashed lines using the right-hand side scale. It can be noted that, the propagation loss of WG1 decreases from 0.39 to 0.27 dB as the T increases to 30 nm, meanwhile the loss of WG2 also decreases but always suffers from higher loss values than that of WG1. It can be concluded that with a larger GST thickness T, the WG1 with the rib structure yields a short device length and smaller loss for the amorphous state. On the other hand, the adoption of a Si nanowire waveguide WG2, shown by dashed lines, although yields a slightly shorter device but with a slightly larger total modal loss.

The modal field profiles for the incident Si rib waveguide and GST-cladded Si rib waveguide at crystalline states were shown in Figs. 4.4 (a) and 4.6 (a). These field profiles were different due to the presence of GST layer and particularly very different for the crystalline GST state. This indicates the possibility of a considerable power loss at junctions 1 and 2. The performance of GST EA modulator may be critically affected by these coupling losses and considered next.

It is desirable to have a lower coupling loss at the junction interface for both the GST states. A powerful numerical approach, the LSBR method, is utilized to calculate the power coupling loss between the input Si waveguide and the active Si-GST waveguide.

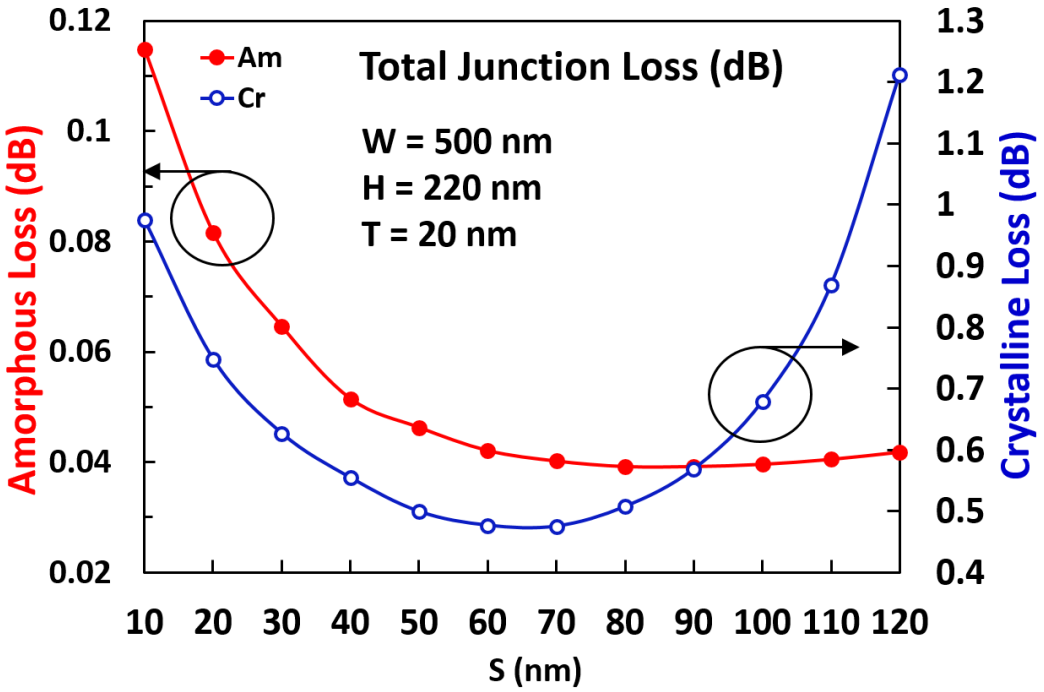

Fig. 4.16. Variation of the total junction loss of WG1 in amorphous and crystalline states with the slab thickness, S.

The effect of slab thickness S on the junction loss is first studied. In this case, the width W is fixed at 500 nm and T = 20 nm, the total junction losses of WG1 from both the input and output side coupling, calculated by the LSBR method for the amorphous state, are shown by a solid red line in Fig. 4.16. It shows that when the slab thickness S increases from 10 to 120 nm, the total junction losses can decrease from a larger value of 0.115 dB at S = 10 nm, and then reach a nearly constant level around 0.04 dB for slab thickness S larger than 60 nm. On the other hand, the total junction loss of WG1 in crystalline state is shown by a solid blue line using the right-hand side scale. This junction loss reduces from 0.98 dB to the minimum 0.475 dB when the S increases to 70 nm. It then increases rapidly to a large value of 1.21 dB at S = 120 nm. This suggests that slab thickness, S between 60-90 nm, can yield a satisfactory design with a lower junction loss at the amorphous state, as additional coupling loss in the crystalline state may not be critical.

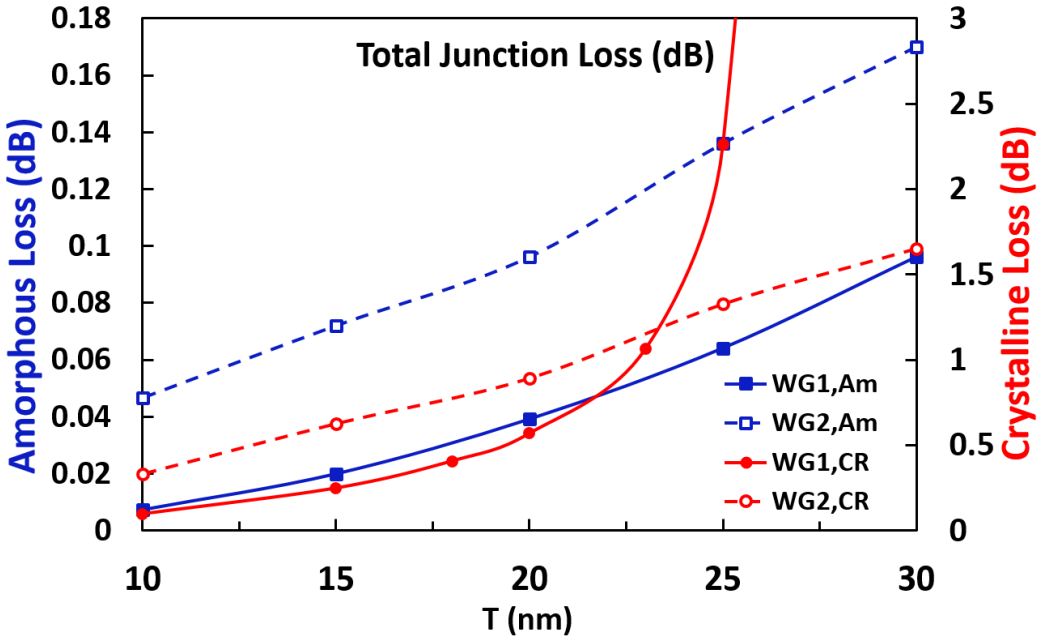

Fig. 4.17. Variation of the total junction loss of WG1 and WG2 in amorphous and crystalline states with the GST thicknesses, T.

Next, effect of GST thickness T on the junction loss is studied. When the width is fixed at 500 nm and S = 90 nm for the amorphous state, the total junction losses from both the input and output junctions for WG1 as a function of GST thickness T are shown by a solid blue line in Fig. 4.17. For comparison, junction loss for GST clad nanowire waveguide WG2 at amorphous state is also shown by a dashed blue line. As T increases from 10 to 30 nm, the junction losses in both WG1 and WG2 increase and the WG2 always suffers from a higher loss value from 0.05 to 0.17 dB. For the crystalline state, the total junction losses in WG1, shown by a solid red line using the right-hand side scale, increase sharply from 0.1 dB to more than 3 dB. On the other hand, the total junction losses for WG2, shown by a dashed red line, increase monotonically from 0.33 to 1.66 dB. It can be concluded that when GST is in the crystalline state, the junction losses in WG1 will be unstable when T is more than 25 nm, but in WG2 the junction loss will be smaller. This study indicates that a thinner, 10-20 nm thickness GST layer would yield a lower junction loss value in both the states.

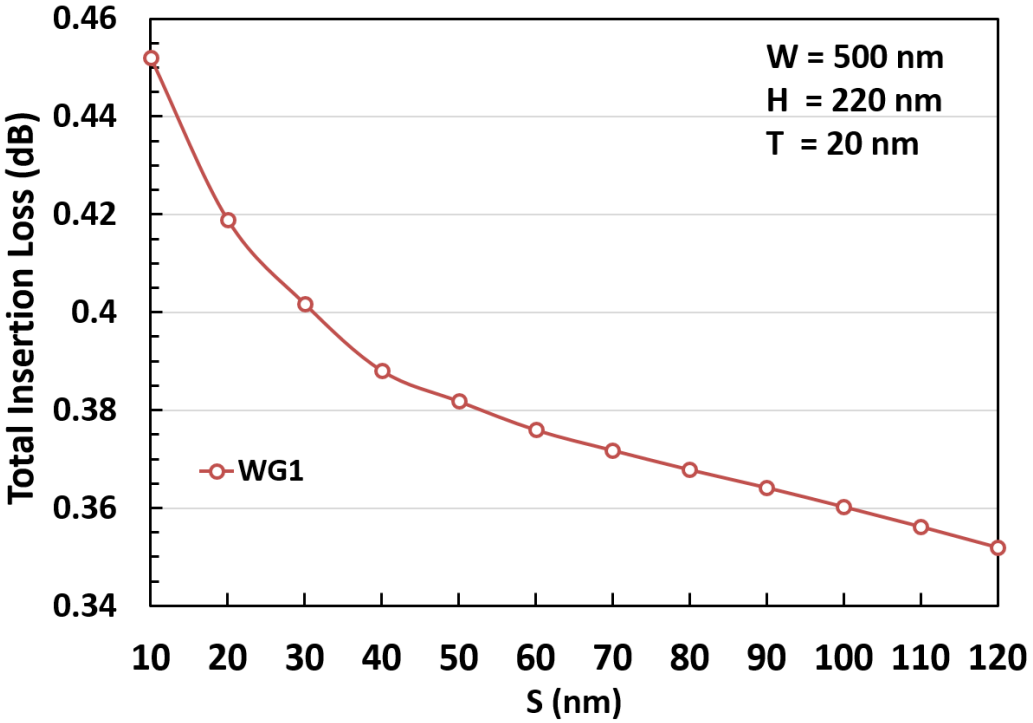

Fig. 4.18. Variations of total insertion loss of WG1 in amorphous state with slab thickness S.

The associated insertion loss suggests that an optical modulator at the "ON" state can be obtained when GST is in amorphous state. The total loss is comprised of the modal loss of the GST-Si hybrid waveguide section due to the absorption in the GST cap and the coupling loss between the passive input and output Si waveguide sections and the active GST-Si hybrid waveguide section. Here, when W is fixed at 500 nm and T = 20 nm, the associated total insertion loss of WG1 is shown by a solid red line in Fig. 4.18. It can be observed that, when the slab thickness S increases from 10 to 120 nm, the total insertion loss of the modulator reduces from 0.452 dB to a relatively lower value of 0.352 dB, yielding a compact device with length smaller than 3.2 μm, as shown previously in Fig. 4.14.

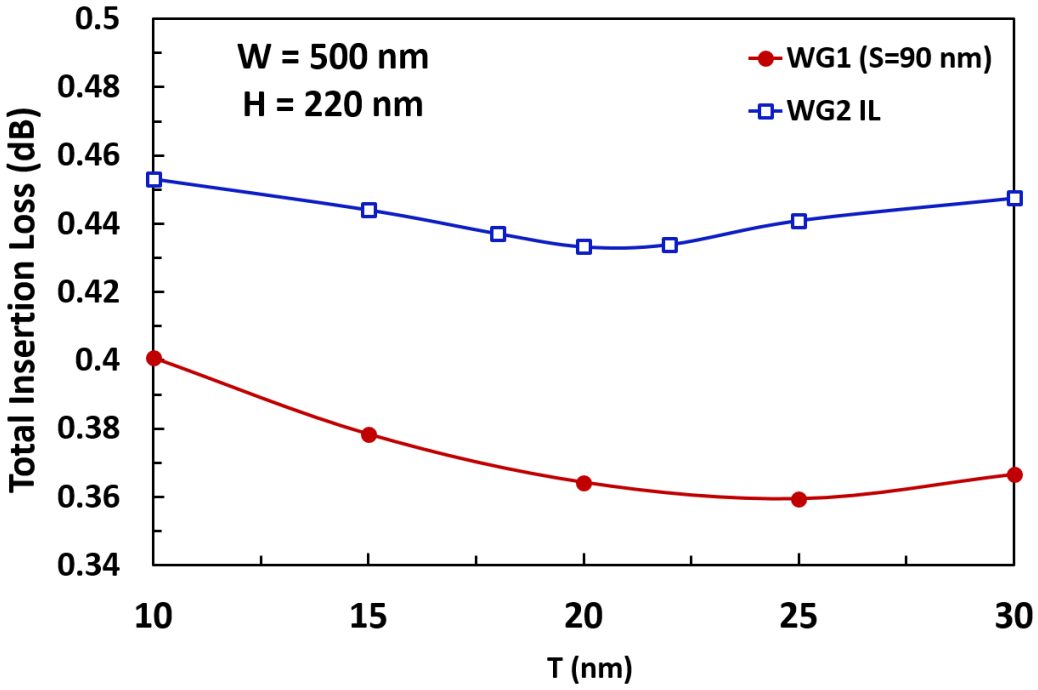

Fig. 4.19. Variations of the total insertion loss for WG1 and WG2 in amorphous state with the GST thickness, T.

Finally, variations of the total insertion loss with the GST thickness T for both the designs are shown in Fig. 4.19. Here, the width W is fixed at 500 nm and S = 90 nm (for WG1), the associated total insertion losses for the modulator based on WG1 and WG2 are shown by the red and blue solid lines, respectively. It should be noted that for a thinner GST layer, although per unit distance modal loss (α_1) was lower, but the overall modal loss was higher, as an increased device length is needed to achieve the targeted 20 dB extinction ratio between the two states. On the other hand, junction loss increases for a thicker GST layer, as the mode field profile deviates considerably from that of the input and output waveguides without a GST clad.

It can be observed from Fig. 4.19, that for the Si rib waveguide WG1, the total insertion loss reduces from 0.4 dB to the minimum 0.36 dB as the T increases from 10 to 25 nm and then increases slightly to 0.367 dB at T = 30 nm. On the other hand, the total insertion loss for the Si nanowire waveguide WG2 also decreases to a lowest value 0.433 dB as the T increases to 20 nm. After that, the insertion loss starts to increase slowly to a higher value with the thicker GST layer. It can be concluded that the Si rib waveguide WG1 will have a smaller total insertion loss

compared to the Si nanowire waveguide WG2, and the minimum insertion loss can be achieved for a 25 nm GST layer.

This modulator has been designed to have modal loss in the crystalline state 20 dB higher than its amorphous state. However, as the junction loss for crystalline state is also higher than that of the amorphous state, so the total loss for the crystalline state would be more than 20 dB higher than the low-loss amorphous state.

4.4 Experimental observation

4.4.1 Experimental Setup

In this section, the experimental process for investigating the effective index change of the Si-GST rib waveguide during the GST phase changing performed by our collaborator Dr. Zhang at SJTU will be discussed, and the experimental results will be compared with our FV-FEM simulation results.

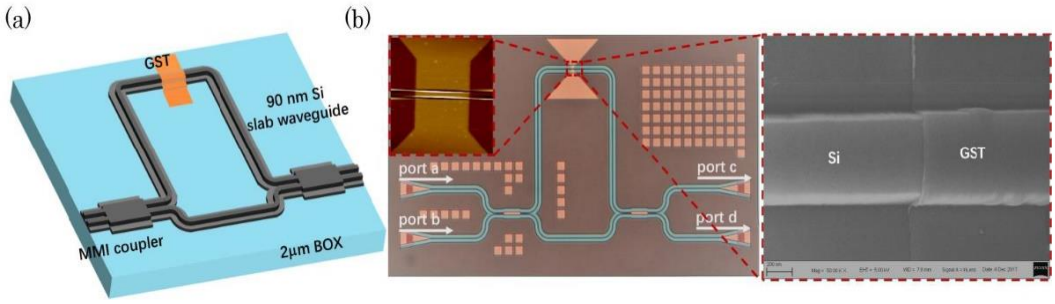

Fig. 4.20. (a) Schematic overview of the unbalanced MZI. (b) Optical microscope of the fabricated MZI [65].

An unbalanced Mach-Zehnder interferometer (MZI) structure shown in Fig. 4.20 (a) will be used to measure the both real and imaginary parts of effective index of the Si-GST waveguide WG1 during phase changing. It can be clearly observed that, in the optical microscope image shown in Fig. 4.20 (b), the proposed MZI have two 2 x 2 MMI couplers connected with two different length waveguides. The Si-GST rib waveguide is placed in the longer arm which have 400 μm extra length than the other arm.

The waveguide WG1 can be fabricated on a silicon-on-insulator (SOI) wafer which have a 220 nm thick top Si layer, and a buried oxide layer (BOX) with 2 μm depth. First, the SOI wafer need to be cleaned well by acetone, then the wafer will be spin-coated with a photoresist and prebaked for minutes. After heating, the photoresist will be exposed to the ultraviolet light with a photomask so that the rib pattern can be defined, then the photoresist needs to be completely removed. The 220 nm thick Si layer can be etched by inductively coupled plasma dry etch, through controlling the voltage and time of etching, the Si rib and slab layer can be achieved. Subsequently, poly-methyl-meth-acrylate (PMMA) resist is spin-coated and electron-beam lithography process will be used to open the GST deposition window. The GST film can be sputtered on the Si layer by a RF (radio frequency) sputtering system from a $Ge_2Sb_2Te_5$ alloy target. Finally, the GST outside the deposition window will be removed in a warm acetone bath [65].

4.4.2 Measurement

The transmission spectrum of the MZI was measured at SJTU by using a tunable laser scanning from 1520 to 1580 nm. The quasi-TE mode source was adjusted by a polarization controller. Then two single-mode fibres mounted at an angle of 10° are used to couple light in and out of the MZI through grating couplers. Once the light is coupled into the MZI, the transmission spectra from two input and output ports was measured. If the GST film undergoes a phase changing, the phase of the arm will be affected by the real part of the effective index changes so that the measured spectral will be shifted. On the other hand, then change of the imaginary part of the effective index will measured by the optical loss of the arm, so that the extinction ratio (ER) in the spectrum can be achieved. By measuring the variations of the spectral shift and ER, both the real and imaginary effective index change of the Si-GST rib waveguide can be obtained [65].

4.4.3 Experimental results

state	Annealing condition	Δn_e	Δk_e	Loss (dB/μm)
1	No	0.0924	0.004	0.05
2	100 °C, 4 min	0.0932	0.0041	0.05
3	200 °C, 4 min	0.237	0.083	2.77
4	245 °C, 4 min	0.263	0.113	3.72

Table 4.2. Measured parameters of the Si-GST hybrid waveguide at GST states 1-4 [65].

The thermal annealing was used to change the phase of GST film in this proposed experiment. This crystallization can be achieved by heating GST above the glass transition temperature and then slowly cooling down. However, during the crystallization of the initial amorphous state GST alloy, the intermediate phase state of the GST film can be incurred which means the GST film can be in mixed portions of amorphous and crystalline phases. It can be noted that, by controlling the degree of partial crystallization, the intermediate phase of GST can be achieved, thus the various optical property of GST can be obtained.

Table 4.2 summarizes the measured parameters for different GST states. At the beginning, the transmission spectra of MZI without GST cladding was tested. Then the MZI will be sputtering-coated with the original amorphous state GST patches followed by measurement as state-1. Next, the MZI device was annealed on a hot plate at 100 °C and 200 °C for 4 min to reach various intermediate state of GST, identified as state 2 and state 3. Finally, a 4-min annealing process at 245 °C was used to achieve the fully crystallized GST as state 4.

It can be noted in the Table 4.3, when the amorphous state GST was deposited on the Si waveguide as state 1, the measured effective index difference between Si waveguide and Si-GST waveguide is 0.0924, the FV-FEM simulation result is 0.1008, only 9% higher than the measured results. After a 4-min annealing process at 245 °C, the crystalline state GST is achieved as state 4, the measured effective index difference between Si waveguide and Si-GST waveguide is 0.263, the FV-FEM simulation result is 0.3004, which is a 14% tolerance but can be acceptable.

The measured effective index tunning range between the amorphous and crystalline state of the Si-GST waveguide is 0.1706, which is slightly smaller than the simulation results 0.1996.

	Experimental [65]	FV-FEM simulation	Tolerance
Effective index difference Δn_e (state 1-AM)	0.0924	0.1008	+ 9%
Effective index difference Δn_e (state 4-CR)	0.263	0.3004	+14%
Effective index difference Δn_e (AM-CR)	0.1706	0.1996	+17%
Propagation loss (AM)	0.05 dB/μm	0.013 dB/μm	-74%
Propagation loss (CR)	3.72 dB/μm	4.038 dB/μm	+8.5%

Table 4.3. Measured parameters of the Si-GST hybrid waveguide versus FV-FEM simulation results and tolerance

The measured propagation loss for the amorphous state Si-GST waveguide is 0.05 dB/μm, however the simulated propagation loss is 0.013 dB/μm only 26% of the experimental results. The discrepancy can be caused by several factors, the GST film thickness is taken as 20 nm in the simulation, but in real fabrication, this thickness may be deviated slightly. This measured higher propagation loss is also probably caused by the scattering loss due to the surface roughness of the thin GST layer, but as the amorphous state propagation loss is quite small, for a 10 μm long device, it only produces 0.3 dB tolerance which can be neglected. The measured propagation loss for the crystalline state Si-GST waveguide is 3.72 dB/μm, which have a good agreement with the simulated results 4.038 dB/μm, the 8.5 % tolerance due to the scattering loss is overwhelmed by the material absorption loss as the GST is in crystalline state. It can be concluded that the experimental results overall agree with the simulation predictions [65].

4.5 Summary

In this Chapter, rigorous modal analysis of a GST-clad Si rib waveguide (WG1) and a GST-clad Si nanowire waveguide (WG2) for comparison at the telecommunication wavelength 1.55 μm is carried out by using an accurate **H**-field based FV-FEM. We have also investigated the coupling loss at the butt-coupled junctions by using a rigorous junction analysis approach. It can be concluded that although GST cladding can yield a high ER value, however due to the associated higher EA values, a conventional MZI design will not be viable. On the other hand, EA-type design would be preferred, which exploits the larger modal loss difference between the GST amorphous and crystalline states. Here, the effects of Si slab thickness S, waveguide width W, and GST layer thickness T, on device performances for both the WG1 and WG2 designs are presented.

It is shown here that the Si slab height larger than 90 nm can yield a lower modal loss 0.34 dB at amorphous state but require a slightly longer device length around 3.1 μm. On the other hand, the slab thickness larger than 60 nm can yield a satisfactory design with a lower junction loss at amorphous state. This suggests that the slab thickness, S = 60-90 nm can be taken as an optimal design to balance the device length and also to achieve a lower insertion loss.

It also can be noted that a narrower Si width W = 450 nm will not only yield a longer device length but also a larger modal loss. Therefore, a wider 500 nm Si waveguide is preferred. It is also observed that, a thicker GST layer not only can reduce the total modal loss but also can yield a shorter device length. However, due to the mismatch of the modal fields, the junction loss would increase with the GST thickness. The optimal design needs to consider both these loss values. Here, T = 15-25 nm is considered as the optimal design as a thicker GST layer may produce unstable junction loss for the crystalline state. For comparison of the Si-GST rib waveguide WG1 with a fully etched Si-GST nanowire waveguide WG2, it is shown here, that the WG2 always suffers from a higher modal loss and a higher junction loss than that of WG1. It thus yields a higher total insertion loss, so the Si rib waveguide WG1 is a preferred option for the optimal waveguide structure adopted for the device. Additionally, WG1 rib waveguide maybe a preferred over fully

etched WG2 as WG1 will also have lower optical loss due to reduced scattering loss at the edges.

In summary, the GST-cladded Si rib waveguide with a width W = 500 nm, a slab thickness S = 60-90 nm, and a GST thickness T = 15-25 nm can be considered as optimal design for the self-sustained 1 x 1 modulator. In this case, a very compact, 2-5 μm long device is expected to show an extinction ratio of more than 20 dB between with the total insertion loss of only 0.36 dB at the amorphous state. The GST-cladded Si rib waveguide with similar design were fabricated at SJTU and experimentally validated.

Chapter 5

Design of Phase Change $Ge_2Sb_2Te_5$ based ON-OFF Electro-Optic switch

5.1 Introduction

Optical switch is an essential element in photonic integrated circuits (PIC_S) which can effectively routing the light into different paths. At present, the electro-optical (EO) and thermo-optical (TO) effects are the primary switching mechanism for the on-chip optical switch designs. Thermo-optical effect, through varying temperature will induce a change in the waveguide material refractive index, and electro-optical effect which operate based on the waveguide material refractive index in response to an applied electrical field. However, both switching mechanisms can only achieve very smaller refractive index change ($\Delta n \approx 0.001$-0.004) in the conventional waveguide material (Si, InP, GaN…) thus resulting in a large device size and with an excessive power consumption.

The application of phase change materials (PCMs) for optical switching is a leading-edge research topic. A considerable real part of refractive index change ($\Delta n > 1$) can be accomplished during the phase transition in PCMs which shows promising to compact optical switch design. The $Ge_2Sb_2Te_5$ (GST) is an emerging phase change material which recently used in the optical storage, which have distinct optical and electrical properties between its amorphous state and crystalline state. Its phase change process can be reversible and nonvolatile with many times repeatable phase transitions. Moreover, the GST also have the self-sustained

features which means no power is needed to maintain any particular switch's phase state.

In this chapter, a novel co-directional coupling between the Si nanowire and the ITO-GST-ITO waveguide for a compact ON-OFF switch at the telecommunication wavelength, 1.55 μm is presented. As the real refractive index (n) and the extinction coefficient (k) of the GST is very high when it is in crystalline, it is necessary to find the phase matching condition of the Si-GST coupled waveguide in order to efficient power transfer between Si nanowire and GST waveguide. The complex mode effective indices of the coupled waveguide with variations of ITO separations and GST thickness are calculated by our in-house codes based on a rigorous **H**-field FV-FEM in conjunction with the perturbation technique. The modal evolution of fundamental TE mode, phase matching condition of the even and odd supermodes and the coupling length of the coupled Si-GST waveguide are also investigated for GST crystalline state. The LSBR will be used as a junction analysis approach to calculate the optical power coupling efficiencies between input Si nanowire and active Si-GST composite waveguide. Furthermore, the power evolution of the active Si-GST waveguide along propagation direction at both amorphous and crystalline state is studied by a finite difference time-domain method (FDTD) solution. The total insertion loss and extinction ration of the device, and the validity of the optimised coupling length are analysed in detail.

5.2 Schematic and principle

5.2.1 Cross-section view and work principle

The three-dimensional (3D) schematic diagram of the proposed Si-GST electro-optic switch is shown in Fig. 5.1 (a) which consists of an input Si nanowire before Junction J_1, followed by an active Si-ITO-GST-ITO coupled section of length L_c also an output Si nanowire.

(a):

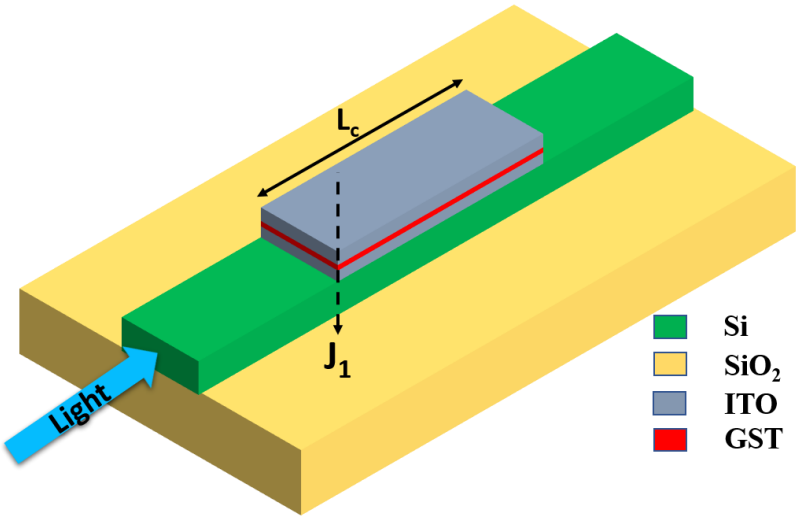

(b):

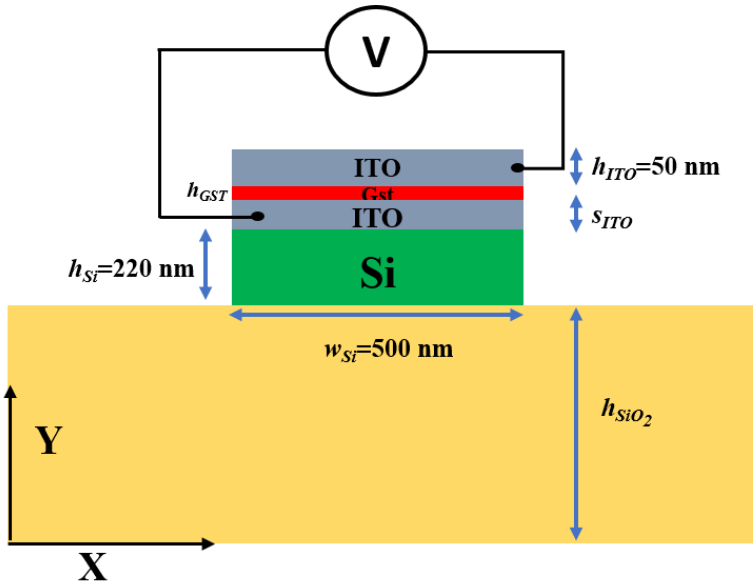

Fig. 5.1. (a) Schematic of the proposed co-directional Si-GST coupled optical switch. (b) Cross-sectional view of the active section of the Si-GST coupled waveguide.

The cross-sectional view of the active Si-GST coupled section is shown in Fig. 5. 1 (b). The coupled section consists of a Si nanowire (wg1) and an ITO-GST-ITO waveguide (wg2). The required electric field for changing GST states between crystalline and amorphous can be provided through the two ITO electrodes. Here, most commonly 220 nm thick Si nanowire is considered, and its width is initially taken as 500 nm. On top of the Si core, an ITO layer with thickness, S_{ITO} is taken

as the separation layers to control the coupling. On top of the first ITO separating layer, a GST layer with thickness h_{GST} is deposited and its thickness can be controlled to achieve the phase matching. On top of the GST layer, another ITO layer of the thickness h_{ITO} = 50 nm is considered to facilitate the application of electric field. These two ITO layers not only used as electrode for triggering GST phase change but also can protect the GST film from being oxidized when exposed to the air.

For a Si strip waveguide with multi layers, the quasi-TE mode is more suitable for as this mode will be more confined well in the Si nanowire than the quasi-TM mode. When the GST crystalline state is triggered, the optical switch will be at "OFF" state, the phase matching condition should be satisfied for the Si-GST coupled waveguide. The input quasi-TE_0 mode excited at the input Si nanowire can be transferred to the quais-TE_1 mode of the upper GST waveguide after propagating along the coupling length, L_c. When the GST amorphous state is triggered at "ON" state, the input quasi-TE_0 mode will propagate along the lower Si nanowire without any mode coupling, because the phase matching condition cannot be met with the Si-GST coupled waveguide.

5.3 Numerical results

5.3.1 Optical property of the materials for simulation

Before the FV-FEM simulations, it is essential to have reliable values of the complex refractive index (n + *j**k) of GST and the other optical material employed to form the Si-GST coupled waveguide. Several literature sources of n and k of GST have been studied as the fundamental precursor to waveguide modelling. In reference [63], H. Liang have shown various of theoretical and experimental GST refractive index as a function of wavelength and optimised them in a table for his simulations. Among them, H. Liang considered the K. Shporkto's values [56] for the GST at wavelength 1.31 and 1.55 μm due to these values have close agreement with other measurement results.

Therefore, for this proposed optical switch simulation, the complex refractive indices of GST at 1.55 μm wavelength are taken as: n (AM) = 4.6 + *j**0.12 and n (CR) =7.45 + *j**1.49 at amorphous and crystalline states, respectively [63]. The refractive indices of Si, SiO_2 and ITO are also taken as 3.47548, 1.44402 and 1.9595+*j**0.0023, respectively at the operating wavelength of 1.55 μm.

5.3.2 Modal analysis for phase matching conditions

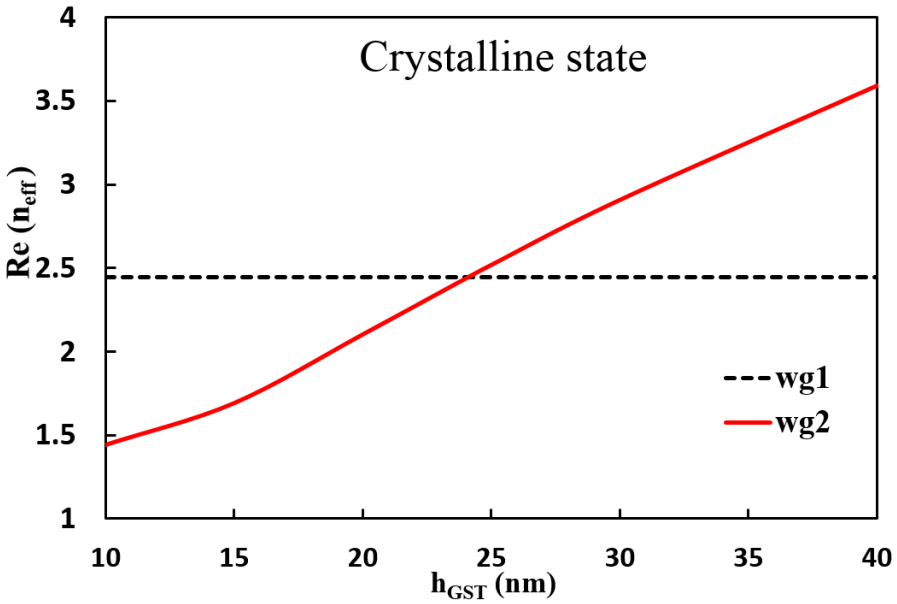

Fig. 5.2. Variations of the real part of effective indices of an isolated Si nanowire wg1 and an isolated ITO-GST-ITO waveguide wg2 as a function of h_{GST}.

As the loss for the crystalline state is much higher than the amorphous state, the phase matching in this state is necessary in order to efficiently transfer power from input Si nanowire wg1 to upper GST waveguide wg2 to attain the "OFF" state. Hence, design objective here is to achieve phase matching the GST waveguide in the crystalline state with the Si nanowire.

In order to achieve the phase-matching condition for the Si-GST coupled waveguide based electro-optic switch at "OFF" state when GST in crystalline state, variations of the effective indices of wg1 and wg2 with the different GST layer thickness are calculated by using the FV-FEM and shown in Fig. 5.2. In this case, the thickness of the ITO separations of wg1 and wg2 are both chosen at 500 nm in order to achieve the comparable effective index of two isolated waveguides.

First, the real part of the effective index n_e of the fundamental quasi-TE (H_y^{11}) mode of the wg1 is calculated to be 2.4465 and denoted by a horizontal black-dotted line in Fig. 5.2. The real part of the effective index of the wg2 is shown by a red solid line in the Fig. 5.2. It is shown that the n_e values of wg_2 increases from 1.45 to 3.6 with the GST thickness h_{GST} increases from 10 to 40 nm and the phase-matching condition should be around h_{GST} = 24 nm.

Although the phase matching condition is shown around 24 nm, when these two waveguides are isolated, however, the phase matching condition for coupled waveguide also need to be studied as the mutual loadings by two waveguides are different. To identify phase matching between two nonidentical waveguides, it is essential to solve the supermodes as the phase matching condition may differ considerably from the solutions of two isolated waveguides, due to the unequal loading of each waveguide.

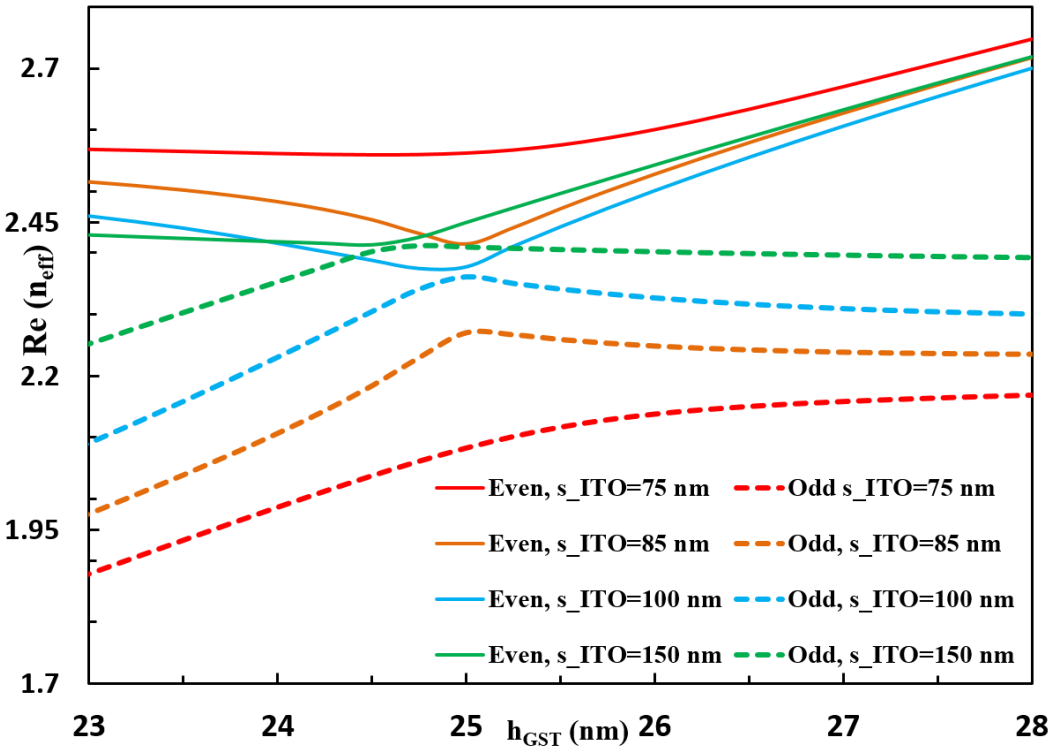

Fig. 5.3. Real part of effective indices of the even and odd supermodes of the coupled section in crystalline state for S_{ITO} = 75, 85, 100 and 150 nm as a function of h_{GST}.

For achieving phase matching of the nonidentical Si-GST coupled waveguide when the GST in crystalline state, variations of the propagation constant (β) or real part of effective index (n_e) need to be calculated with the different separations (S_{ITO}) and the possible phase matching condition. The FV-FEM is used to find the modal characteristics of the supermodes of the Si-GST coupled structure consisting of two nonidentical waveguides. Variations of the real part of effective indices for even and odd supermodes with the of GST layer thickness for four different ITO separations, S_{ITO} are shown in Fig. 5.3.

In Fig. 5.3, when the ITO separation is higher, for S_{ITO} = 150 nm, the real part of effective index of the first supermode which is even or even-like, is shown by a green solid line remains nearly constant around 2.43 until the h_{GST} = 24.5 nm, after that it increase gradually to a higher value 2.7. The real part of effective index of its second supermode, which is odd or odd-like is shown by a green dotted line increases smoothly from 2.25 to 2.4 when the h_{GST} increase from 23 to 24.5 nm then remains nearly constant at 2.4.

For the phase matching condition, two effective indices of even and odd supermodes are close to each other and the phase difference between these modes $\Delta\beta = (\beta_e - \beta_o)$ also Δn_e will be smallest at a certain h_{GST}. It can be noted at h_{GST} = 24.5 nm, is the phase matching condition point for S_{ITO} = 150 nm because the two green n_e curves become closer also have the smallest difference here.

For the smallest ITO separation S_{ITO} = 75 nm, it can be observed that the real part of effective index of the even supermode shown by a red solid line, remains stable around 2.55 when the h_{GST} increases from 23 nm to 25.6 nm, and after that it increases monotonically to a high value 2.75. On the other hand, the real part of effective index of the odd supermode shown by a red dotted line, increase slightly from 1.9 to the peak when the h_{GST} increases from 23 nm to 25.6 nm then level off at n_e = 2.1.

It can be noted that real part of effective index curves for S_{ITO} = 150 nm are closer than those for S_{ITO} = 75 nm also the n_e values of odd and even supermodes become closer for larger separation S_{ITO} due to weaker interaction. When S_{ITO} = 75 nm, the gap between two real part of effective index curves becomes larger due to

the strong coupling and as a result, the minimum Δn_e separation is larger and the phase matching condition point is shifted to h_{GST} = 25.6 nm.

For better understanding of the effect of ITO separation, the real part of effective index for even and odd supermodes with the h_{GST} for S_{ITO} = 85 and 100 nm also calculated and shown by orange and blue lines in Fig. 5.3. It can be noted that the real part of effective index lines of even super-mode starts to decline considerably to a minimum value until h_{GST} = 25 nm, which is the phase matching point for both S_{ITO} = 85 and 100 nm as the odd supermode curves also reach to a peak here, then the even supermode lines are tuned to increase to around 2.7. It can be concluded that, when S_{ITO} = 75, 85 and 100 nm, for the even supermode, the smaller S_{ITO} waveguide can have larger n_e values with the 23-28 nm GST thickness. However, for the odd supermode, smaller S_{ITO} waveguide will have smaller n_e values when the h_{GST} increases from 23 to 28 nm. Moreover, it can be noted that for the ITO separation S_{ITO} = 75, 85, 100 and 150 nm, the larger S_{ITO} waveguide, the n_e curves of even and odd supermodes become more closer and have the smaller n_e values difference between the even and odd supermodes due to weaker interaction between bottom Si nanowire and top GST waveguide with the wider ITO separation. Furthermore, for nonidentical coupled waveguides, the phase matching condition varies as the mutual loadings of the two waveguides are different for various separations. It can be concluded that the Si-GST coupled waveguide with larger S_{ITO} need a slightly smaller h_{GST} for the phase matching condition point.

5.3.3 Fundamental mode field profiles

For the quasi-TE mode, H_y is the dominant and H_x and H_z are the non-dominant components of the magnetic field, **H**. In order to investigate how the GST layer thickness and ITO separation affect the fundamental H_y field so that change the mode effect index, the H_y field profiles of the H_y^{11} even and odd supermodes generated in the Si-GST coupled waveguide with h_{GST} = 23 nm, 24.5 and 28 nm for S_{ITO} = 150 nm is calculated by FV-FEM and plotted in Fig. 5.4. In the Fig. 5.4, it can be observed that, for the even supermodes field plots at left side, the H_y field

have the same sign in Si nanowire wg1 and GST waveguide wg2, while the H_y field have the opposite signs for the odd supermodes.

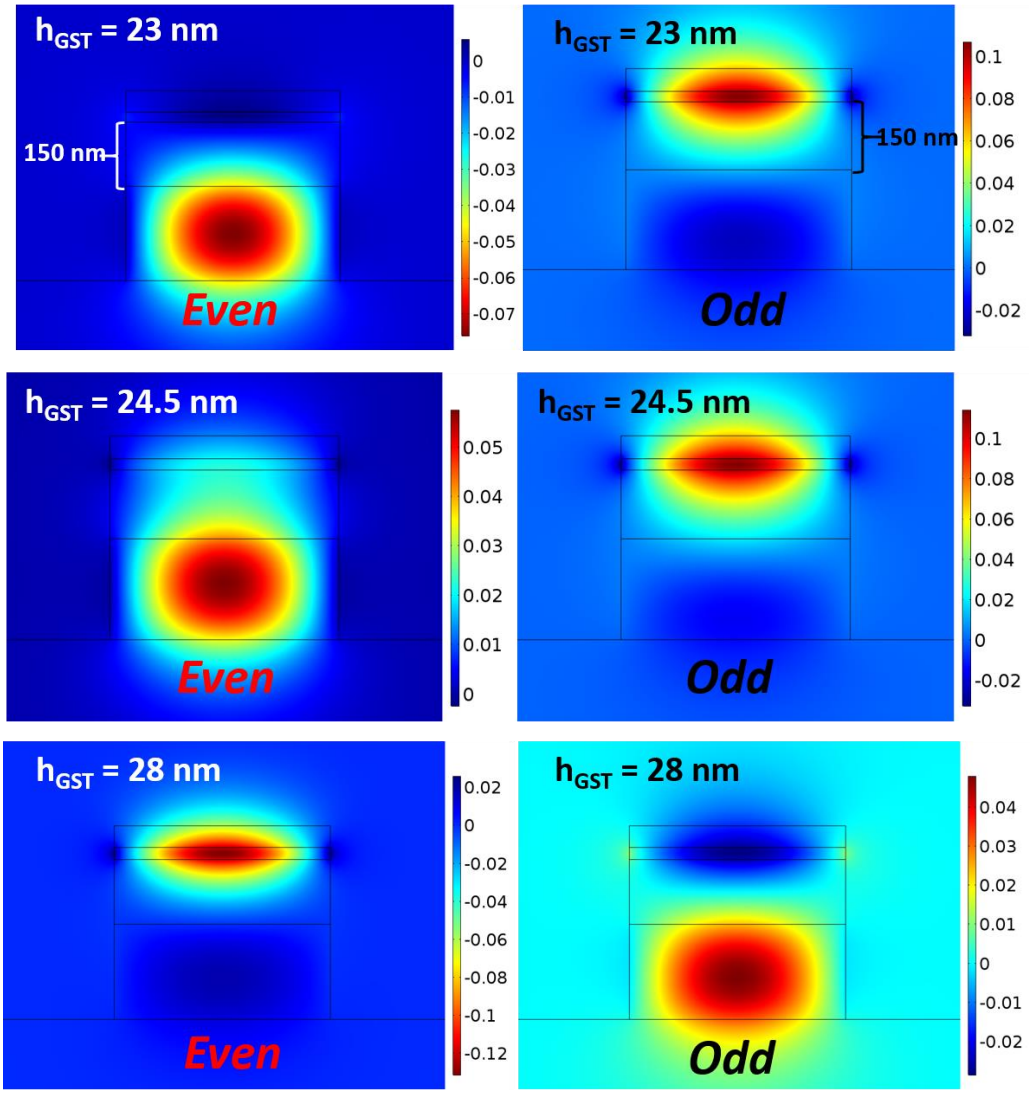

Fig. 5.4. H_y field profiles of the H_y^{11} even and odd supermodes in crystalline state for S_{ITO} = 150 nm and h_{GST} = 23, 24.5 and 28 nm.

Also, it also can be noted that, for h_{GST} = 23 nm, 24.5 nm (even supermode) and 28 nm (odd supermode) plot, a large amount of H_y field well confined into wg1 nanowire and extend little to the upper GST layer. These three field plots can be evaluated as the effective index of the H_y^{11} mode in the Si nanowire wg1 (almost constant) which can be indicated as the steady line section of the two n_e curves of even and odd supermodes for S_{ITO} = 150 nm in Fig. 5.3. On the other hand, for h_{GST} = 23 nm, 24.5 nm (odd supermode) and 28 nm (even supermode) plot, most of H_y

field is extended up to the GST layer and only a small field remains inside the Si nanowire, these plots also represent the effective index of the H_y^{11} mode in the GST waveguide wg2 (increasing) as the h_{GST} increased which can be illustrated as the oblique line section of the two n_e curves for S_{ITO} = 150 nm in Fig. 5.3. Moreover, it is shown clearly in the Fig. 5.4, both even and odd supermodes of the H_y^{11} mode go through a modal profile transformation around the anti-crossing region (h_{GST} = 24.5 nm) although those two n_e curves do not cross each other when h_{GST} increase from 23 to 28 nm. At phase matching point h_{GST} = 24.5 nm, two isolated modes of the H_y^{11} mode in wg1 and wg2 become degenerate, get mixed up and formed the even and odd supermodes of the composite waveguide shown in the middle of Fig. 5.4.

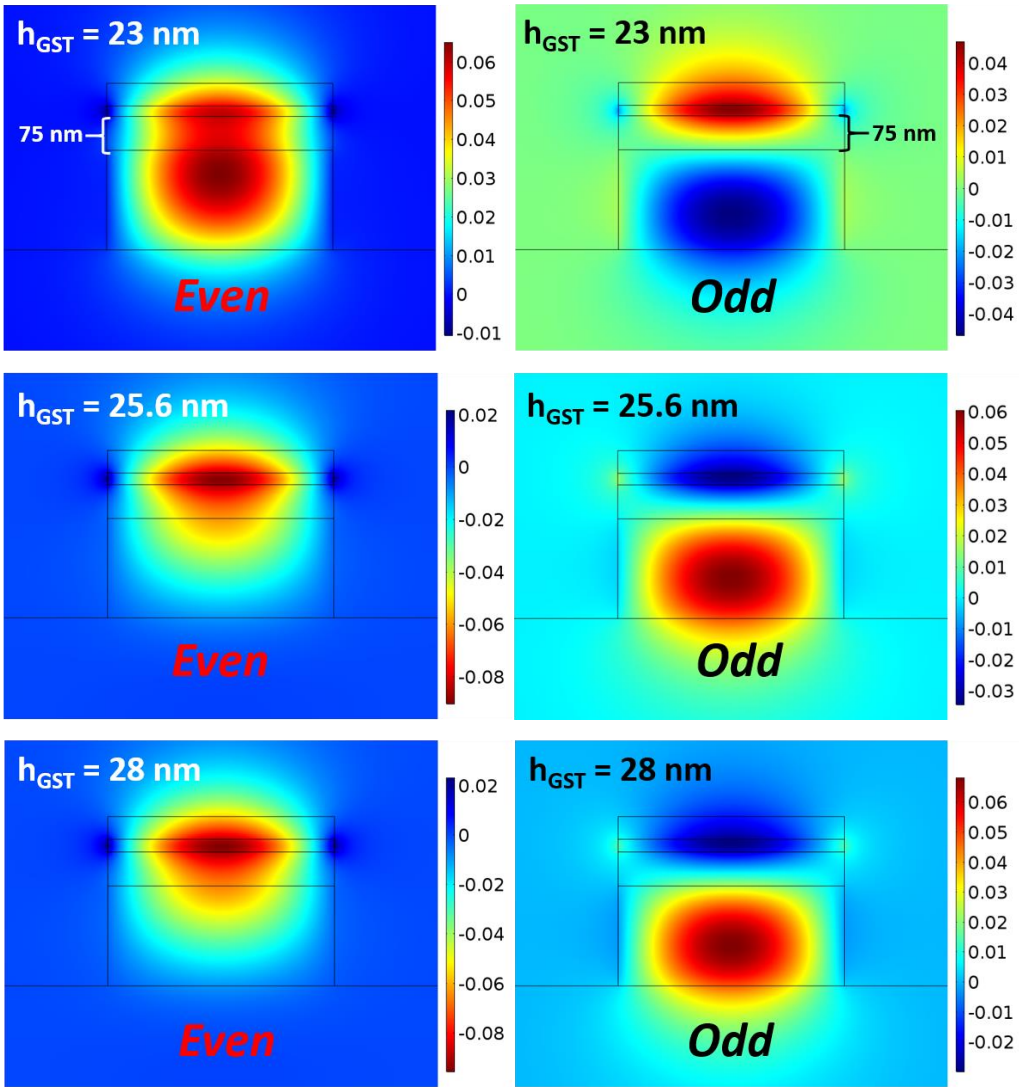

Fig. 5.5. H_y field profiles of the H_y^{11} even and odd supermodes in crystalline state for S_{ITO} = 75 nm and h_{GST} = 23, 25.6, and 28 nm.

When the ITO separation S_{ITO} is decreased considerably to 75 nm, the H_y field profiles of the H_y^{11} even and odd supermodes when the GST in crystalline state with h_{GST} at 23, 25.6 and 28 nm are shown in Fig. 5.5.

For the even supermode plot, at h_{GST} = 23 nm, it can be noted that most of field is located inside the composite Si-GST composite waveguide and two H_y field peaks are confined inside the centre of Si nanowire and GST layers due to the strong coupling between wg1 and wg2 with the 75 nm ITO separation. However, with the h_{GST} increase to 25.6 nm at the phase matching region, the even supermode plot of h_{GST} = 23 nm goes through a transformation to the odd mode, it can be observed that most H_y field is confined in the lower Si nanowire and smaller field is confined inside the GST layer. At h_{GST} = 28 nm, the magnitude of the H_y field is getting larger in the Si nanowire and there is reduced field in the GST layer compared to h_{GST} = 25.6 nm.

On the other hand, for odd supermode plot, at h_{GST} = 23 nm, it can be noted that the magnitude of H_y field are nearly equal and well confined in the upper GST layer and Si nanowire due to the strong interaction between them with a smaller ITO separation also thinner GST layer. Then the GST layer thickness increase to phase matching point 25.6 nm and until at 28 nm, the odd supermode are degenerated to even supermode, most of H_y field is only confined into GST layer and extends slightly to the upper ITO contact and ITO separation regions. It also extends a bit laterally into the lower Si nanowire region.

In order to show the magnitude of the even and odd supermodes field of the Si-GST composite waveguide clearly, the H_y component of the H_y^{11} even and odd supermodes along the vertical directions for S_{ITO} = 150 nm at the phase-matching h_{GST} = 24.5 nm are plotted in Fig. 5.6. The SiO_2 buffer region is shown by a brown shade and Si region with a light green shade, the GST region is shown by red shade in between two ITO layers with grey shade.

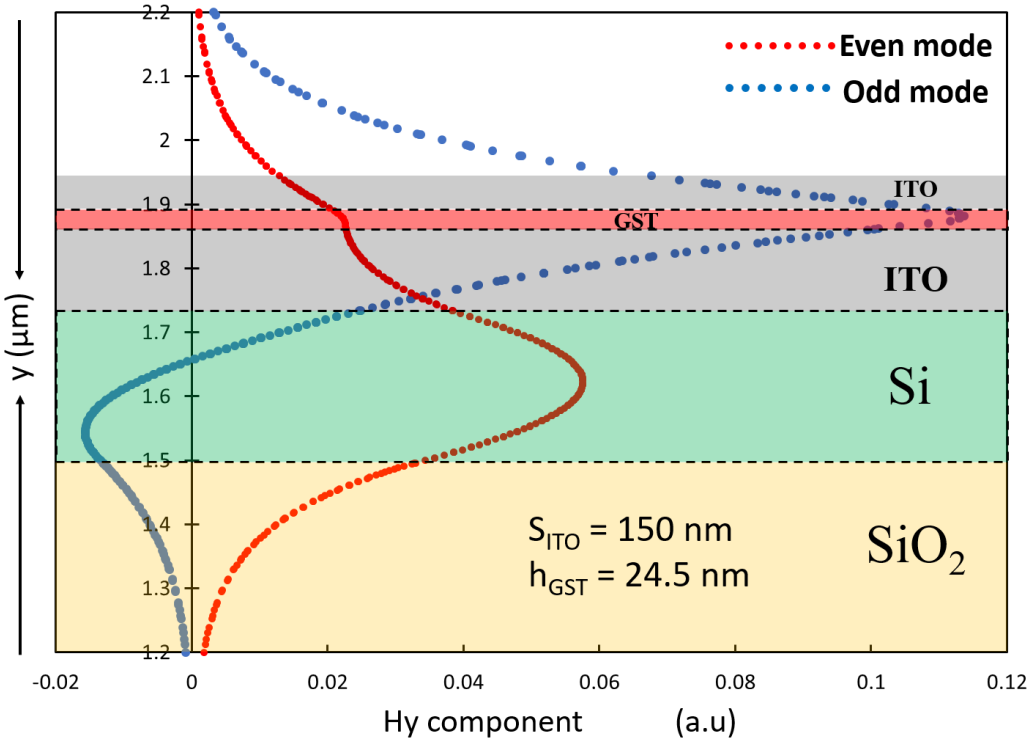

Fig. 5.6. H_y component of the H_y^{11} even and odd supermodes in crystalline state for S_{ITO} = 150 nm and h_{GST} = 24.5 nm along the vertical directions y (µm).

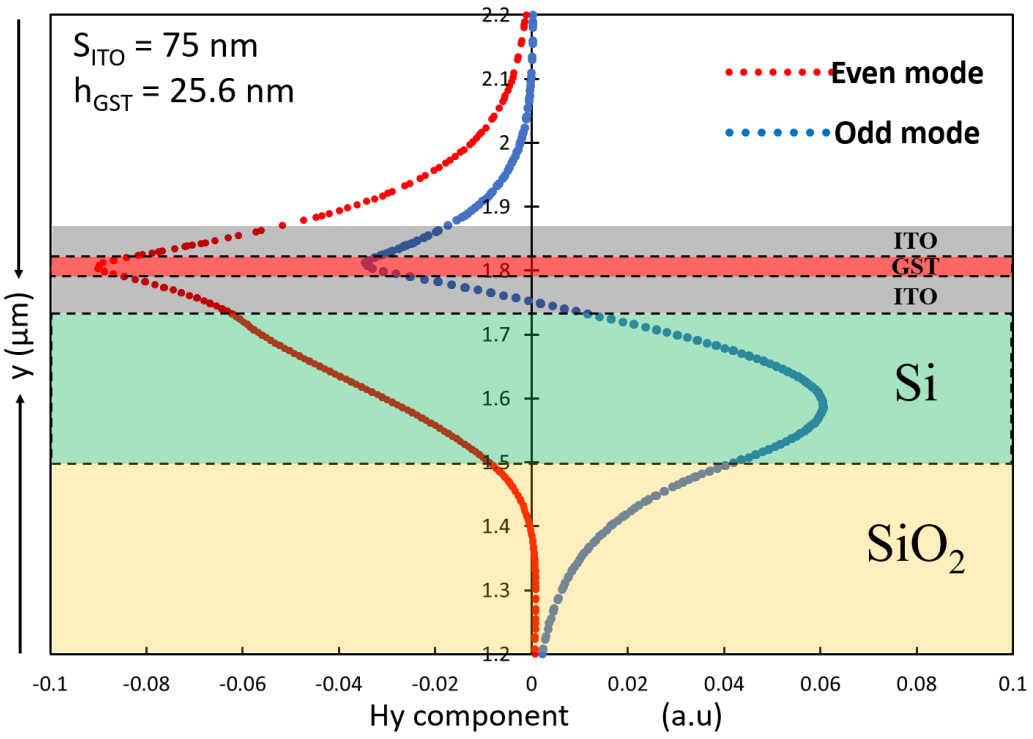

Fig. 5.7. H_y component of the H_y^{11} even and odd supermodes in crystalline state for S_{ITO} = 75 nm and h_{GST} = 25.6 nm along the vertical directions y (µm).

It can be observed that in Fig. 5.6, the H_y^{11} even supermode shown by a red dotted line, there are two field peaks are inside the Si layer and other inside the GST layer, and both have the same positive sign. But the H_y component in the Si layer have much larger field intensity than in the GST layer, also the maximum value can be seen in the middle of Si layer. For the H_y^{11} odd supermode shown by a blue dotted line, it can be noted that the H_y field in the GST layer have positive sign but negative sign in the Si layer. Also, the H_y field in the GST layer have much larger field intensity than the Si layer, and the maximum H_y field component can be obtained at the interface between GST layer and upper ITO layer.

When S_{ITO} is reduced to 75 nm and the phase matching condition shifted to h_{GST} = 25.6 nm, the H_y component of the H_y^{11} even and odd supermodes along the vertical directions are shown in Fig. 5.7. It can be observed that, the H_y field of the even supermode shown by a red dotted line, the H_y component increase considerably from lower SiO_2 buffer to the upper GST layer also achieve the maximum magnitude inside, then decrease exponentially from GST layer to the top air. It also can be noted the even supermode has a larger field intensity in the upper GST and ITO layer than the Si region. For the H_y^{11} odd supermode shown by a blue dotted line, it clearly shows that the H_y component increase gradually from bottom SiO_2 region to achieve the magnitude peak inside Si layer. After that, it decreases rapidly to a minimum value inside the GST layer then it is recovered to increase from the top ITO layer to air clad.

It can be demonstrated that the H_y^{11} even and odd supermodes generated in the Si-GST coupled waveguide when GST in crystalline state can support the “OFF” state for the optical switching. On the other hand, it is necessary to simulate the composite waveguide when the GST in amorphous state. First, the real part of effective indices of the coupled section in amorphous state for different S_{ITO} with 23-28 nm GST layer are calculated and shown in Fig. 5.8.

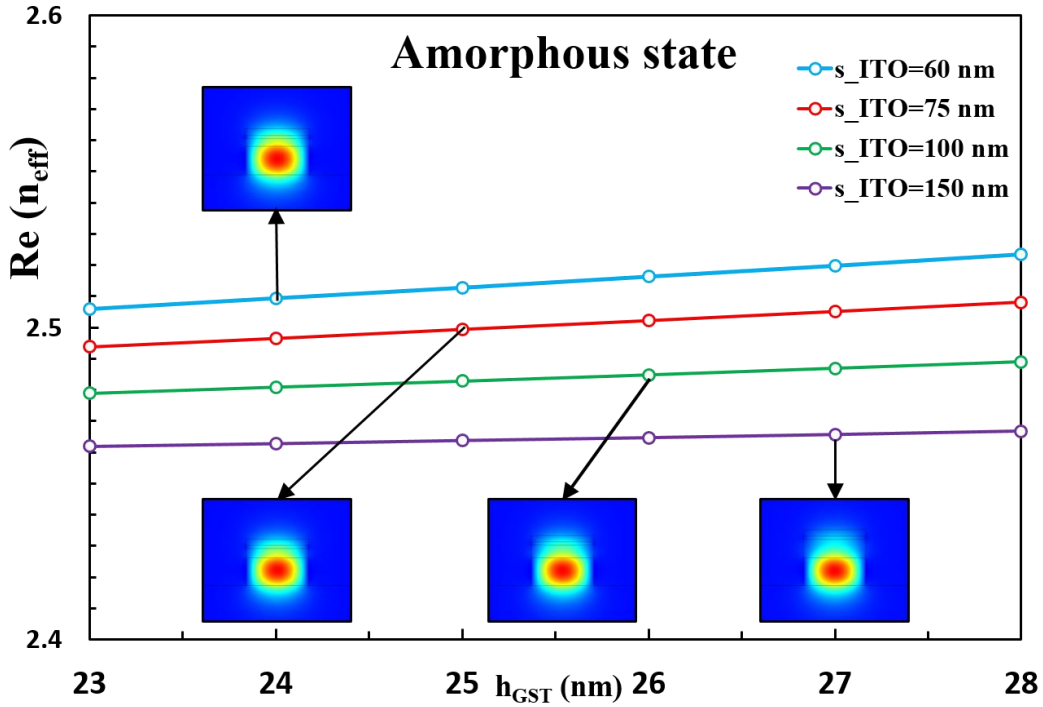

Fig. 5.8. Real part of effective indices and Hy field profiles of the coupled section in amorphous state for S_{ITO} = 60, 75, 100 and 150 nm as a function of h_{GST}.

It can be observed that for a given ITO separation, there are only one guided mode in the Si-GST coupled waveguide, and its n_e increase quite slowly with the h_{GST} grows from 23-28 nm. Moreover, the larger ITO separation coupled waveguide can have the larger n_e values when it has a 23-28 nm GST layer. In this figure, variations of the fundamental H_y field profiles of the H_y^{11} mode with four different ITO spacing is plotted. It can be noted that, for S_{ITO} = 60 and 75 nm most of the field is well confined inside the Si nanowire and some evanescent field can extend slightly to the top ITO contact. However, when the S_{ITO} increase more than 100 nm, the field only extend to the ITO separation layer due to weaker interaction. It can be concluded that the Si-GST coupled waveguide can support the electro-optic switch at "ON" state when GST in amorphous state due to the fundamental H_y field of the coupled waveguide is only confined in the bottom Si nanowire, mode coupling between wg1 and wg2 is neglected, so that the input light only propagates along the bottom Si nanowire wg1 to the end with no considerable interaction with GST waveguide wg2.

5.3.4 Coupling length and mode loss calculation

For the multi-mode coupling section, its coupling length is defined as:

$$L_c = \frac{\pi}{\beta_e - \beta_o} = \frac{\pi}{\left(\frac{2\pi}{\lambda}\right) * n_{e1} - \left(\frac{2\pi}{\lambda}\right) * n_{e2}} = \frac{\lambda}{2 * (n_{e1} - n_{e2})} = \frac{\lambda}{2 * \Delta n_e} \quad (5.1)$$

L_c is the shortest length necessary for maximum power transfer, where β_e and β_o are the propagation constants of the even and odd supermodes of the Si-GST coupled waveguide. λ is the operating wavelength, in our case is 1550 nm, n_{e1} and n_{e2} are the real part of the effective indices of the even and odd supermodes of the coupled structure, respectively.

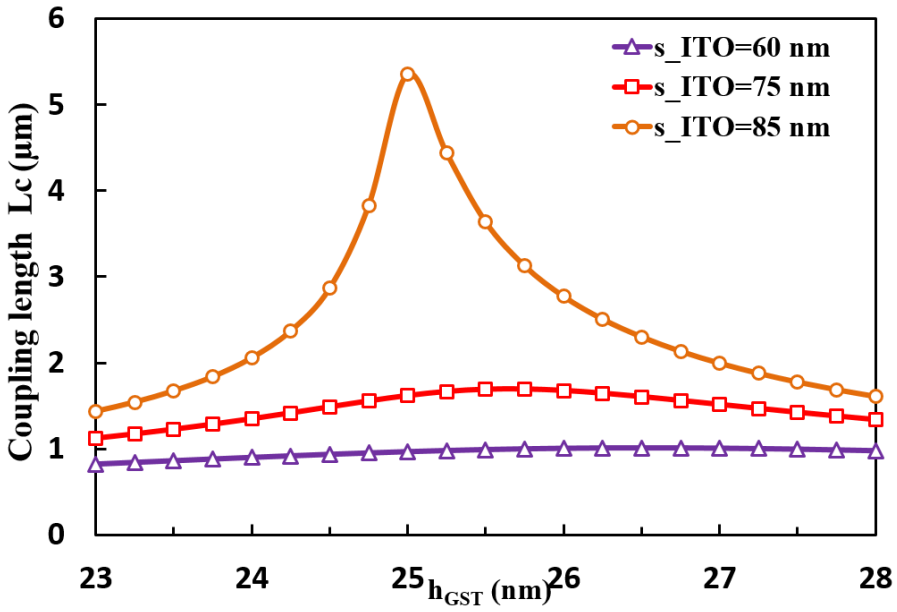

Fig. 5.9. Coupling length Lc of the coupled section with S_{ITO} = 60, 75 and 85 nm.

From the modal solutions of this Si-GST coupled waveguide which were shown in Fig. 5.3, the coupling length L_c of the coupled section can be calculated. Variations of the coupling length L_c with the h_{GST}, for S_{ITO} = 60, 75 and 85 nm are shown in Fig. 5.9 and similarly for S_{ITO} = 100, 150 and 200 nm are shown in Fig. 5.10. It can be noted that when phase matching is achieved, the difference between the propagation constant or real part of effective index is minimum so that the

coupling length will show a maximum value. In the Fig. 5.9, for the S_{ITO} = 85 nm, it can be noted that the coupling length L_c increase dramatically to the peak value of 5.35 μm at the phase matching point h_{GST} = 25 nm, then it decreases exponentially to around 1.6 μm for the h_{GST} = 28 nm. For the S_{ITO} = 75 nm, with the h_{GST} increase from 23 to 28 nm, its L_c grows smoothly from 1.1 μm to its peak of around 1.7 μm at h_{GST} = 25.6 nm, then it reduces gradually to 1.3 μm with the higher h_{GST}. Last, for the S_{ITO} = 60 nm, its coupling length stay almost constant around 0.8 μm with the h_{GST} increase from 23 to 28 nm.

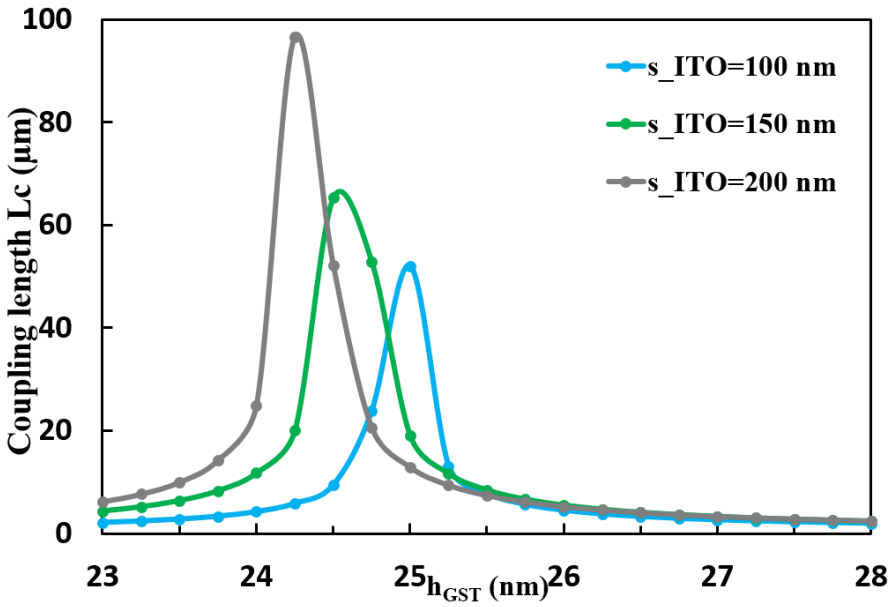

Fig. 5.10. Coupling length L_c of the coupled section with S_{ITO} = 100, 150, and 300 nm

However, when the S_{ITO} increase considerably to 100, 150 and 200 nm shown in Fig. 5.10, it can be observed that all the L_c curves increase sharply to the peak at their phase matching h_{GST} then decline exponentially to less than 10 μm with the h_{GST} increase to 28 nm.

It can be concluded that, as the separation S_{ITO} increase, the peak value of L_c become larger due to weaker coupling near the phase matching condition. On the other hand, for a smaller value of S_{ITO}, the coupling length is shorter, so overall system will be compact and additionally this will also be less sensitive to the change of h_{GST} and hence offers better fabrication tolerance. Therefore, the separation S_{ITO}- = 75 nm is selected as the optimised design of Si-GST coupled waveguide.

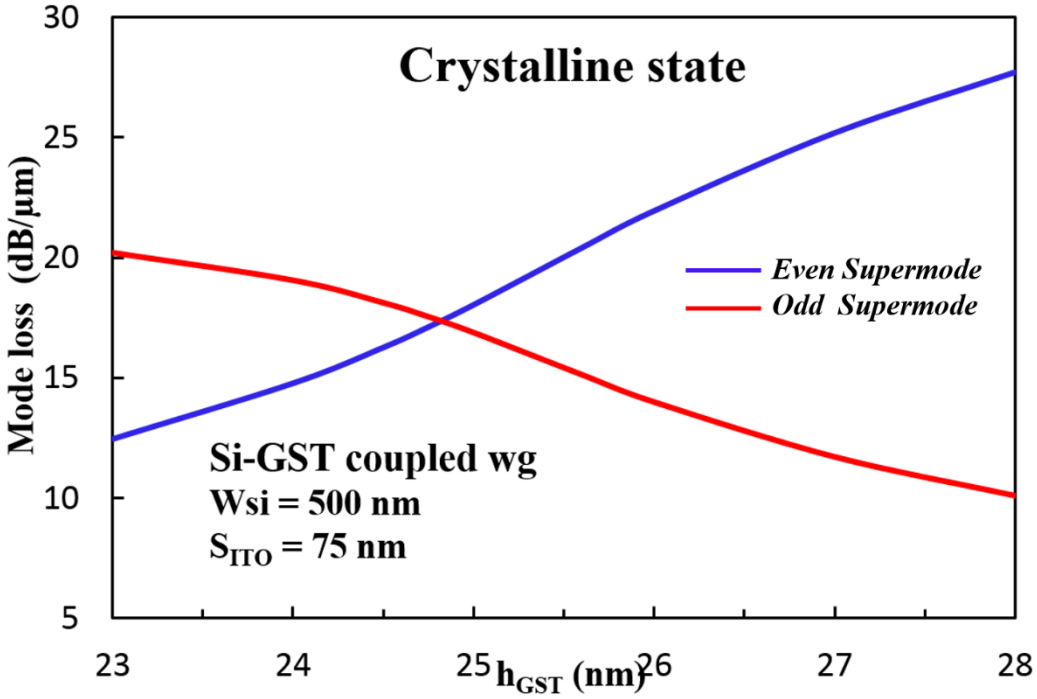

Fig. 5.11. Variations of mode loss of the even and odd supermodes in the crystalline state as a function of h_{GST} for S_{ITO}=75 nm.

As the GST introduces material loss, varied mode loss (dB/μm) of the even and odd supermodes of the Si-GST coupled waveguide as a function of h_{GST} for S_{ITO} = 75 nm are shown in Fig. 5.11. For the even supermode, the mode loss is shown by a blue line, it can be observed that when the h_{GST} increase from 23 to 28 cm, the modal loss increases monotonically from 12.5 dB/μm to 27.7 dB/μm. This increase was due to the power confinement in the GST layer of the coupled waveguide increases from 8.35% to 19.71%, which also leads to a larger absorption loss of the waveguide. On the other hand, the modal loss of the odd supermode shown by a red line, decreases from a higher value of 20.2 dB/μm as the GST layer thickness is increased. It also can be explained by noting that the power confinement in the GST layer is reduced from 10.2% to 5.86%, which leads to the absorption loss of the waveguide decreases to a lower value of 10.1 dB/μm. It can be noted that around h_{GST} = 24.8 nm, both the even and odd supermodes will have the similar modal loss values, which are around 17.5 dB/μm.

5.3.5 Junction analysis

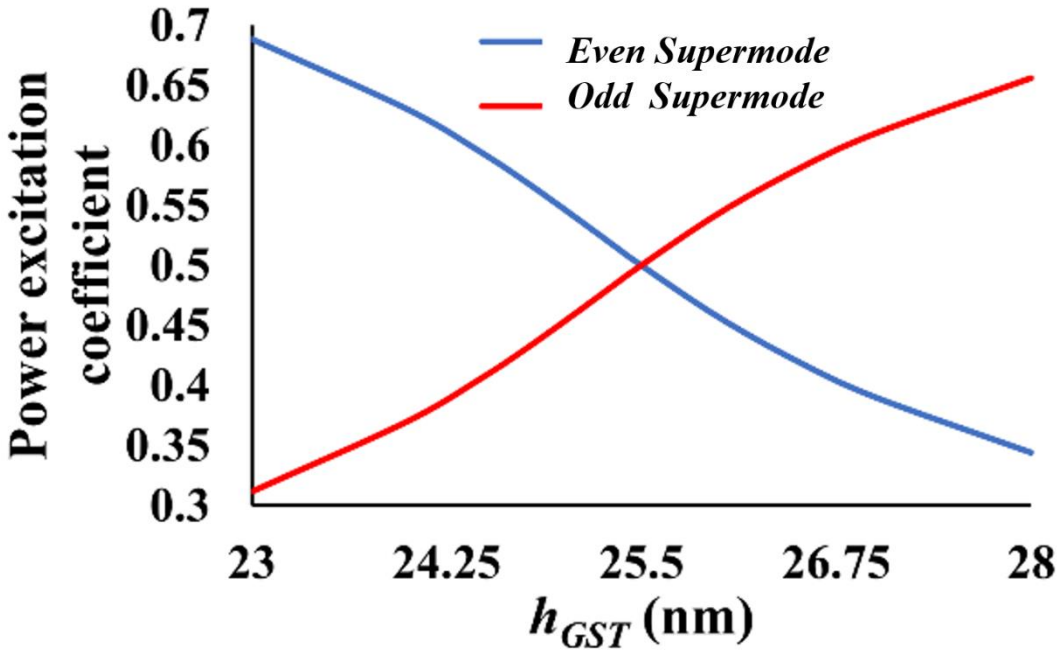

Fig. 5.12. Power excitation coefficient in crystalline state as a function of h_{GST} for S_{ITO}=75 nm.

Since FV-FEM provides accurate modal solutions for the supermodes of the Si-GST coupled structure, the power transfer efficiency between the two supermodes in the Si-GST coupled waveguide can be calculated by using the LSBR method.

The excitation coefficients of the even and odd supermodes, in crystalline state, at the first interfaces J_1 are shown in Fig. 5.12. When the h_{GST} is 23 nm, it can be noted that the even supermode have a relatively higher transmission at 70%, but the transmission coefficient of the odd supermode is only 30%. With the increase of the h_{GST}, this coefficient of the even supermode will reduce considerably to a lower value of 35%. On the other hand, the transmission coefficient of the odd supermode will increase to higher value 65% at this two waveguides junction when the thicker GST layer will be selected at 28 nm. At h_{GST} = 25.6 nm, which is the phase matching condition of the Si-GST coupled waveguide (S_{ITO} = 75 nm), the excitation coefficients curves cross each other. It can be noted that both even and odd supermodes have the same excitation coefficient, which is close to 0.5, it means both the supermodes carry half of the total power, ideal values for strong coupling.

5.3.6 Power evolution of the active section and coupling length validity

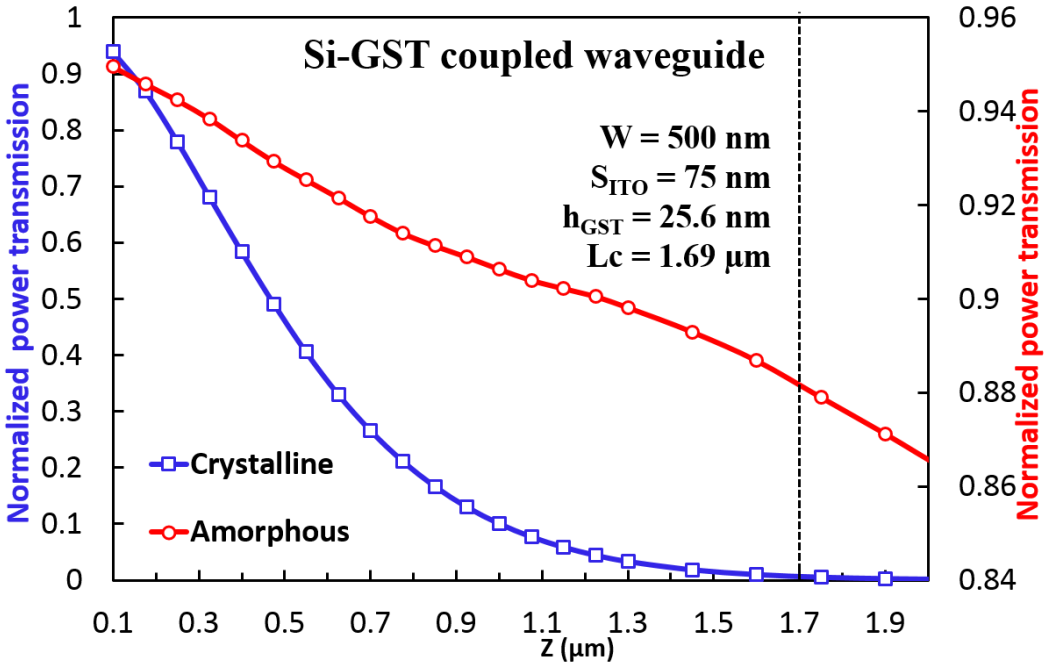

Fig. 5.13. Normalized power transmission in "ON" and "OFF" state of the switch when GST in crystalline state with S_{ITO} = 75 nm, h_{GST} = 25.6 nm and L_c = 1.7 µm by the FDTD simulation.

In order to evaluate the performance of the Si-GST waveguide based electro-optic switch, the Lumerical FDTD solution is used to calculate the power transmission at GST amorphous and crystalline states along the propagation distance Z and plotted in Fig. 5.13. Here, the length of the Si-GST coupled section is fixed at 5 µm which will be long enough for the light propagation simulation.

When GST is switched to crystalline state, the power transmission of the device at "OFF" state which is shown by a blue line with squares using the left-hand scale in the Fig. 5.13. It can be observed that the power transmission starts from 0.94 at Z = 0.1 µm due to the coupling loss at Junction J_1, then decreases monotonically to a low value around 0.005 at the distance Z = 1.7 µm which is a satisfactory value for attain the "OFF" state of the switch. It shows that the coupling length 1.7 µm which was calculate from FV-FEM with phase matching condition have good agreement with the FDTD simulation result.

On the other hand, when GST in amorphous state, the power transmission of the device at "ON" state which is shown by a red line with circles using the right-hand scale. It also can be demonstrated that the power transmission starts from 0.95 at Z = 0.1 µm due to the junction loss, however it is higher than the crystalline state because the field profile in Si-GST coupled section is similar as the input Si nanowire and without any mode coupling. Then the power transmission decreases gradually from 0.95 to 0.88 at the device coupling length Z = 1.7 µm, it means there will be 88% power at another junction between the Si-GST coupled section and output Si nanowire.

5.3.7 Device performance

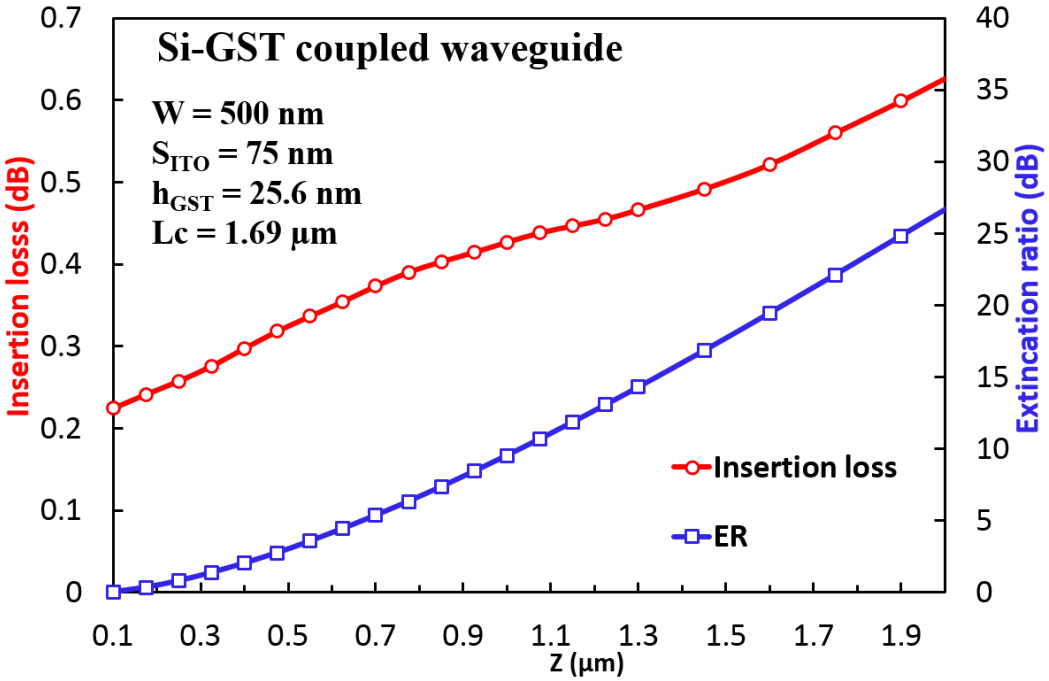

Fig. 5.14. Insertion loss at "ON" state and extinction ratio of the device.

After achieving the power transmission coefficient of the electro-optic switch at "ON" and "OFF" state with the propagation distance, the associated insertion loss (IL) and the extinction ratio (ER) of the device can be calculated. The associated insertion loss suggests that a viable optical switch at the "ON" state can be obtained

when GST is in amorphous state, the extinction ratio ER is defined as the ratio of the two optical power levels when the device at “ON” and “OFF” states.

The total insertion loss of the device at “ON” state, when GST in amorphous state, along the propagation distance Z is shown by a red line using the left-hand scale in Fig. 5.14. It can be observed that there is a 0.225 dB power loss at Z = 0.1 μm, which is a junction loss around 0.225 dB at J_1 due to the generation of higher modes at the discontinuity interface between the input Si nanowire and Si-GST coupled waveguide. Then the total insertion loss increases gradually to 0.56-dB at the Z = 1.7 μm, the sufficient length for the device attain the “OFF” state when GST in crystalline state.

The corresponding extinction ration (ER) of switch is shown by a blue line with squares using the right-hand scale in Fig. 5.14. It can be noted that as the propagation distance Z increase from 0.1 to 1.7 μm, the extinction ratio also increases considerably to a higher value of 22 dB, which is a competitive value of optical switching.

5.4 Summary

Design of electro-optic ON-OFF switches based on well-known phase change material $Ge_2Sb_2Te_5$ (GST) is presented. The electro-optic switch is achieved by implementing by co-directional coupling between a 220 nm thick Si nanowire wg1 and an ITO-GST-ITO waveguide wg2 at the 1.55 μm wavelength. By introducing the electric field via the ITO electrodes, the GST layer can be changed between the amorphous and crystalline states. As the modal loss in the crystalline state is much higher than the amorphous state, through a rigorous modal analysis of the Si-GST composite waveguide by using the FV-FEM, the optimal ITO spacing is obtained at 75 nm which is less sensitive to device parameter variations and thus offering better tolerances. The GST thickness is also optimised for the phase matching point at 25.6 nm in order to efficiently transfer most input light from Si nanowire to GST waveguide to attain the "OFF" state. Once the device length is optimised with the phase matching condition, the input light will propagate along the Si nanowire when GST in the amorphous state with very little interaction with the wg2 resulting in an "ON" state. The LSBR is used as a junction analysis approach to calculate the optical power coupling efficiencies to the output Si nanowire. The extinction ratio of the electro-optic switch and insertion loss at "ON" state can be obtained as a function of the device length. A compact 1.7 μm long device shows a high extinction ratio of 22 dB with an insertion loss only 0.56 dB at "ON" state.

Chapter 6

Design, Optimisation and Performance evaluation of GSST-clad low-loss modulator

6.1 Introduction

Despite the large refractive index contrast, the performance of existing PCM-based phonics device is still having the issues about the high optical absorption in traditional phase change materials. The most common phase change material, GST still suffer from excessive optical losses even in the amorphous state due to its small bandgap and the resulting inter-band absorption in the telecommunication bands. For instance, the imaginary part of GST amorphous refractive index is 0.12 at 1550 nm wavelength, corresponding to 4.2 dB/μm attenuation, which fundamentally limits many waveguide applications.

A new, low-loss optical phase change material which can overcome the limitations of GST based photonic devices has been reported by Q. Zhang [58]. The $Ge_2Sb_2Se_4Te_1$ (GSST), derived in GST by partially substituting Te with Se, which increases the optical bandgap, enabling reduced loss in the 1310 nm and 1550 nm telecommunication bands. Q. Zhang's report also has shown an important theoretical contribution of 1 x 2 and 2 x 2 cross-bar optical switch using two and three waveguides GSST-clad directional couplers, with a 40 and 80 μm long GSST-clad device length respectively. Their simulation results have shown that the

proposed 1 x 2 and 2 x 2 Si-GSST switch can achieve an extremely lower insertion loss only 0.06 dB and 0.013 dB at cross state (amorphous state) which demonstrate significantly enhanced performances compared to state-of-the-art GST devices.

(a):

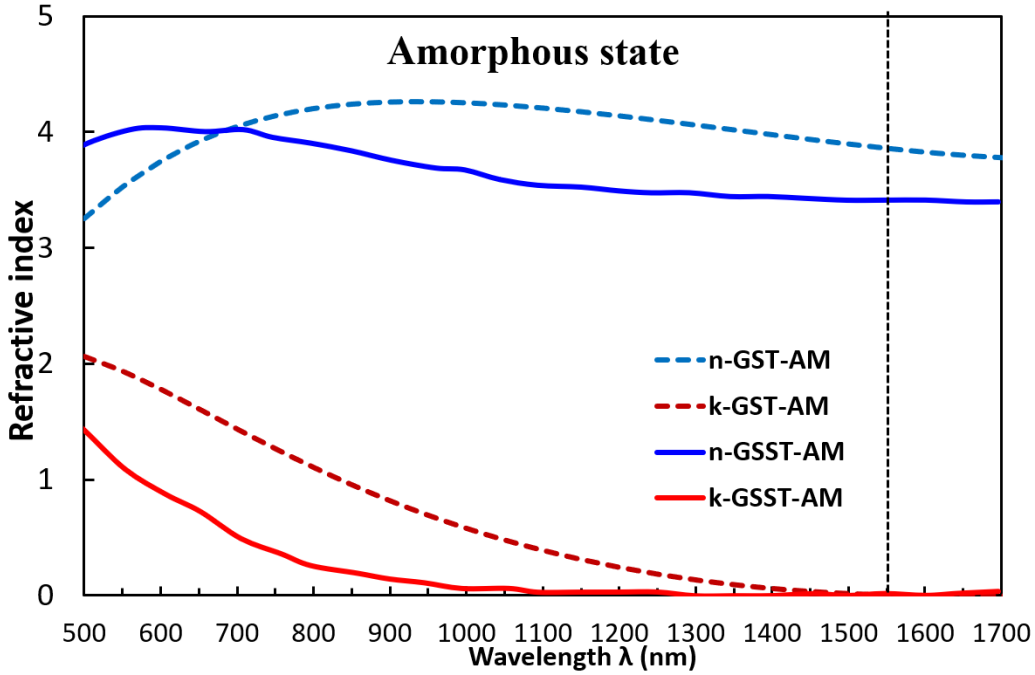

(b):

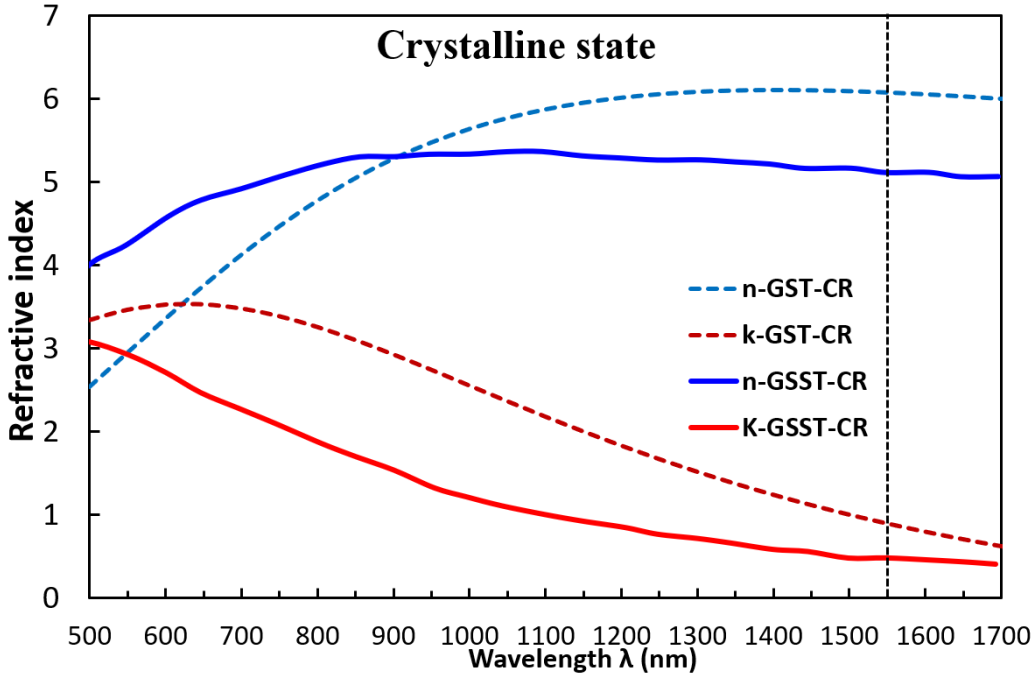

Fig. 6.1. Variations of real (n) and imaginary (k) parts for GST and GSST at (a) amorphous state and (b) crystalline state with a function of wavelength λ. [57]

Figure 6.1 compares the optical constants of GSST with the classical GST, both were measured by ellipsometer on thermally evaporated films [57]. From this figure, it can be noted that the imaginary part of refractive index of GSST shown in red solid curves exhibits reduced loss in both amorphous and crystalline states compared to GST curves which shown by dark red dashed lines in the whole range of wavelength. On the other hand, the GSST will have lower real part of refractive index compare to GST in both states when the wavelength λ is more than 1000 nm due to the reduced free carrier absorption.

The complex refractive index of GSST at operating wavelength 1550 nm from the spectrum in Fig. 6.1 can be taken as n (AM) = 3.4 + j*0.00018,
n (CR) = 5.1 + j*0.5 for amorphous and crystalline state, respectively [58]. The large index contrast between the amorphous and crystalline states and the low optical extinction coefficient of GSST amorphous state, which is only $1.8*10^{-4}$, over 600 times smaller than that of the GST and thus showing considerable promise to be integrated with SOI platform for the low-loss, non-volatile photonic devices design.

In this Chapter, the design optimisation of a compact 1 x 1 modulator based on a novel GSST-Si rib waveguide is proposed at the telecommunication wavelength 1.55 μm. Here, a rigorous full-vectorial **H**-field finite-element method (FV-FEM) in conjunction with the perturbation technique is used to find the complex modal propagation constant with the variations of the waveguide parameters. Following that, the least squares boundary residual (LSBR) method, is used to calculate the coupling loss at the butt-coupled junctions to identify the best waveguide parameters to achieve a lower insertion loss and a higher extinction ratio. Following that, the proposed design is also validated by using the finite difference time-domain (FDTD) simulations.

6.2 Schematic and principle

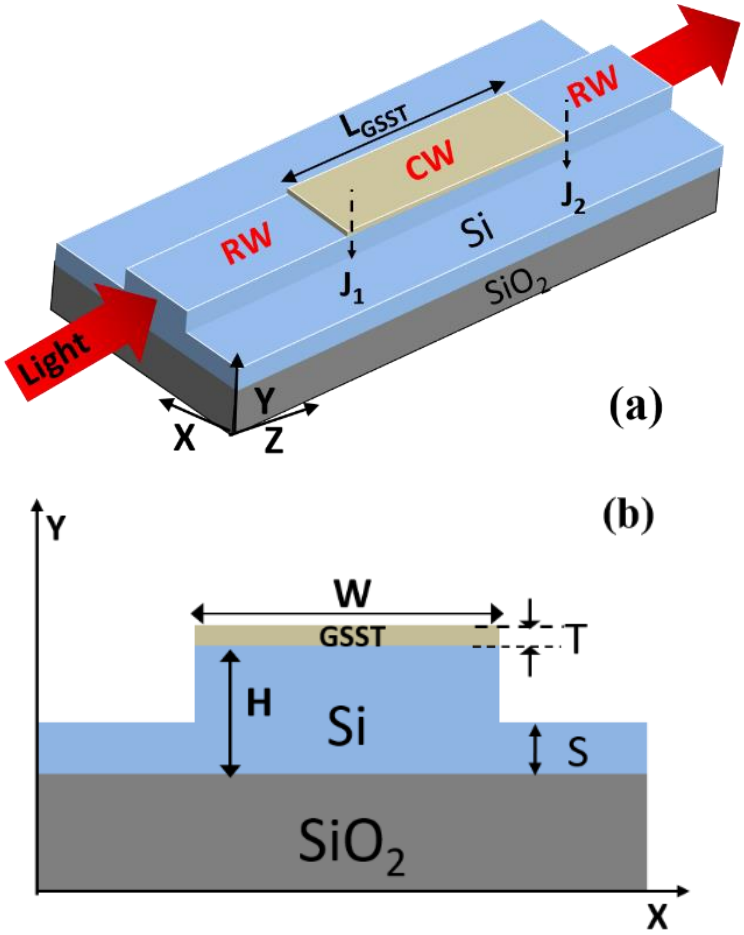

Fig. 6.2. (a) Schematic of the GSST-Si optical modulator, (b) Cross-sectional view of the coupled section CW.

The three-dimensional (3D) view of the self-sustained optical modulator based on the GSST-loaded Si waveguide, identified here as CW is shown in Fig. 6.2 (a). Here, outer two unclad Si waveguide (RW) sections are passive, while the middle CW section is active. The active section consists of a standard single-mode Si rib waveguide with GSST deposited on the top. A rib waveguide is considered over a fully etched nanowire waveguide. From the waveguide fabrication point, it is often difficult to maintain the surface smoothness of the completely etched vertical sidewalls. This surface roughness introduces scattering loss which is not preferable for the integrated optical applications. Compare to the ridge waveguide, a rib waveguide is easy to fabricate and less prone to show the scattering loss due to its partially etched side walls. Therefore, a rib waveguide is considered for the GSST-based modulating application design.

The cross-sectional view of the CW section is shown in Fig. 6.2 (b). Here, thickness of the Si core is identified as H and kept constant at 220 nm, its width identified as W, also kept constant at 500 nm, and the slab layer thickness shown as S, is varied. The length of GSST clad for optical modulating, is taken as L_{GSST}.

6.3 Numerical results

6.3.1 Fundamental mode field profile

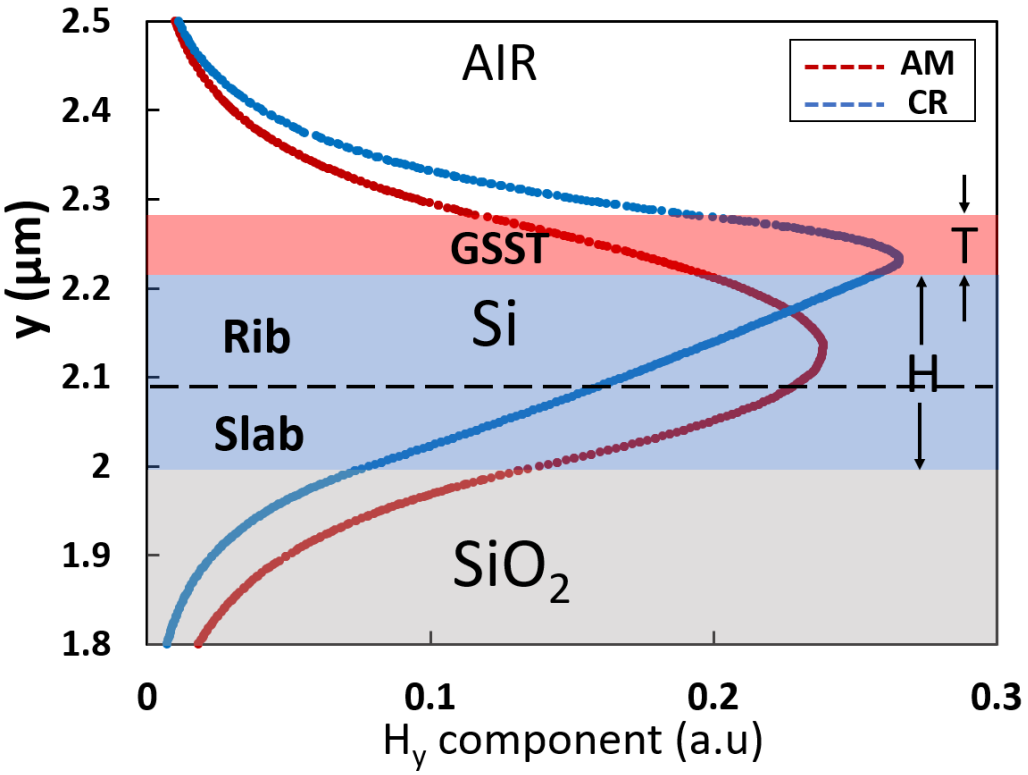

Fig. 6.3. H_y variation along the vertical direction, for GSST-Si CW in amorphous and crystalline state with W=500 nm, H=220 nm, S=90 nm, and T=60 nm.

We have used our in-house FEM codes to obtain the modal solutions of the GSST CW. For the quasi-TE mode, H_y is the dominant component of the magnetic field, **H**. The CW in amorphous state with W = 500 nm, S = 90 nm, T = 60 nm is simulated, and variation of the dominant H_y field of the quasi-TE H_y^{11} modes along the y-axis is shown in Fig. 6.3 by a red line. The SiO_2 buffer region is shown by a lower grey shade and Si region with a light blue shade and a dashed line inside identifies the interface between the slab and rib layers. The GSST layer is also

shown by a red shade above the Si region. It can be noted that, when GSST in amorphous state, the field is mostly confined in the Si rib core and the maximum H_y value is inside the rib and near to the interface between the Si rib and slab.

The H_y field profile for an unclad waveguide RW is not shown here, but this was very similar as that of GSST in amorphous state. However, the GSST refractive index is increased considerably when it is switched to a crystalline state, significantly changing the mode field profile. Variation of H_y field of the H_y^{11} mode of CW in crystalline state along the y-axis is also shown in Fig. 6.3 by a blue line. It can be observed that the field is still confined well inside the Si rib core, but a large modal field is presented in the top GSST region. The maximum H_y value is rather inside the top GSST layer and just above the interface between the Si rib and the top GSST layer. It suggests that if the GSST is transformed to crystalline state, more power is absorbed into the GSST layer. The H_y field decays exponentially both in the upper air and lower SiO_2 regions.

6.3.2 Modal solution characteristics

	n_e	k_e	Mode loss α (dB/μm)
Amorphous	2.5723	$6.8*10^{-4}$	0.00024
Crystalline	2.6773	0.0415	1.46122
Difference	0.105	0.041493	1.46098

Table 6.1. Modal solution characteristics

The calculated modal solution parameters for the H_y^{11} mode of CW (W = 500 nm, S = 90 nm, T = 20 nm) are given in Table 6.1. It can be noted that when GSST is in crystalline state, the waveguide has a larger effective index, both in real and imaginary parts, which also suggests a larger mode loss. Although these values depend on the waveguide design, but for a comparable design both these values are lower than the GST based design in Table 4.1 of **Chapter 4** along with a very low modal loss for the amorphous state.

An optical modulator or switch can be designed by exploiting either Electro-refraction (ER) or Electro-absorption (EA). Electro-refraction, which unitizes the differential of the real part of the effective index, is widely used to design optical

devices. The ER based device can be comprised of Mach-Zehnder interferometer (MZI) with two branches. For a MZ-based device, a larger ER value is preferred for a compact device but also requires lower loss values for both the states. The CW considered here has a strong electro-refraction (ER) = (n_{e2}-n_{e1}) = 0.105, and a very low modal loss only 2.4*10^{-4} dB/μm and may be suitable for the MZI design. On the other hand, the Electro-absorption effect can also be used for modulation, where the differential mode loss between the two states is exploited to achieve the optical switching and modulating. The CW here also has a strong electro-absorption (EA) = (k_{e2}-k_{e1}) =0.0415, because it goes through significant change in the imaginary parts of GSST refractive indices induced by the phase change, which makes it possible to achieve a higher extinction ratio.

In the next section, variations of both ER and EA characteristics of the GSST-Si CW waveguide with its width and height of different layers are thoroughly investigated.

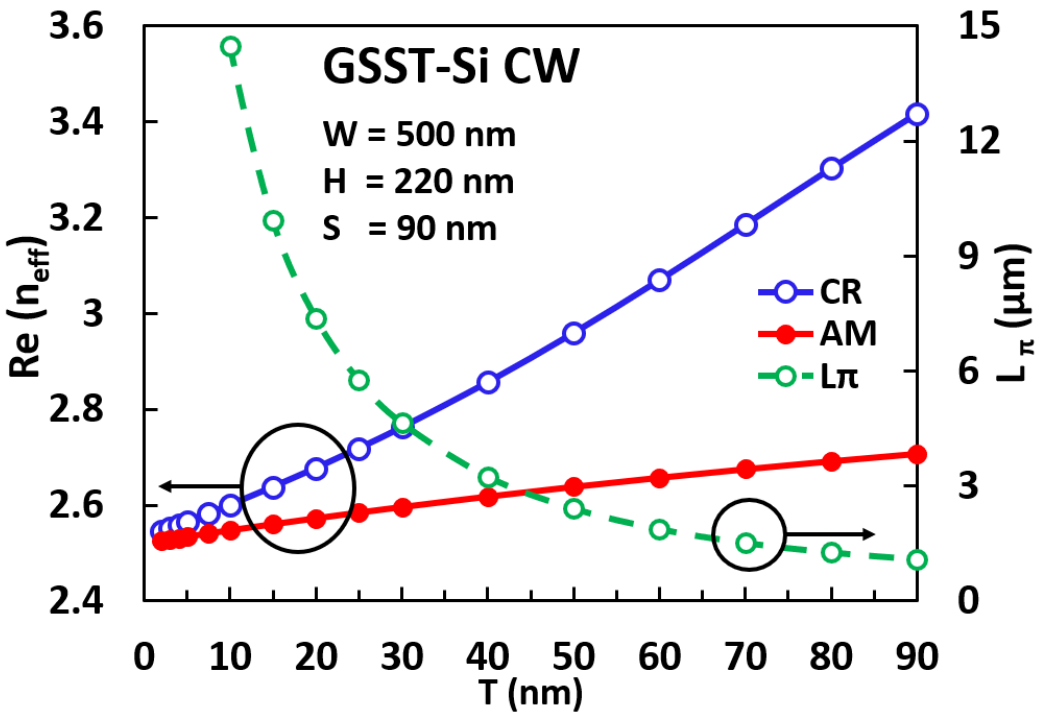

Fig. 6.4. Variations of the real part of effective indices for amorphous and crystalline states also L_π with the GSST thickness, T for CW.

Variations of real part of the effective index with the GSST layer thickness, T, are shown in Fig. 6.4, when W = 500 nm, H = 220 nm, and S = 90 nm. Results for amorphous state (AM) are shown by a red line with solid circles and those for the crystalline state (CR) are shown by a blue line with hollow circles. When GSST is in amorphous state, it can be observed that the n_{e1} increases with T as the deposited GSST layer with higher refractive index increases. On the other hand, the real part of the effective index for the crystalline state n_{e2}, also increases with T, but at a much higher rate than the amorphous state's values. This is because, when the GSST is in crystalline state, its refractive index is 1.5 times larger than that of the amorphous state so that the CW will have a higher effective index value for the crystalline state. For a Mach-Zehnder interferometer (MZI) based design, the value of "$\Delta\varphi$" needs to be equal to π radians. The L_π of the CW decrease gradually from 16 to 1.5 μm, as the difference between n_{e1} and n_{e2} increases with the GSST thickness, T, shown in Fig. 6.4 by a dashed green line using the right-hand side scale.

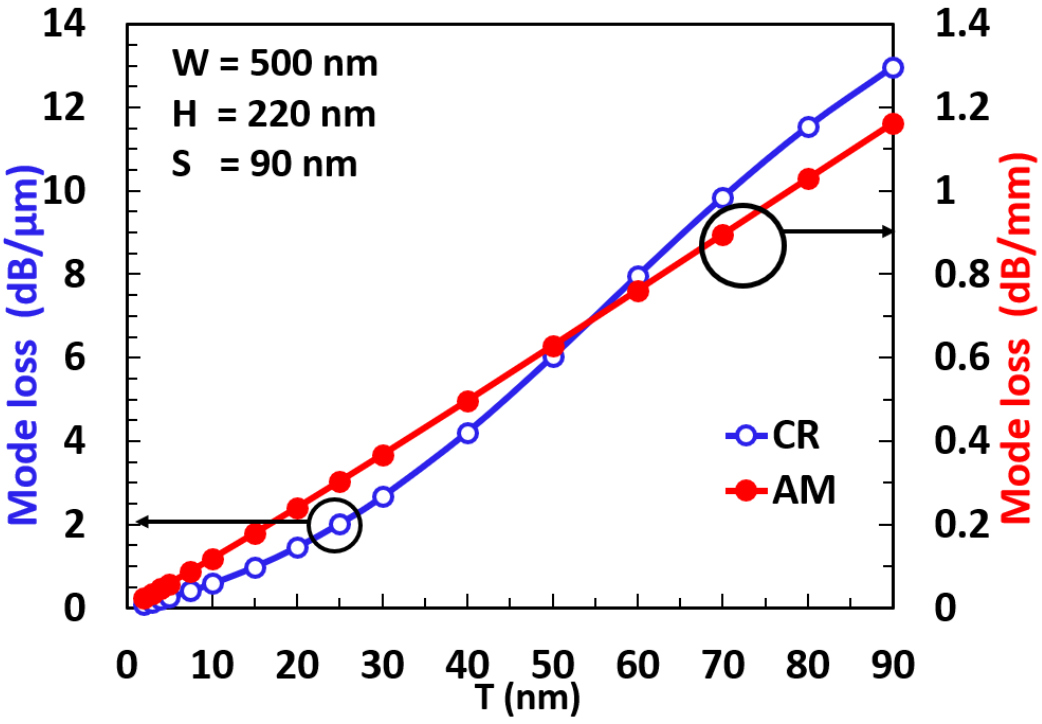

Fig. 6.5. Variations of mode loss of CW in amorphous and crystalline states with GSST thickness, T.

As GSST incurs material loss, so the variations of modal loss for these two states with the GSST thickness T are shown in Fig. 6.5. Results for the amorphous state (AM) are shown by a red line with solid circles, by using the right-hand side scale, while those for the crystalline state (CR) are shown by a blue line using the left-hand side scale incorporating hollow circles. When GSST is in amorphous state, it can be observed that the mode loss increases with T, as the top loaded GSST layer area increases. On the other hand, the mode loss for the crystalline state also increases with T, but these values are nearly four orders of magnitude larger than those in the amorphous state. This is because, for the GSST in the crystalline state, imaginary part of its refractive index is much larger than that in the amorphous state. When the T reduces to lower than 10 nm, the mode loss of CW for both the states will be relatively lower.

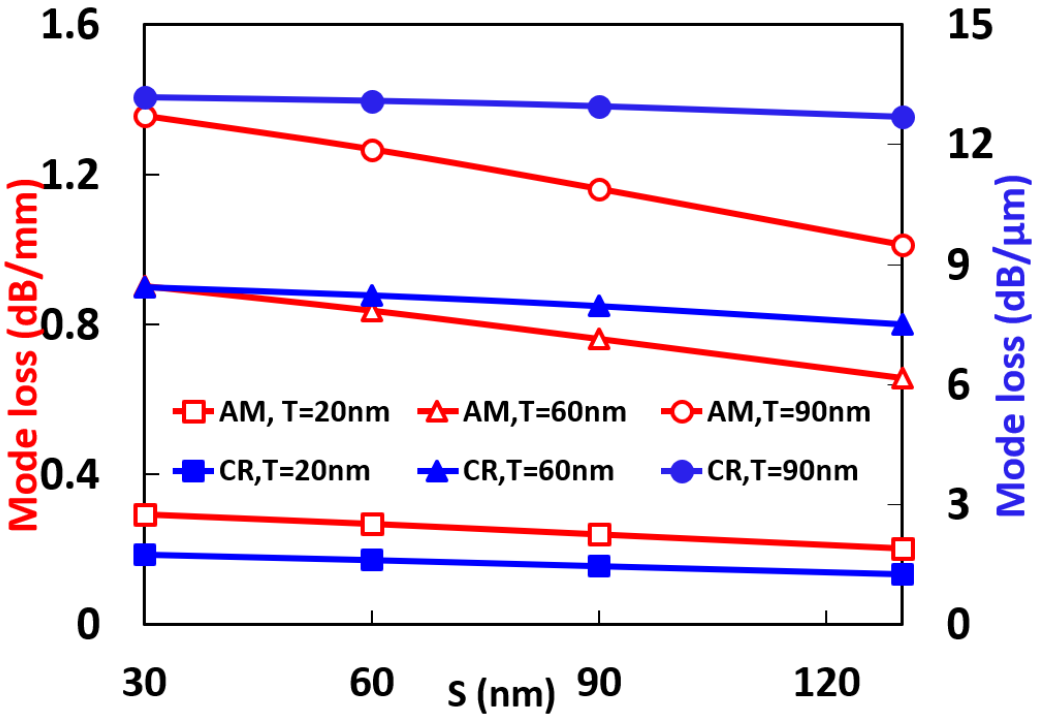

Fig. 6.6. Variations of mode loss of CW in amorphous and crystalline states with Si slab thickness, S of three different values of T (W = 500 nm, H = 220 nm).

Next, variations of modal loss with the Si slab thickness for different GSST thickness T in these two states are shown in Fig. 6.6. Results for the amorphous state (AM) are shown by red lines with hollow symbols, using the left-hand side

scale, while those for the crystalline state (CR) are shown by blue lines with solid symbols using the right-hand side scale. When GSST is in amorphous state, it can be observed that all the GSST thickness waveguide mode loss values decrease when the slab thickness S increase from 30 to 130 nm, as the power confinement in the Si core increases, so power in GSST layer reduces. The waveguide with thicker GSST thickness T suffers from higher mode loss compare to others. On the other hand, the mode loss for the crystalline state also decrease but more slowly with S, and it also shows that for larger T, waveguide suffers from a higher modal loss. It can be concluded that a thinner GSST layer can yield smaller modal loss values and waveguide with a larger slab thickness can also achieve slightly lower modal loss for both the states.

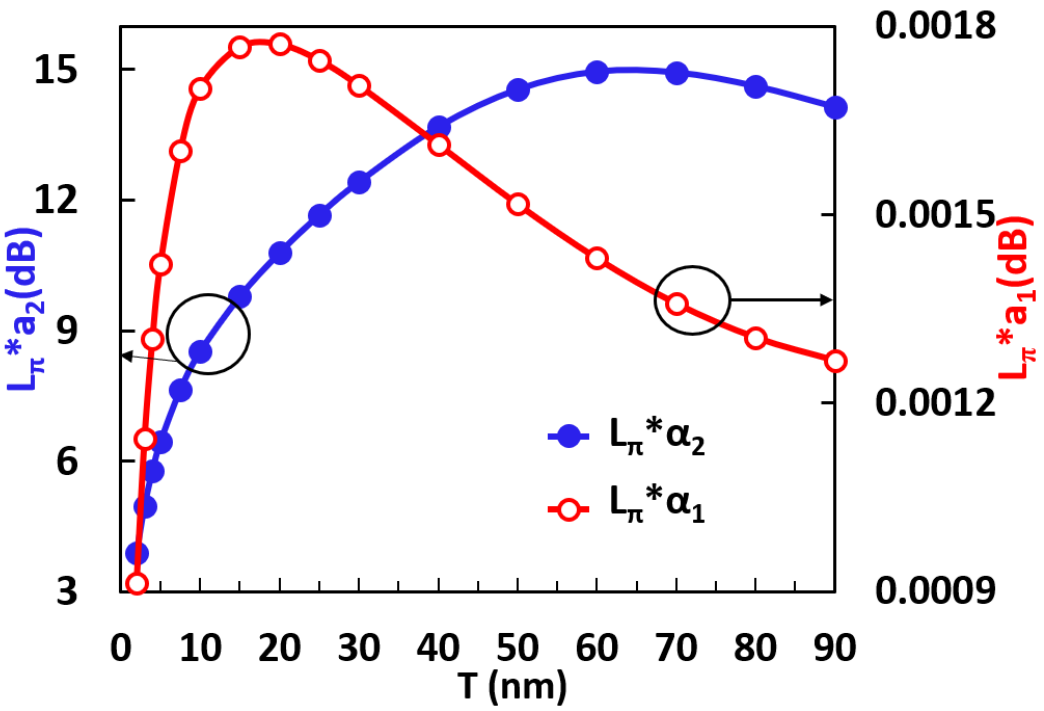

Fig. 6.7. Total modal loss of CW in amorphous and crystalline states with varying GSST thickness T.

Variations of the total modal loss ($L_\pi*\alpha_1$) of CW with the GSST thickness, T, for MZI based device of length = L_π, with W = 500 nm and S = 90 nm for the amorphous state is shown by a red line in Fig. 6.7. When the GSST thickness T increases from 2 to 15 nm, the total loss value increases faster from 0.0009 to 0.0018 dB. After that, the total modal loss decreases slightly from 0.0018 to 0.0013 dB as

the device length reduces more rapidly when the T increases to 90 nm. On the other hand, the total modal loss for the crystalline state ($L_\pi*\alpha_2$) shown by a blue line increases from 4 to 15 dB with the T increase from 2 nm to 60 nm then it decreases a little bit around 14 dB with the T between 60-90 nm. These values are much higher than those for the amorphous state.

Although, a small 4-7 dB total modal loss of CW in crystalline state when the GSST thickness T is between 2 to 10 nm may allow a possible MZI based device, however device length needs to be longer than 20 μm which may be less attractive for a compact MZI design. On the other hand, when the T increase to a higher value, L_π reduces, which although may yield a compact modulator, but the resulting 10-15 dB modal loss for the crystalline states will cause a poor extinction ratio due to incomplete field cancellation.

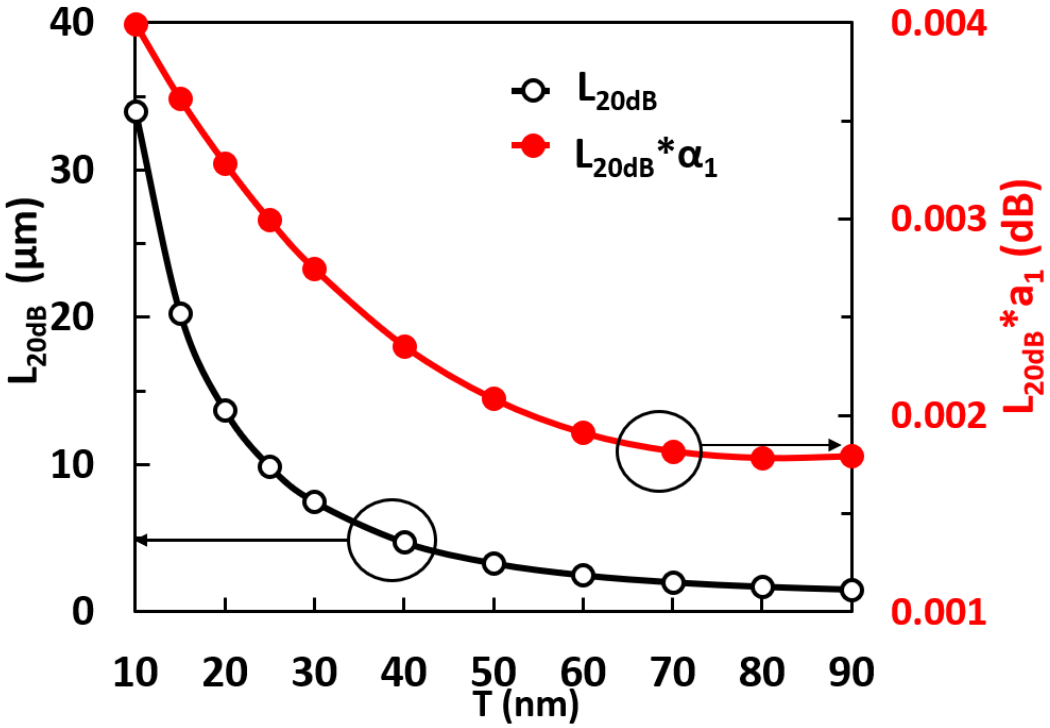

Fig. 6.8. L_{20dB} and total modal loss of CW in amorphous state with varying GSST thickness, T.

It is clear from the previous results that the ER based approach may not be suitable for a possible GSST modulator, so next the EA (k_{e2}-k_{e1}) effect will be used for the possible device design. Here, it is assumed that the device will need a total

extinction ratio of 20 dB between amorphous and crystalline states. If desired, any other preferred extinction ratio can also be considered. If we consider a GSST CW section of length L_{20dB} is considered, then the modal loss for the crystalline state would be 20 dB higher than that of the amorphous state.

When the W = 500 nm and S = 90 nm, variations of device length, L_{20dB} and total modal loss of the amorphous state (L_{20dB}*α1) with the GSST thickness, T are shown in Fig. 6.8. The device length L_{20dB} is shown by a black line with hollow circles. When the T increases from 10 to 40 nm, the L_{20dB} decreases monotonically from 35 μm to a lower 5 μm. When the T increases further to 90 nm, the device length L_{20dB} decreases slowly to 1.54 μm, which shows that a compact optical modulator is viable. Total modal loss of the modulator for a low-loss amorphous state is shown by a red line with solid circles using the right-hand side scale. It can be noticed that the total modal loss of the amorphous state reduces from 0.004 dB to 0.0018 dB when T increases from 10 nm to 90 nm. It can be concluded here, a higher GSST thickness T, around 40-90 nm can yield a compact device shorter than 5 μm, and the total modal loss for "ON" state would be very low around 0.0018 dB.

It also can be noted that when T = 20 nm, the L_{20dB} increases monotonically from 11.5 to 16 μm when the S increase from 30 to 130 nm, but not shown here. However, when T = 60 and 90 nm, their device lengths increase very slowly from around 1.8 to 2.2 μm when S increase from 30 nm to 130 nm. On the other hand, it can also be noted that when T = 20 nm, the modal loss reduces slowly from 0.0034 to 0.0032 dB when the S increase from 30 to 130 nm. Similarity, when T = 60 and 90 nm, their modal loss values also decrease slowly from around 0.0021 to 0.0016 dB when S increase from 30 nm to 130 nm. It can be concluded that when a 60-90 nm GSST layer is loaded on the Si rib waveguide, the larger Si slab thickness S can achieve a short device length around 2 μm and a lower modal loss only 0.0016 dB for the amorphous state.

The modal field profiles for the active CW at amorphous and crystalline states were shown in Fig. 6.3. These field profiles were different due to the significant changes in the GSST refractive index when GSST phase changes. This suggests the

possibility of a considerable power loss at junctions 1 and 2 due to the mismatch between the modes field profiles at these junctions.

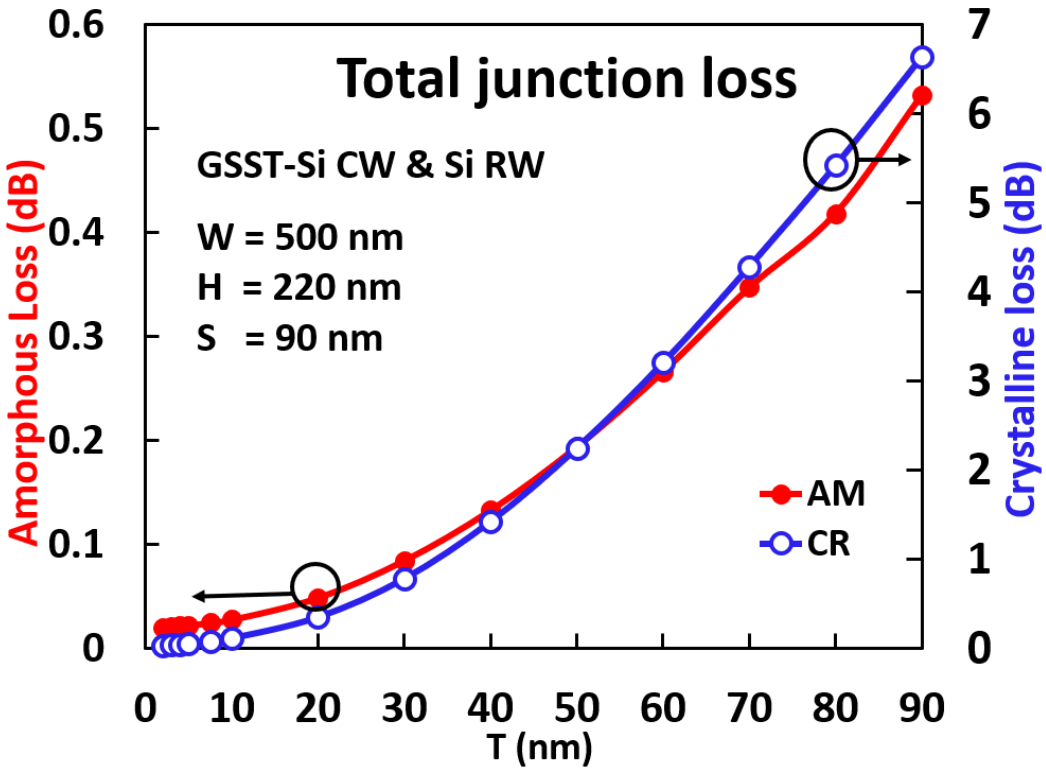

Fig. 6.9. Variation of the total junction loss of CW in amorphous and crystalline states with the GSST thickness, T.

Next, the effect of GSST layer thickness T on the junction loss is studied. In this case, for S = 90 nm, the total junction losses of active CW from coupling to passive RW at both input and output sides, calculated by the LSBR method for the amorphous state, are shown by a red line in Fig. 6.9. It shows that when the slab thickness T increases from 2 to 90 nm, the total junction loss increases from a lowest value of 0.02 dB to 0.53 dB. Total junction loss of CW in crystalline state is also shown by a blue line using the right-hand side scale. In this case, the junction loss increases exponentially from 0.03 dB to 6.64 dB when the T increases from 2 nm to 90 nm. Junction loss for crystalline state is significantly higher as higher index value with thicker GSST layer make the modal field very different than that of the unclad RW.

Here, it can be concluded that smaller GSST thickness T can yield a satisfactory design with a lower junction loss at the amorphous "ON" state, however it will require a much longer device length, so the optimised GSST thickness need to be selected to balance both of these parameters. On the other hand, the additional coupling loss in the crystalline state not that critical as being related to the "OFF" state.

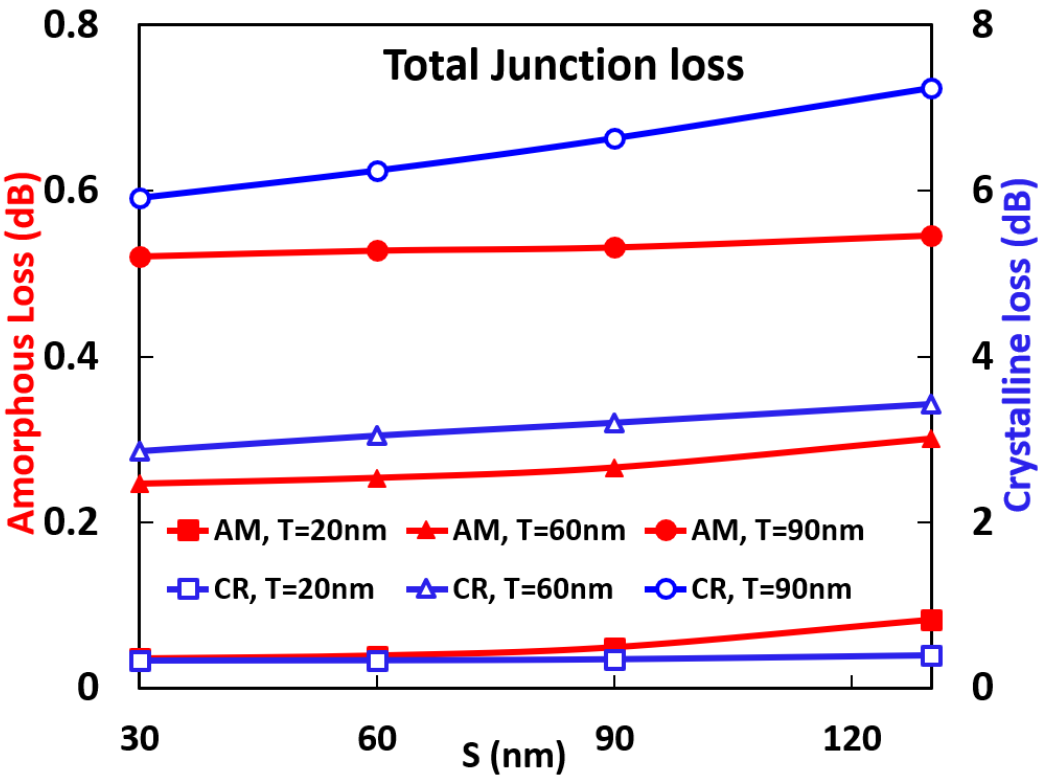

Fig. 6.10. Variation of the total junction loss of CW in amorphous and crystalline states with the slab thickness, S for different GSST thickness T.

The effect of Si slab thickness S of the total junction loss is also calculated. For T = 20, 60 or 90 nm, the total junction loss for these two states from both the junctions as a function of the slab thickness, S are shown in Fig. 6.10. Results for the amorphous state are shown by red lines, using the left-hand side scale, and it can be observed that, the total junction loss of the waveguides with different GSST thickness, T increase slightly with the Si slab thickness, S. A thinner 20 nm GSST layer can yield lower junction loss, only 0.035 dB, but even for 90 nm thick GSST layer could suffer only 0.53 dB, which can still be acceptable for the modulator

design. Total junctions for the crystalline state are shown by blue lines using the right-hand side scale, which increases slowly with S, and it also shows that for larger T, waveguide can incur a higher junction loss. It can be concluded that a thinner GSST layer can provide smaller junction loss and additionally a smaller slab thickness waveguide can also achieve lower total junction loss for both the states.

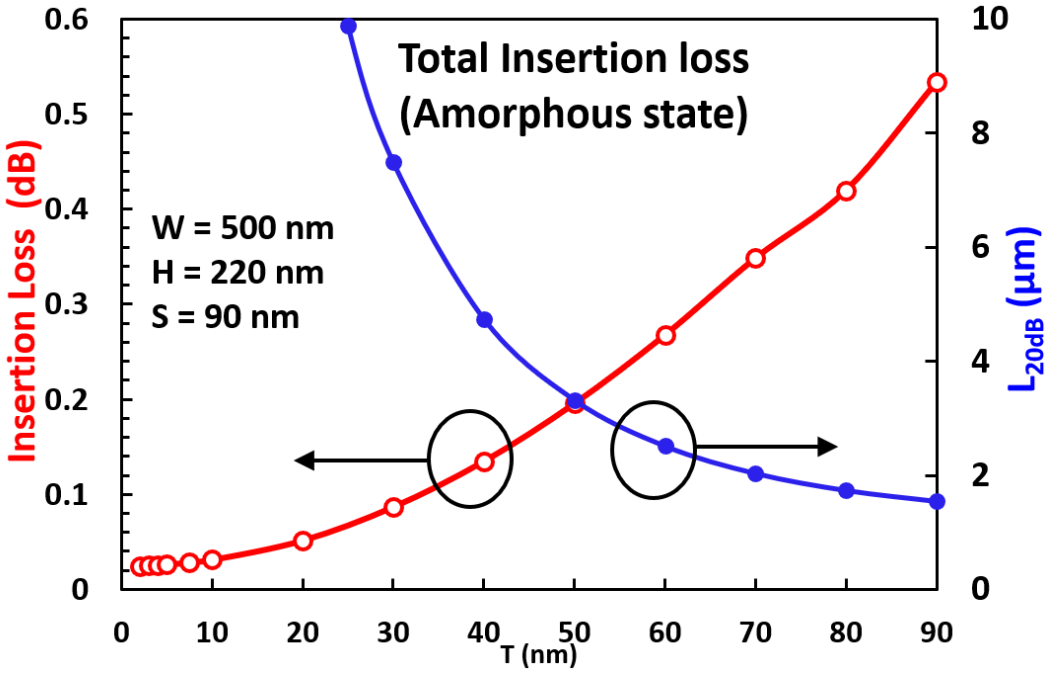

Fig. 6.11. Variations of total insertion loss and L_{20dB} of CW in amorphous state with GSST thickness T.

The associated lower insertion loss suggests that a viable optical modulator at the "ON" state can be obtained when GSST is in amorphous state. The total loss is comprised of the modal loss of the active GSST CW section due to the absorption in the GSST cap and the coupling loss between the passive input and output Si RW sections and the active GSST CW section.

From Figs. 6.9 and 6.10, it was observed that the total junction loss is the dominant factor of the total insertion loss as the total modal loss has been lower than 0.005 dB for the whole range of T considered here. Here, for S = 90 nm, the associated total Insertion loss of GSST CW is shown by a red line in Fig. 6.11. It can be observed that, when GSST thickness T increases from 2 to 10 nm, the total insertion loss of the modulator increases slightly from a relatively low value 0.025

to 0.03 dB. After T=10 nm, the total insertion loss increases exponentially from 0.03 to 0.53 dB with the GSST thickness T increase to 90 nm. The required device length, L_{20dB} is shown again in this figure.

If a compact device with length shorter than 5 μm is preferred, then the GSST thickness T should be larger than 40 nm to achieve it. From Fig. 6.11, it can be concluded that the 40-60 nm thicker GSST layer may be a preferred design, which shows a small total insertion loss value of 0.13-0.27 dB, also yielding a compact device with length between 2.5 and 5.0 μm.

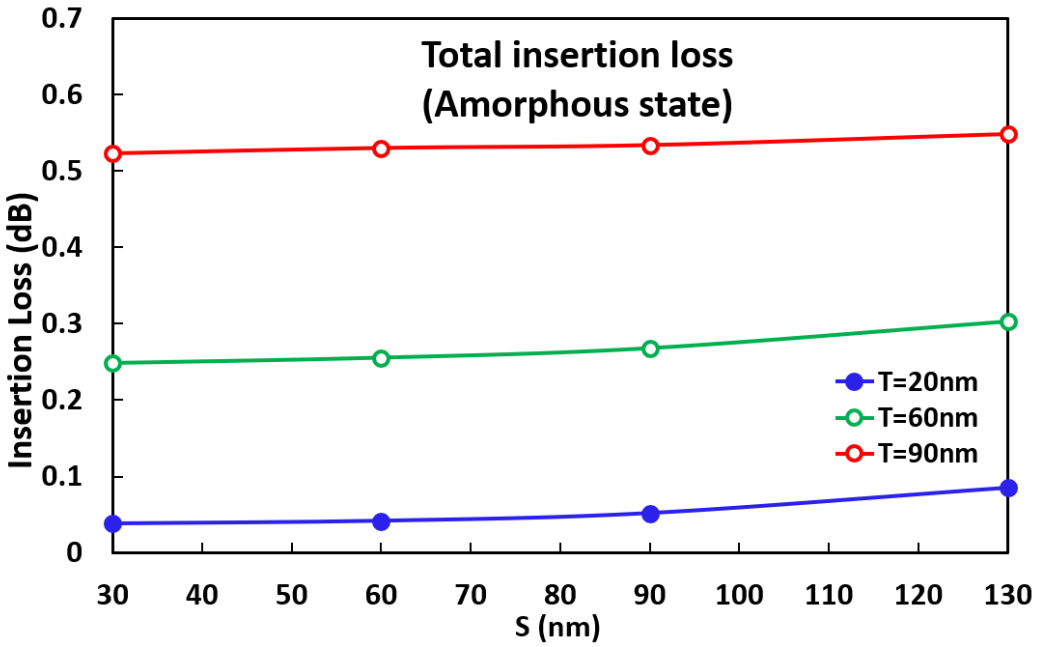

Fig. 6.12. Variations of total insertion loss of CW in amorphous state with Si slab layer S.

On the other hand, the insertion loss variation of the amorphous state with the Si thickness, S is fairly constant is shown in Fig. 6.12. It can be noted that as the total insertion loss increase very slowly with the Si slab thickness, and when the S =60-90 nm, the total insertion loss has the smallest change, and this can be taken as an optimal design for the GSST CW. The modulator is designed and optimised to show a 20 dB higher modal loss in the crystalline state compared to the amorphous state. Additionally, the crystalline state has higher junction loss shows than the

amorphous state. Therefore, the total insertion loss in the 'OFF' state (crystalline) exceeding 20 dB compared to the 'ON' state (amorphous).

PCM	PCM thickness (nm)	Device length (μm)	Min IL (dB)
GST	25	2.27	0.359
GSST	40	4.75	0.135
	50	3.32	0.196
	60	2.51	0.268

Table 6.2 Performance comparison between GST and GSST design.

A GST-clad Si rib waveguide based EA modulator design have been reported in **Chapter 4** with 2.27 μm device length and a minimum insertion loss 0.359 dB and this is given in Table 6.2. However, if low-loss GSST used in the EA modulator design, the minimum insertion loss could be reduced to only 0.135 dB, which is 38% of the earlier GST based design and with a 4.75 μm device length shows a greater potential for low loss PICs. On the other hand, a more compact device with slightly thicker GSST layer, say 60 nm can also be attractive with the total insertion loss still smaller than the GST based designs.

6.4 Benchmark with the FDTD simulations

To validate these results, we have also simulated the complete optical modulator with S = 90 nm, T = 50 nm and L_{20dB} = 3.32 μm using the 3D Lumerical FDTD package and shown in Fig. 6.13. A non-uniform mesh distribution has been considered for the FDTD computations with a mesh accuracy of 7. An extra mesh size of (dy = 5 nm, dz = 5 nm) for the thin GSST layer is added for the better accuracy. Here, evolution of power of the fundamental H_y^{11} mode along the propagation direction Z is shown by a red line. At Junction 1, Z = 0 μm, there is about 1 dB optical loss, which agree with the LSBR simulations. The power loss monotonically increases until Z = 3.32 μm, at junction 2. Here, total power loss of the H_y^{11} mode when GSST in crystalline state is more than 20 dB which agrees to our full-vectorial FEM modal solution. Small ripple is likely due to the periodic interference between the propagating modes.

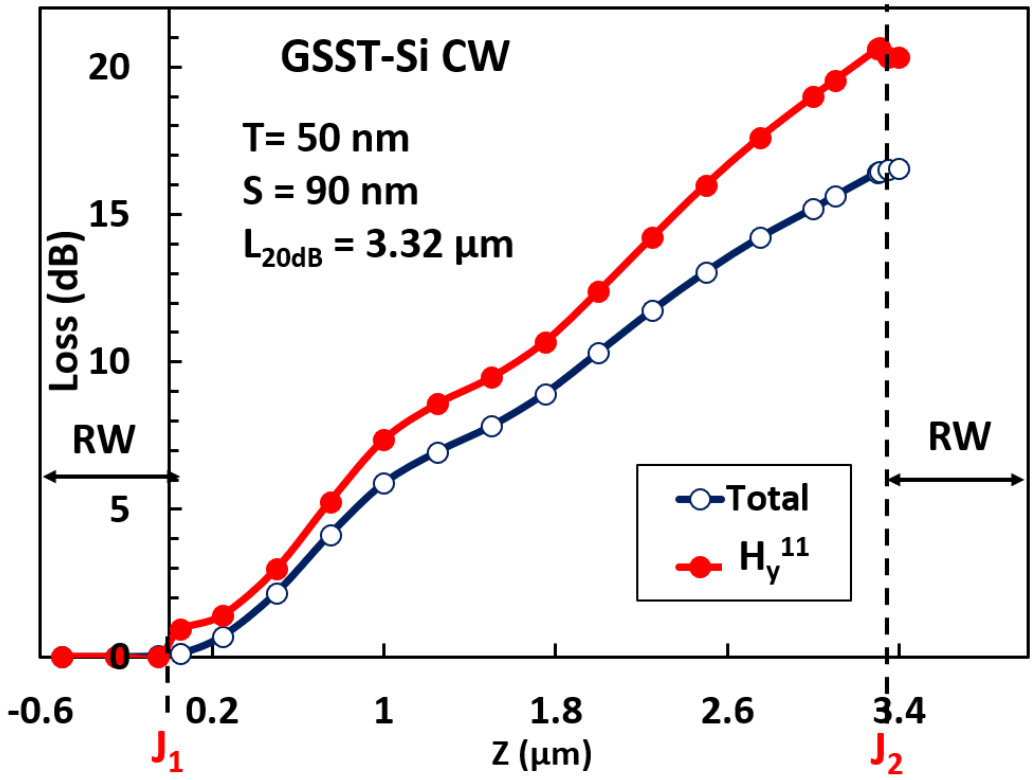

Fig. 6.13. Variations of total insertion loss and fundamental mode insertion loss of modulator when GSST in crystalline state with T = 15 nm, S = 90 nm and L_{20dB} = 3.32 µm by FDTD simulation.

At these junctions, higher order modes are generated to satisfy the boundary conditions. So next, evolution of total power is considered. The total optical power, comprising the H_y^{11} and higher order modes along the propagation direction Z is shown by a blue line in Fig. 6.13. It is noticeable that the total optical loss increases to 16.5 dB at the junction 2. The overall optical power loss of the device was less than 20 dB due to generation of higher order modes at junction 1 followed by recombination of some of them at junction 2. If a 20 dB extinction ratio is required for total power (rather than the fundamental modal loss), then the length of the device needs to be increased slightly.

6.5 Summary

A rigorous modal analysis of a self-sustained loss modulator based on a GSST-Si rib waveguide at the wavelength 1.55 μm is conducted by using an accurate **H**-field based FV-FEM and benchmarked by using the FDTD simulations. It was observed that although GSST layer can yield a high ER value, however due to the associated higher mode loss in crystalline state, a conventional MZI device design will not be viable. Therefore, exploiting the large modal loss between the GSST amorphous and crystalline states, an EA-type design is more effective. In this Chapter, the device performance is enhanced by optimizing the GSST-layer thickness (T) and Si slab thickness (S).

It is observed that a GSST thickness over 40 nm yields a much preferable compact device length < 5 μm with a lower modal loss. A 2 to 90 nm thickness GSST variation in the amorphous state introduces a total modal loss lower than 0.005 dB. Besides, the mode mismatch with the GSST thickness variation incorporates an additional junctional loss which is a dominating fraction in the total insertion loss. It is noticeable that a satisfactory low junctional loss from 0.132 to 0.266 dB can be achieved with a 40 – 60 nm GSST thickness, also considered as an optimal GSST thickness (T) to balance the device length with low insertion loss.

Moreover, the insertion loss slowly varied with the dielectric Si slab thickness. A 60 – 90 nm Si slab thickness is considered as an optimal design for the Si rib waveguide due to its smallest insertion loss changes in this region. Considering the full structure, the Si-GSST rib waveguide is advantageous over fully etched Si nanowire as it introduces an additional scattering loss at the sidewalls and edges.

In summary, a GSST-Si rib waveguide with optimised design parameters, such as width, W = 500 nm, slab thickness, S = 60-90 nm, and GSST thickness, T = 40-60 nm works as a self-sustained 1 x 1 electro-absorption modulator. An extinction ratio more than 20 dB between amorphous and crystalline states is achieved with a small insertion loss of 0.135 dB at the amorphous state. Additionally, it is observed by the FDTD simulations, that power loss of the fundamental H_y^{11} mode was more than 20 dB, however total optical loss was 16 dB due to generation and reconversion of higher order modes.

Chapter 7

Design of asynchronous directional coupler based switches incorporating GSST

7.1 Introduction

The directional couplers (DC) are used for coupling light wave from one waveguide to another parallel waveguide placed in its proximity. By controlling the effective index of the two waveguides, primarily by heating or current injection, it is possible to control the amount of the light coupled between the waveguides.

Directional couplers are the fundamental and widely used component in the integrated photonics devices. For instance, the directional couplers are utilized in optical switch which have a Mach-Zehnder interferometer (MZI) configuration and ring-resonator based optical filters. In the last 20 years, since the advent of integrated optics, every available material system: $LiNbO_3$, Silica-on-Si, GaAs, InP, glass, polymers and SOI all have been demonstrated and tested. Directional coupler based devices were also developed rapidly with the emerging Si photonics in last decades. The first reported fabricated directional coupler in SOI technology was published in 1995 by P. D. Trinh [90], a 3-dB directional coupler based on Si rib waveguide with excess loss of 1.9 dB for several hundreds of μm long interaction length with a gap of 2.5 μm.

Although the Si based directional coupler primary designed by thermo-optic or free-carrier dispersion effect can have the relatively short coupling length also lower loss, however they are still volatile and produce a comparatively weak change

of the real part of effective index in the active switching region, which led to large footprints and power consumption.

In order to enhance the light matter interaction and realize the compact reconfigurable directional coupler, optical phase change material (PCM) integrated with Si waveguide design could be introduced. Recent reports based on GST materials provide a good basis for the present work because they showed high Figure-of-Merit for 2 x 2 and 1 x 2 switches. In the work [63], the authors demonstrated that, by exploiting an asymmetric directional coupler design, the GST-clad Si photonic 1 x 2 and 2 x 2 switches present low insertion loss of ~ 1 dB, a compact coupling length of ~ 30 μm, and crosstalk better than −10 dB over a bandwidth of 30 nm. In F. Leonardis's report [68], they proposed a solution where the new low loss $Ge_2Sb_2Se_4Te_1$ (GSST) is used instead of GST for directional coupler design. That work explored the feasibility of obtaining very high performances for both switches 1 x 2 (IL as low as 0.083 dB and CT of 12.8 dB in the cross state) and 2 x 2 (IL = 0.046 dB and CT = 38.1 dB for the cross states). Their switch architecture was two- and three-waveguide directional couplers on the SOI platform and the phase change was electrically induced.

In this Chapter, a nonvolatile 1 x 2 optical switch based on two-waveguides asymmetrical directional coupler (ADC) integrated with the $Ge_2Sb_2Se_4Te_1$ (GSST) phase change material, which comprise of a Si nanowire coupled with a GSST-loaded waveguide is proposed and optimised. The self-holding "ON" and "OFF" states of the proposed optical switch can be triggered by GSST amorphous state and crystalline state, respectively. The proposed 1x2 optical switch design is optimised by using a full-vectorial finite element method (FV-FEM) for modal solution and a 3D finite difference time domain method (3D-FDTD) to obtain propagation and power transfer characteristics.

7.2 Schematic and principle

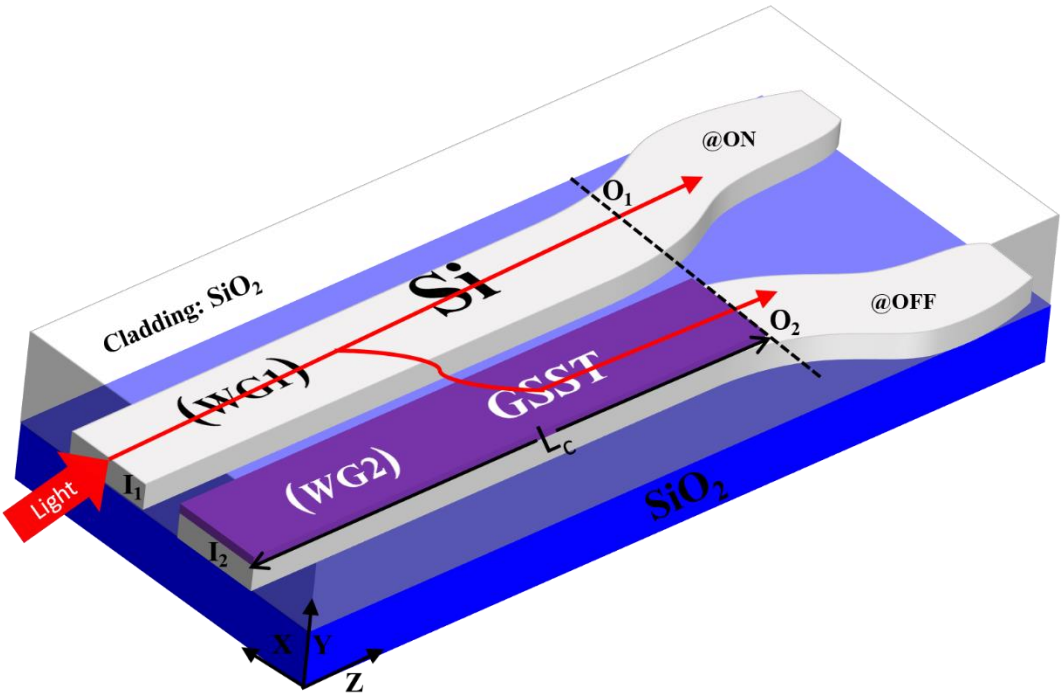

Fig. 7.1. Schematic diagram of the proposed 1 x 2 GSST-Si directional coupler based optical switch.

The schematic and working principle diagram of the proposed 1 x 2 optical switch is shown in Fig. 7.1 based on a two-waveguides asymmetrical directional coupler, which comprises of an input Si nanowire on the upper side identified as WG1, and a bus waveguide with GSST cap layer on the lower side identified as WG2. The "OFF" and "ON" states of the proposed optical switch can be set by changing the GSST between amorphous state and crystalline state. More importantly, when GSST is triggered at amorphous state, the phase matching condition is designed to be satisfied for the two-waveguide based directional coupler. The input quasi-TE_0 mode introduced at port I_1 will propagate along the WG1 at the upper side, then after propagating a coupling length, L_C, the quasi-TE_0 mode will be transferred to WG2 at the lower side then continue propagate till port O_2 in order to achieving the "OFF" state of the switch. If GSST is triggered at crystalline state, the effective index of the WG2 will be changed significantly hence the phase-matching condition will be destroyed for the GSST-Si directional coupler. The input quasi-TE_0 mode will only propagate along the upper Si nanowire WG1 without any mode coupling and exit through port O_1.

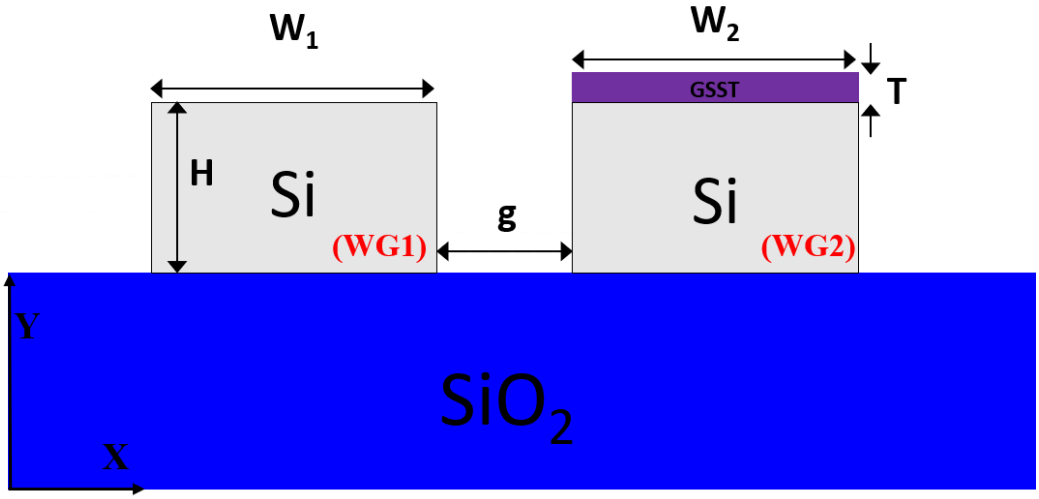

Fig. 7.2. Cross-section of the Si nanowire and GSST-loaded Si waveguide based directional coupler.

The cross-section of the Si nanowire (WG1) and GSST-loaded Si waveguide (WG2) based asymmetrical directional coupler is shown in Fig. 7.2. The widths of the input WG1 and WG2 are denoted by W_1 and W_2, respectively. As the right side WG2 have a GSST clad, so a different W_2 is needed to phase match it with the WG1 of W_1 without any GSST cladding. The height of the Si layer of the WG1 and WG2 are all taken as H. The thickness of the GSST layer of WG2 is identified as T, and the gap between the input WG1 and WG2 is represented by g. The proposed GSST-Si directional coupler is based on the SOI platform with a SiO_2 cladding.

At the operating wavelength of 1550 nm, the refractive indices of the cladding and substrate SiO_2 and Si core are taken as 1.44 and 3.475, respectively. The complex refractive index of GSST for the amorphous state and crystalline state are taken as n (Am-GSST) = 3.4 + j*0.00018 and n (CR-GSST) = 5.1 + j*0.5 [58], respectively.

7.3 Modal solutions

7.3.1 Phase matching conditions

In order to achieve the phase-matching condition for the GSST-Si directional coupler-based switch at "OFF" state, in-house FEM code is used to obtain the modal solutions of the individual waveguides and also of the coupled waveguides.

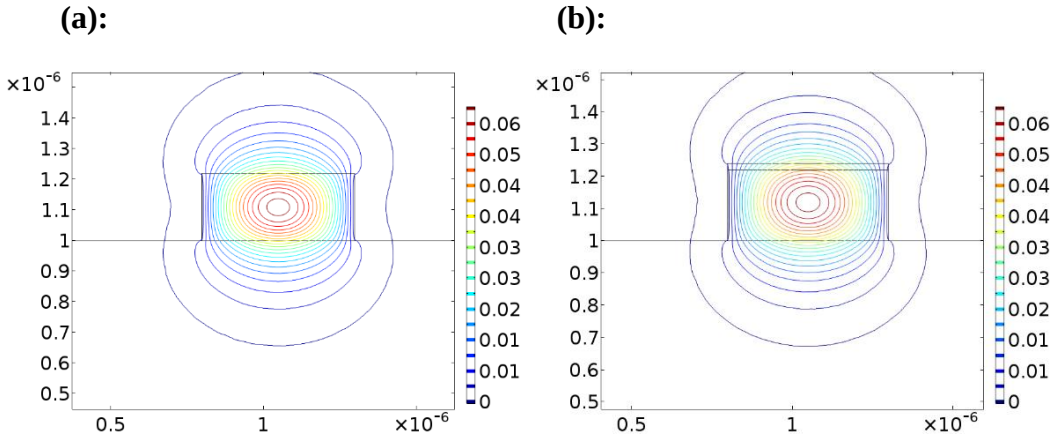

Fig. 7.3. Contour plot of the H_y field of the (a) isolated input Si nanowire (WG1) for W_1 = 500 nm and H = 220 nm, and (b) isolated GSST-Si hybrid waveguide (WG2) for W_2 = 500 nm, H = 220 nm, and T = 20 nm (lower).

For the quasi-TE mode, H_y is the dominant and H_x and H_z are the non-dominant components of the magnetic field, **H**. At first, an input waveguide with W_1 = 500 nm, H = 220 nm is chosen to ensure single-mode operation and simulated as a representative of the Si nanowire WG1, and the H_y field contour plot of the quasi-TE_0 mode of WG1 is shown in Fig. 7.3 (a). The mode effective index (n_e) of the quasi-TE_0 mode of WG1 is calculated as 2.4434. It can be observed that most of its field is concentrated within the Si core. Outside the waveguide core, the H_y field decays exponentially both in upper SiO_2 clad region and lower substrate region.

However, when a GSST cap layer is deposited on this Si nanowire (the thickness of the GSST layer T = 20 nm as representative) and at its amorphous state, the corresponding mode effective index (n_e) of the quasi-TE_0 mode of WG2 is calculated as 2.5087, slightly larger than the WG1. Also, its H_y field contour plot of WG2 is shown in the Fig. 7.3 (b), it can be noted that as a 20 nm GSST layer is deposited, the field is expanded a bit more than WG1, but the maximum field still confined inside the Si core.

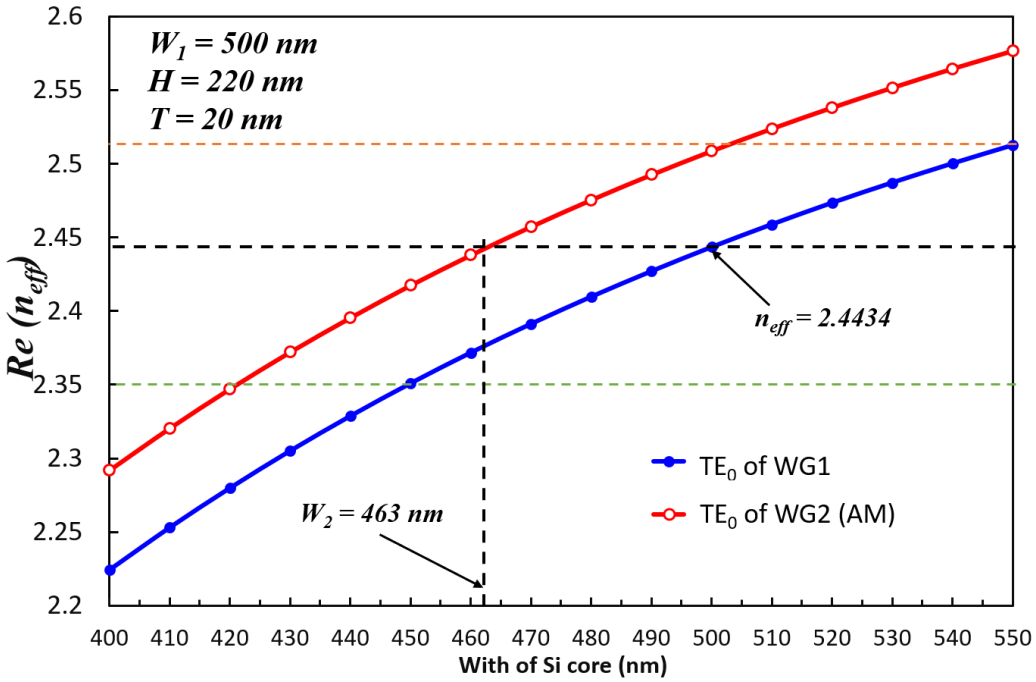

Fig. 7.4. Variations of the effective index with the width of the Si waveguide.

In order to achieve the phase-matching conditions of the directional coupler, variations of the real part of effective index of two isolated Si nanowire (WG1) and GSST-Si waveguide (WG2) with the width of Si core are shown in Fig. 7.4. Variations of effective index for WG1 is shown by a blue line with solid holes, it can be noted that the n_e values increase from 2.22 to 2.52 with the width of Si W_1 increase from 400 to 550 nm. On the other hand, variations of real part of effective index for WG2 is shown by a red line with hollow holes. It can be observed that the n_e values of WG2 always larger than the WG1 curve, which means at same Si width, the WG2 will always have larger n_e, so to match the effective index values, a smaller W_2 of the WG2 should be considered.

For the representative case (W_1 = 500 nm, H = 220 nm), the mode effective index (n_e) of the input Si nanowire WG1 is calculated as 2.4434, denoted by a horizontal black-dotted line in Fig. 7.4. Therefore, the phase matched width W_2 of the WG2 (T = 20 nm) should be taken as W_2 = 463 nm to achieve matched mode effective index (propagation constant) between the two isolated waveguides so that the light can efficiently couple from the input Si nanowire to the lower GSST-Si waveguide.

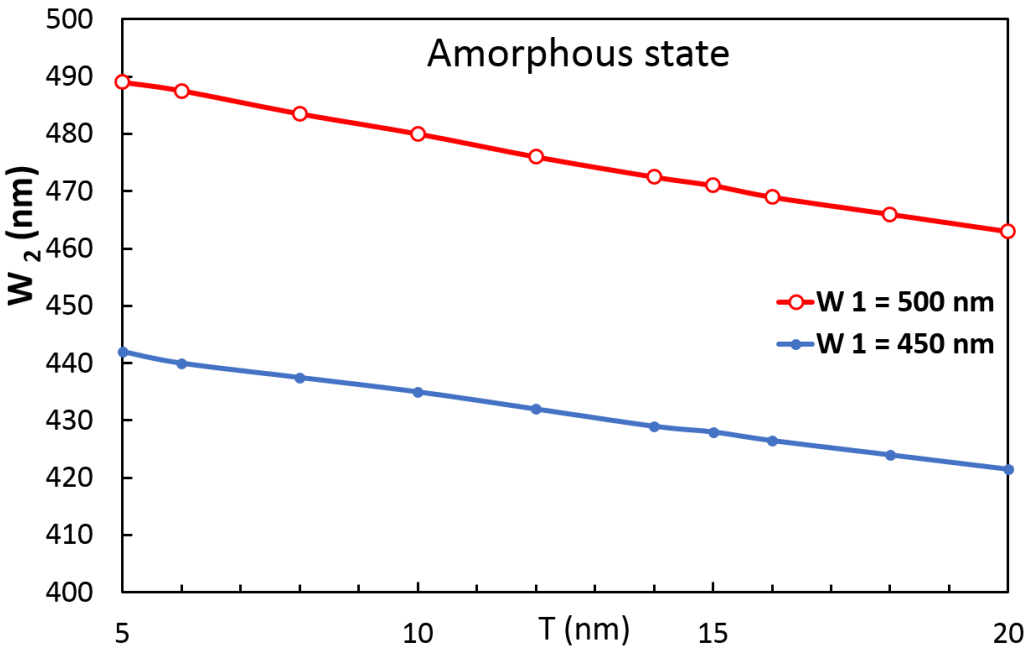

Fig. 7.5. Variations of the phase matched waveguide width W_2 with the GSST layer thickness T for W_1 = 450 and 500 nm.

In order to investigate the effect of the thickness of GSST layer of the phase matched waveguide width W_2 of the GSST-Si waveguide WG2, variations of the W_2 with the GSST thickness, T for W_1 = 450 and 500 nm are calculated then shown in Fig. 7.5. For W_1 = 500 nm shown by a red line, it can be noted that, with the GSST thickness increase from 5 nm to 20 nm, its W_2 also reduce gradually from 490 nm to 463 nm. On the other hand, when the width of Si nanowire W_1 reduce to 450 nm, its W_2 has the same trend but have the lower values which decrease from 442 nm to 421.5 nm.

7.3.2 Phase-matched supermodes field profiles

In general, when light propagates through a dielectric waveguide, most the power will be concentrated within the central core of the waveguide as shown in Fig. 7.3. However, if another waveguide core is placed close to the first waveguide, that second waveguide perturbs the mode of the first waveguide and vice versa. Thus, instead of having two modes have the same effective index, the first supermode localized in both waveguides with the same field sign (either both

positive or both negative) and thus get a symmetric supermode (even-like) shown in Fig. 7.6, with an effective index that is slightly larger than the effective index of the unperturbed waveguide mode. It also generates another antisymmetric supermode (odd-like) shown in Fig. 7.7, with an effective index that is slightly smaller than the effective index of the unperturbed waveguide mode.

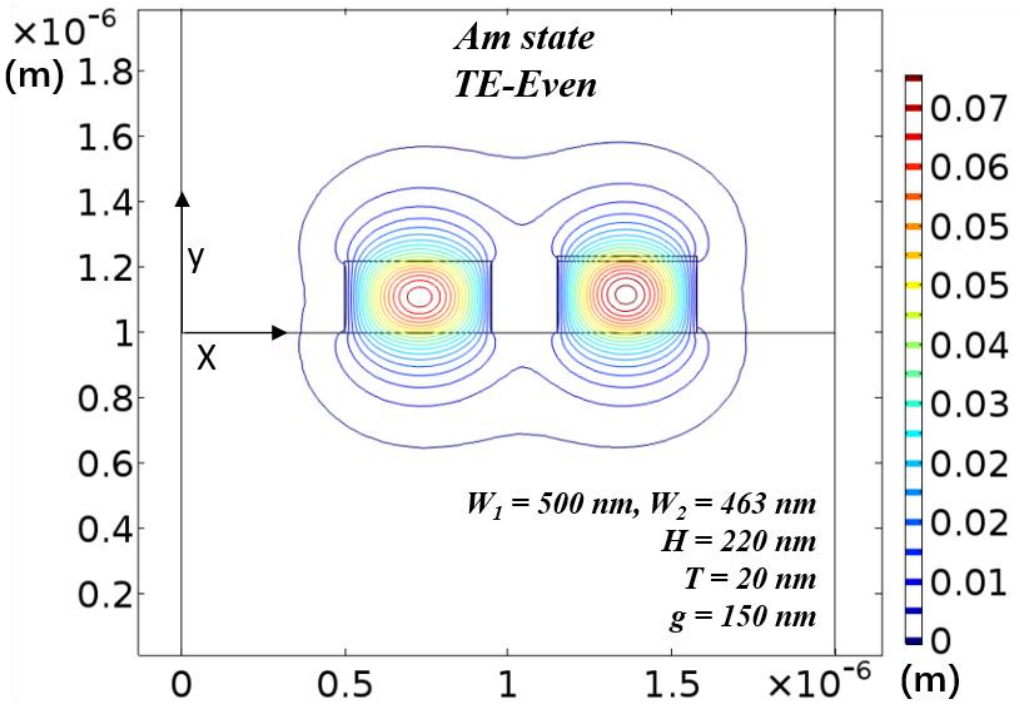

Fig. 7.6. 2D contour plot of the H_y field of the quasi-TE even-like supermode with W_1 = 500 nm, W_2 = 463 nm, H = 220 nm, T = 20 nm and g = 150 nm (GSST-AM).

For the representative case of the directional coupler, the coupled mode solutions of input WG1 (W_1 = 500 nm, H = 220 nm) and its phase matched WG2 (W_2 = 463 nm, H = 220 nm, T = 20 nm) with a gap g = 150 nm are calculated by using FV-FEM. The 2D contour H_y field plot of the even-like supermode of the coupled waveguide are shown in Fig. 7.6. It can be observed that the light confined well in both Si core, and both waveguides have similar field intensity with the same positive sign. Due to the GSST cap layer is loaded, the H_y field in the second waveguide is slightly higher compare to the first waveguide.

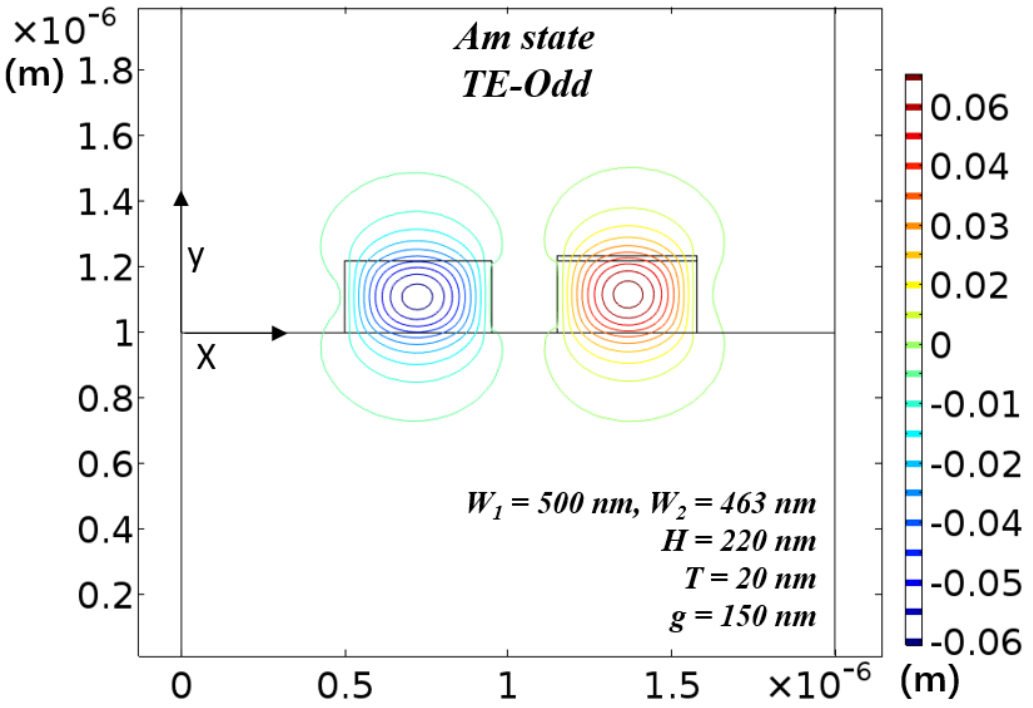

Fig. 7.7. 2D contour plot of the H_y fields of the quasi-TE odd-like supermode with W_1 = 500 nm, W_2 = 463 nm, H = 220 nm, T = 20 nm and g = 150 nm (GSST-AM).

On the other hand, there is another antisymmetric supermode mode which has a lower effective index, the 2D contour H_y field plot of the odd-like supermode of the coupled waveguide are shown in Fig. 7.7. It can be observed that the light is still concentrated within the Si core and extend little bit to the upper clad region and the lower substrate. However, both waveguides have the similar magnitude of the field H_y intensity but with different signs.

(a): **(b):**

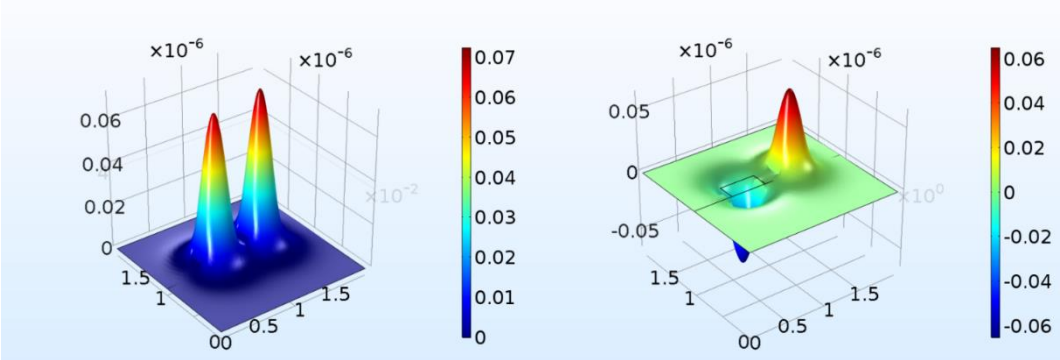

Fig. 7.8. 3D contour plots of the H_y fields of the quasi-TE (a) even and (b) odd supermode with W_1 = 500 nm, W_2 = 463 nm, H = 220 nm, T = 20 nm and g = 150 nm (GSST-AM).

In order to check the field intensity of the coupled waveguide and the validity of the phase matched W_2, the 3D coutour H_y field of the even and odd supermodes are plotted in the Figs. 7.8 (a) and (b). In the two 3D contour plots, it can be noted that, with the phase matched W_2 = 463 nm for the GSST-loaded Si waveguide, the coupled waveguide has two peak field intensity of similar magnitude and same signs in their Si core for the even supermode, and in the odd supermode, there are also two field intensity peaks of similar magnitude and but with opposite signs. It can be concluded that as the similar magnitude field intensity in both two waveguide cores, the phase matched two waveguides are strongly coupled, therefore the input WG1 will be evanescently coupled to the lower WG2 completely at a distance equal to the coupling length.

(a): **(b):**

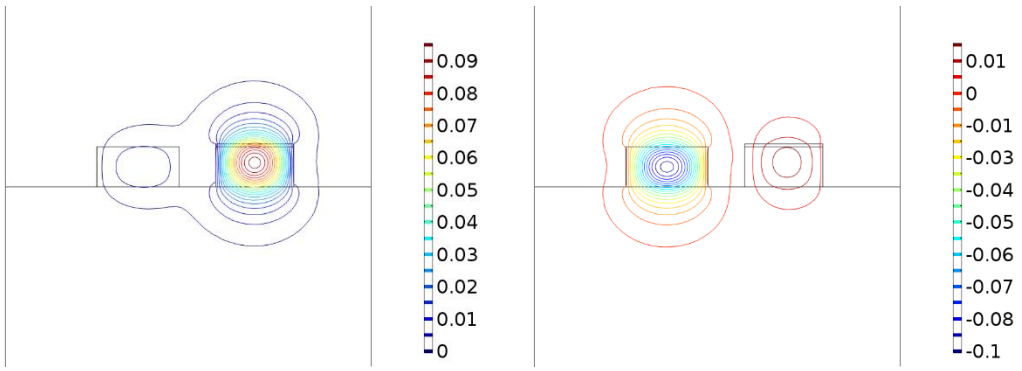

Fig. 7.9. 2D contour plots of the H_y fields of the quasi-TE (a) even and (b) odd supermode with W_1 = 500 nm, W_2 = 463 nm, H = 220 nm, T = 20 nm and g = 150 nm (GSST-CR).

When the GSST is switched to the lossy crystalline state, for the same coupled waveguide parameters (W_1 = 500 nm, W_2 = 463 nm, H = 220 nm, T = 20 nm and g = 150 nm), its 2D contour H_y field plot of the even-like supermode are shown in Fig. 7.9 (a). It can be observed that the light confined well in the lower GSST-loaded Si waveguide WG2 (shown on right) and extend very little to the upper Si nanowire WG1 (shown on left). But these two waveguides still have the field intensity with same positive sign, and the maximum field intensity is located inside the Si core of WG2.

On the other hand, the 2D contour H_y field plot of the odd-like supermode are shown in Fig. 7.9 (b). It can be noted that most of the light is concentrated well within the core of input Si nanowire WG1, and the field extend to the top cladding and bottom substrate region and also quite small amount of field is located inside the WG2. Moreover, there are only H_y field with positive sign in the right WG2, but the left WG1 have the H_y field with both the signs, also most of the intensity in WG1 are with negative signs.

(a): **(b):**

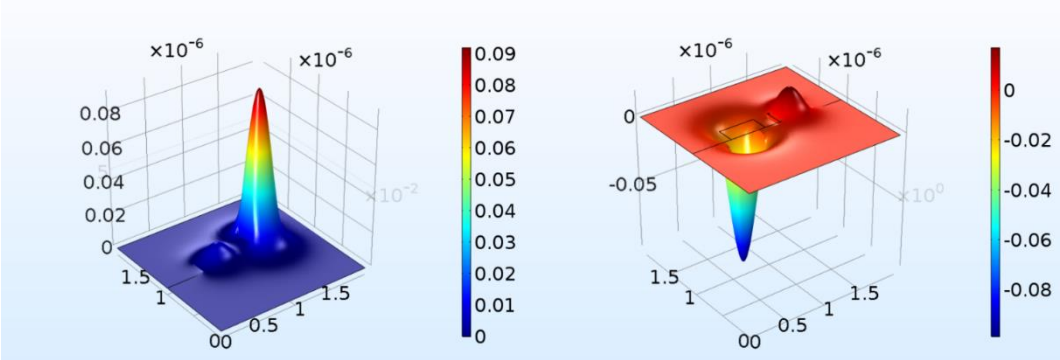

Fig. 7.10. 3D contour plots of the H_y fields of the quasi-TE (a) even and (b) odd supermode with W_1 = 500 nm, W_2 = 463 nm, H = 220 nm, T = 20 nm and g = 150 nm (GSST-CR).

The 3D contour of H_y field of the even and odd supermodes are also plotted in the Figs. 7.10 (a) and (b). For the even supermode, it can be noted that there is a large magnitude field intensity peak in the right-side GSST-Si waveguide WG2, and a small peak in the left-side Si nanowire WG1 but with the same sign. Similarly, there is a large magnitude field intensity peak in the left-side WG1 but with negative sign for the odd supermode, and a small intensity peak inside the right-side WG2 with a positive sign. This is due to the huge effective index difference between the input WG1 and WG2 when GSST in crystalline state, which leads to a large phase mismatch, so that the contour plots are appeared like two isolated modes. Also, as the two waveguides are mismatched and weakly coupled, after propagation equal to the coupling length, the input TE_0 mode will propagate along with the input Si nanowire WG1 to the end without any significant interactions.

7.3.3 Coupling lengths and ratio of the coupling length

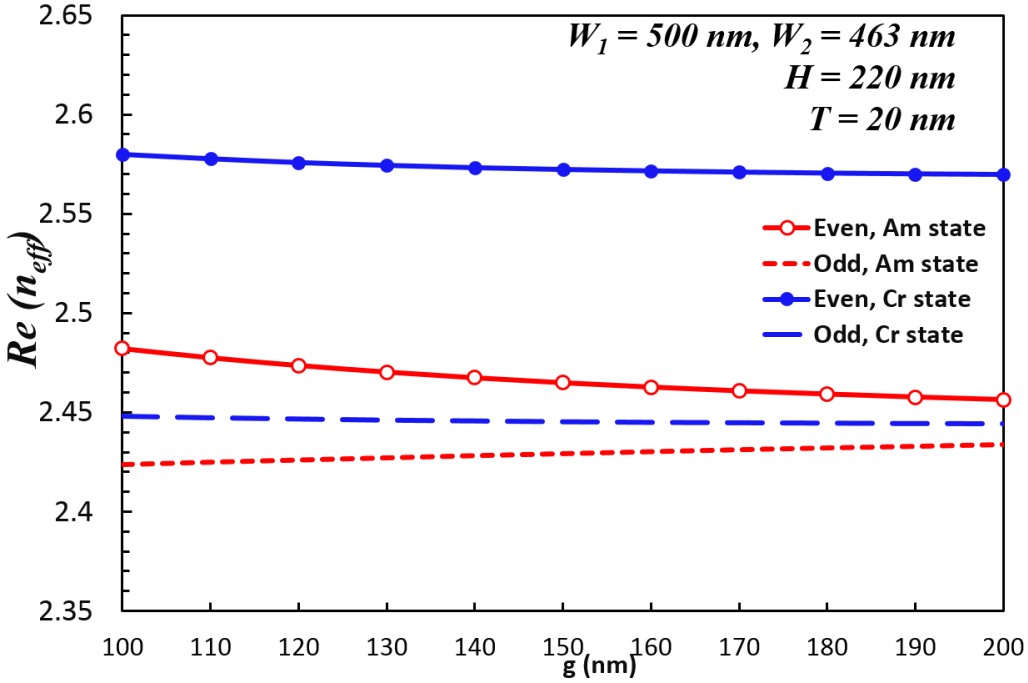

Fig. 7.11. Variations of the real part of the effective index of the even and odd supermodes as a function of the gap, g for phase matched waveguides (W_1 = 500 nm, W_2 = 463 nm, H = 220 nm and T = 20 nm) at GSST AM and CR state.

For the optimal design of a directional coupler based optical switch, it is essential to study the modal characteristics of the supermodes for both the GSST states. At first, a particular GSST thickness T will be chosen and the corresponding phase matched width W_2 of the GSST-Si hybrid will be taken as the special case for the proposed two waveguide directional coupler.

To study the effective index of the supermodes, the coupled waveguide with the parameters of (W_1 = 500 nm, W_2 = 463 nm, H = 220 nm, T = 20 nm) is considered. Variations of the effective indices of the supermodes as a function of the waveguide gap, g, are shown in Fig. 7.11. The n_e values of the even and odd supermode for the GSST amorphous state are shown by two red lines with and without hollow circles, respectively. On the other hand, the n_e values of the even and odd supermode for the GSST crystalline state are shown by two blue lines with and without solid circles, respectively. It can be observed that the n_e values of the even supermodes for GSST both states decrease as the waveguide gap, g increases from 100 to 200

nm. However, the n_e values of the odd supermode are almost constant with the increase of the waveguide gap. It also can be noted that the effective index differences between the even and odd mode when GSSST in amorphous state are become smaller with the waveguide gap increase. But when GSST is triggered at crystalline state, its effective index differences stay stable around 0.13 with the gap increase from 100 to 200 nm.

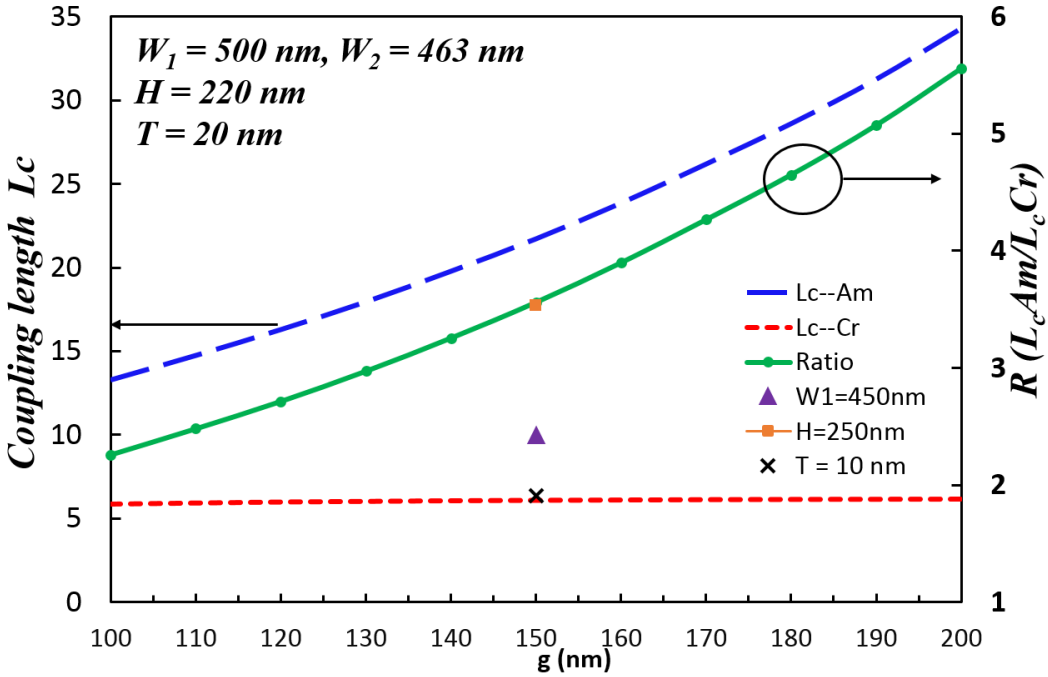

Fig. 7.12. Variations of coupling length and the ratio of the coupling length as a function of the waveguide gap.

For a directional coupler, its coupling length, $L_c = \frac{\pi}{(\beta_e - \beta_o)}$, is the shortest length necessary for maximum energy transfer, where β_e and β_o are the propagation constants of the even and odd supermodes of the coupled waveguide. Due to the higher refractive index of the GSST crystalline state, the coupling length of the coupled waveguide with crystalline GSST always shorter than it with the amorphous state. The concept of the proposed directional coupler based optical switch is to optimize a device which satisfies, $L = L_c^{AM} = 2L_c^{CR}$, where L_c^{AM} and L_c^{CR} are the coupling lengths for the coupling mode when GSST in amorphous state and crystalline state, respectively. The coupling lengths of the amorphous and

crystalline state are dependent on the propagation constants, and the propagation constant differences are changed by the effective index of the even and odd supermodes. So, it is necessary to investigate the waveguide parameters effect such as (height of Si core width and GSST thickness) on the coupling lengths.

At first, the coupling lengths for the representative case of the two-waveguide directional coupler with the parameter (W_1 = 500 nm, W_2 = 463 nm, H = 220 nm and T = 20 nm) are calculated and illustrated in the left-hand side of the Fig. 7.12. When the GSST in amorphous state, the coupling length L_c^{AM} of the directional coupler is shown by a blue dashed line increase rapidly from 13.3 to 34.3 μm when the waveguide gap, g increases from 100 nm to 200 nm. On the other hand, when the GSST is switched into crystalline state, the L_c^{CR} of the directional coupler shown by a red dotted line remains stable at a constant level around 6 μm when the g increase from 100 to 200 nm. This is due to in the GSST crystalline state, the phase mismatched even and odd supermodes are closer to isolated waveguides, so that their propagation constant differences are remained constant.

Next, the ratio of the coupling length, $R = L_c^{AM}/L_c^{CR}$, as a function of the waveguide gap, g is calculated and shown by a solid green line using the right-hand side in the Fig. 7.12. It can be noted that, the ratio increases smoothly from 2.25 to the maximum 5.55 with the waveguide gap increase from 100 to 200 nm. It can be noted unless separation between waveguide, g is significantly reduced, this ideal length ratio of R = 2 cannot be achieved.

In order to achieve the desire ratio, $R = L_c^{AM}/L_c^{CR} = 2$, the effect of the following waveguide parameters: Si core height H, the width of the input Si nanowire W_1 (phase matched W_2 also changed), the GSST layer thickness T and the waveguide gap g are investigated. Before embarking a further investigation, the coupling length ratio, R of the parameters for only one change, such as H = 250 nm, W_1 = 450 nm and T = 10 nm is calculated with the fixed g = 150 nm as initial test. It can be noted that, with the height H increase to 250 nm shown as an orange square, the ratio still remains close to 3.5, similar as the representative case, which means that the height of H has not much influence on the ratio so it will be fixed at 220 nm. When the W_1 of WG1 reduces to 450 nm shown by a purple triangle, the ratio R

reduces significantly to 2.42, so that reduction of the input WG1 width will be possible to achieve the desired ratio. Moreover, when the GSST layer loaded on the WG2 reduces to 10 nm shown by a black cross, the ratio R reduce to a lower 1.9 value, very close to the desired ratio. It can be predicted that if the T just slightly larger than then 10 nm, its desired ratio R = 2 could be achieved. At last, since the last three tests are all with the fixed waveguide gap, g = 150 nm, it also can be concluded that, if both the GSST thickness and waveguide gap are adjusted, the desired ratio also can be obtained.

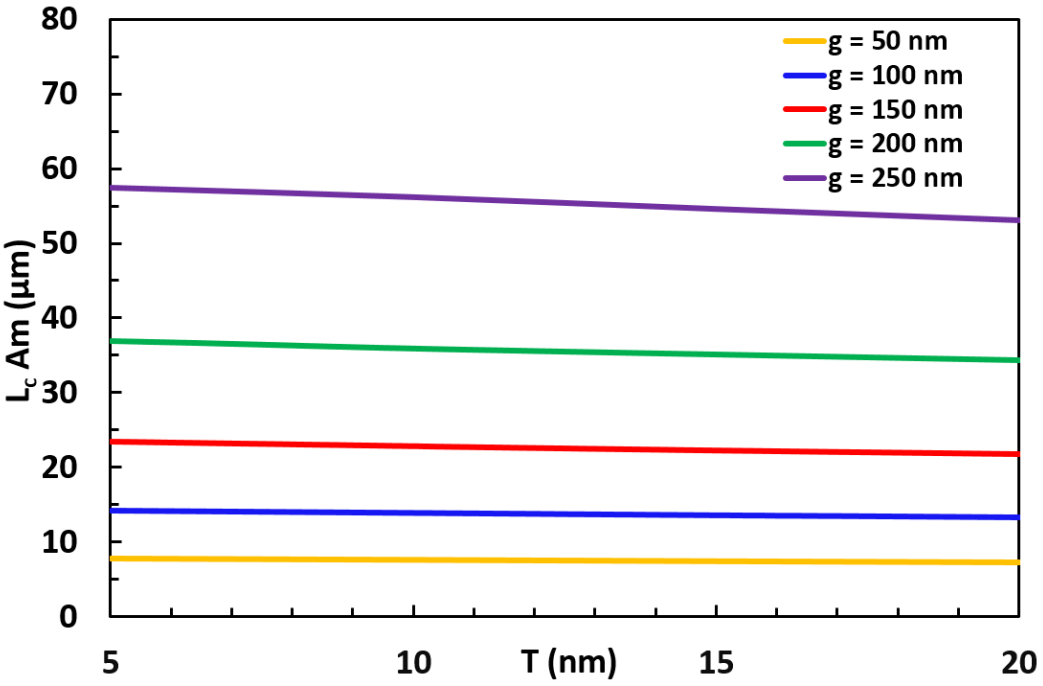

Fig. 7.13. Variations of coupling lengths as a function of the GSST thickness, T for g = 50-250 nm when GSST in amorphous state.

The effect of GSST thickness, T to produce the desired structure with coupling lengths ratio R = L_c^{AM}/L_c^{CR} is studied. In this case, the Si core width W_1 is taken as 500 nm, the corresponding phase matched width W_2 is taken from Fig. 7.5 and the Si height taken as 220 nm. Variation of coupling lengths as a function of GSST clad thickness at amorphous state for g = 50-250 nm are plotted in Fig. 7.13. It can be observed that all the coupling lengths L_C^{AM} curves stay steady with the T increase from 5 nm to 15 nm. For g = 250 nm, the L_C^{AM} decrease slightly from 57 to 53 nm, and the others all have the shorter coupling lengths with the smaller

waveguide gap g. As the directional coupler is phase matched in amorphous state, so that the coupling lengths won't have too much fluctuations with the T increases.

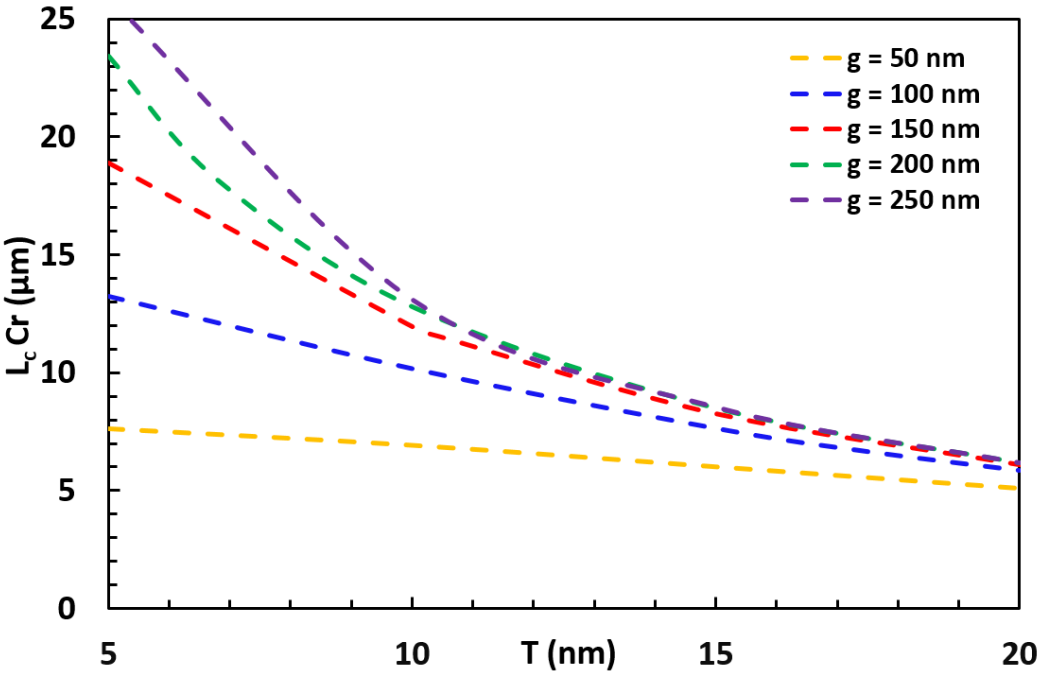

Fig. 7.14. Variations of coupling lengths as a function of the GSST thickness, T for g = 50-250 nm when GSST in crystalline state.

On the other hand, variations of the coupling lengths with the T at GSST crystalline are shown in Fig. 7.14. It can be noted that, the coupling length curves reduce as the GSST layer thickness increases from 5 nm to 20 nm. However, the larger the waveguide gap, the coupling length will have larger variations. For example, for g = 250 nm, the coupling length decrease exponentially from 26 to 6 µm, while when g = 50 nm, the coupling length reduce smoothly from 7.6 to 5 µm. As the phase matching condition never occurs when GSST in crystalline state, so the directional coupler acts like two isolated waveguides. Moreover, for a larger waveguide gap g, the waveguide always has larger coupling length with the smaller T, also when the T increase to a larger range 15-20 nm, all the coupling length curves will decrease to a constant level around 6 µm.

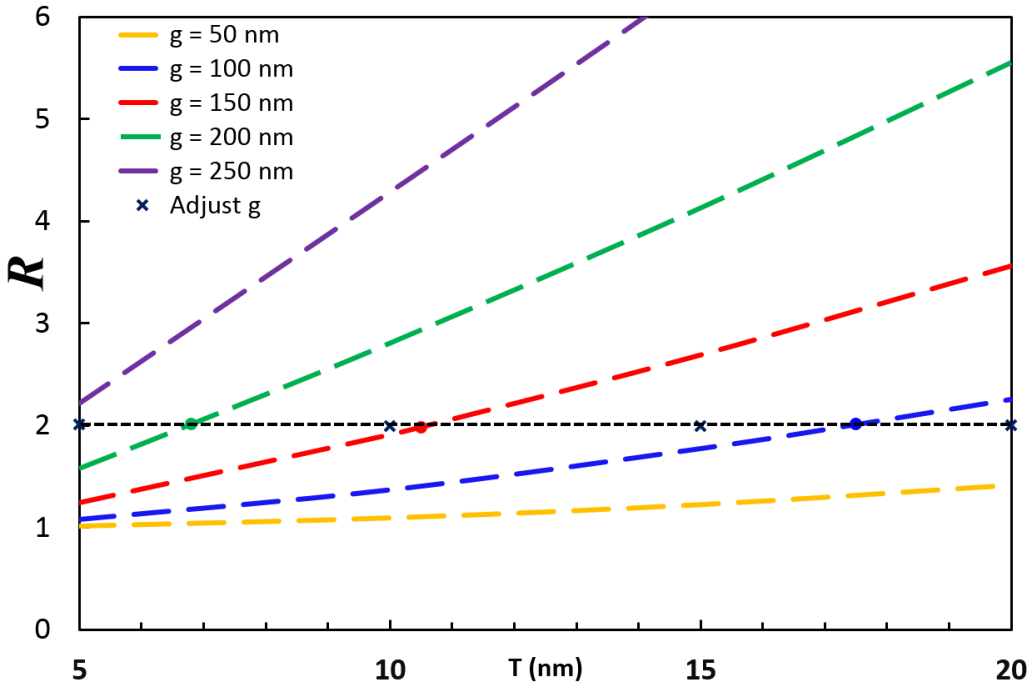

Fig. 7.15. The ratio of the coupling length, R as a function of the GSST thickness, T for waveguide gap, g = 50-250 nm.

The corresponding ratio of the coupling length, R is calculated as: L_c^{AM}/L_c^{CR} with the varied waveguide gap g as a function of the GST thickness T and are illustrated in Fig. 7.15. It can be observed that, the waveguide has larger waveguide gap will have the larger coupling length ratio and when the T increases from 5 to 20 nm, the ratio will increase much more dramatically when it has larger waveguide gap. For the desire coupling lengths ratio, $R = L_c^{AM}/L_c^{CR} = 2$ is shown by a horizontal dotted-black line. It can be noted that, for g = 50 and 250 nm, the ideal ratio is not possible achieved when T increase from 5 nm to 20 nm. And for g = 100, 150 and 200 nm, the desire ratio R = 2 can be obtained when GSST thickness, T is chosen at 17.5, 10.6 and 6.8 nm, respectively. Moreover, considering the fabrication convenience, the desire ratio with the round number of the thickness of the GSST layer such like 5, 10, 15 and 20 nm also shown in Fig. 7.15 by dark blue crosses within the horizontal ratio line. It can be noted here, for T = 5 nm with g = 237 nm, for T = 10 nm with g = 156 nm, for T = 15 nm with g = 114 nm and for T = 20 nm with g = 87 nm, the desired ratio R = 2 can be achieved. It can be concluded that, by controlling the GSST thickness, T and waveguide gap, g parameters, there

are many optimal parameter sets which can be achieved for the desire coupling lengths ratio.

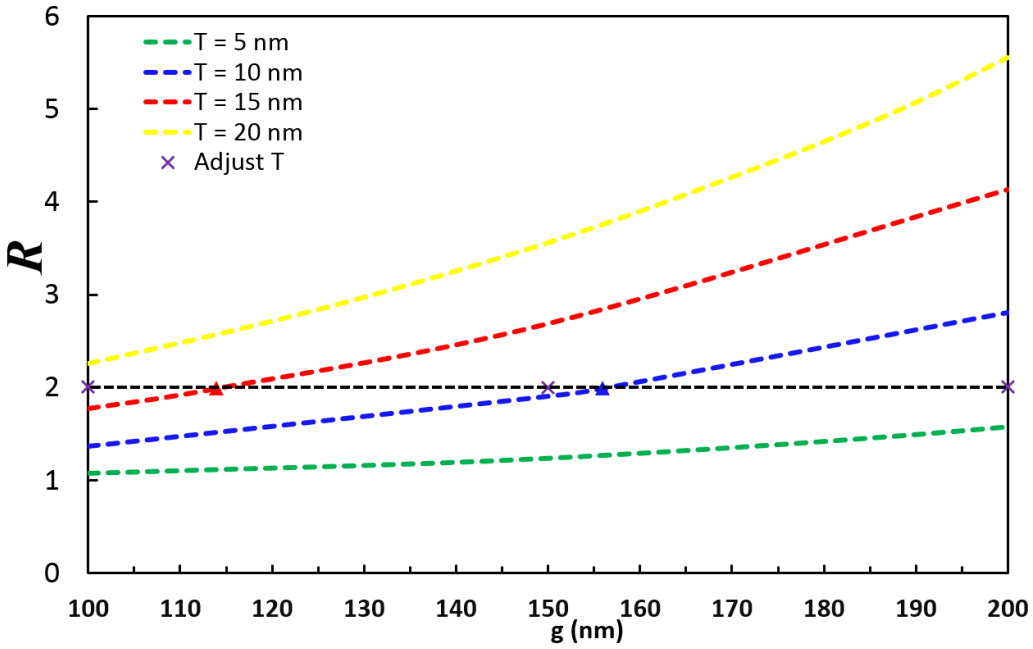

Fig. 7.16. The ratio of the coupling length, R as a function of the waveguide gap, g for GSST layer thickness, T = 5-20 nm.

In order to analysis the influence of the waveguide gap, g on the coupling length ratio R, the variations of R as a function of the waveguide gap for different GSST thickness are shown in Fig 7.16. It can be observed that when the waveguide has larger GSST thickness T can achieve a larger coupling lengths ratio R. For a given T, the coupling length ratio will increase with the waveguide gap, and the coupling length ratio with a larger GSST thickness T will increase significantly to a higher value. For the desire coupling length ratio, $R = L_c^{AM}/L_c^{CR} = 2$ of the GSST-Si two-waveguide directional coupler, it can be noted that the largest and smallest GSST thickness T = 5 and 20 nm is not possible within the waveguide gap range from 100 to 200 nm. It clearly shown that for T = 15 nm, R = 2 can be achieved at g = 114 nm, and for T = 10 nm, R = 2 also can be achieved at g = 156 nm. For the ease of the fabrication, the desire ration with the round number of waveguide gap g = 100, 150 and 200 nm also shown in the Fig 7.16 as purple crosses. However, the corresponding optimal GSST thickness T is not a round number and may need to

be chosen carefully, so that the fabrication tolerances will be analysed in the later part of this Chapter.

T (nm)	g (nm)	W_2 (nm)	L_c^{AM} (μm)	L_c^{CR} (μm)	R
5	237	489	51.3	25.5	2.01
6.8	200	486	36.6	18.2	2.01
10	156	480	24.1	12.1	1.99
10.6	150	479	22.7	11.5	2
15	114	471	15.7	7.9	1.99
17.5	100	467	13.4	6.7	2.01
20	87	463	11.5	5.8	2

Table. 7.1 Waveguide parameter sets for coupling length ratio R = 2

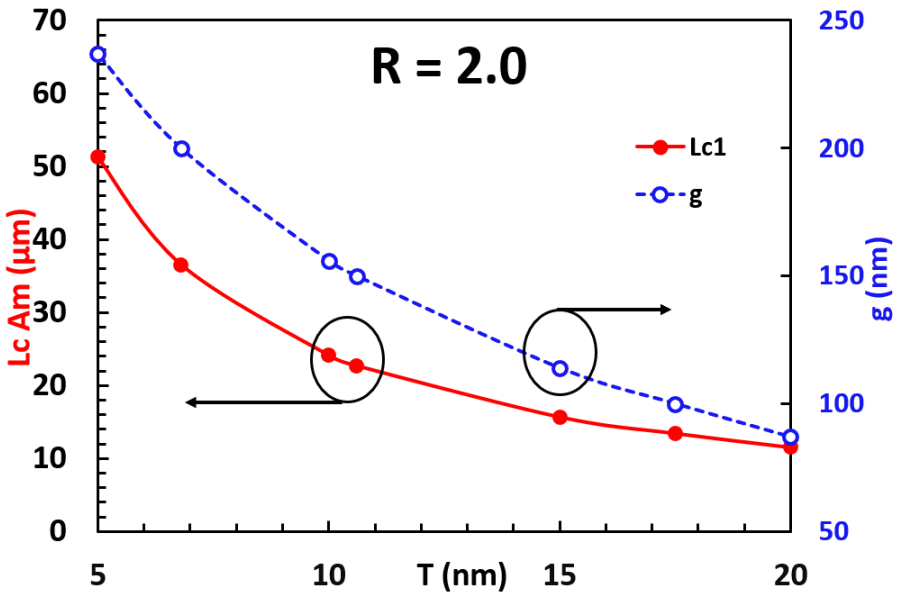

Fig. 7.17. Variations of the coupling length L_c^{AM} with both the GSST thickness T and waveguide gap g under the condition, coupling length ratio R = 2.

The optimal waveguide parameter sets of GSST thickness, T and waveguide gap, g for achieving the desire coupling lengths ratio L_c^{AM}/L_c^{CR} = 2 are shown in Table 7.1 and also shown in Fig. 7.17. The relevant optimal device length with the increase of GSST thickness are shown by a solid-red line with solid circles using the left-hand scale, and the waveguide gap, g is shown by a dotted-blue line with hollow circles using the right-hand scale. It can be observed that, for archiving the

desired ratio R = 2, the waveguide has larger GSST layer will need to have shorter waveguide gap. It also can be concluded that if the thinner GSST layer is chosen, the directional coupler needs longer waveguide gap more than 200 nm also longer device length, more than 50 µm for 5 nm GSST layer. If the GSST layer is chosen more than 10 nm, the directional coupler can have a short waveguide gap from 87-156 nm also the device length will reduce from 24 to 11.5 µm, which may be more attractive for compact photonic device design.

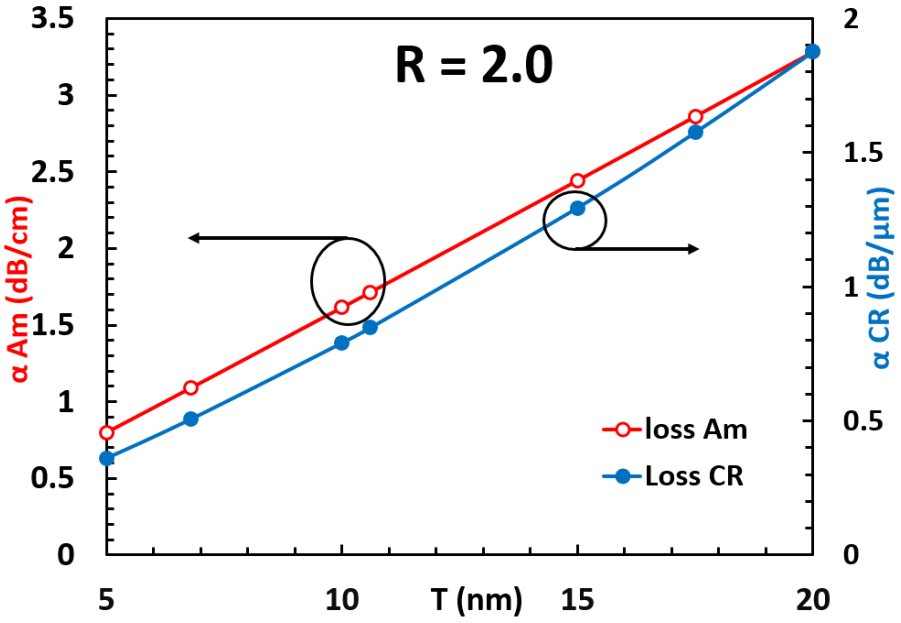

Fig. 7.18. Variations of mode loss with the optimal parameter sets when GSST in AM and CR state under the condition, coupling length ratio R = 2.

However, if a larger GSST thickness is chosen for the optimal waveguide design, it could be resulted in a larger mode loss as GSST refractive index have a larger imaginary value in its crystalline state. The variations of the mode loss of the waveguide when GSST in amorphous state and crystalline state with the optimal parameter sets for R = 2 are shown in Fig. 7.18. The variations mode loss of the GSST amorphous state is shown by a solid-red line with hollow circles for the adjust GSST thickness for R = 2 at the left-hand scale, it can be observed that the mode loss increases from 0.8 to 3.3 dB/cm with the GSST thickness, T increase from 5 nm to 20 nm. On the other hand, mode loss for the GSST crystalline state are shown by a blue line using the right-hand scale, the optimal GSST thickness also shown

by solid circles on the blue line. It can be noted that, the mode loss in crystalline increase considerably from 0.36 to 1.88 dB/μm with the GSST thickness T increase from 5 to 20 nm which is quite higher than its amorphous state as the larger extinction coefficient of the GSST.

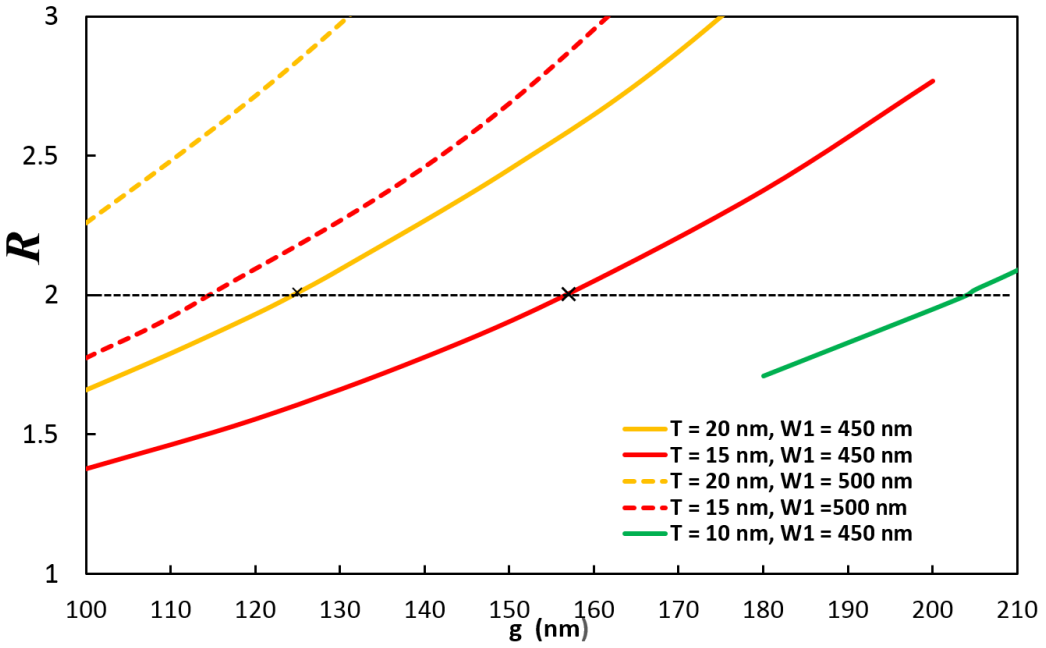

Fig. 7.19. The ratio of the coupling length, R as a function of the waveguide gap, g for GSST layer thickness, T = 5-20 nm with W_1 = 450 and 500 nm.

Next, the effect of the input WG1 width W_1 of the coupling lengths ratio, R = L_c^{AM}/L_c^{CR} are calculated and shown in Figure 7.19. For W_1 = 450 nm, the ratio R with T = 10, 15 and 20 nm are shown by solid green, red and yellow lines, respectively as a function of the waveguide gap g. It can be noted that, all the ratio R curves increase with the waveguide gap, and the waveguide with larger GSST thickness will have larger coupling length ratio R with a given waveguide gap, g. Considering the desire coupling length ratio R = L_c^{AM}/L_c^{CR} = 2, can be achieved at T = 20 nm with g = 125 nm, T = 15 nm with g = 157 nm and T = 10 nm with g = 204 nm, respectively. The ratio R with T = 15 and 20 nm for W_1 = 500 nm are also shown by dashed lines for comparison in Fig. 7.19. For a give waveguide gap like g = 120 nm, the directional coupler has smaller input Si nanowire width W_1 will have the smaller coupling length ratio R. It can also be noted that, for a given GSST thickness like T = 15 nm, the directional coupler has smaller input Si nanowire

width need longer waveguide gap to achieve the desire ratio R = 2. Moreover, if the waveguide gap, g is fixed at the range from 100 to 200 nm, the GSST layer, T = 10 and 15 nm can be chosen for W_1 = 500 nm and the 15 or 20 nm GSST layer can be chosen for W_1 = 450 nm.

In order to achieve the desire coupling length ratio $R = L_c^{AM}/L_c^{CR} = 2$, the larger Si width W_1 can be chosen if the directional coupler need shorter waveguide gap, the larger W_1 also can be chosen as the corresponding GST thickness, T can be taken at wider range from 6.8 to 17.5 μm with the g from 100 to 200 nm, while the T only can be taken from 10 nm to 20 nm for W_1 = 450 nm. For the ease and flexibility of fabrication process, the width of the input Si nanowire W_1 = 500 nm will be considered, and its waveguide parameter sets for desire ratio R = 2 will be used for propagation characteristics studies.

7.4 Propagation and power transfer characteristics

To verify the proposed design, with the desire coupling length ratio $R = L_c^{AM}/L_c^{CR} = 2$, evolution of optical power along the directional coupler propagation direction has been studied by using the FDTD method. When the GSST is triggered at amorphous state, for the optimal parameter set (R = 2 with T = 10.6 nm and g = 150 nm), the field distribution of Si nanowire (WG1) and GSST-loaded Si waveguide (WG2) based directional coupler (top-view) along the propagation direction Z are shown in Fig. 7.20.

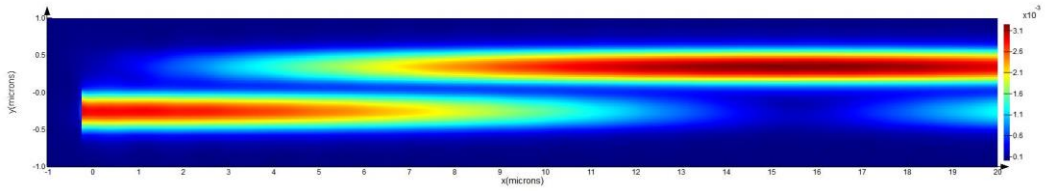

Fig. 7.20. Field distribution of WG1 and WG2 based directional coupler (top-view) at GSST amorphous state for "OFF" state of switch.

It can be noted that, the input field introduced at WG1 port I_1 have transferred completely into the WG2 after propagating a coupling length L_c^{AM} distance. This is because the WG1 and WG2 is strongly phase matched, so that the input light can

be coupled from WG1 to WG2 completely then continue propagate to attain the "OFF" state of the optical switch.

7.4.1 Transmittance of the launching ports

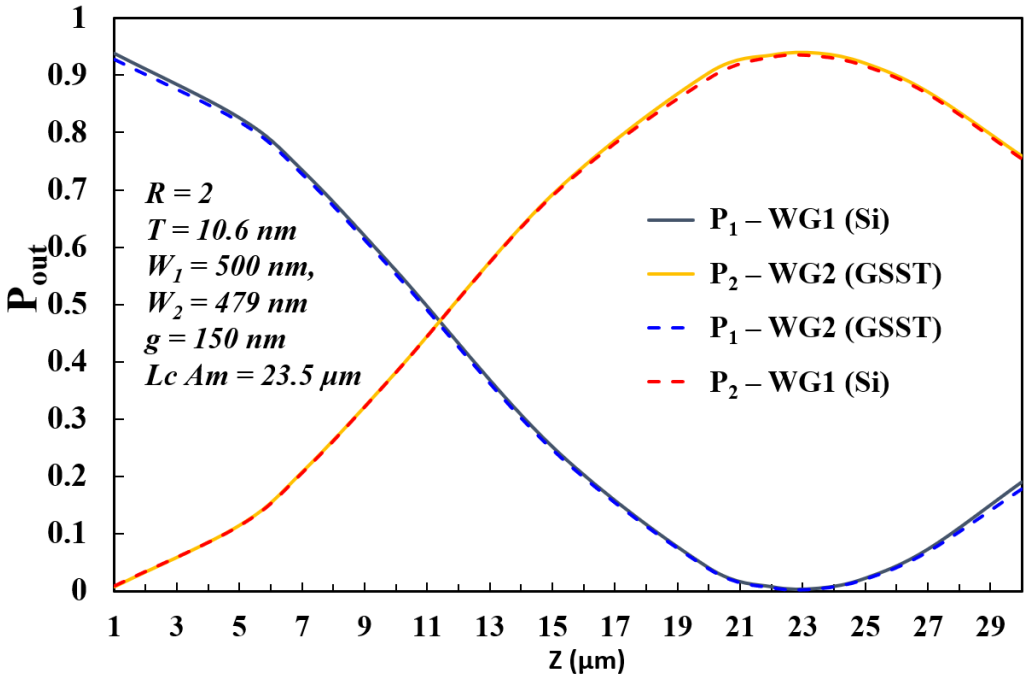

Fig. 7.21. Power transfer, P_{out} with the power launching at I_1 and I_2 for the case R = 2 (T = 10.6 nm, g = 150 nm) along the propagation direction Z.

The output power evolutions between WG1 and WG2 along the propagation direction Z are also shown in Fig. 7.21. When the GSST in amorphous state and the input light is launched at the WG1 port I_1 (shown in Fig. 7.1), the output power at the WG1 and WG2 along the Z direction is shown by solid dark blue and orange lines, respectively. It can be observed that the output power (P_1) at WG1 reduce gradually from 0.94 at Z = 1 µm to the minimum 0.0045 at Z = L_c^{AM} = 23.5 µm, meanwhile the output power (P_2) at WG2 increase gradually from 0.0077 at Z = 1 µm to the maximum 0.939 at Z = L_c^{AM} = 23.5 µm. It can be noted that, a maximum power transfer from the WG1 to WG2 can be achieved for the GSST amorphous state, and there is approximately 94% of power is transferred at the desire coupling length distance which is agreed with the FV-FEM simulation.

For comparison, the input light is also launched at the WG2 port I_2, the output power at the WG1 and WG2 along the Z direction is shown by dashed blue and red

lines, respectively. It can be observed that, when the input power is launched at I_2, there is still a complete power transfer from the WG2 to the WG1 when GSST at amorphous state, however the output power at the input WG2 is always lower than when the WG1 as input waveguide since there is a significantly modal mismatched between the input WG1 and WG2 leads to a junction loss at the discontinuity interface. At Z = L_c^{AM} = 23.5 µm, there is approximately 93.3% of power is transferred from GSST-Si waveguide to the Si nanowire, slightly lower than the case when the input power was launched at the WG1 port I_1.

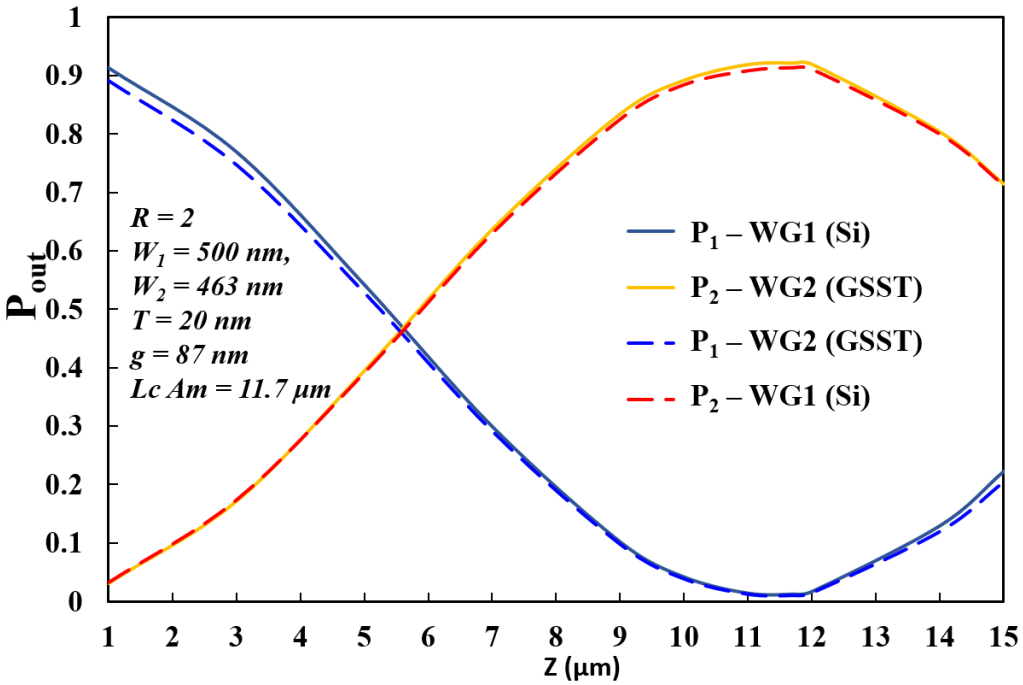

Fig. 7.22. Power transfer, Pout with the power launching at I_1 and I_2 for the case R = 2 (T = 20 nm, g = 87 nm) along the propagation direction Z.

If the GSST thickness, T increase to 20 nm, the desire coupling length L = L_c^{AM} = $2L_c^{CR}$ will become shorter to 11.7 µm, and the power transfer of the two waveguides also will be varied. The output power evolutions at Si nanowire WG1 and GSST-loaded Si waveguide WG2 (T = 20 nm) along the propagation direction Z are shown in Fig. 7.22. When the input power is launched at the WG1 port I_1, the output power at the WG1 and WG2 along the Z direction is shown by solid blue and orange lines, respectively. It can be observed that that the output power (P_1) at Si nanowire reduce gradually from 0.91 at Z = 1 µm to the minimum 0.01 at Z = L_c^{AM} = 11.7 µm, meanwhile the output power (P_2) at GSST-Si waveguide increase

gradually from 0.03 at Z = 1 µm to the maximum 0.92 at Z = L_c^{AM} = 11.7 µm. It can be noted that, and there is approximately 92% of power is transferred at the desire coupling length Z = L_c^{AM} position which is slight lower than the case of T = 10.6 nm. The output power at the WG1 and WG2 along the Z direction when input light is launched at the WG2 port I_2 shown by dashed blue and red lines, respectively. The output power in WG2 at Z = 1-5 µm have the larger difference compare to the output power in WG1 (power input form I_1), because the GSST layer increase to 20 nm, there is a larger junction loss at the interface. On the other hand, the output power at the WG1 also have the difference when the input light propagates near the coupling length region, the maximum transferred power at the position Z = L_c^{AM} in WG1 is slightly smaller than output power in WG2 (power input form I_1).

It can be concluded that, no matter the input light is launched at the WG1 port I_1 or the WG2 I_2, both the waveguides can complete a power transfer, but it is slightly better launching the light at the Si nanowire WG1 I_1 due to at the desire coupling length position Z = L_c^{AM}, it can achieve the larger maximum power at WG2 also the smaller minimum power in the WG1 to perform a better power transfer.

7.4.2 Optical power evolutions for R =2

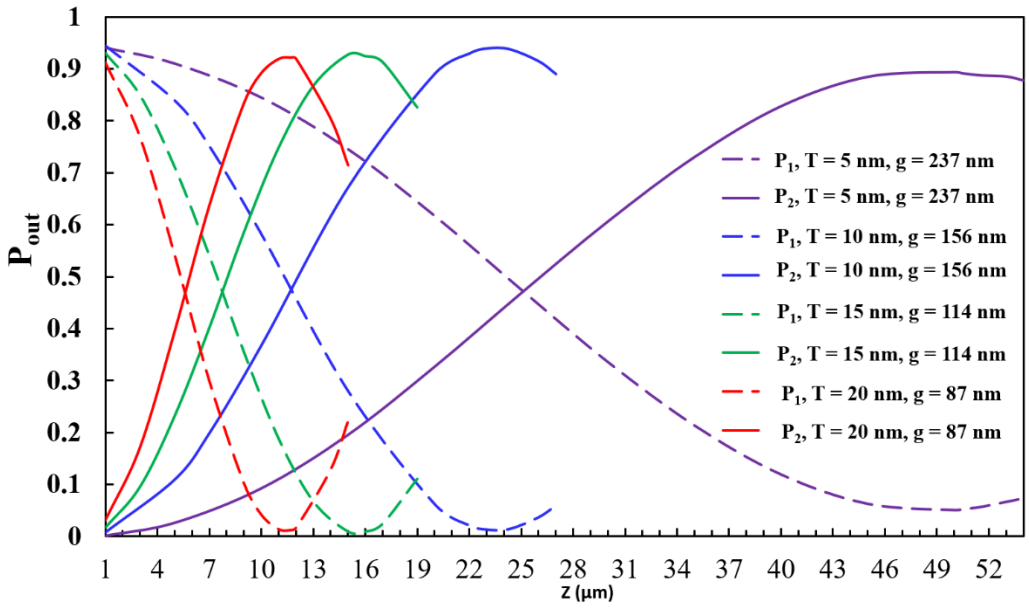

Fig. 7.23. Power transfer, P_{out} at Si nanowire and GSST-Si waveguide with R = 2 set (T = 5, 10, 15, 20 nm) along the propagation direction Z.

As state above, in this section, the input light is launched at the WG1 port I_1, the power transfer for the coupling length ratio (R = 2) with the GSST thickness, T = 5, 10, 15 and 20 nm along the propagation direction at GSST amorphous state are shown in Fig. 7.23. The output power (P_1) in WG1 are shown by dashes lines reduce smoothly from the higher around 0.9 at Z = 1 µm, reduce to lower than 0.1 at its own coupling length position. While the output power (P_2) in WG2 shown by solid lines increase moderately from lower 0.01 to its maximum at the coupling length position. It can be observed that, although the smaller GSST thickness can achieve a higher power at the start Z = 1 µm, and yield a longer coupling length, however, its maximum power and minimum power at the coupling length position is smaller than the others, which means the power transfer is not efficient due to the long device length. The other three GSST thickness cases, all achieve a complete power transfer, can achieved their maximum power transfer at the desire distance $Z = L_c^{AM} = 2L_c^{CR}$. The insertion loss and extinction ratio of the directional coupler will be investigated later for comparison.

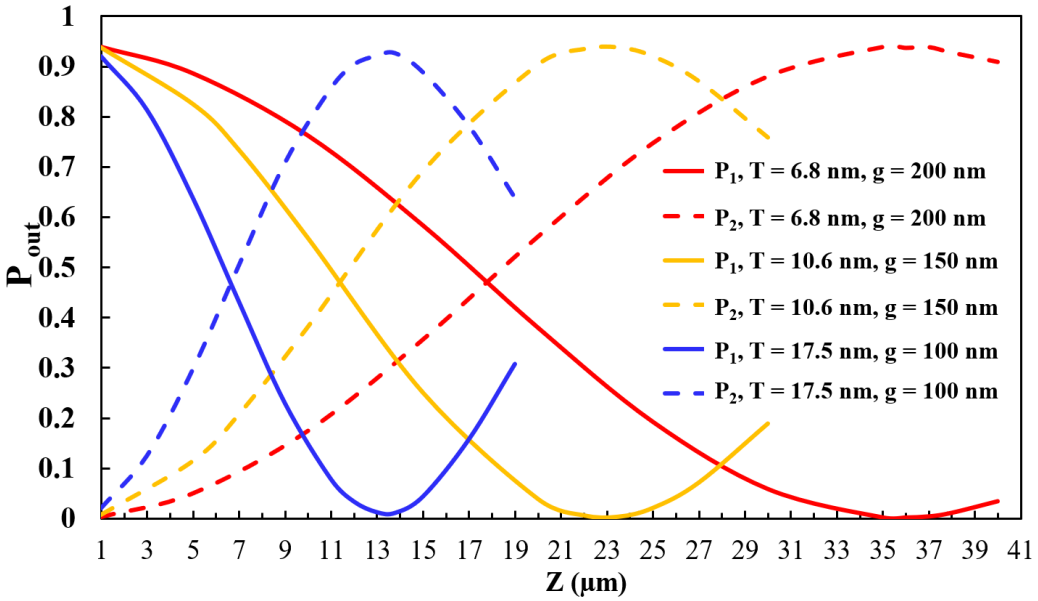

Fig. 7.24. Power transfer, P_{out} at Si nanowire and GSST-Si waveguide with R = 2 set (g = 100, 150, 200 nm) along the propagation direction Z.

In order to study the effect of the waveguide gap to achieve the desired ratio, the power transfer for the desire ratio R = 2 with the integer waveguide gap (g = 200 nm, T = 6.8 nm, g = 150 nm, T = 10.6 nm and g = 200 nm, T = 6.8 nm) along the

propagation direction are calculated and shown in Fig. 7.24. It can be observed that, the output power (P_1) in the WG1 are shown by solid lines decrease monotonically to their own coupling length position at Z = 13.8, 23.5, 37 µm, respectively to get the minimum power then turn arise with the propagation distance increase. On the other hand, the output power (P_2) in the proximity WG2 shown by dashed lines, increase to their peak values at the position $Z = L_c^{AM}$ then decrease with the increase of the propagation distance.

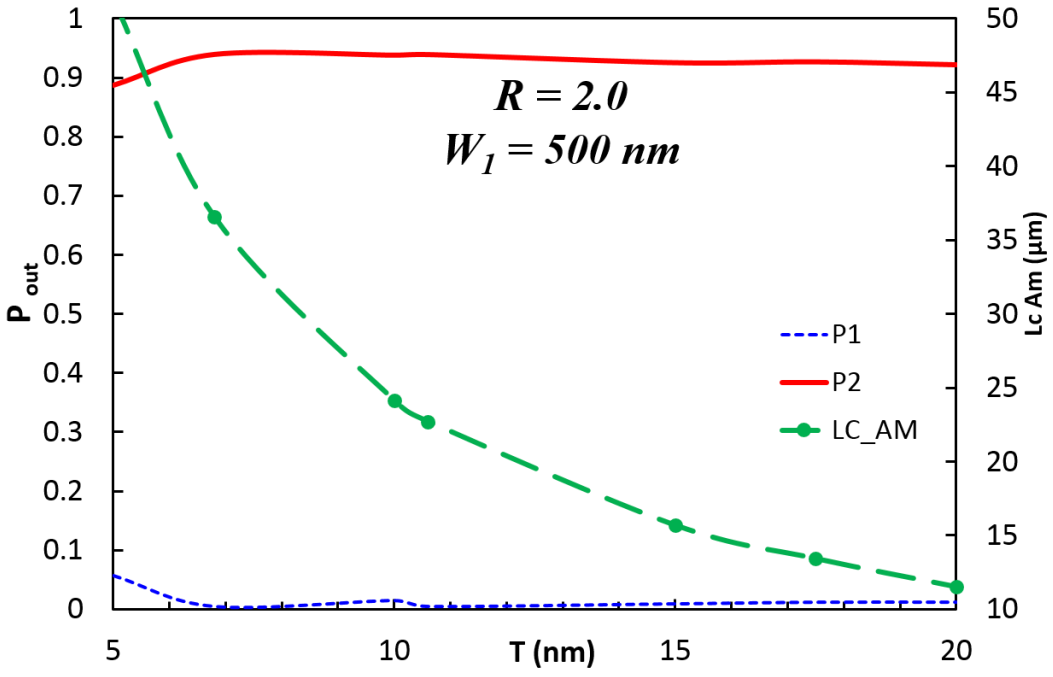

Fig. 7.25. The maximum and minimum output power, P_{out} of Si nanowire and GSST-Si waveguide at the coupling length position $Z = L_c^{AM}$ and coupling length L_c^{AM} as a function of the GSST thickness, T.

As the power transfer efficiency is a key objective of the directional coupler performance, the desire directional coupler waveguide parameters (R = 2) need to be studied and optimised to achieve the better power transfer efficiency. The maximum output power (P_2) in GSST-loaded Si waveguide WG2 with the desire ratio parameters at the coupling length position $Z = L_c^{AM}$ are shown by a solid red line in Fig. 7.25. It can be observed that the maximum output power increase from 0.88 when GSST thickness T = 5 nm then level off at 0.92 with the T increase to 20 nm. The corresponding minimum output power (P_1) in the Si nanowire WG1 at $Z = L_c^{AM}$ with the R = 2 parameters are shown by a dashed blue line, it can be noted

that there is only 5% output power when T = 5 nm, then reduces to 1% when T increase from 5 nm to 20 nm. The coupling lengths L_c^{AM} are shown by a dashed green line using the right-hand scale, and the desire coupling length ratio R = 2 parameters also shown by the solid circles on it.

It can be noted that, for GSST thickness, T larger than 10 nm, a desire coupling length lower than 25 µm can be achieved with the sufficient power transfer between the WG1 and WG2 could be accepted as an optimal design for a compact directional coupler.

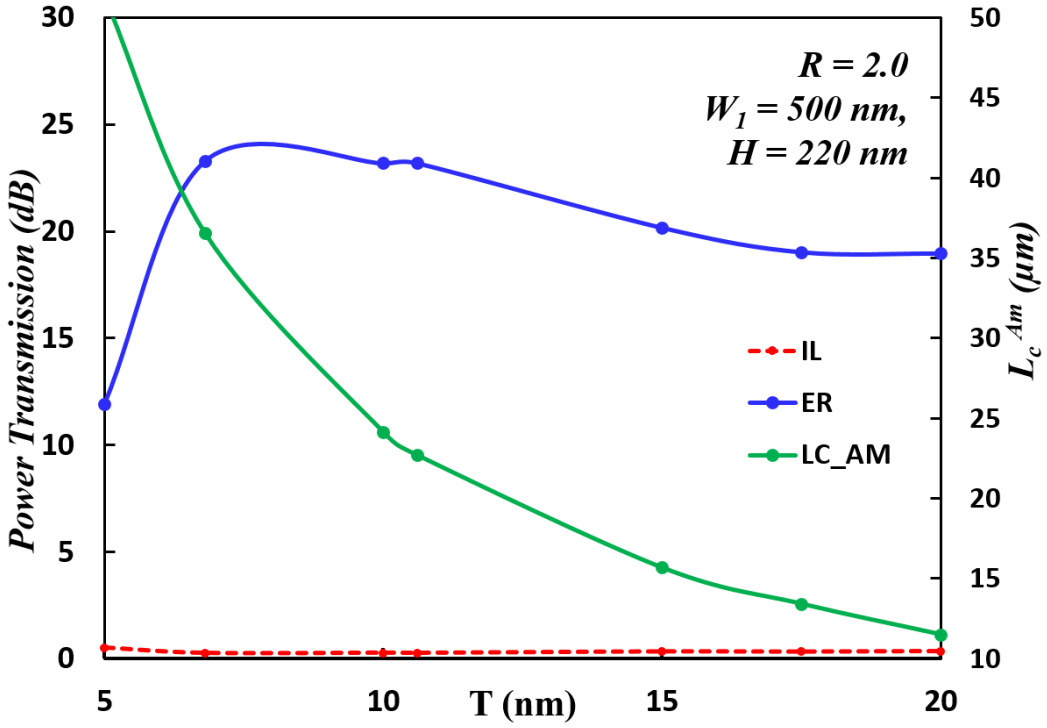

Fig. 7.26. Variations of the insertion loss, extinction ratio and coupling length L_c^{AM} of the directional coupler as a function of the GSST thickness, T at GSST AM state.

In order to characterize the proposed directional coupler based 1 x 2 optical switch, the insertion loss (IL) and extinction ratio (ER) at "OFF" or "ON" state are calculated based on the formulas:

$$IL_{OFF} = -10\log_{10}\left(\frac{P_{O2}}{P_{I1}}\right) \qquad IL_{ON} = -10\log_{10}\left(\frac{P_{O1}}{P_{I1}}\right) \tag{7.1}$$

$$ER_{OFF} = -10\log_{10}\left(\frac{P_{O2}}{P_{O1}}\right) \qquad ER_{ON} = -10\log_{10}\left(\frac{P_{O1}}{P_{O2}}\right) \tag{7.2}$$

P_{I1} is the input power at port I_1, P_{O1} and P_{O2} are the output power at the Si nanowire and GSST-Si waveguide, respectively.

At the operation wavelength 1550 nm, the variations of the insertion loss and extinction ratio of the desire coupling length ratio R = 2 directional coupler based 1 x 2 optical switch at GSST amorphous state is calculated by FDTD and shown in Fig. 7.26. It can be observed that, the insertion loss shown by a dashed-red line reduce from 0.5 dB at T = 5 nm, then bottom out at 0.3 dB with the T increase to 20 nm. While the extinction ratio shown by a solid-blue line, increase from 12 dB to a relevant peak level around 23 dB with the GSST thickness, T increase from 5 to 10 nm. After that, the extinction ratio reduces gradually to 20 dB with the T increase from 10 to 20 nm. The desire coupling length $L_c^{AM} = 2L_c^{CR}$ also shown by a solid-blue line by using right-hand scale. It can be concluded that, the desire directional coupler (R =2) with compact coupling length L_c^{AM} = 11.7-24.7 µm, T = 10-20 nm and g = 87-156 nm can be the optimal design for an optical switch with 0.28-0.35 dB insertion loss and 19-23 dB extinction ratio at "OFF" state.

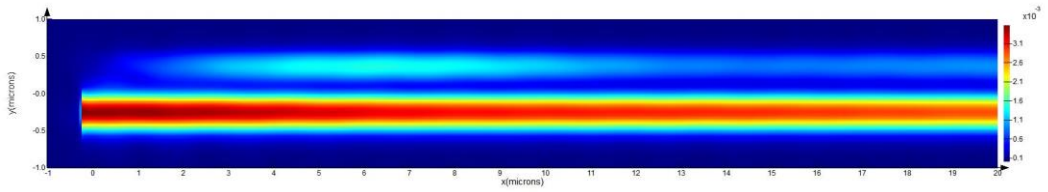

Fig. 7.27. Field distribution of WG1 and WG2 based directional coupler (top-view) at GSST crystalline state for "ON" state of the switch.

On the other hand, it is also necessary to study the power transfer between input Si nanowire WG1 and GSST-loaded waveguide WG2 to attain the "ON" state of the proposed optical switch. The optimised case (W_1 = 500 nm, W_2 = 471 nm, T = 15 nm, g = 114 nm and $L_c^{CR} = L_c^{AM}/2$) is chosen for the device "ON" state simulation when GSST in crystalline state. The field distribution of WG1 and WG2 based directional coupler (top-view) along the propagation direction Z are shown in Fig. 7.27. It can be noted that, when the GSST crystalline state is triggered, the mode coupling between the WG1 and WG2 can be neglected due to the phase-mismatching. Hence, the input light propagates along the Si nanowire WG1 and outputs at O_1.

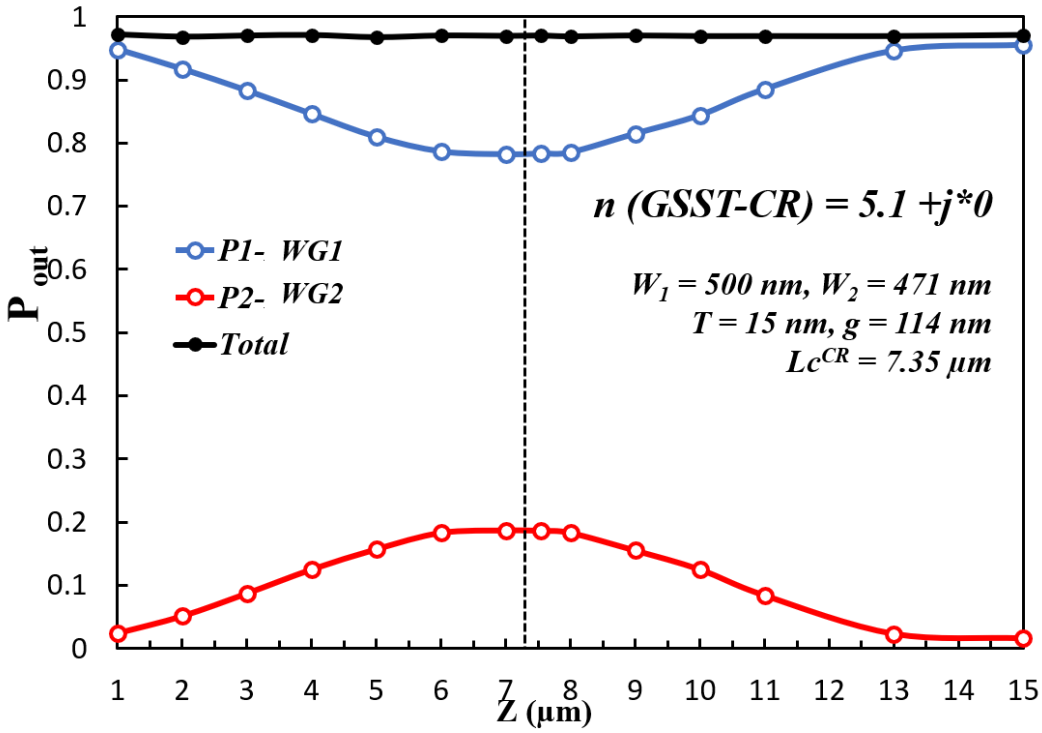

Fig. 7.28. Power transfer, P_{out} at WG1 and WG2 with the desired R = 2 (T = 15 nm, g = 114 nm) when GSST in CR state (n = 5.1) along the propagation direction Z.

Initially, the imaginary part of the refractive index of GSST is neglected and taken as n (GSST-CR) = 5.1 for investigating the power transfer of the directional coupler when there is no modal loss. The power transfer of the WG1 and WG2 with the optimal case without the modal loss are shown in Fig. 7.28. The output power of WG1 (P_1) is shown by a solid blue line decrease smoothly from the 0.95 to a minimum value 0.78 around the $Z = L_c^{CR}$ region then increase back to the higher 0.95 when the light propagates to the Z =14.7 µm = $2L_c^{CR}$. On the other hand, the output power of WG2 (P_2) is shown by a solid red line increase slightly from the 0.024 to a maximum value 0.187 around the $Z = L_c^{CR}$ region then drop back to 0.02 when the light propagates to the $Z = 2L_c^{CR}$. This is due to the refractive index of the GSST (n = 5.1) still higher, the propagation constant of WG1 and WG2 is strongly mismatched, not much power can be transferred and at $Z = L_c^{CR}$. However, as it can be observed that 22% power can still be transferred at $Z = L_c^{CR}$ position, so we had considered an innovative approach to have $L = L_c^{AM} = 2L_c^{CR}$, so that whatever power is coupled, the transferred power will return to WG1. The total output power of the directional coupler shown by a black line remains constant near 0.97 only

owing to the junction loss at the discontinuity interface and slightly propagation loss.

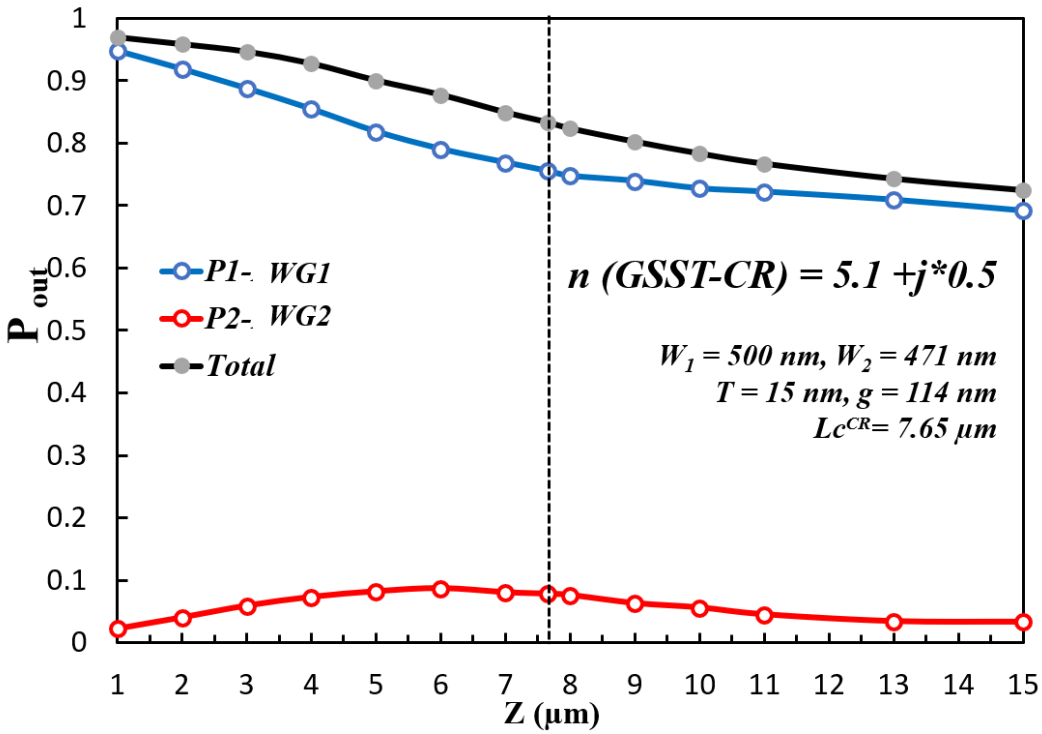

Fig. 7.29. Power transfer, P_{out} at WG1 and WG2 with the desired R = 2 case (T = 15 nm, g = 114 nm) when GSST in CR state (n = 5.1+ 0.5*j) along the propagation direction Z.

Next, the imaginary part of the refractive index of GSST is included and taken as n (GSST-CR) = 5.1 + *j**0.5, the power transfer of the WG1 and WG2 of the optimal case (T = 15 nm) with the GSST absorption loss are shown in Fig. 7.29. The output power of WG1 (P_1) is shown by a blue line decrease monotonically from the 0.95 to a low value 0.75 around the Z = L_c^{CR} region then continue reducing but slowly to a lower value 0.69 when the light propagates to the Z = $2L_c^{CR}$. On the other hand, the output power of WG2 (P_2) is shown by a red line increase slightly from the 0.022 to a maximum value 0.08 around the Z = L_c^{CR} region then decrease to the lower value around 0.03 when the light propagates to the Z = $2L_c^{CR}$. It can be noted that as the GSST absorption loss is introduced, it has significantly suppression of the mode coupling and power transfer between the WG1 and WG2. So that the total output power of the directional power shown by a black line will decrease monotonically from 0.97 to 0.69 at the output port O_1 when Z = $2L_c^{CR}$.

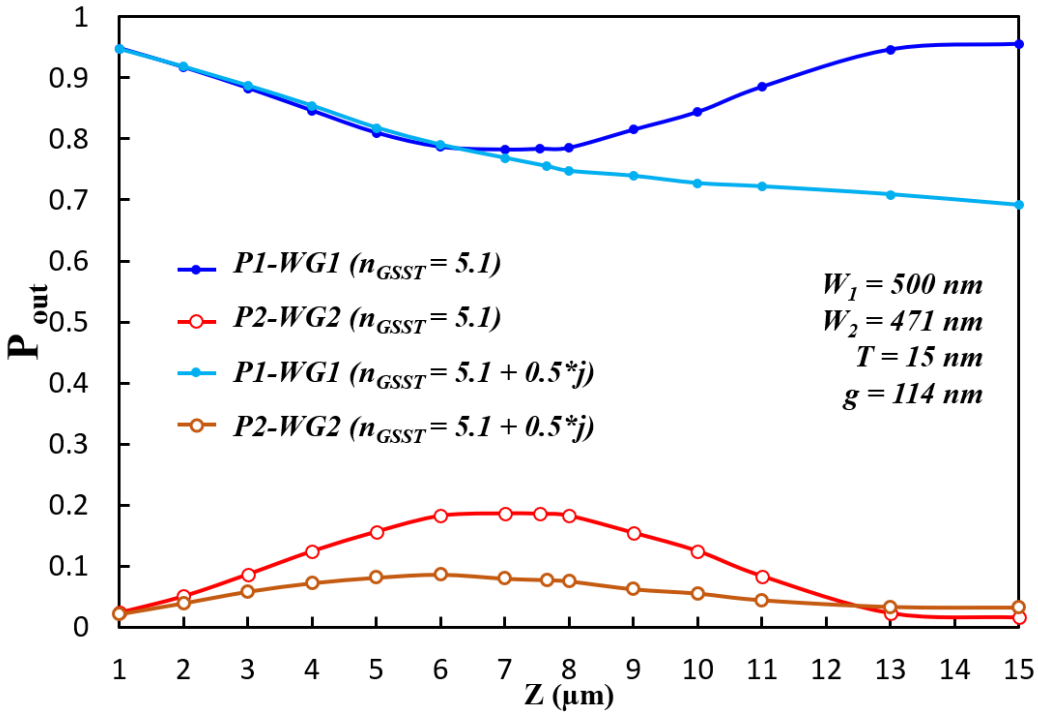

Fig. 7.30. Power transfer, P_{out} at WG1 and WG2 for the desired R = 2 case (T = 15 nm, g = 114 nm) when GSST in CR state with refractive index (n = 5.1) and (n = 5.1+ 0.5*j) along the propagation direction Z.

Additionally, the power transfer of the WG1 and WG2 of the optimal case (T = 15 nm, g = 114 nm) with and without the GSST modal loss in crystalline state are plotted in Fig. 7.30 for comparison. For the output power in WG1, it can be noted that the waveguide has the GSST modal loss can achieve slightly higher output power before Z = 6 µm, after that, the waveguide has the GSST absorption loss always lower than the waveguide without absorption loss. For WG2, it can be noted that the waveguide has the GSST absorption loss have smaller output power and variations compare to the waveguide have no modal loss before Z = 12.5 µm. After that, the waveguide has the GSST absorption loss can achieve slightly higher output power. As the optimised device length of the proposed optical switch is designed with desire ratio R = 2, so that the insertion loss of the "ON" state of the device needs to be calculated at the port O_1 ($Z = L_c^{AM} = 2L_c^{CR}$ position).

It can be noted that, although GSST crystalline introduce higher absorption loss, but for the particular parameter case, the total insertion loss and extinction ratio of the optical switch at "ON" state ("bar" state) are calculated as 1.6 dB and 12.73 dB,

respectively, at the device output position ($Z = L_c^{AM} = 2L_c^{CR}$). which is still acceptable for the low-loss optical switch design.

7.4.3 Fabrication process and fabrication tolerances

The fabrication process of the directional coupler can be completed in following steps. The directional coupler can be fabricated on a SOI wafer with a 220-nm thick Si layer and a 3-µm thick buried oxide layer. The wafer can be spin-coated with e-beam resist and prebaked for 3 mins at 180 temperature. Then the e-beam lithography will be used to define the Si waveguide patterns. The pattern was transferred to Si layer with inductively coupled plasma (ICP) dry etch and the residual e-beam resist is removed. The GSST deposition window was opened using the second e-beam lithography process, then the GSST film will be sputtered on the wafer using am RF sputtering system. After that, the lift-off process is used to remove the GSST outside the deposition window in a warm acetone bath. At last, a SiO_2 layer could be deposited on top of the waveguides, to act as a cladding layer.

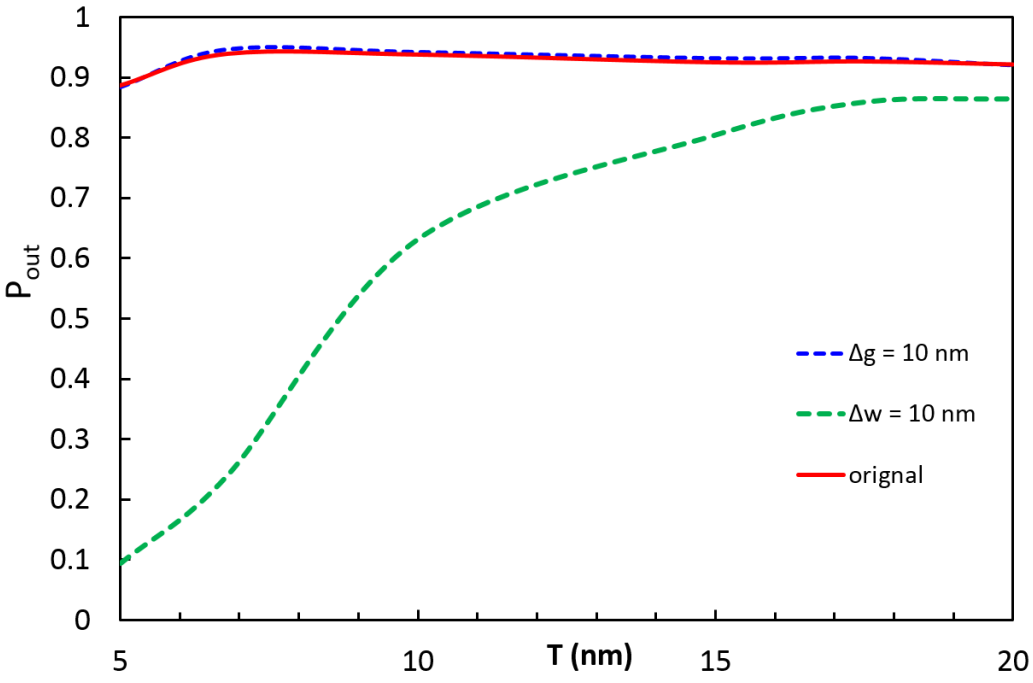

Fig. 7.31. Power transfer, Pout of the GSST-loaded Si waveguide at the coupling length position $Z = L_c^{AM}$ with the case: (g + 10 nm), (W_2+10 nm) and the desire R = 2 as a function of the GSST thickness, T at GSST AM state.

A fabrication-tolerant directional coupler is of great importance to guarantee the performance in practice. The fabrication tolerances of the proposed directional coupler with coupling length ratio R = 2 are also investigated with respect of the change of waveguide gap, g and the width of WG2, W_2, respectively. Variations of the output power in the WG2 with the change of the waveguide gap, g and W_2 also the original optimal parameter set (R = 2) at GSST amorphous state are shown in Fig. 7.31. It can be noted that with a +10 nm change of waveguide gap g shown by a blue-dashed line, the deteriorations of the output power less than 0.01 with the GSST thickness increase from 5 to 20 nm so that the influence of the waveguide gap g can be neglected.

On the other hand, with a +10 nm change of the GSST-Si waveguide width W_2, the output power in the GSST-Si bus waveguide is shown by a dashed-blue line. It can be observed that, the output power increase from 0.1 to 0.85 with the GSST thickness T increase from 5 to 20 nm. The deteriorations of the output power are significantly large more than 0.8 then reduce to 0.1 with the GSST thickness increase from 5 to 15 nm due to the phase matching condition between the two waveguides is not satisfied with changed W_2, so that the input TE_0 mode of WG1 cannot propagate and transferred to the GSST-Si waveguide WG2. However, if the GSST thickness is taken at 15-20 nm, the deteriorations of the output power less than 0.1 could be acceptable level for the desire device design.

7.5 Summary

In summary, a non-violate 1 x 2 optical switch based on a two-waveguide directional coupler has been proposed in this chapter, which consists of an input Si nanowire WG1 and a GSST loaded Si-bus waveguide WG2. The input light at WG1 can be transferred to the bus-waveguide WG2 to attain "OFF" state of the switch at GSST amorphous state, while the input light only propagates along the WG1 without mode coupling with WG2 to attain "ON" state at GSST crystalline state.

The modal solution and phase matching conditions of the directional coupler when GSST in amorphous state has been calculated by using the FV-FEM. In order to achieve the desire coupling length ratio $R = L_c^{AM}/L_c^{CR} = 2$, the effect of GSST thickness (T), the input Si nanowire width W_1 and waveguide gap (g) are investigated. Seven combination waveguide parameter sets with GSST thickness, T = 5-20 nm and waveguide gap, g = 87-237 nm, have been obtained for the desire R = 2 directional coupler structure.

To verify the validity of the desire directional coupler design, the field distribution, launching port accuracy, output power transfer, and the fabrication tolerance of the desire waveguide parameter sets are calculated by using the 3D-FDTD. It can be concluded that, for a desire coupling ratio R = 2 design with T = 15-20 nm and g = 87-114 nm, a compact and tolerant 11.7-16 μm long directional coupler based 1 x 2 optical switch shows a high extinction ratio of 19-20 dB with the insertion loss only 0.33-0.35 dB at "OFF" state.

Chapter 8

Conclusion and future work

8.1 Conclusion

The research focus has been on the design, characterisation and optimisation of the Si-PCM integrated waveguides for optical modulating and switching. The aim set out at the start of the research have been successfully achieved and presented in this thesis. The objectives of this research were to rigorously characterise the Si-PCM hybrid waveguides for applications in photonic devices and study their propagation properties by using accurate and efficient numerical methods.

The basic and fundamental knowledge of the numerical methods which were used in this thesis are presented in Chapter 3. The FEM is more advantageous than other numerical methods as it can consider any arbitrary shaped waveguide. The **H**-field formulation has several advantages over the other formulations to setup a FEM code as it can be applied for general anisotropic problems and its natural boundary condition is the perfect electric wall, which can be left free for any arbitrary shaped boundary wall. Thus, a full-vectorial **H**-field based FEM can be used to study the Si-PCM hybrid waveguides with multi-layers. The implementation of the FV-FEM including the domain discretisation, shape functions, natural boundary conditions and the global matrices formulation are also evaluated. The LSBR method is also studied for analysing the discontinuities in optical waveguides. By combining the FV-FEM with LSBR, the coupling loss between two waveguides at butt-coupled junctions are calculated. The 2D FV-FEM only implemented to simulate the

fundamental light guiding phenomenon at a waveguide cross-section. However, this approach is incapable to modelling optical modulator or switch as a whole device to verify the device performance. Thus, a three-dimensional approach was required to solve the problem. A commercial 3D-FDTD (Lumerical) based code is implemented for studying the light propagation, power transfer and mode conversion characteristics of the device in this thesis.

In Chapter 4, a GST-clad Si rib waveguide is designed and applied for a 1x1 modulator with a GST-clad Si nanowire for design comparison at the 1.55 μm telecommunication wavelength. The phase transition of GST could be triggered by annealing in this case. In order to improve simulation accuracy, the refractive index of GST measured by ellipsometer was used so that simulation results can be compared with experimental results by our research collaborators. It has shown that both GST-clad Si waveguides have a strong ER and EA effect, however, a 18-20 dB modal loss for the crystalline will cause incomplete power cancellation and thus a poor extinction ratio in the ER design. On the other hand, EA-type design is preferred, and the device is designed with a 20 dB extinction ratio. The total insertion loss of the device comprises of the modal loss in the GST-clad Si waveguide section and the coupling loss at the input/output junctions. The Si core width is chosen at 500 nm, as it not only yields a short device length but also a smaller modal loss. The Si slab thickness is optimised at 60-90 nm as it can balance the device length and junction loss in the amorphous state so that achieve a lower total insertion loss. The GST clad thickness is considered between 15-25 nm as the thicker GST layer not only yield short device length but also lower modal loss and if GST thickness more than 25 nm, it is likely producing unstable junction loss for the crystalline state. Additionally, the GST-clad Si rib waveguide structure is preferred, because the Si nanowire always suffer from higher modal loss and junction loss thus higher total insertion loss. The simulated modal loss results are slightly lower than the experimental results in the GST amorphous state which is probably due to the additional scattering loss caused by surface roughness of the GST layer. It can be concluded, a self-sustained 1 x 1 modulator with only 0.36 dB insertion loss and more than 20 dB extinction ratio can be achieved by the optimised

design combination as: a GST-clad Si rib waveguide with 500 nm Si width, 60-90 nm Si slab thickness and 15-25 nm GST clad thickness.

In Chapter 6, a new low-loss phase change material GSST is introduced, it can be derived in GST alloy by partially substituting Te with Se, which increase the optical bandgap, so that reduce the material loss at the 1550 nm wavelength. We use the similar device design as Chapter 4, but the full GST layer is replaced by a GSST cap loaded on the Si rib waveguide for analyses and comparison. It was shown that, for the ER design, a 4-7 dB modal loss in crystalline can be achieved with 2-10 nm GSST layer allow a possible MZI type design, however the device needs to be more than 20 μm long which make it less attractive. Hence, the 20 dB EA-type is chosen for the effective device design and enhanced by GSST layer and Si slab thickness. In this case, the coupling loss at the junctions between the access and active waveguides is a dominating fraction in the total insertion loss. The GSST layer is optimised at 40-60 nm clad thickness as it not only yields a compact device length short than 5 μm, but also achieve a lower 0.132 to 0.266 dB junction loss. The Si slab thickness is taken between 60 to 90 nm as the optimal design due to the total insertion loss has the smallest change in this region. It can be concluded that, a GSST-clad Si rib waveguide with 500 nm Si width, 60-90 nm Si slab thickness and 40-60 nm GST clad thickness can be considered as the optimal design. An insertion loss only 0.135 dB, which is 38% of the GST based design, as shown in Chapter 4 and with a 4.75 μm device length shows a great potential for present optical modulator design. Moreover, the proposed design is verified by the FDTD simulation, the total power loss of the fundamental quasi-TE mode is more than 20 dB agreed with the FV-FEM modal solutions. However, total optical loss of the device was 16 dB due to generation and reconversion of the higher order modes.

A novel design of co-directional coupling between a Si nanowire and ITO-GST-ITO waveguide at the 1.55 μm wavelength is also designed and optimised for a ON-OFF electro-optic switch in Chapter 5. In this chapter, the GST phase transition is assumed to be triggered by applying the electric field via the ITO electrodes. The effect of ITO spacing thickness and GST layer thickness on the Si-GST composite waveguide modal solution is studied by using FV-FEM. The ITO spacing is optimised at 75 nm as it was less sensitive to the device length around 1-2 μm so

that offering better tolerance. The GST thickness is optimised at 25.6 nm for the phase-matching point in order to efficiency transfer power from lower Si nanowire to the upper GST waveguide to attain "OFF" state and a compact 1.7 μm coupling length can be achieved. Once the device is phase matched in crystalline state, the light in the amorphous state will propagate along the Si nanowire with minimal interaction with GST waveguide to attain "ON" state. It also has shown that at the phase-matching condition, the even and odd supermodes are excited with the same 50% excitation coefficient at the input Si nanowire and composite waveguides interface shows a strong coupling. Additionally, the device performance is evaluated by FDTD simulation, it has shown that only 0.5% power for crystalline state and 88% power for amorphous state as "ON" state for a 1.7 μm long device, which means the waveguide is phase matched and agreed with FV-FEM simulations. It can be concluded that, a compact 1.7 μm long electro-optic switch shows a lower insertion loss only 0.56 dB with a higher extinction ratio of 22 dB.

Finally, in Chapter 7, a two-waveguide asymmetrical directional coupler which consists of a GSST-loaded Si waveguide and a standard Si nanowire is also designed and optimised for a sustained 1 x 2 optical switch. For the 500 nm width Si nanowire, the phase-matching condition of the Si-GSST waveguide (Amorphous state) width is calculated as 463 nm due to these two isolated waveguides can achieve matched propagation constant so that the light can efficiently transfer from the input Si nanowire to the Si-GSST waveguide to attain "OFF" state. If the GSST is triggered at crystalline state, the larger modal effective index will lead to a larger phase mismatch, the light will propagate along the input Si nanowire without any considerable interaction to the end. It has shown that, for a given GSST layer, the wider waveguide gap between two waveguides cannot change the crystalline state coupling length (Lc^{CR}) but can increase the amorphous state coupling length (Lc^{AM}), thus a desire ratio $R = Lc^{AM}/Lc^{CR} = 2$ can be introduced for directional coupler design. The effect of Si nanowire width, Si layer height and GSST thickness on the desire coupling length ratio are studied, it was identified that the Si height have less effect on the R and the smaller width is limited as it need combine with 10-20 nm GSST thickness to achieve R = 2. Seven waveguide parameter combinations with 5-20 nm GSST thickness and 87-237 nm waveguide gap were

considered for the target R = 2 directional coupler design. The propagation characteristics of the directional coupler are also investigated by FDTD, it can be noted that swapping the light launching ports didn't change the power transfer between two waveguides, only a little power will be lost when the light is launched from Si-GSST waveguide. For the proposed R = 2 design, all the optimised waveguides have sufficient power transfer at the coupling length position. Moreover, the proposed directional coupler can achieve maximum power more than 90% also minimum residual power was lower than 1%, and the larger GSST thickness will yield short coupling length. Additionally, the GSST thickness is optimised at 15-20 nm which was less sensitive to the waveguide gap also the Si-GST waveguide width hence will show better tolerance for fabrication. In conclusion, an optimised waveguide parameter combination: 500 nm Si width, 15-20 nm GSST layer and 87-114 nm waveguide gap can be used to design a compact and tolerant 12-16 μm long (R = 2) directional coupler based 1 x 2 optical switch shows a high extinction ratio of 19-20 dB and an insertion loss only 0.33-0.35 dB at "OFF" or "Cross" state.

Overall, the phase change materials and particularly GST and GSST integrated with Si photonics are expected to play a significantly role in the short and long-term development of PICs, opening new front to promising applications.

Design, optimisations, and performance evolution of the Si-PCM composite waveguides is primary object of this thesis. Due to the PCM has its imaginary part of the refractive index, I have developed the modified FV-FEM code integrated with the perturbation analysis as a special modelling tool to simulate the 2D Si-PCM hybrid waveguide. By using this FV-FEM with perturbation technique, I have calculated the complex effective index of the proposed Si-PCM waveguide so that the corresponding propagation loss and device length can be achieved to choose the EA or ER effect. One the design is chosen, I simulated the Si-PCM waveguide with different waveguide parameters to find the relatively shorter device length and lower modal loss. Due to the 3D FDTD takes longer time and larger resource to simulate the whole device, I have integrated the FV-FEM with LSBR as a new 3D simulation tool to achieve the device insertion loss and extinction ratio which have

shown in Chapter 4,5 and 6. The simulation results of the device performance have been experimentally validated with our collaborator SJTU in Chapter 4, also benchmarked with the 3D FDTD simulation results in Chapter 5 and 6 which shows a good agreement. I also have designed a 1 x 2 optical switch based on a directional coupler with a new low loss PCM GSST. By using the FV-FEM, I have achieved several combination parameters sets to perform the directional coupler have a coupling length ratio R = 2 as the power can be transferred efficiently. I also have used the 3D FDTD to verify the directional coupler design by calculating the power transmission at specific position along the device. I also have calculated the power transfer at "ON" and "OFF" state of the device with the corresponding insertion loss and extinction ratio. At last, I have simulated the directional coupler with error parameters to check their influence on the power transmission so that a compact and fabrication tolerant optical switch can be achieved.

8.2 Suggestions for future work

It is difficult to explore and investigate all the aspects of the phase change material and its integration with Si photonics in such a short time. All the results presented in this thesis is considered as a small contribution of the on-going global research on integration and miniaturisation of the Si photonics devices.

It already has been reported that the GST suffers much lower loss in the longer wavelength band from 1800 nm to 2100 nm [63], and its extinction coefficient can be as lower as 0.006 and 0.4 for amorphous and crystalline state, respectively, at 2100 nm. Moreover, there is special interest in switching near 2000 nm because a new generation of hollow-core photonic fibre is developed for 1900 to 2100 nm wavelength and its transmission is increasing the information capacity of global fiber-optic networks. Thus, the Si-GST hybrid waveguide propagation loss can be reduced considerably in this wavelength band, also achieve a wider bandwidth of the photonic device.

For the directional coupler based optical switch design, three or four waveguide directional coupler can be designed and simulated, the GSST can be used as the active material in the middle or bus waveguide. The 1 x 2 optical switch can be

extended to 2 x 2 switch and may provide feasibility to attain the advanced N x N matrix switching network also with the self-holding and non-volatile features.

Moreover, the input and bus Si waveguide in the directional coupler can be replaced with Si rib and slot waveguides. Si rib waveguide can provide low optical loss due to reduced scattering loss and the edges and the simplification of etching at the fabrication process. The Si slot waveguide also be used in the directional coupler design, the phase change material can be deposited inside the horizontal slot of the bus waveguide. It has shown that the slot waveguide can guide and confine the light well in the slot region thus enhance the optical intensity of the waveguide. There are considerable interests to simulate a Si-PCM hybrid slot waveguide based directional coupler and compare the result with other type waveguides.

Furthermore, as we know the PCM phase transition can be triggered by thermally, electrically and optically. It is essential to study the dynamic phase transition process of the PCM and it could be simulated by Multiphysics software like COMSOL or Lumerical Device. For instance, by introducing a heater and the thermal and electrical parameters of the material in the simulation, the PCM phase transition tuning time and the require heating power can be achieved. And, the tuning time and heating power can be optimised by different heaters and their position. This thermal simulation can be combined with the FV-FEM simulation to give a strong improvement to experimental and fabrication of PCM integrated Si photonics devices.

Appendix

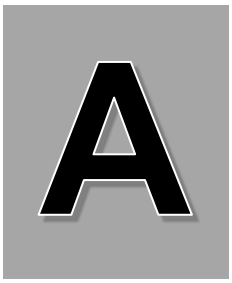

Calculation of Element Matrices

The element matrices of $[A]_e$ and $[B]_e$ from Eq. (3.27) and (3.28) can be evaluated as:

$$[A]_e = \varepsilon^{-1} \int_{xy} [Q]^* \cdot [Q] dxdy \tag{3.27}$$

$$= \varepsilon^{-1} \int_{xy} \begin{bmatrix} \beta^2 [N]^T [N] + \frac{\partial [N]^T}{\partial y} \frac{\partial [N]}{\partial y} & -\frac{\partial [N]^T}{\partial y} \frac{\partial [N]}{\partial x} & \beta [N] \frac{\partial [N]}{\partial x} \\ -\frac{\partial [N]^T}{\partial x} \frac{\partial [N]}{\partial y} & \beta^2 [N]^T [N] + \frac{\partial [N]^T}{\partial x} \frac{\partial [N]}{\partial x} & \beta [N] \frac{\partial [N]}{\partial y} \\ \beta [N] \frac{\partial [N]^T}{\partial x} & \beta [N] \frac{\partial [N]^T}{\partial y} & \frac{\partial [N]^T}{\partial y} \frac{\partial [N]}{\partial y} + \frac{\partial [N]^T}{\partial x} \frac{\partial [N]}{\partial x} \end{bmatrix} dxdy$$

$$(A.1)$$

$$[B]_e = \mu \int_{xy} [N]^T \cdot [N] dxdy \tag{3.28}$$

$$= \mu \int_{xy} \begin{bmatrix} [N]^T [N] & [0] & [0] \\ [0] & [N]^T [N] & [0] \\ [0] & [0] & [N]^T [N] \end{bmatrix} dxdy \tag{A.2}$$

The integration of the shape functions in Eq. (A.1) and (A.2) can be evaluated for a triangular element expression as:

$$\int_{xy} N_1^i \, N_2^j N_3^k \, dxdy = \frac{i!\, j!\, k!\, 2!}{(i+j+k+2)!} A_e \qquad (A.3)$$

Where A_e is the area of the triangular element.

Therefore, the numerical integration of different forms can be obtained as:

$$\int_{xy} N_1^2 \, dxdy = \int_{xy} N_2^2 \, dxdy = \int_{xy} N_3^2 \, dxdy = \frac{A_e}{6} \qquad (A.4)$$

$$\int_{xy} N_1 N_2 \, dxdy = \int_{xy} N_2 N_3 \, dxdy = \int_{xy} N_1 N_3 \, dxdy = \frac{A_e}{12} \qquad (A.5)$$

$$\int_{xy} dxdy = A_e \qquad (A.6)$$

Therefore, with the help of Eq. (3.20), some of the $[A]_e$ element matrix Eq. (A.1) can be obtained as:

$$[A]_{e(1,1)} = \varepsilon^{-1} \int_{xy} (\beta^2 N_1^2 + \left(\frac{\partial N_1}{\partial y}\right)^2) dxdy = \frac{1}{\epsilon}\left[\frac{\beta^2 A_e}{6} + c_1^2 A_e\right] \qquad (A.7)$$

$$[A]_{e(1,2)} = \varepsilon^{-1} \int_{xy} (\beta^2 N_1 N_2 + \frac{\partial N_1}{\partial y}\frac{\partial N_2}{\partial y}) dxdy = \frac{1}{\epsilon}\left[\frac{\beta^2 A_e}{12} + c_1 c_2 A_e\right] \qquad (A.8)$$

$$[A]_{e(1,3)} = \varepsilon^{-1} \int_{xy} (\beta^2 N_1 N_3 + \frac{\partial N_1}{\partial y}\frac{\partial N_3}{\partial y}) dxdy = \frac{1}{\epsilon}\left[\frac{\beta^2 A_e}{12} + c_1 c_3 A_e\right] \qquad (A.9)$$

$$[A]_{e(1,4)} = -\varepsilon^{-1} \int_{xy} \left(\frac{\partial N_1}{\partial x}\frac{\partial N_1}{\partial y}\right) dxdy = -\frac{1}{\epsilon} b_1 c_1 A_e \qquad (A.10)$$

$$[A]_{e(1,5)} = -\varepsilon^{-1} \int_{xy} \left(\frac{\partial N_2}{\partial x}\frac{\partial N_1}{\partial y}\right) dxdy = -\frac{1}{\epsilon} b_2 c_1 A_e \qquad (A.11)$$

$$[A]_{e(1,6)} = -\varepsilon^{-1} \int_{xy} \left(\frac{\partial N_3}{\partial x}\frac{\partial N_1}{\partial y}\right) dxdy = -\frac{1}{\epsilon} b_3 c_1 A_e \qquad (A.12)$$

And so on.

Similarly, the $[B]_e$ element matrix Eq. (A.2) can be obtained as:

$$[B]_{e(1,1)} = \mu \int_{xy} N_1^2 \, dxdy = \mu \frac{A_e}{6} \tag{A.13}$$

$$[B]_{e(1,2)} = \mu \int_{xy} N_1 N_2 \, dxdy = \mu \frac{A_e}{12} \tag{A.14}$$

$$[B]_{e(1,4)} = 0 \tag{A.15}$$

And it contains several null values:

$$[B]_e = \mu \begin{bmatrix} \frac{A_e}{6} & \frac{A_e}{12} & \frac{A_e}{12} & 0 & 0 & 0 & 0 & 0 & 0 \\ \frac{A_e}{12} & \frac{A_e}{6} & \frac{A_e}{12} & 0 & 0 & 0 & 0 & 0 & 0 \\ \frac{A_e}{12} & \frac{A_e}{12} & \frac{A_e}{6} & 0 & 0 & 0 & 0 & 0 & 0 \\ 0 & 0 & 0 & \frac{A_e}{6} & \frac{A_e}{12} & \frac{A_e}{12} & 0 & 0 & 0 \\ 0 & 0 & 0 & \frac{A_e}{12} & \frac{A_e}{6} & \frac{A_e}{12} & 0 & 0 & 0 \\ 0 & 0 & 0 & \frac{A_e}{12} & \frac{A_e}{12} & \frac{A_e}{6} & 0 & 0 & 0 \\ 0 & 0 & 0 & 0 & 0 & 0 & \frac{A_e}{6} & \frac{A_e}{12} & \frac{A_e}{12} \\ 0 & 0 & 0 & 0 & 0 & 0 & \frac{A_e}{12} & \frac{A_e}{6} & \frac{A_e}{12} \\ 0 & 0 & 0 & 0 & 0 & 0 & \frac{A_e}{12} & \frac{A_e}{12} & \frac{A_e}{6} \end{bmatrix} \tag{A.16}$$

References

[1] G. Lifante, "Introduction to Integrated Photonics: Fundamentals", *Wiley and Sons*, (2003).

[2] A. Liu, R. Jones, L. Liao, D. Rubin, O. Cohen, R. Nicolaescu, and M. Paniccia, "A high speed silicon optical modulator based on a metal-oxide semiconductor capacitor", *Nature*, **472**, 615–618 (2004).

[3] T. Baba, S. Akiyama, M. Imai, N. Hirayama, H. Takahashi, Y. Noguchi, T. Horikawa, and T. Usuki, "50-Gb/s ring-resonator-based silicon modulator", *Optics Express*, **21**(10), 11869–11876 (2013).

[4] M. Wuttig and N. Yamada, "Phase-change materials for rewriteable data storage", *Nature Mater*, **6**(11), 824–832 (2007).

[5] M. Wuttig, H. Bhaskaran, and T. Taubner, "Phase-change materials for non-volatile photonic applications", *Nature Photonics*, **11**(8), 465–476 (2017).

[6] Z. Yang and S. Ramanathan, "Breakthroughs in photonics 2014: Phase change materials for photonics", *IEEE Photonics Journal*, **7**(3), 1–5 (2015).

[7] B. M. A. Rahman and J. B. Davies, "Finite-element solution of integrated optical waveguides", *Journal of Lightwave Technology*, **2**(5), 682–688 (1984).

[8] https://en.wikipedia.org/wiki/Photonics.

[9] G. E. Moore, "Cramming more Components onto Integrated Circuits", *Electronics*, **38**(8), 114-117 (1965).

[10] https://www.investopedia.com/terms/m/mooreslaw.asp.

[11] S. E. Miller, “Integrated optics: an introduction”, *Bell Syst. Tech. Journal*, **48**, 2059-2069 (1969).

[12] A. S. Hedaoo, “Silicon Photonics: A review”, *International Journal of Innovative Science, Engineering & Technology*, **3**(4), 392-398 (2016).

[13] R. Soref and J. P. Lorenzo, “All-silicon active and passive guided-wave components for λ = 1.3 and 1.6 μm”, *IEEE Journal of Quantum Electronics*, **22**(6), 873 – 879 (1986).

[14] X. Chen, M. M. Milosevic, S. Stankovic, S. Reynolds, and G. T. Reed, “The emergence of silicon photonics as a flexible technology platform,” *Proceedings of the IEEE*, **106**(12), 2101–2116 (2018).

[15] E. Cortesi, F. Namavar, and R. Soref, “Novel silicon-on-insulator structures for silicon waveguides”, *IEEE SOS/SOI Technology Conference, Stateline, USA*, 109 (1989).

[16] T. Bestwick, “ASOC/sup TM/-a silicon-based integrated optical manufacturing technology”, *48th Electronic Components and Technology Conference, Seattle, USA*, 566-571 (1998).

[17] Y. Vlasov and S. McNab, “Losses in single-mode silicon-on-insulator strip waveguides and bends”, *Optics Express*, **12**(8), 1622-1631 (2004).

[18] L. Lin, Z. Li, J. Feng, and Z. Zhang., “Indirect to direct band gap transition in ultra-thin silicon films”, *Physical Chemistry Chemical Physics*, **16**, 6063-6067 (2013).

[19] G. T. Reed, G. Mashanovich, F. Y. Gardes, and D. J. Thomson, "Silicon-optical modulator", *Nature Photonics*, **4**, 518-526 (2010).

[20] G. T. Reed and A. P. Knights, "Silicon Photonics: An Introduction", *John Wiley & Sons*, Chapter. 4, 97-103 (2004).

[21] R. Soref and B. Bennett, "Electrooptical effects in silicon", *IEEE Journal of Quantum Electronic*, **23**(1), 123–129 (1987).

[22] G. Cocorullo and I. Rendina, "Thermo-optical modulation at 1.5 μm in silicon etalon", *Electronics Letters*, **28**(1), 83-85 (1992).

[23] C. Barrios, V. R. Almeida, R. Panepucci, and M. Lipson, "Electrooptic modulation of silicon-on-insulator submicrometer-size waveguide devices", *Journal of Lightwave Technology*, **21**(10), 2332-2339 (2003).

[24] F. Y. Gardes, G. T. Reed, N. Emerson, and C. Png, "A sub-micron depletion type photonic modulator in silicon on insulator", *Optics Express*, **13**(22), 8845-8854 (2005).

[25] T. Moriyama, D. Tanaka, P. Jain, H. Kawashima, and M. Kuwahara, "Ultra-compact, self-holding asymmetric Mach-Zehnder interferometer switch using $Ge_2Sb_2Te_5$ phase-change material", *IEICE Electronics Express*, **11**(15), 20140538 (2014).

[26] K. J. Miller, R. F. Haglund, and S. M. Weiss, "Optical phase change materials in integrated silicon photonic devices: review", *Optical Materials Express*, **8**(8), 2415-2429 (2018).

[27] S. R. Ovshinsky, "Reversible electrical switching phenomena in disordered structures", *Physical Review Letters*, **21**(20), 1450–1453 (1968).

[28] S. H. Lee, Y. Jung, and R. Agarwal, "Highly scalable non-volatile and ultra-low-power phase-change nanowire memory", *Nature Nanotechnology*, **2**(10), 626-630 (2007).

[29] H. Tong, Z. Yang, N. N. Yu, L. J. Zhou, and X. S. Miao, "Work function contrast and energy band modulation between amorphous and crystalline $Ge_2Sb_2Te_5$ films", *Applied Physics Letters*, **107**(8), 082101 (2015).

[30] Q. Wang, J. Maddock, E. T. F. Rogers, T. Roy, C. Craig, and K. F. Macdonald, "1.7 Gbit/in.^{2} gray-scale continuous-phase-change femtosecond image storage", *Applied Physics Letters*, **104**(12), 121105 (2014).

[31] L. Zou, M. Cryan, and M. Klemm, "Phase change material based tuneable reflectarray for free-space optical inter/intra chip interconnects", *Optics Express*, **22**(20), 24142-241428 (2014).

[32] R. Soref, "Phase-change materials for Group-IV electro-optical switching and modulation", *12th International Conference on Group IV Photonics, Vancouver, Canada*, 157-158 (2015).

[33] C. N. Berglund, "Thermal filaments in vanadium dioxide", *IEEE Transactions on Electron Devices*, **16**(5), 432-437 (1969).

[34] F. Morin, "Oxides which show a metal-to-insulator transition at the Neel temperature", *Physical Review Letters*, **3**(1), 34–36 (1959).

[35] B. Wu, A. Zimmers, H. Aubin, R. Ghosh, Y. Liu, and R. Lopez, "Electric-field-driven phase transition in vanadium dioxide", *Physical Review B*, **84**(24), 241410 (2011).

[36] K. Appavoo, B. Wang, N.F. Brady, M. Seo, J. Nag, R.P. Prasankumar, and D.J. Hilton, "Ultrafast phase transition via catastrophic phonon collapse driven by plasmonic hot-electron injection", *Nano Letters*, **14**(3), 1127–1133 (2014).

[37] M. Liu, H. Y. Hwang, H. Tao, A. C. Strikwerda, K. Fan, G. R. Keiser, and A. J. Sternbach, "Terahertz-field-induced insulator-to-metal transition in vanadium dioxide metamaterial", *Nature*, **487**, 345-348 (2012).

[38] M. Nakano, K. Shibuya, and D. Okuyama, "Collective bulk carrier delocalization driven by electrostatic surface charge accumulation", *Nature*, **487**, 459–462 (2012).

[39] Z. Yang, C. Ko and S. Ramanathan, "Metal-insulator transition characteristics of VO_2 thin films grown on Ge (100) single crystals," *Journal of Applied Physics*, **108**(7), 073708 (2010).

[40] A. Joushaghani, "Sub-volt broadband hybrid plasmonic-vanadium dioxide switches", *Applied Physics Letters*, **102**(6), 061101 (2013).

[41] M. D. Goldflam, "Reconfigurable gradient index using VO_2 memory metamaterials", *Applied Physics Letters*, **99**(4), 044103 (2011).

[42] A. Joushaghani, J. Jeong, S. Paradis, D. Alain, J. S. Aitchison, and J. K. Poon, "Wavelength-size hybrid Si-VO_2 waveguide electro-absorption optical switches and photodetectors", *Optics Express*, **23**(3), 3657–3668 (2015).

[43] R.M. Briggs, I.M. Pryce, and H.A. Atwater, "Compact silicon photonic waveguide modulator based on the vanadium dioxide metal-insulator phase transition," *Opt. Express* **18**(11), 11192-11201 (2010).

[44] M. Kuwahara, S. Takehara, Y. Kashihara, and K. Watabe, "Experimental study of high-density rewritable optical disk using a blue-laser diode", *Japanese Journal of Applied Physics*, **42**(1), 1068 (2003).

[45] W. Zhang, M. Wuttig, and R. Mazzarello, "Effects of stoichiometry on the transport properties of crystalline phase-change materials", *Scientific Reports*, **5**, 13496 (2015).

[46] S. Guerin, B. Hayden, D.W. Hewak, and C. Vian, "Synthesis and screening of phase change chalcogenide thin film materials for data storage", *ACS Combinatorial Science*, **19**(7), 478–491 (2017).

[47] J. C. Phillips, "Topology of covalent non-crystalline solids I: Short-range order in chalcogenide alloys", *Journal of Non-Crystalline Solids*, **34**(2), 153–181 (1979).

[48] O. Ueno and H. Kobayashi, "Optical Recording Medium", *U.S. Patent*, 5254382 (1993).

[49] P. Guo, A. Sarangan, and I. Agha, "A review of germanium-antimony-telluride phase change materials for non-volatile memories and optical modulators", *Applied Sciences*, **9**(3), 530 (2019).

[50] T. Kato and K. Tanaka, "Electronic properties of amorphous and crystalline $Ge_2Sb_2Te_5$ films", *Japanese Journal of Applied Physics*, **44**(1), 7340 (2005).

[51] A. Pirovano, A.L. Lacaita, A. Benvenuti, F. Pellizzer and R. Bez, "Electronic Switching in Phase-Change Memories", *IEEE Transactions on Electron Devices*, **51**(3), 452-459 (2004).

[52] J. Park, S. Eom, and H. Lee, "Optical properties of pseudobinary GeTe, $Ge_2Sb_2Te_5$, $GeSb_2Te_4$, $GeSb_4Te_7$, and Sb_2Te_3 from ellipsometry and density functional theory", *Physical Review B*, **80**(11), 115209 (2009).

[53] N. Yamada, E. Ohno, K. Nishiuchi, N. Akahira, and M. Takao, "Rapid-phase transitions of GeTe-Sb_2Te_3 pseudobinary amorphous thin films for an optical disk memory", *Journal of Applied Physics*, **69**(5), 2849–2856 (1991).

[54] S. Kohara, K. Kato, S. Kimura, H. Tanaka, T. Usuki, K. Suzuya, and H. Tanaka, "Structural basis for the fast phase change of $Ge_2Sb_2Te_5$: Ring statistics analogy between the crystal and amorphous states", *Applied Physics Letters*, **89**(20), 201910 (2006).

[55] T. Cao, L. Zhang, R. E. Simpson, and M. J. Cryan, "Mid-infrared tunable polarization-independent perfect absorber using a phase-change metamaterial", *Journal of the Optical Society of America B*, **30**(6), 1580-1585 (2013).

[56] K. Shportko, S. Kremers, M. Woda, D. Lencer, J. Robertson, and M. Wuttig, "Resonant bonding in crystalline phase-change materials", *Nature Materials*, **7**(8), 653–658 (2008).

[57] Y. Zhang, J. Li, J. B. Chou, Z. Fang, A. Yadav, H. Lin, and Q. Du, "Broadband transparent optical phase change materials", *Conference on Lasers and Electro-Optics (CLEO), OSA Technical Digest (online)*, JTh5C.4 (2017).

[58] Q. Zhang, Y. Zhang, J. Li, R. Soref, T. Gu, and J. Hu, "Broadband nonvolatile photonic switching based on optical phase change materials: beyond the classical figure-of-merit", *Optics Letters*, **43**(1), 94-97 (2018).

[59] K. J. A. Ooi, P. Bai, H. S. Chu, and L. K. Ang, "Ultracompact vanadium dioxide dual-mode plasmonic waveguide electroabsorption modulator", *Nanophotonics*, **2**(1), 13–19 (2013).

[60] J. Choe and J. Kim, "Design of vanadium dioxide based plasmonic modulator for Both TE and TM Polarization Mode", *IEEE Photonics Technology Letters*, **27**(5), 514-517 (2015).

[61] J. Kim, "CMOS-compatible hybrid plasmonic modulator based on vanadium dioxide insulator-metal phase transition", *Optics Letters*, **39**(13), 3997-4000 (2014).

[62] L. Sánchez, S. Lechago, and P. Sanchis, "Ultra-compact TE and TM pass polarizers based on vanadium dioxide on silicon", *Optics Letters.* **40**(7), 1452-1455 (2015).

[63] H. Liang, R. Soref, J. Mu, A. Majumdar, X. Li, and W. Huang, "Simulations of silicon-on-insulator channel-waveguide electrooptical 2 × 2 Switches and 1 × 1 modulators using a $Ge_2Sb_2Te_5$ self-holding layer", *Journal of Lightwave Technology*, **33**(9), 1805-1813 (2015).

[64] H. Zhang, L. Zhou, L. Lu, J. Chen, and B. M. A. Rahman, "Non-volatile optical switch based on a GST-loaded directional coupler", *IEEE 3rd Optoelectronics Global Conference (OGC), Shenzhen, China,* (2018).

[65] H. Zhang, L. Zhou, B. M. A. Rahman, X, Wu, L. Lu, Y. Xu, J. Song, and J. Chen, "Ultra-compact Si-GST hybrid waveguides for nonvolatile light wave manipulation", *IEEE Photonics Journal*, **10**(1), 2200110 (2018).

[66] H. Zhang, L. Zhou, L. Lu, J. Xu, N. Wang, H. Hu, B. M. A. Rahman, Z. Zhou, and J. Chen, "Miniature multilevel optical memristive Switch Using Phase Change Material", *ACS Photonics*, **6**(9), 2205-2212 (2019).

[67] Z. Yu, J. Zheng, P. Xu, W. Zhang, and Y. Wu, "Ultracompact electro-optical modulator-based $Ge_2Sb_2Te_5$ on Silicon", *IEEE Photonics Technology* Letters, **30**(3), 250-253 (2018).

[68] F. D. Leonardis, R. Soref, V. M. N. Passaro, Y. Zhang, and J. Hu, "Broadband electro-optical crossbar switches using low-loss $Ge_2Sb_2Se_4Te_1$ phase change material", *Journal of Lightwave Technology*, **37**(13), 3183-3191 (2019).

[69] W. Jiang, “Reconfigurable mode (De)multiplexer using $Ge_2Sb_2Se_4Te1$ based triple-silicon-waveguide”, *IEEE Photonics Technology Letters*, **30**(24), 2119-2122 (2018).

[70] W. Jiang, “Reconfigurable mode (de) multiplexer via 3-D triple-waveguide directional coupler with optical phase change material”, *Journal of Lightwave Technology*, **37**(3), 1000-1007 (2019).

[71] N. Dhingra, J. Song, G. J. Saxena, E. K. Sharma, and B. M. A. Rahman, “Design of a compact low-loss phase shifter based on optical phase change material”, *IEEE Photonics Technology Letters*, **31**(21) ,1757-1760 (2019).

[72] R. Zia, M. D. Selker, P. B. Catrysse and M. L. Brongersma, “Geometries and materials for subwavelength surface plasmon modes”, *Journal of the Optical Society of America A*, **21**(12), 2442–2446 (2004).

[73] K. Kawano, T. Kitoh, M. Kohtoku, T. Ito and Y. Hasumi, “Bidirectional finite -element method-of-line beam propagation method (FE-MoL-BPM) for analyzing optical waveguides with discontinuities”, *IEEE Photonics Technology Letters*, **10**(2), 244–245 (1998).

[74] S. Ahmed, “Finite Element Method for Waveguide Problems”, *Electron Letters*, **4**, 381-389 (1968).

[75] B. M. A. Rahman and A. Agrawal, “Finite Element Modeling Methods for Photonics”, Artech House, USA, (2013).

[76] A. Berk, “Variational principles for electromagnetic resonators and waveguides”, *IRE Transactions on Antennas and Propagation*, **4**(2), 104–111 (1956).

[77] J. M. A. Svedin, "A numerically efficient finite-element formulation for the general waveguide problem without spurious modes", *IEEE Transactions on Microwave Theory and Techniques*, **37**(11), 1708-1715 (1989).

[78] W. J. English and F.J. Young, "An **E** vector variational formulation of the maxwell equations for cylindrical waveguide problems", *IEEE Transactions on Microwave Theory and Techniques*, **19**(1), 40-46 (1971).

[79] B. M. A. Rahman and J. B. Davies, "Finite-element analysis of optical and microwave waveguide problems", *IEEE Transactions on Microwave Theory and Techniques* **32**(1), 20-28 (1984).

[80] B. M. A. Rahman and J. B. Davies, "Penalty function improvement of waveguide solution by finite elements", *IEEE Transactions on Microwave Theory and Techniques*, **32**(8), 922-928 (1984).

[81] B. M. A. Rahman and J. B. Davies, "Finite-element solution of integrated optical waveguides", *Journal of Lightwave Technology*, **2**(5), 682–688 (1984).

[82] J. B. Davies, F. A. Fernandez, and G. Y. Philippou, "Finite element analysis of all modes in cavities with circular symmetry", *IEEE Transactions on Microwave Theory and Techniques*, **30**(11), 1975-1980 (1982).

[83] B. M. A. Rahman and J. B. Davies, "Analyses of optical waveguide discontinuities", *Journal of Lightwave Technol*ogy, **6**(1), 52–57 (1988).

[84] C. Themistos, B. M. A. Rahman, A. Hadjicharalambous, and K. T. V. Grattan, "Loss/gain characterization of optical waveguides", *Journal of Lightwave Technol*ogy, **13**(8), 1760–1765 (1995).

[85] L. Chrostowski and M. Hochberg, "Silicon Photonics Design: From Devices to Systems", Cambridge, Cambridge University Press, (2015).

[86] K. Yee, "Numerical solution of initial boundary value problems involving Maxwell's equations in isotropic media", *IEEE Transactions on Antennas and Propagation*, **14**(3), 302–307 (1966).

[87] A. Taflove, "Application of the finite-difference time-domain method to sinusoidal steady-state electromagnetic-penetration problems", *IEEE Transactions on Electromagnetic Compatibility*, **EMC-22**(3), 191–202 (1980).

[88] N. Ali and R. Kumar, "Design and simulations of photonic switch using hybrid $Ge_2Sb_2Te_5$-silicon waveguides in mid-IR region", *17th International Conference on Optical Communications and Networks, Zhuhai, China*, Proceedings Volume **11048**, 1104836 (2019).

[89] H. Zhang, L. Zhou, J. Xu, L. Lu, J. Chen, and B. M. A. Rahman, "All-optical non-volatile tuning of an AMZI-coupled ring resonator with GST phase-change material", *Optics Letters*, **43**(22), 5539-5542 (2018).

[90] P. D. Trinh, S. Yegnanarayanan, and B. Jalali, "Integrated optical directional couplers in silicon-on-insulator", *Electronics Letters*, **31**(24), 2097-2098 (1995).

[91] J. Song, S. Ghosh, N. Dhingra, H. Zhang, L. Zhou, and B. M. A. Rahman, "Feasibility study of a $Ge_2Sb_2Te_5$-clad silicon waveguide as a non-volatile optical on-off switch", *OSA Continuum*, **2**(1), 49-63 (2019).

[92] J. Song, S. Ghosh, H. Zhang, L. Zhou, and B. M. A. Rahman, "Design, optimization, and performance evaluation of GSST clad low-loss non-volatile switches", *Applied Optics*, **58**(31), 8687-8694 (2019).

[93] N. Dhingra, J. Song, S. Ghosh, L. Zhou, and B. M. A. Rahman, "Design of phase change $Ge_2Sb_2Te_5$ based on-off electro-optic switch", *Silicon Photonics XIII, SPIE. Photonics West, San Francisco, California, United States*, **10537**, pp. 105370Z (2018).

[94] H. Zhang, X. Yang, L. Lu, J. Chen, B. M. A. Rahman, and L. Zhou, "Comparison of the phase change process in a GST-loaded silicon waveguide and MMI," *Opt. Express*, **29**(3), 3503-3514 (2021).